Measurement of neutral current Drell-Yan production at 8 TeV with the ATLAS detector

by

Tony Kwan
B.Sc., University of Victoria, 2010
M.Sc., University of Victoria, 2012

A Dissertation Submitted in Partial Fulfillment of the
Requirements for the Degree of

DOCTOR OF PHILOSOPHY

in the Department of Physics and Astronomy

Measurement of neutral current Drell-Yan production at 8 TeV with the ATLAS detector

by

Tony Kwan
B.Sc., University of Victoria, 2010
M.Sc., University of Victoria, 2012

Supervisory Committee

Dr. Richard Keeler, Supervisor
(Department of Physics and Astronomy)

Dr. Robert Kowalewski, Departmental Member
(Department of Physics and Astronomy)

Dr. Robert McPherson, Departmental Member
(Department of Physics and Astronomy)

Dr. Cornelia Bohne, Outside Member
(Department of Chemistry)

Supervisory Committee

Dr. Richard Keeler, Supervisor
(Department of Physics and Astronomy)

Dr. Robert Kowalewski, Departmental Member
(Department of Physics and Astronomy)

Dr. Robert McPherson, Departmental Member
(Department of Physics and Astronomy)

Dr. Cornelia Bohne, Outside Member
(Department of Chemistry)

ABSTRACT

Neutral current Drell-Yan production, $q\bar{q} \to Z/\gamma^* \to e^-e^+$, in proton-proton collisions at the LHC was studied with the ATLAS detector. The 20.1 fb^{-1} data set used in this precision measurement was collected in 2012 during which the LHC collided protons at a centre-of-mass energy of 8 TeV. The production rate or differential cross-section was measured in three-dimensions: invariant mass M_{ee}, absolute rapidity $|y_{ee}|$, and cosine of the polar angle θ^* in the Collins-Soper frame. A measurement of the forward-backward asymmetry A_{FB} was obtained from the differential cross-section by summing over the $\cos\theta^* > 0$ (forward) and the $\cos\theta^* < 0$ (backward) events and taking their difference. The three-dimensional differential cross-section measurement presented in this dissertation can be used to constrain the M_{ee}- and $|y_{ee}|$-dependent parton distribution functions of the proton and the A_{FB} results can be used to extract a measurement of the weak mixing angle θ_{W}.

Contents

List of Tables

List of Figures

DECLARATION

Having over 3000 members from 175 institutions spread across the world, the scientific results produced by the ATLAS experiment are made possible by the collective efforts of many people. The same is true for the material presented in this dissertation which relies on the work of fellow ATLAS members. Given that one of the main purposes of a dissertation is to judge the quality of the author's research, it is important to distinguish the work of the student from the work of his colleagues.

While the collection of the data and the derivation of many of the corrections to the data and simulation used was performed by others, the data analysis itself, the precision measurement of Drell-Yan production in the electron channel, was done by the author. The measurement required filtering the data for signal events, estimating the background contamination, and unfolding the data to generator-level. Additionally, all major uncertainties affecting the measurement needed to be quantified and propagated to the final measurement. These tasks are described in Chapters 7 to 9 and were performed by the author.

In addition to the main analysis presented, a second electron channel measurement was made. Where the main analysis studied electrons reconstructed in the central region of the ATLAS detector, this second measurement looked at events in which one of the two electrons was reconstructed in the forward region. Use of forward electrons presented a whole new set of challenges, namely the need for a dedicated calibration of the energy of forward electrons. This calibration and the measurement, which are outlined in Appendix B, was also done by the author.

Discussed in Appendix C, the electron measurements along with a muon channel measurement constitute an ATLAS analysis which, at the time of writing this dissertation, is in the process of being published. It was observed that measurements of muon momentum showed a charge bias which significantly degraded the muon results. As a solution, the author derived a set of corrections that minimized the effect of the bias greatly improving the muon measurement and the analysis as a whole.

The publication process in ATLAS is extensive requiring many presentations – most of which were given by the author – of the work to physics groups consisting of ATLAS management and experts in the type of physics being published. Defending the work to the ATLAS collaboration is nearing completion. The author has been involved at every step of this process.

ACKNOWLEDGEMENTS

Many people made this possible. I would like to give a special thanks to the following:

Dr. Michel Lefebvre, for his leadership and inspiration.

The Z3D analysis team, it's been a pleasure working alongside you and an even greater pleasure getting to know you.

My supervisory committee, who have kept a watchful eye on me pretty much since day one.

Dr. Richard Keeler, a grad student couldn't ask for a better supervisor and a young man couldn't ask for a better mentor.

My family and friends.

To Mom

Chapter 1

Introduction

Until 1956, it was believed that the fundamental forces of nature were invariant under parity transformations. Both theory and experiment supported this assumption as no evidence was found to contradict it. This all changed when an experiment was designed [1] then conducted [2] proving parity is not always conserved. Today, after significant advances in both theoretical and experimental particle physics, we know that electromagnetic and strong interactions conserve parity while weak interactions violate it. Weak interactions are mediated by the $W^{\pm}$ and Z^0 bosons and due to their parity violating nature, final state particles produced in collision events involving the $W^{\pm}$ and Z^0 exhibit asymmetry in their angular distributions.

Drell-Yan [3] events are produced at the LHC when a quark, q, from one proton and an antiquark, $\bar{q}$, from another annihilate to form a Z boson or virtual photon, γ^*, which then decays into a lepton-antilepton pair $\ell^-\ell^+$:

$$q\bar{q} \to Z/\gamma^* \to \ell^-\ell^+, \quad \ell = e, \mu, \tau,$$

where the lepton can be an electron e^-, muon μ^-, or tau τ^-. This dissertation outlines a precision measurement of the neutral current Drell-Yan production rate or *differential cross-section* at the LHC in 2012 using the ATLAS detector. Only $Z/\gamma^* \to e^-e^+$ or *electron channel* events will be included in the analysis. From the differential cross-section, a measurement of the asymmetry exhibited in Drell-Yan events resulting from weak interactions can be obtained. Both the differential cross-section and asymmetry measurements will be presented in detail and compared to state-of-the-art theoretical predictions.

1.1 The LHC and the ATLAS Detector

As deep as 175 m underground, near the France-Switzerland border is the LHC (Large Hadron Collider) [4], a circular particle accelerator approximately 26.7 km in circumference that collides hadrons at very high energies. Under the banner of CERN (European Organization for Nuclear Research) thousands of scientists and engineers from all over the world constructed the LHC from 1998 to 2008. It was designed to reach a proton-proton colliding centre-of-mass energy of 14 TeV and an instantaneous luminosity of 10^{34} $\mathrm{cm}^{-2}\mathrm{s}^{-1}$. The LHC has the potential to produce physics at the energy frontier for many years to come.

Seven experiments are currently being conducted at CERN collecting and analyzing data from the LHC – one being the ATLAS (A Toroidal LHC ApparatuS) experiment [5]. The ATLAS experiment is a collaboration of more than 3000 physicists from 175 institutions in 38 different countries. Construction of many of its components began in 1994 by universities and labs across the globe and by 2004, these parts were shipped to and assembled in an underground cavern in Geneva, Switzerland where the ATLAS detector still collects data to this day. ATLAS is a massive machine, 24 m in diameter and 44 m in length, and cylindrical in shape. Designed to be a general purpose detector, the ATLAS detector is capable of measuring a wide array of physical phenomena.

The LHC and ATLAS detector were conceived with several physics goals in mind: to find the Higgs boson [6, 7, 8, 9, 10] and measure its properties, to find physics beyond the Standard Model such as Supersymmetry [11] and dark matter [12], and to improve on current measurements of the Standard Model.

On July 4, 2012, ATLAS, along with its sister experiment CMS (Compact Muon Solenoid) [13], publicly announced the discovery of a Higgs-like particle at a statistical confidence of 5-sigma which corresponds to a probability of one in 3.5 million that a random fluctuation would yield such a result [14, 15]. Current measurements of the properties of this particle are consistent with it being the Higgs boson predicted by the Standard Model [16]. This discovery stands as one of the great triumphs of modern particle physics.

The Standard Model is not a complete theory of particle physics as there are many questions it cannot answer. Supersymmetry is a theoretical extension of the Standard Model which provides some answers to these questions. Searches for signatures that hint at the validity of Supersymmetry have been conducted and although nothing yet

has been discovered, large areas of phase space have been excluded as possible regions where Supersymmetry may exist [17]. Efforts have been made [18, 19] and continue to be made searching for dark matter which is known to exist in the universe from astronomical observations of galaxy rotations [20, 21]. So far it has not been observed at the LHC.

Using the LHC and ATLAS detector, Standard Model processes have been measured at new energy scales which allow us to test and expand our current theoretical understanding of the Standard Model. In particular, measurements of $W^{\pm}/Z^{0}$ production – similar to the topic of this dissertation – are used to improve upon many different past measurements of, for example, the structure of the proton, the mass of the $W^{\pm}$, and the dynamics of strong interactions. Standard Model measurements are also used to study and calibrate the performance of the detector which benefits the entire ATLAS physics programme.

1.2 Dissertation Organization

The dissertation is organized into the following chapters:

Chapter 1, Introduction - an introduction to the measurement along with a few remarks on the LHC and ATLAS experiment.

Chapter 2, Theoretical Motivation - a motivation of the measurement using theories from the Standard Model and Parton Model of particle physics.

Chapter 3, The ATLAS Experiment - a discussion focused on the technical aspects of the LHC and the ATLAS detector.

Chapter 4, Data and Monte Carlo - an overview of the format of ATLAS data and simulation and those specifically used in this measurement.

Chapter 5, Electrons in ATLAS - a description of electron reconstruction, identification, and performance in ATLAS.

Chapter 6, Methodology - an introduction to the measurement methodology used in this analysis.

Chapter 7, Measurement - a detailed description of the differential cross-section measurement.

Chapter 8, Uncertainties - a report on the uncertainties and their effect on the cross-section.

Chapter 9, Results - a presentation of the cross-section and asymmetry measurements.

Chapter 10, Conclusions - concluding remarks on the measurements and their future uses.

Chapter 2

Theoretical Motivation

The Standard Model of particle physics is a theoretical framework that describes the dynamics of elementary particles as they undergo electromagnetic, weak, and strong interactions. Since its development in the latter half of the 20th century, many experiments have tested its validity and astonishingly, the Standard Model has been able to predict the outcomes of these experiments with great accuracy time and time again. In this chapter, a brief description of the mathematical formalism behind the Standard Model is presented and its relevance to this dissertation topic will be highlighted. Following is an introduction to the Parton Model and a description of the kinematic observables of interest.

2.1 The Standard Model

Twelve elementary *fermions* of spin 1/2 are postulated in the Standard Model which are divided evenly into two categories, *leptons* ℓ and *quarks* q as shown in Table 2.1. The first generation of fermions, which include the up, down, electron, and electron neutrino, are the constituents of the known matter in the universe. Fermions interact with each other via three fundamental forces known as the electromagnetic, weak, and strong forces which are mediated by spin-1 particles known as *gauge bosons*. The electromagnetic force is mediated by the massless photon, γ, while the weak force is mediated by massive bosons known as the $W^{\pm}$ and Z^0. Mediating the strong force are eight gluons, $g_1, g_2, ..., g_8$, each corresponding to a linearly independent *colour charge* state and, like the photon, they are massless. The final particle predicted by the Standard Model and the last to be discovered is the scalar spin-0 Higgs boson which

is related to the weak gauge bosons as well as the leptons and quarks having nonzero masses. The gauge bosons and the Higgs are listed in Table 2.2 along with several of their properties.

According to the Standard Model, all fermions are capable of interacting weakly. Electrically charged leptons can additionally interact electromagnetically and quarks, which possess electric and colour charges, can engage in weak, electromagnetic, and strong interactions. It becomes apparent at very high momentum transfer that the electromagnetic and weak forces are related to each other. *Electroweak* interactions are described by a quantum field theory (QFT) with a broken gauge symmetry. Purely electromagnetic interactions form a subset of electroweak interactions which are described with quantum electrodynamics (QED). Based on the mathematical formalism of QED, strong interactions are described by quantum chromodynamics (QCD). A brief introduction to these theories is given in the following sections.

Generation	Quark	Symbol	Charge	Mass	Lepton	Symbol	Charge	Mass
First	up	u	$+2/3$	2.3 MeV	electron	e	-1	0.511 MeV
	down	d	$-1/3$	4.8 MeV	electron neutrino	ν_e	0	< 2.3 eV
Second	charm	c	$+2/3$	1.27 GeV	muon	μ	-1	106 MeV
	strange	s	$-1/3$	104 MeV	muon neutrino	ν_μ	0	< 0.2 MeV
Third	top	t	$+2/3$	173 GeV	tau	τ	-1	1.8 GeV
	bottom	b	$-1/3$	4.7 MeV	tau neutrino	ν_τ	0	< 18.2 MeV

Table 2.1: Elementary fermions of the Standard Model. They are categorized into three generations with the first being the constituents of ordinary matter.

Boson	Symbol	Spin	Charge	Mass	Function
photon	γ	1	0	0	Mediates electromagnetic force
W boson	$W^\pm$	1	± 1	80.4 GeV	Mediates weak force
Z boson	Z^0	1	0	91.2 GeV	Mediates weak force
gluon	$g_1, g_2, ..., g_8$	1	0	0	Mediates strong force
Higgs boson	H	0	0	125.1 GeV	Generation of mass

Table 2.2: Bosons of the Standard Model. The γ, $W^\pm$, Z^0, and g mediate the electromagnetic, weak, and strong forces, respectively. The Higgs field is responsible for the generation of mass in the $W^\pm$ and Z^0 bosons and the leptons and quarks.

2.1.1 Quantum Electrodynamics

Just as in classical mechanics, the Lagrangian of a QFT is used to determine the dynamics of a system. Given a Lagrangian $\mathcal{L}$, a prescription known as *Feynman rules* [22] can be used to calculate a quantity known as the *amplitude* or *matrix element*, denoted as $\mathcal{M}$. The amplitude is a key quantity as it is used in calculations of observables such as cross-sections and decay widths. The Standard Model is comprised of several Lagrangians, the most important of which are highlighted in the following discussions.

Quantum electrodynamics is a local gauge theory [23], a type of field theory in which the Lagrangian is invariant under a continuous group of transformations known as *local gauge transformations*. In particular, QED is invariant under $U(1)$ symmetry transformations. Describing interactions between electrically charged fermions, the QED Lagrangian of the Standard Model is given by

$$\mathcal{L}_{\text{QED}} = i\bar{\psi}\partial_\mu\psi + m\bar{\psi}\psi - q\bar{\psi}\gamma^\mu\psi A_\mu - \frac{1}{4}F_{\mu\nu}F^{\mu\nu}, \tag{2.1}$$

where $\psi = \psi(x)$ is a Dirac spinor [23] that represents a spin-1/2 or fermion field; $\bar{\psi}$ is defined as $\bar{\psi} \equiv \psi^\dagger\gamma^0$; and γ^μ are the Dirac matrices. The first and second terms in Equation (2.1) represent the kinetic energy and mass terms of ψ whose excitations or particles have mass m. In a vacuum, $\mathcal{L}_{\text{QED}}$ would consist of only these two terms. The third term describes the interactions between ψ and the vector field A_μ, the strength of which is governed by coupling constant q which is the electric charge of the fermion. Excitations of the vector field A_μ correspond to photons and the absence of a term of the form $M_A^2 A_\mu A^\mu$ correctly predicts that the photon is massless. The last term in Equation (2.1) describes the electromagnetic field $F_{\mu\nu}$ defined as $F_{\mu\nu} = \partial_\mu A_\nu - \partial_\nu A_\mu$.

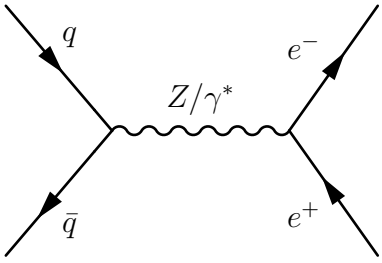

Figure 2.1: Leading order Drell-Yan diagram.

QED is used in this dissertation to predict the likelihood of photons being emitted

by the initial state quark and antiquark, known as *initial state radiation*, and the final state leptons, known as *final state radiation*. In Figure 2.1 is the simplest or *leading order* (LO) Feynman diagram of the Drell-Yan process. Diagrams with an additional photon, two of which are illustrated in Figure 2.2, are *next-to-leading order*[1] (NLO) in QED. Due to Z^0 exchange, QED is unable to fully describe the Drell-Yan process; it can, however, predict initial and final state radiation to extraordinary accuracy.

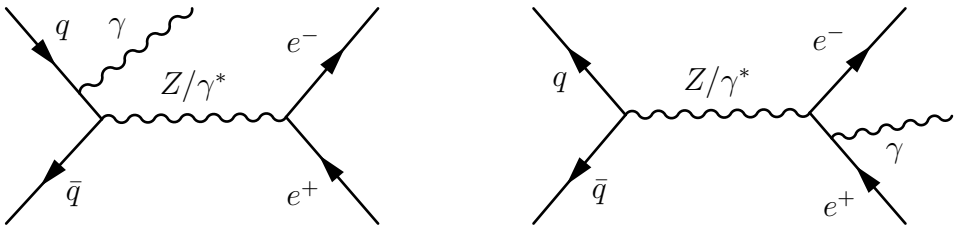

Figure 2.2: Examples of next-to-leading order QED Drell-Yan diagrams.

2.1.2 Quantum Chromodynamics

Quantum chromodynamics describes strong interactions between quarks which carry colour charge [24]. Unlike electric charge which can be described by a single number, colour charge comes in three varieties referred to as red, green, and blue. For example, a quark may possess either red, green, or blue colour charge while antiquarks carry antired, antigreen, or antiblue charge.

Constructed using much of the same formalism used in QED but invariant under $SU(3)$ transformations, the QCD Lagrangian of the Standard Model is

$$\mathcal{L}_{\text{QCD}} = \sum_f i\bar{\psi}_f \not{D}\psi_f - m_f\bar{\psi}_f\psi_f - \frac{1}{4}G^a_{\mu\nu}G^{\mu\nu}_a, \tag{2.2}$$

where the sum is over all quark flavours f and ψ_f are the fermion spin-1/2 fields whose excitations have mass m_f. Ensuring that the theory is gauge invariant, the covariant derivative in Equation (2.2) is defined as

$$D_\mu = \partial_\mu + ig_s\lambda^a G^a_\mu, \tag{2.3}$$

[1]The LO diagram is not unlike the zeroth-order term of a Taylor series while the NLO terms are analogous to the first-order terms. There exist an infinite number of Drell-Yan Feynman diagrams with varying numbers of photon emissions and exchanges just as there an infinite number of terms in a Taylor series.

where g_s is the strong coupling constant; λ^a are the Gell-Mann matrices; and G^a_μ correspond to the gluon fields. Feynman's slash notation, $\not{D}_\mu = \gamma^\mu D_\mu$, is used. The field strength tensors are defined as

$$G^a_{\mu\nu} = \partial_\mu G^a_\nu - \partial_\nu G^a_\mu + g_s h^a_{jk} G^j_\mu G^k_\nu, \tag{2.4}$$

analogous to $F_{\mu\nu}$ in QED. Again there are no terms in the Lagrangian of the form $M_G G^a_\mu G^{a\,\mu}$ predicting that gluons are massless. Substituting the expression for $G^a_{\mu\nu}$ into the third term in Equation (2.2) reveals that three and four gluon interactions are permitted in QCD, the strength of which are proportional to g_s and structure constants h^a_{jk} of $SU(3)$.

The strength of strong interactions varies greatly depending on the momentum transfer of the interacting particles. At low momentum transfer, the coupling between the particles is strong making it impossible to free constituent quarks from their hadrons. This phenomenon is known as *confinement* and it is the reason why colour charged states or free quarks and gluons do not exist in nature. Moreoever, when a quark or gluon is sufficiently separated from its hadron, quark-antiquark pairs travelling in the same direction as the original particle are created until a colourless state is formed. Collectively, these particles are known as a *jet* and the process which leads to their creation is known as *hadronization*. On the other hand, at sufficiently high momentum transfer, the coupling between the constituents of hadrons is weak enough such that the quarks and gluons can be mathematically treated as free particles, an approximation known as *asymptotic freedom*.

The Drell-Yan process is characterized by the annihilation of a quark and an antiquark. Carrying colour charge, the quark, antiquark, or potentially both may emit gluons which hadronize to form jets. Initial state radiation of this type can significantly alter the dynamics of the process ultimately affecting observables such as the energy and momentum of the final state lepton and antilepton. In order to make accurate predictions of the Drell-Yan process, QCD must be used to calculate the probability of gluon radiation. Figure 2.3 shows two NLO QCD Drell-Yan diagrams that can be accounted for using QCD.

2.1.3 Electroweak Theory

Electromagnetic and weak interactions are unified into a single gauge theory called *electroweak theory* [25, 26, 27]. In this theory, fermions are either left-handed, L,

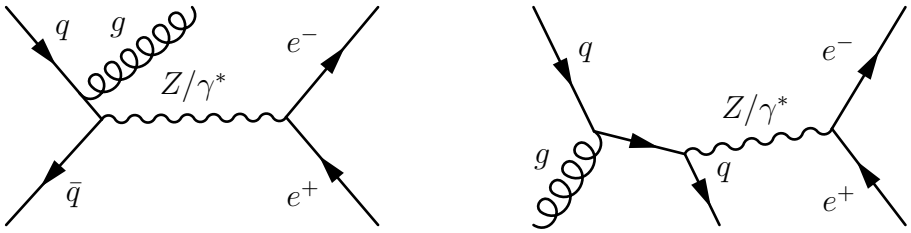

Figure 2.3: Examples of next-to-leading order QCD Drell-Yan diagrams.

or right-handed, R, and depending on the handedness, undergo electroweak interactions very differently. Experimentally, only left-handed neutrinos have been observed; therefore, in the Standard Model, charge changing weak interactions are all left-handed. With this knowledge, a logical grouping of the left-handed fermion fields is

$$\mathcal{L}_L = \begin{pmatrix} \ell_L \\ \nu_L \end{pmatrix}, \qquad \mathcal{Q}_R = \begin{pmatrix} q_L^u \\ q_L^d \end{pmatrix}, \tag{2.5}$$

where doublets have been formed with the left-handed lepton, ℓ_L, and neutrino, ν_L, fields and the left-handed up-type, q_L^u, and down-type, q_L^d, quark fields of each of the three families of leptons and quarks. For the right-handed fields, singlets

$$\mathcal{L}_R = \ell_R, \qquad \mathcal{Q}_R^u = q_R^u, \qquad \mathcal{Q}_R^d = q_R^d \tag{2.6}$$

are formed. The Lagrangian of this theory can then be written in terms of Equations (2.5) and (2.6):

$$\mathcal{L}_{\text{EW}} = \sum_{\ell,\,\nu,\,q} i\bar{\mathcal{L}}_L \not{D} \mathcal{L}_L + \sum_{\ell,\,\nu,\,q} i\bar{\mathcal{L}}_R \not{D} \mathcal{L}_R - \frac{1}{4} W_{\mu\nu}^k W^{k\,\mu\nu} - \frac{1}{4} B_{\mu\nu} B^{\mu\nu}, \tag{2.7}$$

where $W_{\mu\nu}^k$ $(k = 1, 2, 3)$ and $B_{\mu\nu}$ are the gauge field strength tensors defined in terms of the electroweak boson fields W_μ^1, W_μ^2, W_μ^3, and B_μ to be

$$W_{\mu\nu}^k = \partial_\mu W_\nu^k - \partial_\nu W_\mu^k + g\epsilon^{k\ell m} W_\mu^\ell W_\nu^m \tag{2.8}$$

and

$$B_{\mu\nu} = \partial_\mu B_\nu - \partial_\nu B_\mu, \tag{2.9}$$

where $\epsilon^{k\ell m}$ is the completely antisymmetric tensor. The covariant derivative in Equa-

tion (2.7) is

$$D_\mu = \partial_\mu - ig\tau^k W_\mu^k - ig'YB_\mu, \tag{2.10}$$

where g and g' are the coupling constants to fields W_μ^k and B_μ, respectively; τ^k is defined as $\tau^k = \sigma^k/2$ with σ^k being the Pauli matrices; and Y is the hypercharge of the fermion coupled to B_μ. Analogous to the electric charge q being the conserved quantum number of QED, $Y = 2(q - T_3)$, where T_3 is the third component of the weak isospin, is the conserved quantum number of electroweak theory.

Nowhere in Equation (2.7) are there mass terms of the form $M_{W^k}W_{\mu\nu}^k W^{k\,\mu\nu}$ or $M_B B_{\mu\nu}B^{\mu\nu}$. This contradicts the fact that the $W^\pm$ and Z^0 gauge bosons of weak interactions are known from experiment to be massive. This discrepancy is resolved by a construct known as the *Higgs mechanism* [6, 7, 8, 9, 10]. The Higgs mechanism introduces a scalar spin-0 field ϕ to the Standard Model. Known as the *Higgs field*, ϕ comes in the form of a complex doublet:

$$\phi = \begin{pmatrix} \phi^+ \\ \phi^0 \end{pmatrix} = \frac{1}{\sqrt{2}} \begin{pmatrix} \phi_1 + i\phi_2 \\ \phi_3 + i\phi_4 \end{pmatrix}. \tag{2.11}$$

The Higgs Lagrangian is

$$\mathcal{L}_{\text{Higgs}} = (D^\mu\phi)^\dagger(D_\mu\phi) - V(\phi), \tag{2.12}$$

where V is the Higgs potential defined as

$$V(\phi) = \kappa^2(\phi^\dagger\phi) + \lambda(\phi^\dagger\phi)^2. \tag{2.13}$$

Parameters κ and λ define the structure of the Higgs potential. If $\kappa^2 < 0$, minimizing V with respect to ϕ reveals that its minimum no longer corresponds to a vanishing field $\phi = (0, 0)$. Instead the minimum potential is obtained when

$$\phi^\dagger\phi = -\frac{\kappa^2}{2\lambda} = \frac{1}{2}v^2, \tag{2.14}$$

where $v = (-\kappa^2/\lambda)^{1/2}$ is known as the *vacuum expectation value*. A solution to Equation (2.14) is

$$\phi_0 = \frac{1}{\sqrt{2}} \begin{pmatrix} 0 \\ v + h \end{pmatrix}, \qquad \phi_1 = \phi_2 = \phi_3 = 0, \tag{2.15}$$

where real scalar field $h = h(x)$ is the *physical Higgs field*. To see how electroweak gauge bosons gain mass through the Higgs mechanism, it suffices to write the scalar terms of the Higgs Lagrangian:

$$\mathcal{L}_{\text{Higgs}} = (D^{\mu}\phi)^{\dagger}(D_{\mu}\phi) - V(\phi) + ..., \tag{2.16}$$

where the covariant derivative is

$$D_{\mu} = \partial_{\mu} - ig\tau^{k}W_{\mu}^{k} - i\frac{1}{2}g'B_{\mu}. \tag{2.17}$$

Substituting all known expressions into Equation (2.16) yields

$$\mathcal{L}_{\text{Higgs}} = \frac{v^2}{8}g^2\left[(W_{\mu}^{1} + W_{\mu}^{2})(W_{\mu}^{1} - W_{\mu}^{2}) + (gW_{\mu}^{3} - g'B_{\mu})(gW_{\mu}^{3} + g'B_{\mu})\right] + ... \tag{2.18}$$

Identifying terms of the form $M_{W^k}W_{\mu\nu}^{k}W^{k\,\mu\nu}$ and $M_B B_{\mu\nu}B^{\mu\nu}$ in Equation (2.18) reveals that there are three massive vector bosons and a single massless vector field:

$$\begin{aligned} W_{\mu}^{\pm} &= \frac{1}{\sqrt{2}}(W_{\mu}^{1} \mp iA_{\mu}^{2}), \qquad & M_W &= \frac{1}{2}gv; \\ Z_{\mu}^{0} &= \frac{1}{\sqrt{g^2 + g'^2}}(gW_{\mu}^{3} - g'B_{\mu}), \qquad & M_Z &= \frac{1}{2}(g^2 + g'^2)^{\frac{1}{2}}v; \\ A_{\mu} &= \frac{1}{\sqrt{g + g'^2}}(g'W_{\mu}^{3} + gB_{\mu}), \qquad & M_A &= 0. \end{aligned} \tag{2.19}$$

The $W^{\pm}$ of mass M_W are the physical charged gauge bosons that mediate the weak force. As for the other two, it is convenient to define a quantity known as the *weak mixing angle* θ_{W} that changes the basis from (W^3, B) to (Z^0, A) or the mass eigenstates:

$$\begin{pmatrix} Z^0 \\ A \end{pmatrix} = \begin{pmatrix} \cos\theta_{\text{W}} & -\sin\theta_{\text{W}} \\ \sin\theta_{\text{W}} & \cos\theta_{\text{W}} \end{pmatrix} \begin{pmatrix} W^3 \\ B \end{pmatrix}. \tag{2.20}$$

Possessing a mass of M_Z, Z^0 is the neutral mediator of the weak force and A is the massless photon of the electromagnetic force. It can be shown that θ_{W} is dependent on the coupling constants g and g':

$$\cos\theta_{\text{W}} = \frac{g}{\sqrt{g^2 + g'^2}}, \qquad \sin\theta_{\text{W}} = \frac{g'}{\sqrt{g^2 + g'^2}}. \tag{2.21}$$

The weak mixing angle is an important parameter in the Standard Model. The elementary charge can be defined in terms of θ_{W} as $e = g\sin\theta_{\text{W}}$ and the masses of the

$W^{\pm}$ and Z^0 can be related to each other as $M_W = M_Z \cos\theta_{\mathrm{W}}$ at leading order. It will be shown later on that a measurement of θ_{W} can be extracted using the measurement presented in this dissertation.

2.2 The Parton Model

Proposed by Richard Feynman in 1969 [28], the Parton Model is used to describe high energy collisions involving hadrons. The proton is not a fundamental particle but is instead comprised of three valence quarks (up, up, and down), gluons, and quark-antiquark pairs (also called *sea quarks*). Any one of these objects may be referred to as a *parton*. Suppose two protons with four-momenta P_1 and P_2 collide. The Parton Model states that it is the partons of the proton that undergo the hard scattering process [29]. Their four-momenta can be written as

$$p_1 = x_1 P_1, \qquad p_2 = x_2 P_2, \tag{2.22}$$

where x_1 and x_2 are the fractions of the total momentum of the protons carried by the interacting partons. In terms of initial state quantities, the momentum transferred from the initial state to the final state particles is

$$Q^2 = (p_1 + p_2)^2. \tag{2.23}$$

Assuming a sufficiently large Q^2 where asymptotic freedom can be approximated, the Parton Model makes the following statement regarding neutral current Drell-Yan production from proton-proton collisions:

$$\sigma = \sum_q \int dx_q dx_{\bar{q}} \left[f_{q/P_1}(x_q, Q^2) f_{\bar{q}/P_2}(x_{\bar{q}}, Q^2) + (q \leftrightarrow \bar{q}) \right] \hat{\sigma}, \tag{2.24}$$

where the sum is over all quark q flavours. Quantities $f_{q/P_1}(x_q, Q^2)$ and $f_{\bar{q}/P_2}(x_{\bar{q}}, Q^2)$ are known as *parton distribution functions* or PDFs. Determined using experimental data, PDFs give the probability of parton q carrying x_q of the total momentum of proton P_1 colliding with $\bar{q}$ carrying $x_{\bar{q}}$ of the total momentum of P_2 at a momentum transfer of Q^2. The term

$$q \leftrightarrow \bar{q} \equiv f_{\bar{q}/P_1}(x_q, Q^2) f_{q/P_2}(x_{\bar{q}}, Q^2) \tag{2.25}$$

accounts for the cases in which $\bar{q}$ is a constituent of P_1 and q is constituent of P_2.

And finally, $\hat{\sigma}$ is the subprocess cross-section for $q\bar{q} \to Z/\gamma^* \to \ell^-\ell^+$ calculated from electroweak theory assuming that the quarks are free particles.

In Figure 2.4, several PDFs of the proton are plotted as a function of fraction x for Q^2 values of 10 and 10^4 GeV^2. At low x, the total momentum is shared amongst a greater number of partons which leads to an increase in interactions involving sea quarks and gluons. When there are few partons or at high x, the majority of the total momentum is carried by the valence quarks denoted in these plots as u_v and d_v, consistent with the naive model of the proton. Also note that the valence quark peaks flatten as Q^2 increases due to an increase in the sea quark and gluon densities.

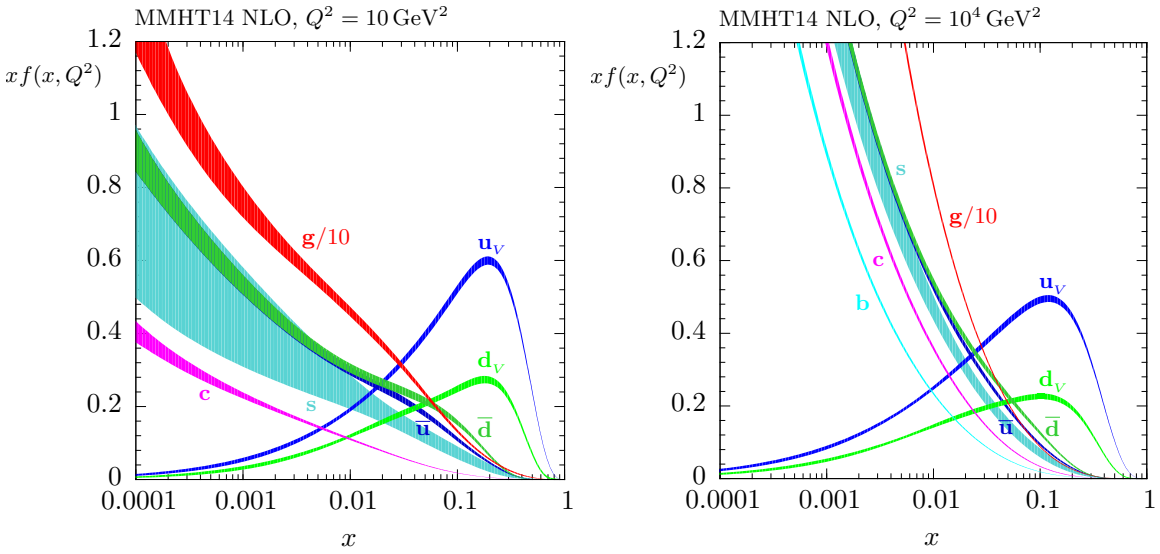

Figure 2.4: Parton distribution functions from the MMHT14 PDF group [30] for $Q^2 = 10$ GeV^2 (left) and 10^4 GeV^2 (right).

Parton distribution functions must be determined experimentally as there is no existing theory that describes their evolution as a function in x. There is however a set of equations called the Dokshitzer-Gribov-Lipatov-Altarelli-Parisi (DGLAP) equations [31] that can be used to extrapolate PDFs in Q^2. One of the major motivations behind this research is to provide an experimental measurement of Equation (2.24) which can be used to extract measurements of the PDFs of the proton.

The factorization theorem [32] states that parton distribution functions are universal. PDFs determined from the fixed target deep inelastic scattering experiments of the 1960s [33] can be used to model LHC proton-proton collisions and vice versa. This measurement can therefore be included with past measurements to improve on

the current estimates of the PDFs of the proton. Figure 2.5 shows the subset of the total ATLAS PDF space, x versus Q^2, accessible to this analysis. Also plotted is the area that was probed by deep inelastic scattering experiments conducted using electron-proton collisions from HERA [34, 35]. Several different processes at the LHC can be used to determine PDFs which are listed in Table 2.3. As indicated in the first two rows of this table, this measurement can be used to probe the PDFs of all quark flavours and their respective antiquarks.

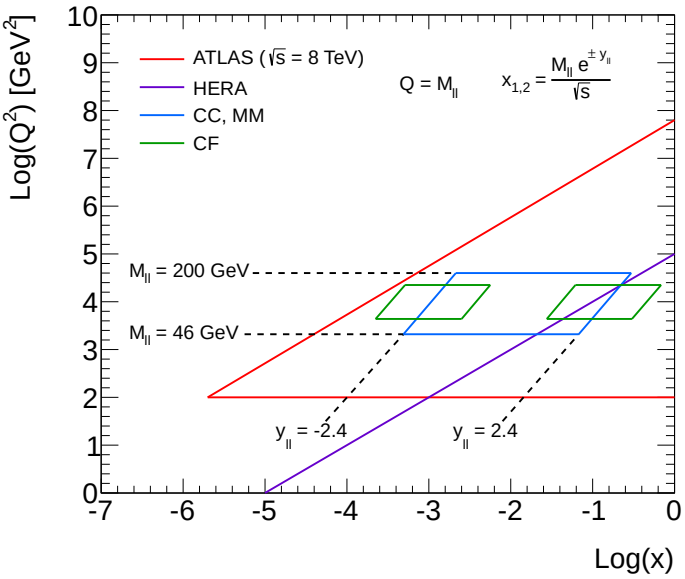

Figure 2.5: Parton distribution function kinematic phase space accessible to this measurement, labelled "CC" (central-central). The regions accessible to its sister analyses, muon-muon "MM" and central-forward "CF" [36], are also shown. For more information on these analyses, see Appendices B and C.

Process	Subprocess	Partons
$PP \to \gamma^* \to \ell^-\ell^+X$	$u\bar{u}, d\bar{d}, ... \to \gamma^*$	$\bar{u}, \bar{d}, ...$
$PP \to Z \to \ell^-\ell^+X$	$u\bar{u}, d\bar{d}, ... \to Z$	$u, d, ...$
$PP \to \text{jet} + X$	$gg, gq, qq \to \text{jet jet}$	g, q
$PP \to W^\pm \to l^\pm\nu + X$	$u\bar{d} \to W^+, d\bar{u} \to W^-$	$u, d, \bar{u}, \bar{d}$
$PP \to b\bar{b} + X$	$gg \to b\bar{b}$	g
$PP \to \gamma + X$	$gq \to \gamma q, g\bar{q} \to \bar{q}$	g

Table 2.3: The LHC processes that can be used to measure proton PDFs. The process, subprocess, and the partons they are sensitive to are given.

2.3 The Drell-Yan Process

The process of interest is neutral current Drell-Yan production [3] in the electron channel, $q\bar{q} \to Z/\gamma^* \to e^-e^+$, from proton-proton collisions at the LHC. The goal is to measure a differential cross-section that can be used to determine the asymmetry exhibited in Drell-Yan events resulting from the weak interaction component of the Drell-Yan process. To accomplish this, the differential cross-section will be measured or binned in three dimensions. In this section, these dimensions will be defined and their use motivated.

Consider again the scenario in which quark q carries x_q of the total momentum of its proton and $\bar{q}$ carries $x_{\bar{q}}$ of its proton which is illustrated in Figure 2.6. Let the four-momenta of the quarks be p_q and $p_{\bar{q}}$ and those of the protons, P_q and $P_{\bar{q}}$; these quantities are related as follows:

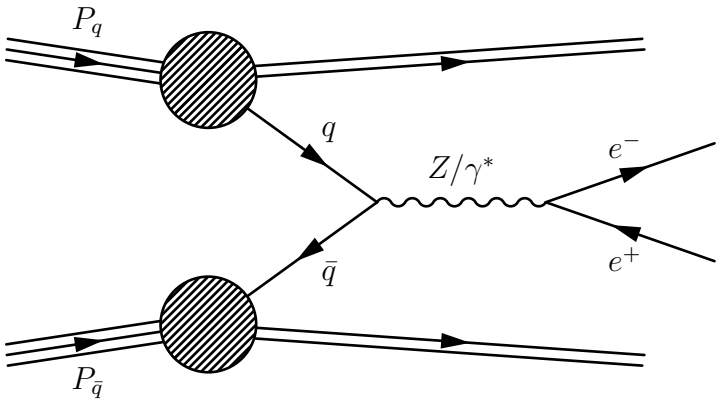

Figure 2.6: The Drell-Yan process according to the Parton Model where the individual quarks of each proton undergo hard scattering.

$$p_q = x_q P_q, \qquad p_{\bar{q}} = x_{\bar{q}} P_{\bar{q}}. \tag{2.26}$$

A relativistic invariant of the colliding partons is given by

$$\hat{s} = (p_q + p_{\bar{q}})^2 = x_q x_{\bar{q}} s, \tag{2.27}$$

where $\sqrt{\hat{s}}$ is the centre-of-mass energy of the quark-antiquark pair and $\sqrt{s}$ is the centre-of-mass energy of the colliding protons. The invariant of the parton system

must of course equal the invariant of the resulting final state dielectron pair:

$$\hat{s} = Q^2 = M_{ee}^2, \tag{2.28}$$

where M_{ee} is the *invariant mass* of the electron-positron pair and can be calculated using the four-momenta $p_1 = (E_1, \vec{p}_1)$ and $p_2 = (E_2, \vec{p}_2)$ of the two electrons as

$$M_{ee}^2 = (E_1 + E_1)^2 - |\vec{p}_1 + \vec{p}_2|^2. \tag{2.29}$$

Invariant mass is one of the three measurement dimensions of this analysis.

If the transverse energy of the partons is negligible, then their four-momenta can be written as

$$p_q = \frac{\sqrt{s}}{2}(x_q, 0, 0, x_q), \qquad p_{\bar{q}} = \frac{\sqrt{s}}{2}(x_{\bar{q}}, 0, 0, -x_{\bar{q}}). \tag{2.30}$$

The second measurement dimension is the *rapidity* of the dielectron pair which is defined as

$$y_{ee} = \frac{1}{2} \ln \left(\frac{E + P_z}{E - P_z} \right), \tag{2.31}$$

where E is the energy and P_z is the magnitude of the longitudinal momentum of the dilepton system. Using conservation laws and Equation (2.30), the rapidity of the electron-positron pair can be written in terms of fractions x_q and $x_{\bar{q}}$:

$$y_{ee} = \frac{1}{2} \ln \left(\frac{x_q}{x_{\bar{q}}} \right). \tag{2.32}$$

Solving Equation (2.32) for x_q and $x_{\bar{q}}$ and substituting Equations (2.27) and (2.28) into the resulting expressions yields

$$x_q = \frac{M_{ee}}{\sqrt{s}} e^{y_{ee}}, \qquad x_{\bar{q}} = \frac{M_{ee}}{\sqrt{s}} e^{-y_{ee}}. \tag{2.33}$$

Setting $Q^2 = M_{ee}^2$ and having expressions for x_q and $x_{\bar{q}}$, by measuring the Drell-Yan cross-section differentially in M_{ee} and y_{ee}, measurements of parton distribution functions $f_{q/P}(x_q, Q^2)$ and $f_{\bar{q}/P}(x_{\bar{q}}, Q^2)$ can be extracted using Equation (2.24).

The third and final dimension of interest is the *polar angle* θ^* in a frame of reference called the *Collins-Soper frame* [37] which is illustrated in Figure 2.7. Starting from the centre-of-mass frame of the final state electron-positron pair, the axis $\hat{z}$ is defined in the Collins-Soper frame to bisect the angle between the momentum of the incoming

quark and the negative momentum of the incoming antiquark. Angle θ^* is measured from $\hat{z}$ to the outgoing electron e^- and can be calculated using lab frame quantities:

$$\cos\theta^* = \frac{P_z}{|P_z|}\frac{2(p_1^+p_2^- - p_1^-p_2^+)}{M_{ee}\sqrt{(M_{ee})^2 + (P_T)^2}}, \tag{2.34}$$

where P_T is the transverse momentum of the dielectron pair and

$$p_i^{\pm} = \frac{1}{\sqrt{2}}(E_i \pm p_{z,i}), \qquad i = 1 \text{ or } 2, \tag{2.35}$$

where, for $i = 1$, E_1 is the energy and $p_{z,1}$ is the longitudinal momentum of the electron. Similarly for $i = 2$, the variables correspond to those of the positron.

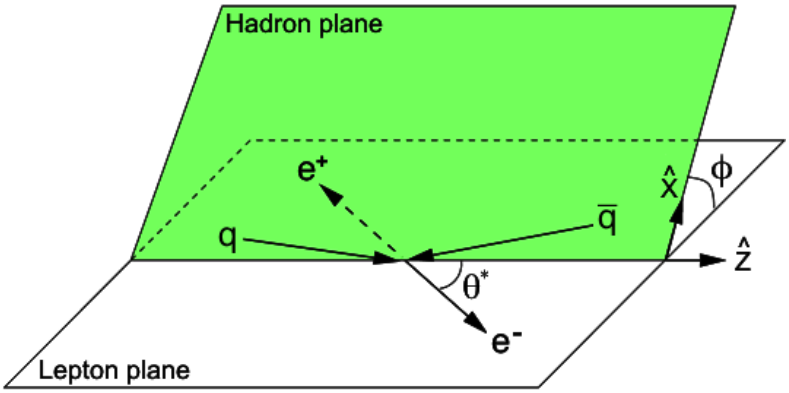

Figure 2.7: The Collins-Soper frame. The polar angle θ^* in this reference frame is measured from the $\hat{z}$-axis, which bisects the angle between the momentum vector of the quark and the negative momentum vector of the antiquark, to the final state electron. When the interacting q and $\bar{q}$ do not possess transverse momenta, the Collins-Soper frame is simply the dielectron centre-of-mass frame.

The differential cross-section of interest written as a function of M_{ee}, y_{ee}, and $\cos\theta^*$ at leading order takes the form

$$\begin{aligned}\frac{d^3\sigma}{dM_{ee}dy_{ee}d\cos\theta^*} = \frac{\pi\alpha^2}{3sM_{ee}}\sum_q \left[f_{q/P_1}(x_q,Q^2)f_{\bar{q}/P_2}(x_{\bar{q}},Q^2) + (q \leftrightarrow \bar{q})\right] \\ \times \left(P_q^{\gamma} + P_q^{\gamma Z} + P_q^{Z}\right),\end{aligned} \tag{2.36}$$

where α is the fine-structure constant. The terms P_q^{γ}, $P_q^{\gamma Z}$, and P_q^{Z} are defined as

follows:

$$P_q^{\gamma} = q_e q_q (1 + \cos^2\theta^*),$$

$$P_q^{\gamma Z} = \frac{q_e q_q}{\sin^2\theta_{\mathrm{W}} \cos^2\theta_{\mathrm{W}}} \frac{2M_{ee}^2(M_{ee}^2 - M_Z^2)}{(M_{ee}^2 - M_Z^2) + \Gamma_Z^2 M_Z^2} \left[v_e v_q (1 + \cos^2\theta^*) + 2a_e a_q \cos\theta^* \right],$$

$$P_q^{Z} = \frac{1}{\sin^4\theta_{\mathrm{W}} \cos^4\theta_{\mathrm{W}}} \frac{M_{ee}^4}{(M_{ee}^2 - M_Z^2) + \Gamma_Z^2 M_Z^2} \left[(v_e^2 + a_e^2)(v_q^2 + a_q^2) + 8 v_e a_e v_q a_q \cos\theta^* \right],$$

where q_e and q_q are the electric charges of the electron and quarks, respectively; Γ_Z is the Z boson decay width; and v and a are the vector and axial vector coupling constants of the fermions (subscript e for the electron and q for the quarks) to the Z/γ^*. The values of v and a for all fermions are shown in Table 2.4.

Fermion	v	a
u, c, t	0.25	0.5
d, s, b	-0.33	-0.5
e, μ, τ	-0.038	-0.5
ν_e, ν_μ, ν_τ	0.5	0.5

Table 2.4: Vector and axial vector couplings of fermions.

Drell-Yan events can be classified into two types: *forward* or *backward*. Forward events are defined as having $\cos\theta^* > 0$ or equivalently, the final state electron travels in the same direction as the initial state quark. Conversely, backward events have $\cos\theta^* < 0$ or equivalently, the positron travels in the same direction as the quark. Due to the parity violating nature of the weak force, an imbalance in the production rate of forward and backward events at the LHC [38] is expected. The difference in rates is known as *forward-backward asymmetry* and it is defined as

$$A_{\mathrm{FB}} = \frac{\sigma_{\mathrm{F}} - \sigma_{\mathrm{B}}}{\sigma_{\mathrm{F}} + \sigma_{\mathrm{B}}}, \tag{2.37}$$

where σ_{F} and σ_{B} are the cross-sections for forward and backward events, respectively. Nonzero measurements of A_{FB} indicate parity violating physics processes have occurred. Along with the differential cross-section in Equation (2.36), determining the forward-backward asymmetry is one of the measurement goals of this analysis.

Forward-backward asymmetry is expected to vary as a function of both M_{ee} and y_{ee}. Figure 2.8 shows the relative contributions to the total Drell-Yan cross-section

from pure γ^* and Z boson[2] exchange and their interference as a function of M_{ee}. The behaviour of $A_{\rm FB}$ as a function of M_{ee} can be deduced from Equation (2.36). As Figure 2.8 shows, at low mass where mediation of the Drell-Yan process is primarily through photon exchange, the P_q^γ term is dominant. P_q^γ is mathematically an even function[3] hence little asymmetry is expected in these events. At the Z-peak, the e^-e^+ pairs are mostly produced through Z decay making P_q^Z the dominant term. Although P_q^Z does have an odd function[4] part, $\cos\theta^*$, its coefficient $v_e a_e v_q a_q$ is small making forward-backward asymmetry effects at the Z-peak negligibly small. This term does, however, determine the value of M_{ee} at which the zero crossing occurs. And finally, for regions in M_{ee} where the interference between the electromagnetic and weak interactions is non-negligible, i.e. below the Z-peak and at high M_{ee}, the $P_q^{\gamma Z}$ term of Equation (2.36) has a measurable effect on the cross-section. This term has an odd part whose coefficient $a_e a_q$ is not negligible and it is precisely this term that leads to forward-backward asymmetry in the Drell-Yan process. Below M_Z, the interference term leads to negative values of $A_{\rm FB}$ while above M_Z, $A_{\rm FB}$ values are positive.

As for the dependency of $A_{\rm FB}$ on y_{ee}, the larger the rapidity the greater sensitivity there is to forward-backward asymmetry effects. Large values of $|y_{ee}|$ result from a significant imbalance in momentum between the interacting partons. The direction of the dielectron system is assumed to be the direction of the quark q because on average the interacting q carries more momentum than its counterpart $\bar{q}$. Therefore, at large values of $|y_{ee}|$, it is easier to identify the q from the $\bar{q}$. At small $|y_{ee}|$ it is impossible to distinguish the two and the measurement of $A_{\rm FB}$ suffers from a *dilution* effect.

Measurements of $A_{\rm FB}$ are sensitive to the weak mixing angle $\theta_{\rm W}$ [39, 40]. To explore this, $A_{\rm FB}$ can be written as

$$A_{\rm FB} = \frac{3A_1}{8A_0}, \tag{2.38}$$

with the following definitions:

$$\begin{aligned} A_0 &= q_q^2 q_e^2 + 2\mathcal{R}\mathrm{e}[\xi] q_q q_e v_q v_e + |\xi|^2 \left(v_q^2 + a_q^2\right)\left(v_e^2 + a_e^2\right), \\ A_1 &= 4\mathcal{R}\mathrm{e}[\xi] q_q q_e a_q a_e + 8|\xi|^2 v_q a_q v_e a_e. \end{aligned} \tag{2.39}$$

[2]The superscript 0 is omitted from the Z. It should be implied from here on out.
[3]Defined as $f(x) = f(-x)$.
[4]Defined as $f(-x) = -f(x)$.

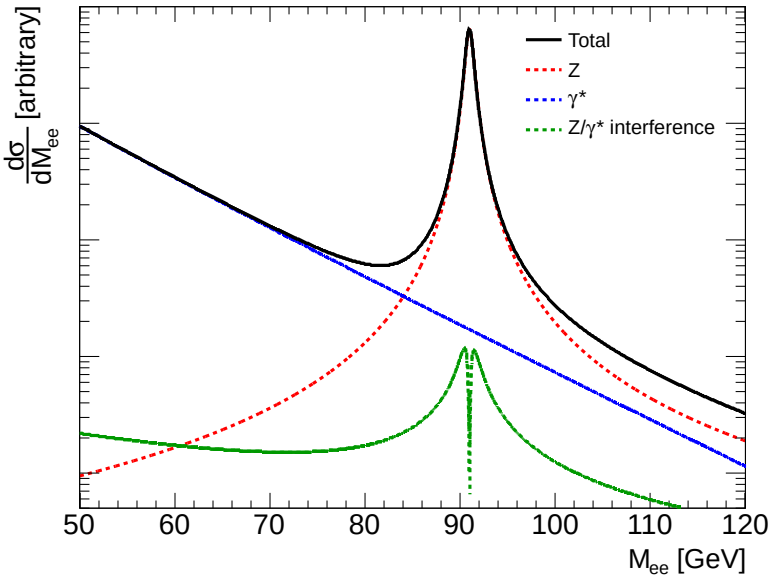

Figure 2.8: The Drell-Yan differential cross-section as a function of M_{ee}. The contributions from pure γ^* and Z production are shown along with their interference.

In terms of T_3 and θ_{W}, the vector and axial vector couplings can be written as

$$v = T_3 - 2q \sin^2 \theta_{\mathrm{W}}, \qquad a = T_3. \tag{2.40}$$

The quantity ξ is the ratio of the coefficients of the Z to γ^* amplitudes given by

$$\xi = \left(\frac{1}{\cos^2 \theta_{\mathrm{W}} \sin^2 \theta_{\mathrm{W}}} \right) \left(\frac{M_{ee}^2}{M_{ee}^2 - M_Z^2 - i\Gamma_Z M_Z} \right). \tag{2.41}$$

From the expressions for v and a in Equation (2.40), their ratio can be written as

$$\frac{v}{a} = 1 - \frac{2q}{T_3} \sin^2 \theta_{\mathrm{W}}, \tag{2.42}$$

which depends on θ_{W}. To summarize, A_{FB} is sensitive to v/a and this sensitivity can be exploited to extract a measurement of θ_{W} which, as was shown, plays an important role in the Standard Model.

2.3.1 Background Processes

Processes, other than the Drell-Yan process, that produce an electron and positron in the final state are designated as background processes. In addition, background processes include those in which one or two objects, namely jets, are mistakenly

identified as an electron-positron pair. Using QCD and electroweak theory, many of these backgrounds, specifically their contributions to a sample of Drell-Yan events measured from a collider experiment, can be estimated.

In Figures 2.9 to 2.11, leading order Feynman diagrams of several of the major background processes can be seen. Figure 2.9 is the process $Z/\gamma^* \to \tau^-\tau^+$ in which the taus subsequently undergo semi-leptonic decay to produce an electron-positron pair. This is in fact a tau channel Drell-Yan event which is considered to be background in the electron channel measurement. Figure 2.10 shows the possible backgrounds involving two massive gauge bosons which consist of W^+W^-, $W^\pm Z$, and ZZ events. Photon-induced background, illustrated in Figure 2.11, occur in proton-proton collisions when two photons are emitted which then electromagnetically interact to form an electron-positron pair. Note that the background processes described above are purely electroweak in nature.

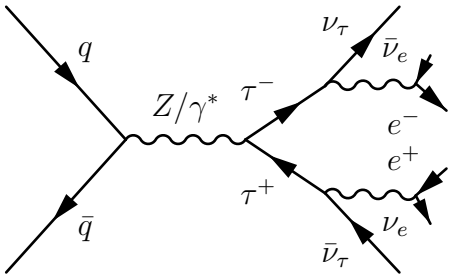

Figure 2.9: $Z/\gamma^* \to \tau^-\tau^+X$ process.

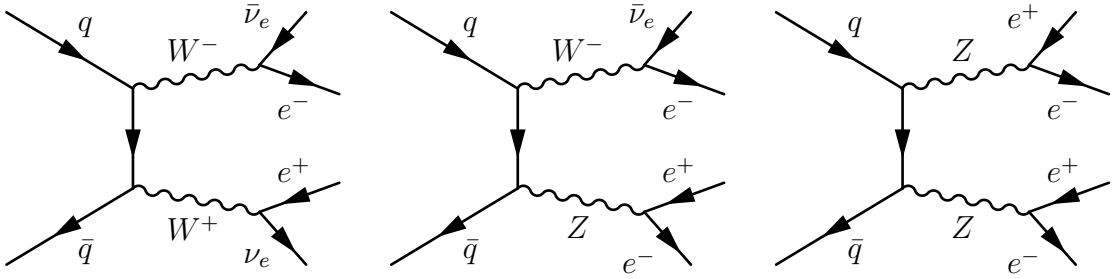

(a) $W^+W^- \to e^-e^+X$ (b) $W^\pm Z \to e^-e^+X$ (c) $ZZ \to e^-e^+X$

Figure 2.10: Diboson processes.

Another class of background processes exist which involve QCD physics. Such processes include W production in associated with a gluon which hadronizes to form

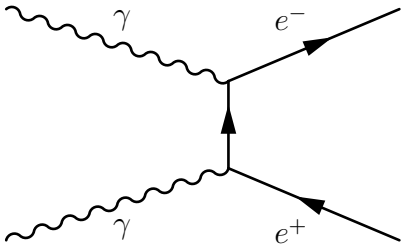

Figure 2.11: $\gamma\gamma \to e^- e^+$ process.

a jet mismeasured as an electron or positron. The W may decay directly into an electron or positron as depicted in Figure 2.12a, or a tau or antitau which further decays into an electron or positron, shown in Figure 2.12b. Several background processes involving one or more top quarks are possible. Figure 2.13a shows one such process involving a $t\bar{t}$ pair decaying into two W bosons, which subsequently decay into an electron-positron pair, along with two b quarks. Additional background processes involving a single top quark in the final state exist. Figures 2.13b, 2.13c, and 2.13d correspond to the s-channel, t-channel, and Wt production of top quarks, respectively. In all three cases, at least one jet is mistakingly identified as an electron or positron.

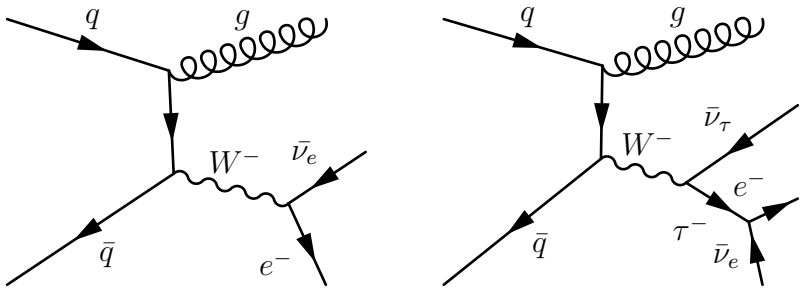

(a) $W^\pm \to e^\pm \nu$ (b) $W^\pm \to \tau^\pm \nu$

Figure 2.12: W+jet processes.

The Feynman diagrams shown in this section do not form a complete description of the background. Some background processes cannot be efficiently or accurately modelled using QFTs. One such background comes from heavy flavour quark pairs, namely $b\bar{b}$ and $c\bar{c}$ pairs, which can decay in the following ways: both quarks semi-leptonically decay into electrons, one decays while the other hadronizes into a jet which is misidentified as an electron, or both hadronize to form jets. Rather than using theory, these background processes are typically estimated from the data itself

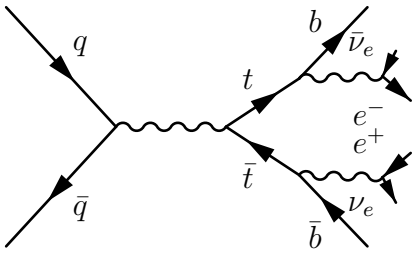

(a) $t\bar{t} \to e^- e^+ X$

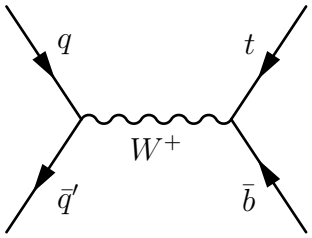

(b) s-channel

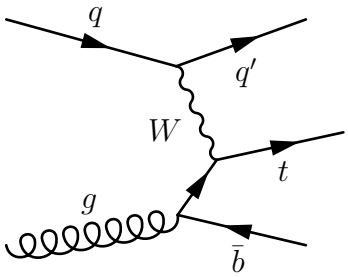

(c) t-channel

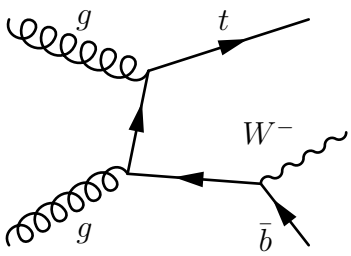

(d) Wt production

Figure 2.13: Top processes.

using data-driven methods.

Chapter 3

The ATLAS Experiment

The origin of particle physics dates as far back as the 6th century BC when Greek philosophers reasoned that all matter was composed of *atomos* (Greek for "indivisible") particles. By the 19th century, physicist and chemist John Dalton and his contemporaries hypothesized that each of the chemical elements found in nature are comprised of elementary objects named *atoms* and these are the true building blocks of matter. Not long after, particles even more fundamental were found by J. J. Thomson who discovered the electron, Ernest Rutherford who found the proton, and James Chadwick, the neutron. Although no experiments to date have shown that electrons are not fundamental particles, the same cannot be said for protons and neutrons. The deep inelastic scattering experiments of the late 1960s used highly energetic electrons to probe the structure of protons and in the process of doing so discovered quarks. These experiments would come to be the first of many high energy particle physics experiments that have been and continue to be conducted across the world today.

3.1 The LHC

Located near the border between France and Switzerland is the LHC (Large Hadron Colldier) [41], a synchrotron particle accelerator 26.7 km in circumference housed in an underground tunnel whose depth ranges from 50 to 175 m. Constructed by CERN (European Organization for Nuclear Research) between 1998 and 2008, the LHC consists of two beam pipes, containing counter-circulating beams of protons[1]. The beams are kept in circular paths using 1232 superconducting dipole magnets

[1]The LHC also collides lead ions which create quark-gluon plasma, a state of matter believed to have existed ten millionths of a second after the Big Bang.

made of a niobium-titanium alloy. They are cooled using a cryogenics system to approximately 1.9 K, a temperature at which the dipole magnets can sustain a current of 11850 A which corresponds to a magnetic field as strong as 8.3 T. Three hundred ninety-two quadrupole magnets spread out along the LHC ring are used to focus the proton beams. Sixteen radio-frequency cavities along the LHC tunnel impart an electric force to the protons causing them to accelerate. Having reached the desired centre-of-mass energy $\sqrt{s}$, the oppositely circulating proton beams are aligned along a common axis and collided, producing physics events for analysis. There are seven such collision points along the LHC each used by one of the seven experiments: ALICE [42], MoEDAL [43], TOTEM [44], LHCf [45], LHCb [46], CMS [13], and ATLAS. The CERN accelerator complex and the locations of the largest of these experiments (ALICE, LHCb, CMS, and ATLAS) can be seen in Figure 3.1.

3.1.1 LHC Parameters

The LHC was designed and built to collide two 7 TeV proton beams resulting in a $\sqrt{s} = 14$ TeV centre-of-mass collision. Due to a violent magnet quench in 2008, the LHC started producing collisions at a conservative $\sqrt{s} = 7$ TeV in 2010, increased it to $\sqrt{s} = 8$ TeV in 2012, and today is operating at $\sqrt{s} = 13$ TeV. The centre-of-mass energy is arguably the most important beam parameter; certain physics processes may be impossible to produce if $\sqrt{s}$ is not sufficiently large. For example, the Tevatron [47], a proton-antiproton collider with a maximum centre-of-mass energy of $\sqrt{s} = 1.96$ TeV, was unable to conclusively claim that the Higgs had been discovered – though they were close [48].

Another important beam parameter is the *instantaneous luminosity* L defined as the number of particles crossing paths per unit of transverse area per unit time. The LHC accelerates and collides *bunches* of protons which are discrete packets of protons spaced apart equally by a set distance or time and collectively, the bunches in a given beam are referred to as a *bunch train*. The instantaneous luminosity depends on the number of protons filling each bunch and the number of bunches and their spacing in a train:

$$L = \frac{f n_1 n_2 n_b}{4\pi \Sigma_x \Sigma_y}, \tag{3.1}$$

where f is the frequency at which the bunches collide (a function of the bunch spacing); n_1 and n_2 are the numbers of protons populating the two colliding bunches; n_b

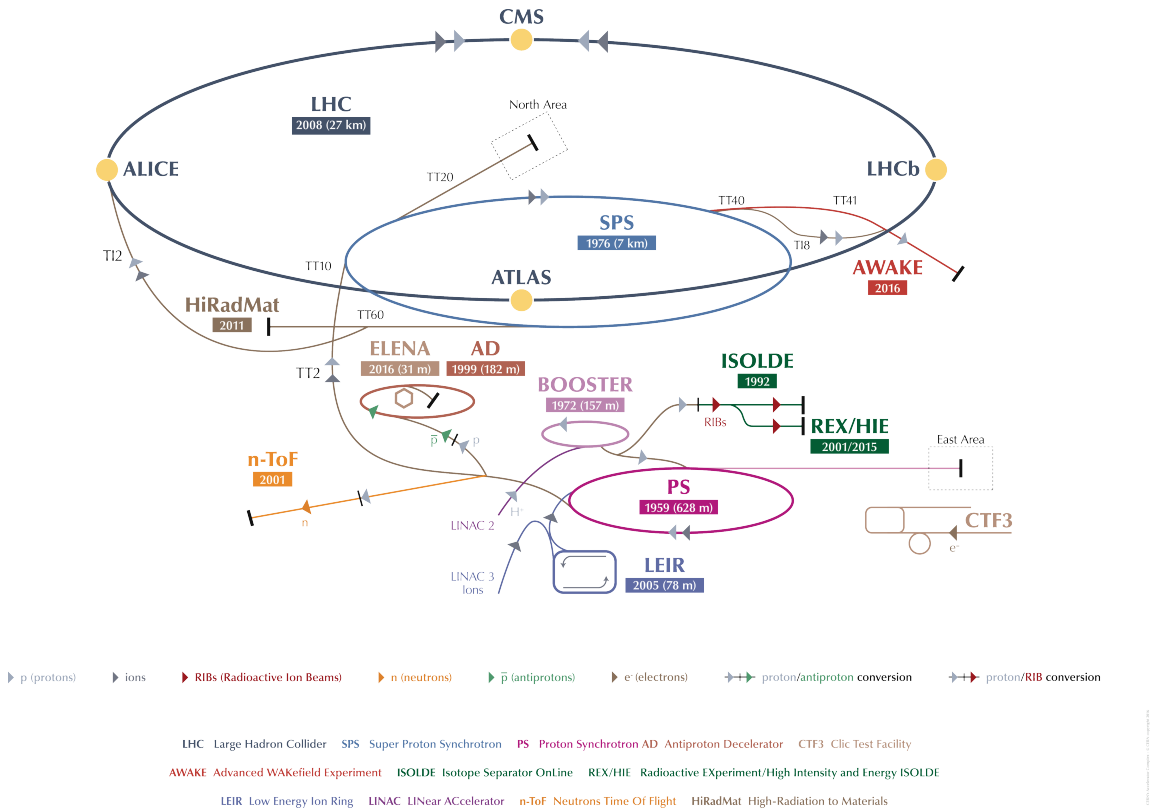

Figure 3.1: The CERN accelerator complex. Protons sourced from a tank of hydrogen gas are accelerated by the LINAC2 to an energy of 50 MeV and are then guided into the PSBooster (Proton Synchrotron Booster) accelerating them to 1.4 GeV. Following the PSBooster is the PS (Proton Synchrotron) which further accelerates the protons to 25 GeV before reaching the penultimate accelerator, the SPS (Super Proton Synchrotron) accelerating them to 450 GeV. Finally, the protons are then injected into the LHC ring which accelerates them to energies on the TeV scale. Marked on this diagram are the four main interaction points along the LHC used by the ALICE, LHCb, CMS, and ATLAS experiments.

is the number of bunches per train; and Σ_x and Σ_y characterize the horizontal and vertical profile widths of the beams. In 2012, the year in which the data used in this measurement was collected, the LHC ran with approximately 1.7×10^{11} protons per bunch and 1374 bunches per train spaced 50 ns apart with a bunch collision frequency of about 20 MHz. The instantaneous luminosity during the run averaged around 2.5×10^{33} cm^{-2}s^{-1} peaking at 7.7×10^{33} cm^{-2}s^{-1} – nearly reaching the LHC design luminosity of 10^{34} cm^{-2}s^{-1}.

Integrating the instantaneous luminosity over the run time t yields the integrated

luminosity $\mathcal{L}$,

$$\mathcal{L} = \int L dt, \tag{3.2}$$

which is the most common measure of the amount of data delivered, recorded and analyzed. In 2012, approximately 22.8 fb^{-1} of integrated luminosity was delivered to the ATLAS experiment, most of which was recorded and used for analysis. For some physics process of interest, $i \to f$, the expected number of such events in a data set of size $\mathcal{L}$ is

$$N^{i \to f} = \sigma^{i \to f} \mathcal{L}, \tag{3.3}$$

where $\sigma^{i \to f}$, the cross-section, can be interpreted as the probability of process $i \to f$ occurring.

Defined as the presence of proton-proton interactions in addition to the hard scattering process of interest, the *pileup*, μ, is proportional to the instantaneous luminosity:

$$\mu = \frac{\sigma_{PP} L}{f n_b}, \tag{3.4}$$

where σ_{PP} is the inelastic proton-proton collision cross-section which in 2012 was measured to be 71.73 ± 0.71 mb [49]. There are two types of pileup: *in-time* and *out-of-time* pileup. In-time pileup occurs when these additional collisions result from the same bunch crossing as the hard scatter. A measure of in-time pileup is the number of *primary vertices*, defined as the spatial position where protons collide, per event. Out-of-time pileup occurs when the additional collision events originate from an earlier bunch crossing and can be quantified by the average pileup which was approximately 20.7 during the 2012 run.

3.2 The ATLAS Detector

The ATLAS (A Toroidal LHC ApparatuS) detector [50] is one of several particle detectors constructed along the LHC used to record physics. Illustrated in Figure 3.2, the ATLAS detector is 44 m in length and 25 m in diameter, weighing about 7000 tonnes. Proton-proton collisions occur in a vacuum tube at the centre of the detector and from there concentric layers of subdetectors are in place each designed

to independently measure specific properties of the final state particles. The ATLAS detector is divided into three main sections, the centrally located *barrel* which is cylindrical in shape and two *end-caps* situated at each of the ends of the barrel. Together they provide a detector coverage of nearly 4π in solid angle.

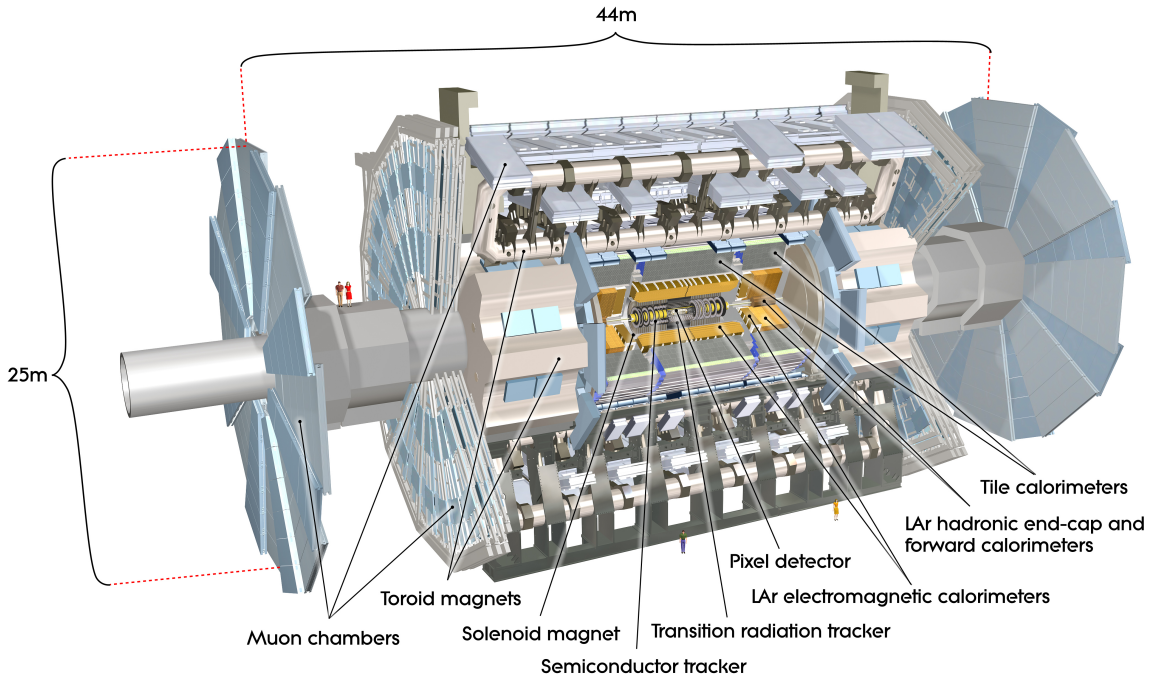

Figure 3.2: The ATLAS detector with its subdetectors labelled.

3.2.1 Coordinate System

Using both Cartesian and spherical polar coordinates, the origin of the ATLAS coordinate system is located at the interaction point. The z-axis runs along the beam axis with its positive direction forming a right-handed coordinate system with the positive x-direction which points towards the centre of the LHC ring and the positive y-direction pointing upwards. The polar angle $\theta = \sqrt{x^2 + y^2}/z$ is measured with respect to the z-axis and the azimuthal angle $\phi = \tan(y/z)$ is measured with respect to the x-axis in the transverse plane (x, y). The radial distance r from the origin is defined as $r = \sqrt{x^2 + y^2}$.

The total momentum of each of the colliding protons is shared amongst its con-

stituent partons. While the longitudinal momenta of the partons are unknown, their momenta in the transverse plane are known to be negligible. By conservation of momentum, the sum of the momentum vectors of all final state particles in the transverse plane should equal zero. For this reason, it is the *transverse momentum* $p_T = \sqrt{p_x^2 + p_y^2}$ of a particle that is most often used to describe LHC physics rather than the total momentum. *Rapidity*, defined as $y = 1/2 \ln[(E + p_z)/(E - p_z)]$ along the z-axis, is another useful observable since differences in y are invariant under Lorentz boosts. For light particles with momentum magnitudes far greater than their masses, rapidity can be approximated by a quantity known as *pseudorapidity*, $\eta = -\ln \tan(\theta/2)$, which is often used in place of θ. Finally, to quantify the angular separation between two objects, one with angular coordinates (η_1, ϕ_1) and the other (η_2, ϕ_2), $\Delta R = \sqrt{(\eta_2 - \eta_1)^2 + (\phi_2 - \phi_1)^2}$ is often used. A large value of ΔR indicates a large separation between the two objects while for a small value, the objects are in close proximity.

3.2.2 Inner Detector

From the interaction point outwards several subdetectors dedicated to measuring electrically charged particles are layered one after the other. These subdetectors comprise the inner detector [51] which is illustrated in Figure 3.3. A charged particle traversing through the inner detector ionizes the atoms of the materials leaving a series of signals [52] which are then reconstructed to give the path or *track* of the particle. A superconducting solenoid magnet surrounding the inner detector produces a 2 T magnetic field inside the inner detector causing the particle track to be curved. The degree of curvature is used to determine the momentum of the particle and the direction of curvature reveals its electric sign.

The inner detector is responsible for providing measurements of position and momentum of electrically charged particles. Additionally, all vertex (the point of origin of the final state particles) information is supplied by the inner detector. Providing a coverage of $|\eta| < 2.5$, the inner detector itself is split into three subsystems: a high resolution pixel detector, a semiconductor tracker (SCT), and a lower resolution transition radiation tracker (TRT). Their layout and relative sizes can be seen in Figure 3.4.

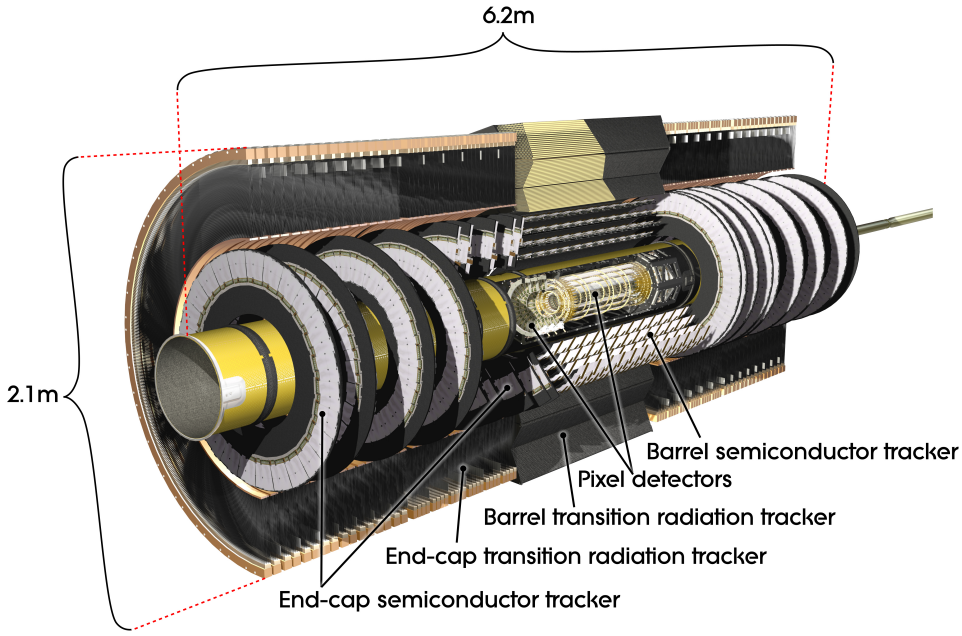

Figure 3.3: The ATLAS inner detector. In both the barrel and end-caps, the inner detector is split into three subsystems: a pixel detector, a semiconductor tracker, and a transition radiation tracker.

Pixel Detector

The first layer of the inner detector is the pixel detector [53] which in the barrel consists of three concentric cylindrical layers of radiation hardened silicon sensors aligned to face the beam pipe. They are placed at radii of 5.05, 8.85, and 12.25 cm and each have a length of approximately 1.3 m. In the end-caps, three pixel detectors in the shape of disks are positioned perpendicular to the beam axis at distances of 49.4, 58.0, and 65.0 cm from the interaction point. The pixel detector provides three *hits* or points of a track measurement. In total, there are approximately 80 million pixel sensors identical in size, $r\phi \times z = 50 \times 400\ \mu\text{m}^2$, each having its own readout channel with an intrinsic resolution of $r\phi = 10\ \mu$m and $z = 115\ \mu$m. The high resolution of the pixel detector makes it the most precise of the three tracking detectors.

Semiconductor Tracker

The semiconductor tracker follows the pixel detector. It consists of four cylindrical layers in the barrel [54] and nine disks in each of the two end-caps [55]. The barrel lay-

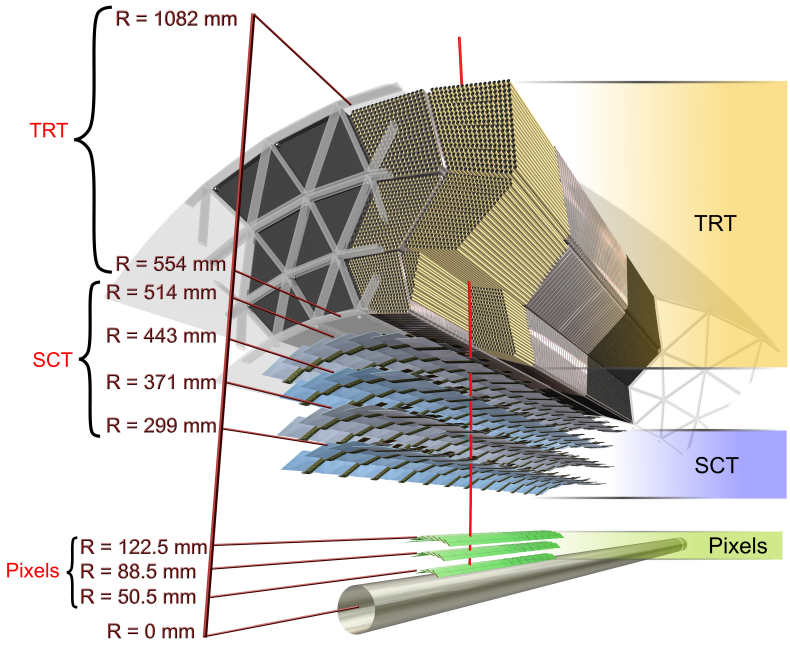

Figure 3.4: The layering of the pixel, semiconductor, and transition radiation detectors is shown relative to the beam pipe.

ers are positioned at radii 28.4 cm, 35.5 cm, 42.7 cm, and 49.8 cm from the interaction point and are approximately 1.5 m in length. Like the pixel detector, the SCT uses silicon strip sensor technology, possessing 6.3 million readout channels grouped into 4088 modules. The SCT provides 8 hits, more than the pixel detector but typically less precise. The intrinsic resolution of the silicon strips is approximately $r\phi = 17$ μm and $z = 580$ μm.

Transition Radiation Tracker

The third and final subsystem of the inner detector is the transition radiation tracker (TRT) [56]. Like the pixel detector and the semiconductor tracker, it has both a barrel and two end-cap modules. The TRT is comprised of 4 mm diameter Kapton drift tubes coated with a conducting layer of aluminium. Filled with a xenon gas mixture, each tube contains a gold-plated tungsten wire which runs along the length of the tube. The tubes are embedded into polypropylene fibres in the barrel and foils

in the end-caps. As a charged particle passes through the transition radiation tracker, it ionizes the xenon atoms of the gas and a high voltage set up between the wall of the tube and the tungsten wire causes the ejected electrons and xenon ions to drift to the anode and cathode, respectively. The current generated is related to the energy of the incident particle.

In the barrel, the TRT has an inner radius of 56 cm and an outer radius of 106 cm. The straw tubes are 1.44 m in length and run parallel to the beam pipe in the barrel covering a region of $|\eta| < 2.0$. The TRT end-cap modules are split into 18 wheels per side each having an inner radius of 63 cm and an outer one of 103 cm. The wheels are positioned 83 to 340 cm from $z = 0$. Arranged in a wheel pattern, the straw tubes in the end-caps are 37 cm in length. In total, the TRT provides about 36 hits, the most of the three tracking detectors but with the lowest precision.

The TRT possesses a very important second function. Photons called *transition radiation* are emitted when a charged particle travels through polypropylene inserted between the straw tubes. These photons are detected using the xenon gas in the tubes and the amount of radiation emitted is proportional to the ratio of the energy E to the mass m of the incident particle. Electrons, which are light particles, typically produce significant amounts of transition radiation. Hence large values of E/m measured in the TRT help identify final state electrons.

3.2.3 Calorimetry

After the inner detector and the solenoid magnet come the ATLAS calorimeters, shown in Figure 3.5. Covering a region of $|\eta| < 4.9$, the ATLAS calorimetry system consists of an electromagnetic (EM) calorimeter specializing in energy and position measurements of electromagnetic particles namely electrons and photons and a hadronic calorimeter designed to measure hadronic particles such as neutrons and pions. Both use *sampling calorimetry* which employs two types of materials, a dense absorber and an active material which are layered, alternating between the absorber and the active detector material. As an electron or photon passes through the absorber layers of the EM calorimeter, a cascade of secondary particles or *particle shower* is induced. High energy electrons lose energy mainly through bremsstrahlung while photons undergo pair production [52]. These secondary particles then interact, mainly through ionization, with the layers of active material which are connected to readout electronics. This process continues until the secondary particles lack the energy

themselves to further the cascade. The sum of the signals registered in the readout electronics provides a measurement of the energy of the primary particle and the energy-weighted mean position of the signals provides a position measurement.

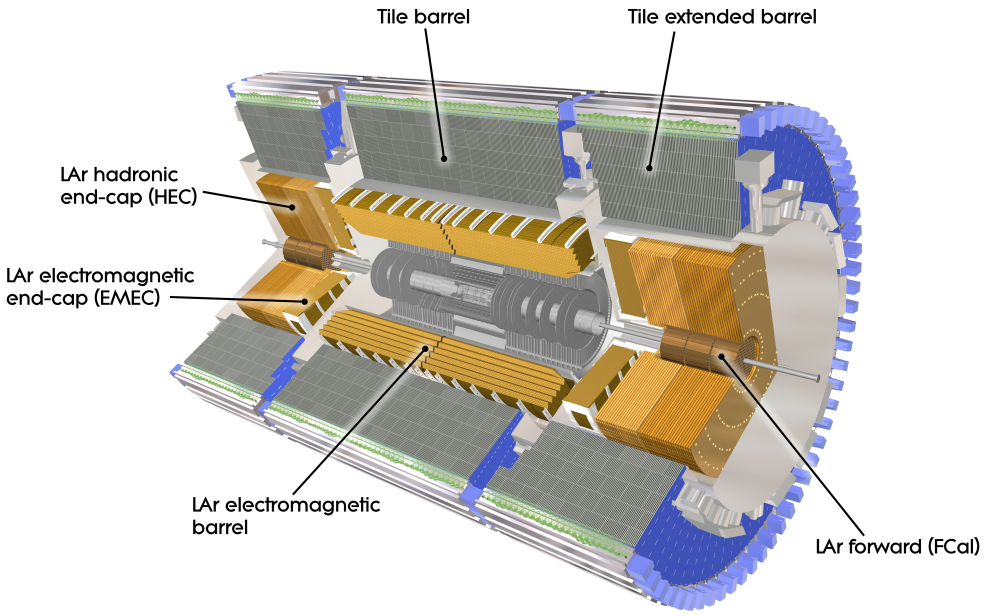

Figure 3.5: The ATLAS calorimetry system. It is comprised of both a barrel and two end-cap modules which use a combination of LAr and scintillating tile detector technologies to measure the energy and position of electromagnetic and hadronic particles. It also includes a forward detector designed to detect particles whose trajectories run close to the beam.

Both the EM calorimeter and the hadronic calorimeter, which is further from the interaction point, have barrel modules and detectors at each of the end-caps. The ATLAS forward calorimeter (FCal) is positioned close to the beam pipe and specializes in measuring particles with large longitudinal momenta. Comprised of three layers, FCal1 measures the energy and position of EM particles while FCal2 and FCal3 specialize in hadronic measurements.

Electromagnetic Calorimeter

The ATLAS electromagnetic calorimeter [57] has three subdetectors, one in the barrel and one in each of the end-caps, all of which use LAr calorimetry. Each are housed inside a cryostat filled with liquid argon (LAr), the active material, and maintained

at an approximate temperature of 88 K (−185 °C). In the barrel, the EM calorimeter is split into two halves at $\eta = 0$ with a 4 mm crack between the two. Each half barrel has an inner radius of 2.8 m and an outer one of 4 m and a length of 3.2 m. In terms of pseudorapidity, the barrel has a coverage of $|\eta| < 1.475$ while the EM end-caps are comprised of an inner wheel ($2.5 < |\eta| < 3.2$) and an outer wheel ($1.375 < |\eta| < 2.5$) which covers a total range of $1.375 < |\eta| < 3.2$. A gap, often referred to as the *crack region*, in coverage exists between the barrel and end-caps at $1.37 < |\eta| < 1.52$ which is used to route cables and services from the inner detector. Although scintillators have been placed inside the crack region to offer some form of detection, it is still typically excluded from physics analyses.

Lead plates are used by the EM barrel and end-cap calorimeters as the absorber material to initiate electromagnetic showers and to contain the length of the shower within the calorimeter. The shower particles ionize the liquid argon and the resultant negative charges and positive ions drift toward positive and negative readout plates, respectively. Since the drift speed of the negative charges is orders of magnitude larger than the positive argon ions, the current induced by the movement of the negative charges is sampled and used to produce energy measurements. (The energy calibration and resolution of the EM calorimeter are discussed in Chapter 5.) The readouts are made of copper electrodes separated by insulating layers of polymide. Both the lead absorbers and copper electrodes have been arranged into an accordion shape which provides excellent ϕ symmetry and helps regularize the thickness of the LAr ionization gaps. The angle of folding and the amplitude of the waves vary in order to keep the combined thickness of the lead absorbers and copper electrodes constant in the η-direction thus maintaining a uniform response from the calorimeter. In the barrel, illustrated in Figure 3.6, the accordion geometry is arranged axially with the waves oscillating along the radial direction; in the end-caps, the accordion waves oscillate along the beam direction. In total, there are 101760 readout channels in the barrel and 62208 channels in each end-cap.

The electromagnetic calorimeters are approximately 22 radiation lengths in thickness in the barrel and 24 radiation lengths in the end-caps. For $|\eta| < 2.5$, the modules comprising the EM calorimeter consist of three layers, as shown in Figure 3.6, with the layer closest to the beam pipe having the finest granularity, $\Delta\eta \times \Delta\phi = 0.0031 \times 0.1$, while the middle and outermost layers have granularities of $\Delta\eta \times \Delta\phi = 0.025 \times 0.025$ and $\Delta\eta \times \Delta\phi = 0.05 \times 0.025$, respectively. These three layers have approximate thicknesses of 4, 16, and 4 radiation length, respectively. As these thicknesses indicate,

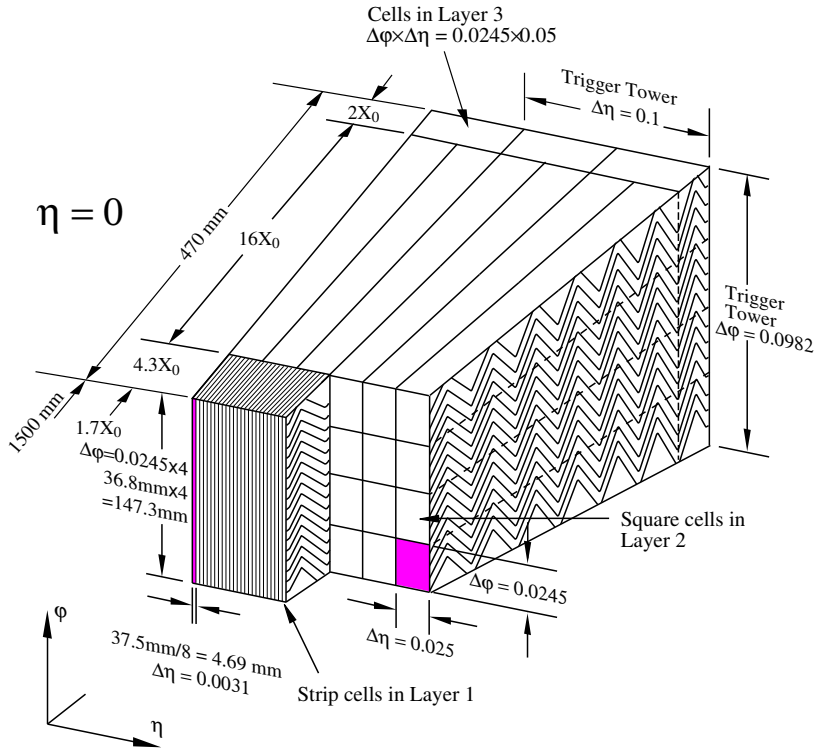

Figure 3.6: The ATLAS EM barrel calorimeter module. The accordion shape of the LAr EM calorimeters is illustrated along with the three layers that make up this subdetector.

the majority of the energy of EM particles is deposited in the middle layer.

Positioned at $|\eta| < 1.8$ in front of each module is an active layer of LAr known as the *presampler* which has a granularity of $\Delta\eta \times \Delta\phi = 0.025 \times 0.1$. The presampler is used to correct for energy losses in the uninstrumented materials located in front of the EM calorimeter modules. In the barrel, the presampler has a thickness of 1.1 cm and 7808 readout channels while in the end-caps, it is 0.5 cm thick with 1536 readout channels.

Hadronic Calorimeter

The hadronic calorimeter [58] is comprised of several subdetectors designed to provide energy measurements of hadronic particles such as protons, neutrons, and pions. The longitudinal depth of the hadronic calorimeters is approximately 10 nuclear interaction lengths, long enough to contain highly energetic hadrons. Two types of detector technologies are utilized by the hadronic calorimeter: tile scintillating and LAr calorimetry.

In the ATLAS barrel, the hadronic calorimeter is split into a central barrel component covering $|\eta| < 1.0$ and two extended barrels with a coverage of $0.8 < |\eta| < 1.7$, all three of which use tile scintillating technology. Like the EM calorimeter, these scintillating plastic tiles are interspaced with layers of absorber material which in this case is steel. The steel also acts as the return yoke of the magnetic field produced by the solenoid surrounding the inner detector. Hadronic particles that pass through the EM calorimeter interact with the steel absorbers resulting in hadronic showers comprised of secondary particles which traverse the scintillating tiles causing light to be emitted. These light signals are fed into photomultiplier tubes by fibre cables that line the plastic tiles. Via the photoelectric effect, the photomultiplier tubes convert the light signals into a current which is measured using external electronics connected to the calorimeter. In the end-caps, the hadronic calorimeters are comprised of layers of 2.5 cm thick copper plates spaced 8 mm apart with LAr filling the gaps. The hadronic end-cap modules cover a pseudorapidity of $1.5 < |\eta| < 3.2$.

Forward Calorimeter

The ATLAS forward calorimeter has the task of providing energy measurements of EM and hadronic particles that are emitted in the range $3.1 < |\eta| < 4.9$. The layout of the FCal can be seen in Figure 3.7 which shows that it is split into three layers each roughly 45 cm in length. The FCal uses LAr as its active material suspended in less than 2 mm thick gaps between absorption plates. The first layer of the forward calorimeter is designed to measure EM particles by using copper absorber plates. The second and third layers are used for hadronic particle detection; they use tungsten as the absorber material which has a large nuclear interaction length.

3.2.4 Muon Spectrometer

Surrounding all other subdetectors is the muon spectrometer [59], illustrated in Figure 3.8. Muons do not significantly interact with the ATLAS calorimeter. Consequently, energetic muons leave hits in the inner detector, pass through the calorimeters, and reach the muon spectrometer. Since muons primarily lose energy via ionization, the muon spectrometer is comprised of many gas-filled chambers. Muons that pass through these chambers ionize the gas atoms creating electron-ion pairs and under an electric field, the freed charges further ionize the gas creating a cascade. The electric current resulting from this process is then fed to electronics connected to the muon

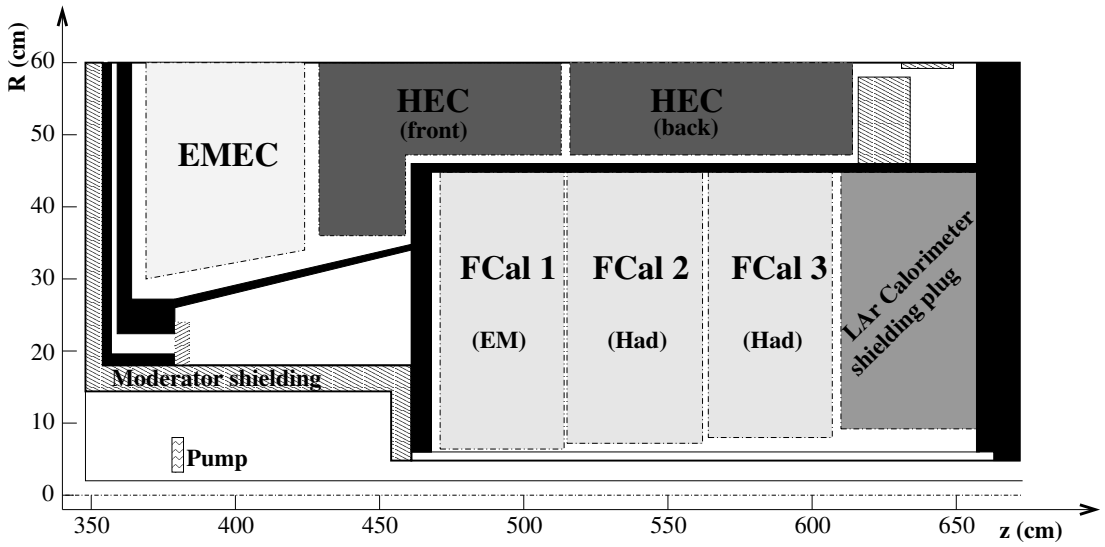

Figure 3.7: The ATLAS forward calorimeter. Designed to measure the energy and position of both electromagnetic and hadronic particles, the FCal is composed of three layers. The first layer specializes in EM measurements and the other two are used to detect hadronic particles.

spectrometer.

The muon spectrometer has a coverage of $|\eta| < 2.7$ save for a 4 mm gap at $\eta = 0$ used for the passage of cables and services for the interior subdetectors. It consists of a barrel component which has an outer radius of 6.5 m and two end-cap modules. The muon spectrometer is comprised of more than a thousand chambers fitted into three concentric cylindrical shells in the barrel and trapezoids in the end-caps giving the ATLAS detector its distinctive appearance. Two main detector technologies are used by the muon spectrometer: monitored drift tubes (MDT) and cathode-strip tubes (CST). MDT chambers are filled with several layers of tubes, much like the TRT, providing precision track measurements in a range of $|\eta| < 2.7$. The CST chambers are multi-wire proportional chambers used to measure the momentum of muons in the range $2.0 < |\eta| < 2.7$. Additionally, resistive plate chambers (RPC) and thin gap chambers (TGC) are used to assist in the triggering and reconstruction of muon tracks.

In order to measure their momenta, the trajectories of muons are bent by a magnetic field. The field is created by eight superconducting air-core toroidal magnets positioned around the barrel, as shown in Figure 3.8, which creates a magnetic field up to 4 T in strength for $|\eta| < 1.4$. In the end-cap regions, two large barrel toroid magnets are used to generate magnetic fields in the region $1.6 < |\eta| < 2.7$. Between

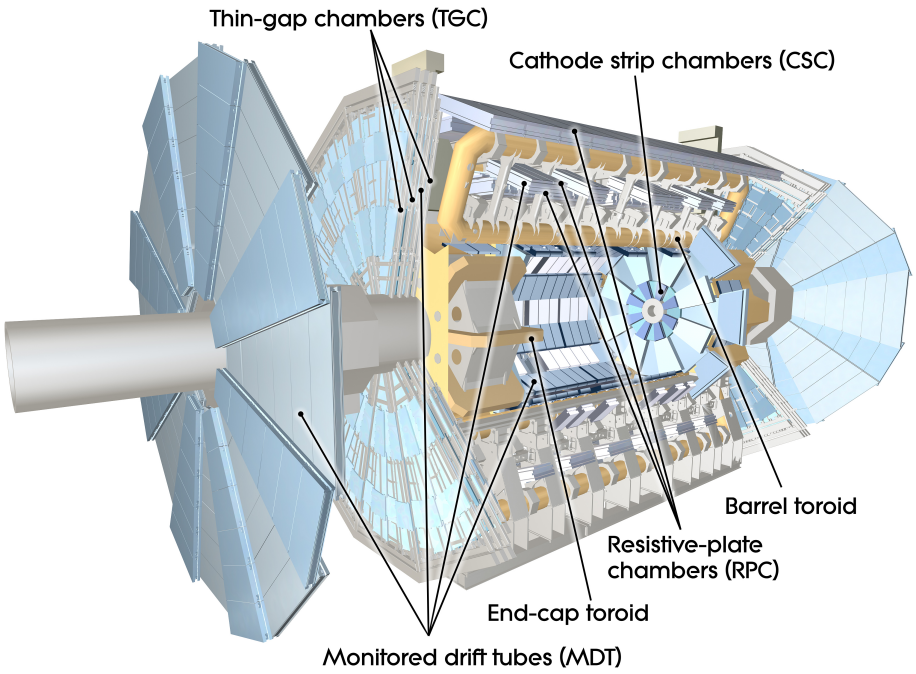

Figure 3.8: The ATLAS muon spectrometer. The largest of all the subdetectors, the muon spectrometer provides measurements of muon position and momentum. Large toroidal magnets apply a force to muons as they travel away from the interaction point causing their trajectories to be bent. Momentum measurements are extracted from the curvature.

$1.4 < |\eta| < 1.6$, the trajectories are bent by a combination of the barrel and end-cap magnetic fields.

3.2.5 Trigger System

The LHC collides protons at an overwhelmingly high rate. In 2012, the bunch crossing rate averaged to be 20 MHz or 20 million bunch crossings per second with an average of 20.7 proton-proton collisions at every crossing. For each bunch crossing in which one or more proton collisions have occurred, about 1.5 megabytes of storage space is required to record the event. For ATLAS to record every event, 30 terabytes of data would need to be stored every second. This is of course unfeasible due to the high data recording rate and the tremendous amount of storage space required. To circumvent this problem, each event is sent to the ATLAS trigger system which determines whether the event should be recorded to disk to be used later for physics analysis or discarded based on the signatures of the objects detected in the event. The

ATLAS trigger system consists of three stages or levels, the first of which is known as the level-1 (L1) trigger [60], the most primitive of the three. The others, known as the level-2 (L2) and the event filter (EF) triggers, are increasingly sophisticated using additional information from the detector (at the cost of decision time or *latency*) to determine if an event is worth recording. Collectively, the L2 and EF triggers are commonly referred to as the *high level trigger* or HLT [61] and the entire series is known as the *trigger chain*.

Level-1 Trigger

The simplest of the three levels, the L1 trigger uses purpose-built hardware. The L1 trigger requires the least amount of decision time to decide if an interesting event has occurred. Only information from the calorimetry system and the muon spectrometer is used by the L1 trigger to determine if an event should be passed on to the next level. For example, if a candidate electron is found in the EM calorimeter that satisfies some energy threshold and cluster shape requirement, the entire event, i.e. all objects found in the event, is passed to the next trigger level. Having a latency of about 2 μs, the L1 trigger reduces the bunch crossing rate from 20 MHz to 75 kHz. In addition to keeping or rejecting events, the L1 trigger also identifies regions in the calorimeter or muon spectrometer where potentially interesting physics objects were found. These regions are known as *regions of interest* or ROI which are then passed on to the HLT reducing its decision time by saving it the need to go directly to the calorimeter or muon spectrometer for this information.

Level-2 Trigger

Information from the L1 trigger is fed to the L2 trigger which is software-based. In this phase of the trigger chain, events undergo a simplified reconstruction, recreating particles like electrons and muons in the regions of interest using whichever necessary subdetectors, a process that takes approximately 40 ms per event. If the event is deemed physics worthy, it is passed on to the EF trigger. The L2 trigger reduces the data rate from 75 kHz to about 1 kHz.

Event Filter

The last level of the ATLAS trigger system is the EF which, like the L2 trigger, is software-based. Using complex software algorithms, the EF trigger uses all available

information from the detector to reconstruct the potentially interesting physics objects seeded by the L2 trigger. For each event, 1 to 4 s is taken by the EF trigger to decide if it is worth saving to disk to be used for offline physics analysis. The EF brings the data rate from 1 kHz to the required rate of 400 Hz set by the ATLAS storage rate.

Data Acquisition System

The ATLAS data acquisition (DAQ) system operates in conjunction with the trigger system. Before a decision is made by the L1 trigger, event data is stored in a data buffer independent from the trigger chain. If an event is rejected by the L1 trigger, the data is also deleted by the DAQ system; however, if the event is passed forward, the ROI information is sent to DAQ readout drivers and stored in readout buffers. The L2 trigger accesses the ROI through the DAQ system and events that pass L2 are fully reconstructed by the DAQ event builder in conjunction with the EF. This involves reconstructing physics objects such as leptons, hadrons, and jets from track hits in the inner detector and energy deposits in the calorimeters. The DAQ system then passes these objects onto the EF which makes the final decision.

Chapter 4

Data and Monte Carlo

Between April 4 and December 6, 2012, the LHC delivered 22.8 fb^{-1} of collision data [62] and amazingly, the ATLAS detector was able to record 21.3 fb^{-1} of these events as illustrated in Figure 4.1. The mark set in 2012 far eclipsed those set in 2010 and 2011 when 45 pb^{-1} and 5.23 fb^{-1} were collected. In this chapter, brief discussions on the structure of ATLAS data and the 2012 data set are given. Following is a description of the production and uses of ATLAS Monte Carlo samples which are collections of simulated data events. To conclude the chapter, the Monte Carlo samples specific to this measurement along with the corrections used to improve their description of the data are presented.

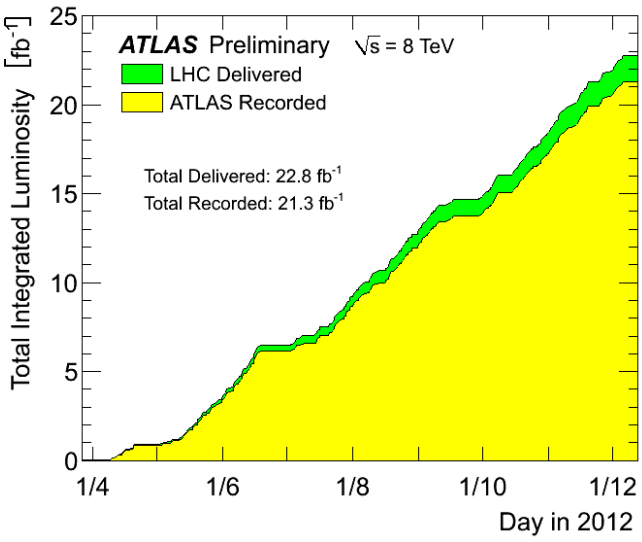

Figure 4.1: The total integrated luminosity delivered by the LHC and recorded by the ATLAS detector between April 4 and December 6, 2012.

4.1 ATLAS Data

ATLAS data is comprised of proton-proton collision events that have been accepted by the trigger system. Events are classified by the event filter into several physics data streams which include electron and photon, muon, and jet streams. For example, an event with a candidate electron is sent to the electron and photon or *EGamma* stream. This categorization is done for every event recorded by the ATLAS detector producing separate data sets for each physics stream. For a particular physics study, running over data from a specific physics stream reduces the number of irrelevant events that need to be analyzed.

ATLAS data taking is divided into *periods* each typically lasting for several weeks. Periods are classified by consistent running conditions of the LHC and ATLAS detector which include, for example, the luminosity or bunch spacing. They are further split into sustained intervals of data collection called *runs* which typically last for hours. Finally, a run is divided into *luminosity blocks*; these are small collections of data recorded over a minute.

Runs and luminosity blocks collected with stable LHC and ATLAS conditions are tabulated in a file called the *good runs list* (GRL). Quality checks such as the stability of the LHC beams, the absence of any hardware malfunctions, and the operation of all ATLAS subdetectors are performed before a run or luminosity block is added to the GRL. In practice, only events belonging to runs or luminosity blocks found in the GRL are used for physics analysis.

4.2 Analysis Data

The measurement described in this dissertation uses LHC proton-proton collision data at $\sqrt{s} = 8$ TeV collected in 2012 with the ATLAS detector. In particular, data periods A, B, C, D, E, G, H, I, J, and L belonging to the EGamma stream are analyzed[1]. The runs used in this analysis are found in the ATLAS good runs list PHYS_StandardGRL_All_Good, a generic GRL that requires all subdetector systems to be fully operational at the time of data collection. In Table 4.1, the periods, GRL integrated luminosity, $\mathcal{L}$, and the number of events are listed. Though ATLAS recorded 21.3 fb^{-1} in 2012, 20.1 fb^{-1} of the data is found in the GRL and used in

[1]Period F contains proton-lead ion collision data while period K contains cosmic-ray background measurements.

this analysis. An uncertainty of 1.9% is assigned to the integrated luminosity as recommended by the ATLAS luminosity group [62].

Period	$\mathcal{L}$ [pb^{-1}]	Events [10^6]
A	785	40
B	5046	171
C	1398	48
D	3276	110
E	2371	77
G	1280	43
H	1453	50
I	1022	35
J	2611	91
L	847	29
Total	20089	694

Table 4.1: The 2012 data periods used in this measurement along with their corresponding GRL integrated luminosities $\mathcal{L}$ and numbers of events.

Plotted in Figure 4.2 is the recording efficiency of ATLAS data taking measured over time. ATLAS averaged an efficiency of 93.5% over the entire 2012 collection period, the same efficiency that was averaged in 2011. Maintaining this efficiency was a great achievement given that in 2012 there was an average pileup of $\langle\mu\rangle = 20.7$, a nearly 3.7 fold increase from the 5.6 interactions averaged in 2011. Figure 4.3 shows a histogram of the recorded luminosity as a function of the pileup.

4.3 ATLAS Monte Carlo

Monte Carlo (MC) simulations play an integral role in calibrating the ATLAS detector and analyzing LHC physics. They are used to study detector response which often does not have an analytic representation, compare theoretical predictions to measurements, estimate the background contamination in signal data, and evaluate both theoretical and experimental uncertainties. ATLAS MC is processed the same way and uses the same framework as experimental data; therefore, software written to analyze data can also be used for ATLAS MC allowing for a direct comparison to be made between the two. In ATLAS, Monte Carlo is produced in three stages: *generation*, *simulation*, and *reconstruction*.

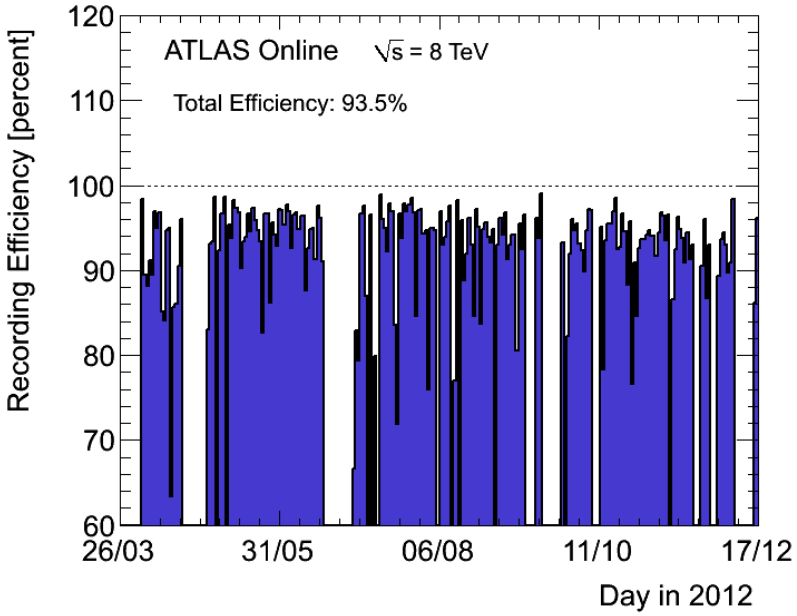

Figure 4.2: The recording efficiency of the ATLAS detector during the 2012 run. Between the start of collection and the end, an average recording efficiency of 93.5% was achieved.

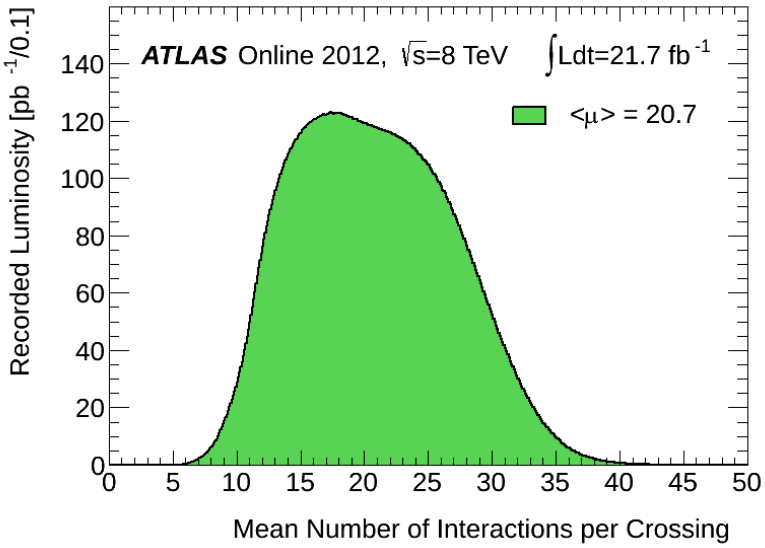

Figure 4.3: Histogram of the mean number of interactions per bunch crossing (pileup) for each 1 pb^{-1} of data collected in 2012. An average pileup of $\langle\mu\rangle = 20.7$ was observed.

4.3.1 Generation

The first stage of ATLAS MC production is generation which includes the following steps:

1. The amplitude or matrix element $\mathcal{M}$ of a hard scattering process of interest is calculated to some order in QCD and EW (for example LO or NLO) which determines the number of higher order Feynman diagrams to be included in the calculation;

2. Using $\mathcal{M}$ and the parton distribution functions of the proton, the four-momenta of all final state particles involved in the hard scatter are computed;

3. Initial and final state particles that take part in the hard scatter are allowed to radiate photons or gluons, which subsequently split into quark-antiquark pairs;

4. The partons that do not take part in the hard scatter form a coloured state resulting in the emission of gluons which themselves may radiate gluons collectively forming *parton showers*;

5. Partons in the final state, including those that were not involved in the hard scatter, hadronize to form jets which may be unstable and further decay.

Having completed these steps, all final state particles in the MC event have now been generated.

At generator-level, there are three standard definitions of final state leptons used in ATLAS measurements which differ in their treatment of QED radiation from the leptons [63]:

- Born lepton: A lepton *before* any QED radiation has been emitted;

- Bare lepton: A lepton *after* all QED radiation has been emitted which is then excluded from any subsequent calculations involving the lepton;

- Dressed lepton: A hybrid of the Born and bare definitions where the bare lepton and all emitted QED radiation within a cone of $\Delta R < 0.1$ around the lepton are resummed.

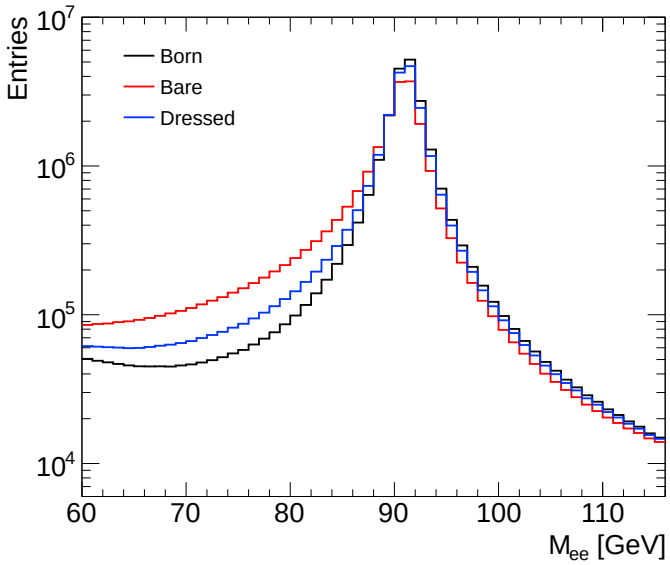

Figure 4.4: Invariant mass distributions of Born, bare, and dressed leptons.

All three lepton types are readily accessible in ATLAS Monte Carlo samples. Figure 4.4 shows invariant mass distributions constructed using Born, bare, and dressed leptons centred around the Z-peak. For a Born dilepton pair whose invariant mass is near the Z-peak, its bare counterpart would have a lower invariant mass since any energy carried by radiated photons is ignored. As a result, the bare distribution is the flattest of the three invariant mass spectra. Conversely, by restricting the leptons from radiating, no energy is carried away making the Born distribution the one with the sharpest peak. Finally, by definition the behaviour of the dressed distribution lies between the Born and bare distributions. It should be noted that the dressed lepton most resembles the leptons that are measured in the detector as both have finite sizes.

4.3.2 Simulation

The next stage in MC production is simulation. All generated final state particles are simulated to pass through a virtual model of the ATLAS detector created using GEANT4 [64], a simulation software package. Interactions between generated particles and the simulated ATLAS detector have been tuned to match those from real events. Energy deposits from the generated particles and the particles resulting from their interactions with the detector are recorded. A process then converts these deposits into simulated signals mimicking the signals from the real ATLAS detector.

In order to replicate the pileup conditions in data, inelastic events passed by a

maximally inclusive trigger or minimum bias MC events [65] are generated and their interactions with the detector are simulated. The simulated signals from the original hard scatter of interest are overlaid with the signals from the minimum bias events. This produces MC events in which seemingly multiple interactions take place, similar to what happens in real LHC collisions.

4.3.3 Reconstruction

Finally, reconstruction occurs whens the information produced in the simulation stage is passed on to the reconstruction software which recreates physics objects such as electrons, photons, and jets from the simulated signals. Reconstruction is performed using the same software that is used for analyzing the data so that a direct comparison can be made between reconstructed events in MC and data. At the completion of reconstruction, the set of MC events produced is called a *Monte Carlo sample*.

4.4 Analysis Monte Carlo Samples

This measurement uses several Monte Carlo samples to fully model all the physics processes potentially present in data. Samples are used to model both the signal process, $q\bar{q} \to Z/\gamma^* \to e^-e^+$, and many of the major background processes. The samples are generated using various *Monte Carlo generators*, each with its own specialization and method of generating particles:

- POWHEG [66]: POWHEG is an event generator that calculates hard scatter matrix elements to NLO in QCD, a very important feature for modelling LHC collisions which produce large numbers of hadronic jets, and EW. Modelling of parton showers is done by interfacing POWHEG with a parton shower generator.

- PYTHIA [67]: PYTHIA is a multi-purpose generator capable of modelling lepton-lepton, lepton-hadron, and hadron-hadron events. It contains a large library of hard processes and various other phenomena such as multiple parton interactions, parton showers, and hadronization. PYTHIA generates hard scattering events at LO with higher order corrections made by including parton showers. PHOTOS [68], a precision generator, is commonly used in combination with PYTHIA to generate QED radiative effects in $W^{\pm}$ and Z decay events.

- HERWIG [69]: Like PYTHIA, HERWIG is a multi-purpose event generator which produces LO in QCD hard scattering events using matrix elements. It models initial and final state QCD radiation using parton showers. For MC samples generated with HERWIG, multiple parton interactions are typically included by using the event generator JIMMY [70] in conjunction with HERWIG.

- LPAIR [71]: LPAIR specializes in processes in which lepton pairs are produced electromagnetically from lepton-lepton, lepton-hadron, and hadron-hadron interactions via two photon processes. LPAIR Monte Carlo samples are used in this analysis to model events in which diffractive dissociation occurs.

4.4.1 Signal Monte Carlo Samples

In Table 4.2, the signal MC samples used in this analysis are summarized. The samples were produced using POWHEG for event generation and PYTHIA for modelling parton showers [72, 73]. The first three entries in this table correspond to samples generated with an invariant mass requirement of $M_{ee} > 60$ GeV on the final state Born electrons. Additionally, requirements on the electrons or *lepton filters* were applied to these samples. Requirements of two electrons and one electron in the final state are applied to the first two samples, respectively. These electrons must satisfy the following pseudorapidity and transverse momentum requirements: $|\eta^e| < 2.7$ and $p_T^e > 15$ GeV. The third sample listed in Table 4.2 requires an electron with $|\eta^e| > 2.7$ and $p_T^e < 15$ GeV in each event. The combination of these three samples forms a complete $q\bar{q} \to Z/\gamma^* \to e^- e^+$ sample. The three remaining signal MC samples in the table were generated in finite M_{ee} regions with only the first sample being filtered for two electrons with $|\eta^e| > 2.7$ and $p_T^e < 15$ GeV in each event. The production cross-section, lepton filter efficiency, and number of events are listed for each sample.

4.4.2 Background

In this analysis, MC samples are used to model several of the largest sources of background. The contributions from the processes illustrated as Feynman diagrams in Section 2.3.1 are all simulated using Monte Carlo. A number of generators are used to produce these background samples: POWHEG with PYTHIA, HERWIG, and LPAIR. A complete list of the background MC sample used are shown in Tables 4.3 and 4.4. From hereafter, the sum of these background contributions will be

Process	M_{ee} [GeV]	Lepton filter	σ [pb]	ϵ^{filter} [%]	Events [10^3]
$Z/\gamma^* \to ee$	> 60	Two e	1109.9	55.65	50000
$Z/\gamma^* \to ee$	> 60	One e	1109.9	31.47	20000
$Z/\gamma^* \to ee$	> 60	Remainder	1109.9	12.89	3000
$Z/\gamma^* \to ee$	20-60	Two e	373.64	25.55	9848
$Z/\gamma^* \to ee$	120-180	None	9.8460	100.00	5000
$Z/\gamma^* \to ee$	180-250	None	1.5710	100.00	1000

Table 4.2: Signal Monte Carlo samples used in this analysis. Generated using POWHEG, the CT10 [74] parton distribution functions are used with the AU2 tune [75]. The first column gives the signature of the process being simulated followed by the invariant mass M_{ee} range in which the events were generated, lepton requirements or filters applied, cross-section σ, filter efficiency ϵ^{filter}, and number of events in the sample.

referred to as the *Monte Carlo background*.

Although the MC background constitutes a large portion of the total background, a significant fraction of background remains due primarily to semi-leptonic heavy-flavour quark decays ($b\bar{b}$ or $c\bar{c} \to e^-e^+X$), Dalitz decay ($\pi^0 \to e^+e^-\gamma$), and photon conversions. This background is called the *multijet background* and it is formally defined as the background from processes other than those of the Monte Carlo background. The multijet background cannot be estimated using MC simulations. Being highly complex objects, jets are described by QCD processes which are extremely difficult and computationally intensive to model well. Instead, this analysis chooses to estimate the multijet background using a data-driven technique described in detail in Chapter 7.

4.4.3 Normalization

The Monte Carlo samples used in this measurement were produced to have integrated luminosities different from the integrated luminosity of the data set, $\mathcal{L} = 20.1$ fb^{-1}. In order to properly model the data, each sample must be normalized to $\mathcal{L}$ by weighting each and every event by

$$w_{\text{MC}} = \frac{\sigma \epsilon^{\text{filter}} \mathcal{L}}{N^{\text{evt}}}, \tag{4.1}$$

where σ is the highest order cross-section of the modelled process available and N^{evt} is the number of events in the sample.

Process	Generator	σ^{LO} [pb]	σ^{NLO} [pb]	$\delta\sigma$ [%]	$\epsilon^{\mathrm{filter}}$ [%]	Events [10^3]
$Z/\gamma^* \to \tau\tau$	POWHEG	1109.9	1143.2	5.0	100.0	5000
$WW \to eX$	HERWIG	32.501	58.7	10.0	38.21	2500
$ZZ \to eX$	HERWIG	4.6914	7.2	4.2	21.17	245
$WZ \to eX$	HERWIG	12.009	20.3	4.0	30.55	1000
$W^+ \to e\nu$	POWHEG	6891.0	7073.8	5.0	100.0	23000
$W^- \to e\nu$	POWHEG	4790.2	5016.2	5.0	100.0	17000
$W^+ \to \tau\nu$	POWHEG	6890.0	7103.6	5.0	100.0	29949
$W^- \to \tau\nu$	POWHEG	4790.9	4920.3	5.0	100.0	5000
$t\bar{t} \to eX$	POWHEG	210.84	252.88	6.0	54.30	50000
t (s-channel)	POWHEG	1.6424	1.8176	6.0	100.00	6000
t (t-channel)	POWHEG	17.519	18.395	6.0	100.00	5000
$Wt \to X$	POWHEG	20.461	22.644	6.0	100.00	1000

Table 4.3: Background Monte Carlo samples used in this analysis. The first column is the physics process simulated followed by its corresponding event generator. Next are the LO cross-section σ^{LO}, NLO cross-section σ^{NLO}, and cross-section uncertainty $\delta\sigma$. Finally, the filter efficiency $\epsilon^{\mathrm{filter}}$ and the number of events are given. The cross-sections and uncertainties are obtained from various sources [76, 77, 78, 79, 80, 81].

4.5 Monte Carlo Corrections

ATLAS Monte Carlo has been tuned to data using ATLAS test beam experiments [85, 86] and to subsequent measurements from past and present experiments. Disagreements between data and MC represent unknown physical effects in the former or errors and approximations in the latter. This analysis applies several ad hoc corrections to Monte Carlo in the form of event weights to improve the agreement with data.

Pileup

The shapes of the distributions for pileup μ and for the number of primary vertices N^{vtx} in data and MC differ slightly. Monte Carlo events are reweighted by pileup correction factors to improve the distributions to better match what is observed in data. Additionally, a constant weight of 1/1.09 is applied to all MC events to correct for a residual mismatch in the N^{vtx} distributions [65]. In Figure 4.5, the effect these corrections have on the distribution of N^{vtx} can be seen.

Process	Generator	M_{ee} [GeV]	σ [pb]	$\delta\sigma$ [%]	ϵ^{filter} [%]	Events [10^3]
$\gamma\gamma$ (SD)	LPAIR	20-60	27.728	40.0	4.2290	500
$\gamma\gamma$ (SD)	LPAIR	60-200	1.447	40.0	14.569	500
$\gamma\gamma$ (SD)	LPAIR	200-600	0.038	40.0	22.015	200
$\gamma\gamma$ (DD)	PYTHIA	20-60	5.601	40.0	100.0	500
$\gamma\gamma$ (DD)	PYTHIA	60-200	0.946	40.0	100.0	500
$\gamma\gamma$ (DD)	PYTHIA	200-600	0.042	40.0	100.0	200
$\gamma\gamma$ (QED)	HERWIG	20-60	18.657	40.0	32.48	500
$\gamma\gamma$ (QED)	HERWIG	60-200	1.8883	40.0	100.0	500
$\gamma\gamma$ (QED)	HERWIG	200-600	0.0853	40.0	100.0	200

Table 4.4: Photon-induced background Monte Carlo samples used in this analysis. The first column is the physics process simulated followed by its corresponding event generator and the invariant mass M_{ee} range in which the events were generated. Next is the cross-section σ then its uncertainty $\delta\sigma$. Finally, the filter efficiency ϵ^{filter} and the number of events are given. The cross-sections and uncertainties are obtained from various sources [82, 83]. The samples labelled "SD" and "DD" correspond to single- and double-dissociative photon induction processes while "QED" correspond to the exclusive process [84].

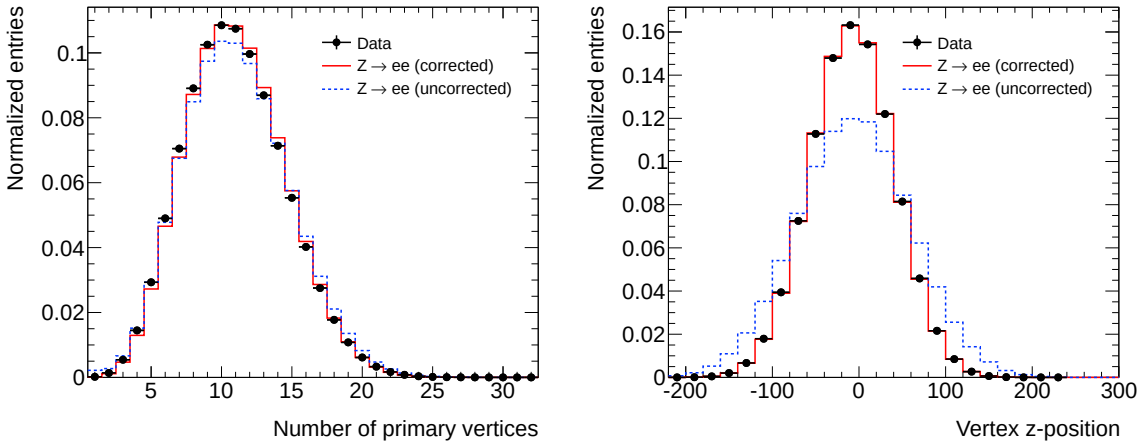

Figure 4.5: The number of primary vertices (left) and vertex z-position (right) observed in data and predicted in signal ($Z \to ee$) MC before and after applying corrections.

Vertex Position

The Monte Carlo samples used in this analysis were simulated with broader beam spot parameters than those measured in data. In particular, the distribution of the position of the reconstructed primary vertex along the z-axis is wider in simulation

than it is in data. To correct for this, Monte Carlo events are additionally weighted by correction factors that narrow this distribution to better resemble data. The effect these corrections have on the MC can be seen in Figure 4.5.

k-Factors

The signal MC samples are generated with POWHEG which calculates matrix elements at NLO. The normalization and shape of the cross-section modelled using these samples may not adequately resemble those measured in data since NLO may be insufficient in fully describing what is observed. To include some higher order effects, signal Monte Carlo events are further weighted by invariant mass-dependent *k-factors* [87] defined as

$$k_i = \frac{\sigma_i^{\mathrm{FEWZ}}}{\sigma_i^{\mathrm{POWHEG}}}, \qquad i = 1, 2, 3, ..., \tag{4.2}$$

where σ^{FEWZ} is the Drell-Yan cross-section calculated to NNLO in QCD and include additional higher order EW corrections using theoretical simulation software FEWZ [88]; σ^{POWHEG} is the cross-section of the POWHEG signal MC; and i indexes the mass bins in which the k-factors are calculated. Application of these k-factors, which are illustrated in Figure 4.6, enhances the signal MC to include the corrections that are present in the FEWZ calculation.

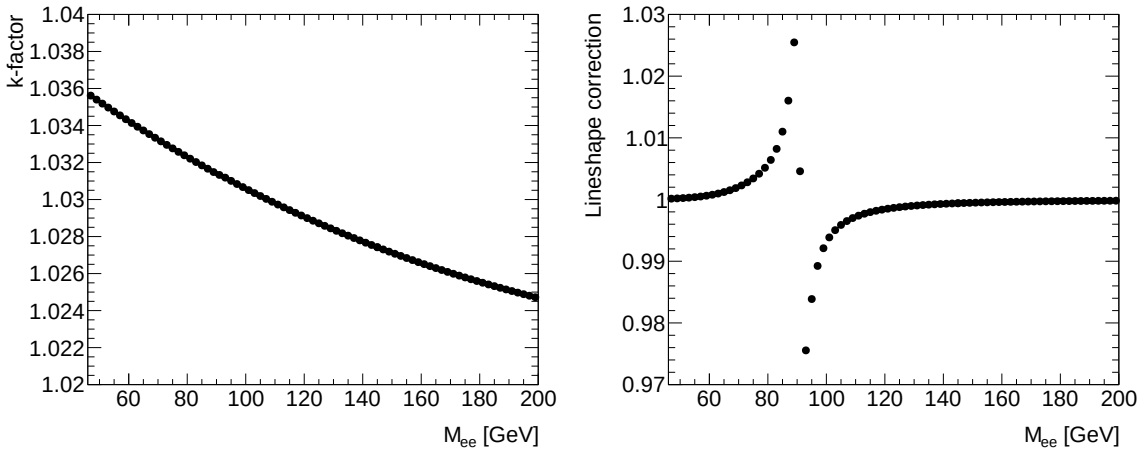

Figure 4.6: Invariant mass-dependent k-factors (left) and lineshape corrections (right).

Lineshape

A final event correction is applied to signal MC to improve the agreement between the POWHEG predicted and the measured Z lineshape. The Z boson peak follows a relativistic Breit-Wigner distribution but POWHEG generates Z events using a fixed or constant Breit-Wigner width Γ_Z. Higher order electroweak corrections such as improved descriptions of photon-lepton coupling and Z-lepton coupling are made to the signal MC by scaling the fixed width with $\hat{s}$, the partonic centre-of-mass energy:

$$M_Z\Gamma_Z \longrightarrow \frac{\hat{s}}{M_Z}\Gamma_Z, \tag{4.3}$$

which resolves the lineshape problems in POWHEG. The lineshape corrections have the greatest effect near the Z mass, M_Z, as can be seen in Figure 4.6.

Chapter 5

Electrons in ATLAS

This dissertation presents a measurement of events with an electron-positron pair in the final state. Experimentally, electrons can be defined in a number of ways depending on the algorithm used to reconstruct candidate electrons and the criteria used to identify candidates as indeed electrons. ATLAS uses different electron reconstruction algorithms for electrons detected in the central region and electrons in the forward regions of the detector. Three standard sets of identification criteria are used which tradeoff between retaining the largest number of electrons and rejecting the most *fakes* or objects misidentified as electrons. In this chapter, electron reconstruction and identification are described along with a discussion on electron performance.

5.1 Electron Reconstruction

Electrons that travel through the central region ($|\eta| < 2.47$) of the detector leave tracks in the inner detector and energy deposits in the electromagnetic calorimeter. Reconstruction of *central electron* candidates begins with track reconstruction. Candidate tracks are parametrized with information from the pixel detector and semiconductor tracker which is used to initialize the position, direction, and curvature of the tracks. From the interaction point outwards, candidate tracks are constructed by including more and more hits in the inner detector. Initially, they are built assuming negligible energy losses due to radiation. However, if a candidate track cannot be matched to a region of interest in the EM calorimeter, radiative losses are permitted which may potentially resolve the mismatch between the track and energy deposit [89].

Next, vertex reconstruction is performed by extrapolating the reconstructed tracks back towards the interaction point. The point of intersection of multiple tracks with $p_T > 0.5$ GeV is taken as a vertex. Among the reconstructed vertices, the one having the largest sum of $|p_T|$ is assigned to be the primary vertex.

Clustering or grouping of energy deposits in the EM calorimeter is performed by dividing the calorimeter into a grid with a cell size of $\Delta\eta \times \Delta\phi = 0.025 \times 0.025$; this cell size corresponds to the granularity of the middle layer of the electromagnetic calorimeter. For each of the grid cells, the energy in all three layers of the EM calorimeter are summed into an *energy tower*. An algorithm called the *sliding window method* [90] scans the array of energy towers using a window of $3\,\Delta\eta \times 5\,\Delta\phi$ in size. The window is positioned such that the energy contained is a local maximum and if the transverse energy is at least 2.5 GeV, the energy cluster is recorded. The position of the cluster is determined using a smaller window, which is less sensitive to noise, of size $3\,\Delta\eta \times 3\,\Delta\phi$ centred at the energy tower with the most energy. The barycentre of this window is taken as the position of the energy cluster.

The reconstructed tracks are then extrapolated to the middle layer of the EM calorimeter and if a track passes through the barycentre of the energy cluster within a cone of size $\Delta R < 0.3$, that track and the energy cluster are paired to form an electron candidate. If multiple tracks match to the same cluster, the track with the most pixel hits and closest to the barycentre is chosen. In a final step, the electron energy cluster is rebuilt from towers of sizes $3\,\Delta\eta \times 7\,\Delta\phi$ if detected in the electromagnetic barrel and $5\,\Delta\eta \times 5\,\Delta\phi$ in the end-caps, sizes chosen as a compromise between including the maximum amount of energy from an EM shower and excluding the most pileup and electronic noise. In Figure 5.1 is an event display of a reconstructed dielectron event.

The four-momentum of a central electron is computed using a combination of electron energy cluster and track measurements. The energy component is set to the cluster energy while the directional components are obtained from the track. Let E be the energy measured from the electron cluster and θ and ϕ the polar and azimuthal angles measured from the track that is matched to the cluster. The four-momentum of the electron is

$$p^\mu = (E,\, p_x,\, p_y,\, p_z) = (E,\, p\sin\theta\cos\phi,\, p\sin\theta\sin\phi,\, p\cos\theta), \tag{5.1}$$

where $p = \sqrt{E^2 - m^2} \approx E$ assuming that the energy is much greater than the electron mass m.

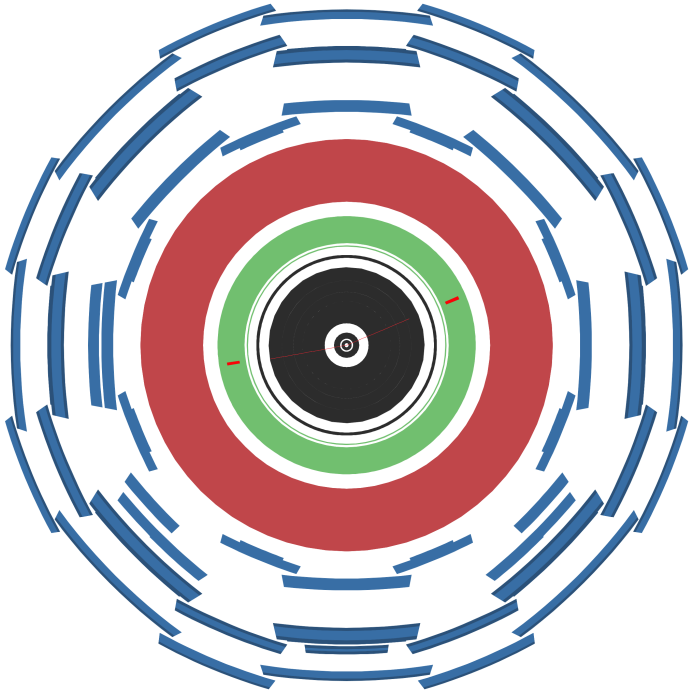

Figure 5.1: Cross-sectional display of an ATLAS event with two final state electrons reconstructed in the barrel. The inner detector is shown in black while the electromagnetic calorimeter is represented by the green circular band.

Forward Electrons

In the forward regions ($2.5 < |\eta| < 4.9$) of the ATLAS detector, electron reconstruction relies solely on the calorimeters since the inner detector only covers $|\eta| < 2.5$. *Forward electron* reconstruction uses the *topological method* algorithm [90] which clusters energy deposits with a variable perimeter, in contrast to the fixed window used for central energy clusters. The energy deposited in a group of cells is compared to the expected noise determined from calibration studies. The cell containing the most energy must have a signal-to-noise ratio of 4 or higher. For its neighbouring cells in all directions to be included, they must meet a threshold of at least 2. The final set of cells included are required to have a signal-to-noise ratio greater than 0. The resultant topological cluster is recorded as a forward electron candidate whose four-momentum is constructed from the total energy measured in the cells and the position of the barycentre of the topological cluster. Since no tracking exists in the forward region, the charge of forward electrons cannot be determined.

5.2 Electron Identification

A set of reconstructed electron candidates will consist not only of electrons but also objects such as jets whose passage through the detector may resemble that of an electron. Additionally, some candidates may be secondary electrons produced from the decay of jet constituent particles or photon conversions. Energy clusters of secondary electrons are typically found near large energy deposits belonging to their parent particles. In this analysis, the electrons of interest are produced from Z/γ^* decay which leave isolated clusters. To distinguish signal electrons from these other objects, the characteristics of the reconstructed electron candidates must be further examined, a process known as *electron identification*.

For central electrons, identification is based on variables that describe the properties of the electromagnetic shower shape, the properties of the track, and the quality of match between the two. The variables used in central electron identification along with a brief description are summarized in Table 5.1. For each of the variables listed, a threshold window is set for which electron candidates must satisfy. There are three standard electron identification criteria used in ATLAS [91]: *loose*, *medium*, and *tight*. To satisfy loose idenification, the candidate electron must satisfy 9 of the 17 identification criteria listed in Table 5.1. Loose identification selects real electrons at the highest efficiency but at the expense of poor jet rejection. Requiring all 17 cuts to be passed, tight identification is highly efficient at rejecting jets but has the poorest selection efficiency of the three definitions. Lastly, falling in between loose and tight is medium identification which requires 14 of 17 cuts to be satisfied.

Forward Electrons

Identification of forward electrons is based on the differences between electromagnetic and hadronic shower shapes and quantities known as *cluster moments* defined as

$$\langle x^n \rangle = \frac{\sum_i E_i x_i^n}{\sum_i E_i}, \tag{5.2}$$

where x is some observable of the forward electron energy cluster, E its energy, and i runs over the number of cells in the cluster. Several of the requirements used to identify forward electrons are listed in Table 5.2.

Like central electrons, there are three main definitions used to identify forward

Name	Type	Description	Loose	Medium	Tight
R_{had}	Hadronic leakage	Ratio of the E_T in the hadronic calorimeter to the E_T of the EM cluster in the range $0.8 < \|\eta\| < 1.37$	✓	✓	✓
R_{had1}	Hadronic leakage	Ratio of the E_T in the first layer of the hadronic calorimeter to the E_T of the EM cluster in the range $\|\eta\| < 0.8$ or $\|\eta\| > 1.37$	✓	✓	✓
f_3	EM calorimeter	Ratio of the energy in the third layer to the total energy in the EM calorimeter		✓	✓
$W_{\eta 2}$	EM calorimeter	Lateral EM shower width measured in a window of 3×5 cells	✓	✓	✓
R_η	EM calorimeter	Ratio of the energy in 3×7 to the energy in 7×7 centred at the electron cluster position	✓	✓	✓
w_{stot}	EM calorimeter	Shower width measured in a window of size $\eta \times \phi \approx 0.0625 \times 0.2$	✓	✓	✓
E_{ratio}	EM calorimeter	Ratio of the energy difference between the largest and second largest energy deposits in the cluster over their sum	✓	✓	✓
n_{Blayer}	Track quality	Number of hits in the first layer of the pixel detector, also known as the B-layer		✓	✓
n_{pixel}	Track quality	Number of hits in the pixel detector	✓	✓	✓
n_{Si}	Track quality	Number of hits in the pixel detector and semiconductor tracker	✓	✓	✓
d_0	Track quality	Transverse distance to the interaction point or impact parameter		✓	✓
n_{TRT}	Track quality	Total number of hits in the TRT		✓	✓
F_{HT}	Track quality	Ratio of the number of high-threshold or 6-7 keV hits to the total number of hits in the TRT		✓	✓
$\Delta\eta_1$	Matching	Difference in η between the extrapolated track and energy cluster in the first or strip layer of the EM calorimeter	✓	✓	✓
$\Delta\phi_2$	Matching	Difference in η between the extrapolated track and energy cluster in the middle layer			✓
E/p	Matching	Ratio of the cluster energy to the track momentum			✓
isConv	Conversions	Reject electron candidates matched to reconstructed photon conversions			✓

Table 5.1: Shower and track properties used in the identification of central electrons. The variables used in loose, medium, and tight electron identification are indicated.

Type	Description
Shower depth	The distance between the electromagnetic shower barycentre and the front face of the EM layer of the FCal measured along the shower axis
Maximum cell energy	The ratio of the maximum energy deposited in a single cell to the energy of the remaining cells
Longitudinal second moment	A measure of the longitudinal extension of the cluster, defined as the second moment of the distance of each cell to the shower center measured along the longitudinal axis
Transverse second moment	A measure of the transverse extension of the cluster, defined as the second moment of the distance of each cell to the shower center in the transverse direction

Table 5.2: Variables used in the identification of forward electrons.

electrons: *forward loose*, *forward medium*, and *forward tight*. Going from forward loose to forward tight, electron selection efficiency decreases while jet rejection increases.

5.3 Energy Corrections

The ATLAS electromagnetic calorimeter was calibrated primarily using the results of ATLAS test beam experiments [92]. Monte Carlo simulations were tuned using the data from these tests to ensure similar energy responses in data and simulation. However, residual differences between the two exist due to, for example, calorimeter inhomogeneities and imperfect simulation of the energy resolution. To illustrate the effect of these differences, consider an electron with true energy E_{true}. Suppose that this electron passes through the ATLAS detector and an energy E_{data} is measured. Imagine now that a Monte Carlo electron is generated with energy E_{true} which then undergoes simulation and reconstruction. The reconstructed energy, E_{MC}, should equal the measured value, E_{data}, since both electrons started with E_{true}. However, due to energy response differences between the detector and simulation, the data and MC energies are in general different. In order to minimize these residual differences, *energy scale* corrections are applied to data while *energy resolution* corrections are applied to MC.

To obtain a corrected energy $E_{\text{data}}^{\text{corr}}$ that matches the energy predicted in MC, an energy scale correction α is applied to the data in the following way:

$$E_{\text{data}}^{\text{corr}} = \left(\frac{1}{1+\alpha}\right) E_{\text{data}} = E_{\text{MC}}. \tag{5.3}$$

Energy scale corrections in bins of electron η are provided by the EGamma group [93]. They are determined by comparing the invariant mass spectra of $Z \to ee$ events in data and in MC and performing an unbinned log-likelihood fit to find the optimal α in a given η bin that yields the best match between the two Z-peaks. The effect of these corrections on the data can be seen in Figure 5.2.

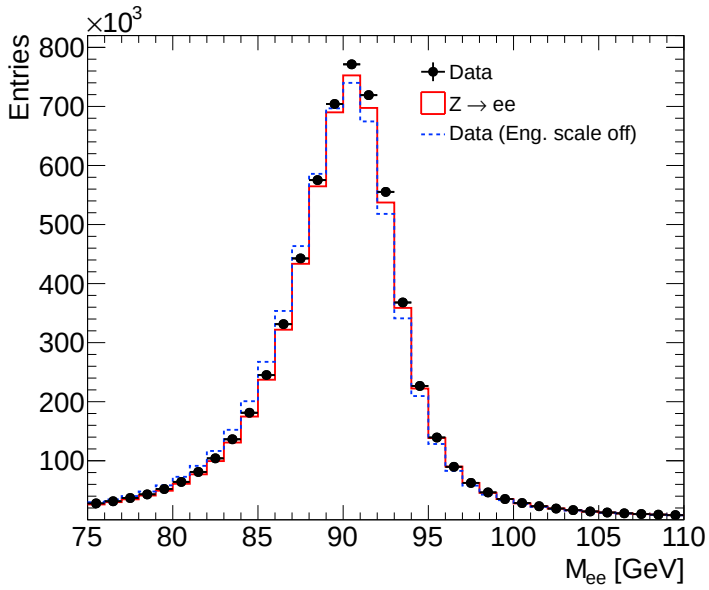

Figure 5.2: Invariant mass distributions measured from data with and without energy scale corrections applied and predicted by Monte Carlo. The corrections improve the alignment of the data and MC Z-peaks.

A second energy correction, applied to MC electrons, is used to match the electron energy resolution in MC to what is observed in data. The widths of the Z-peaks measured in data and MC differ due to mismodelling of the EM calorimeter energy resolution which is defined as

$$\frac{\sigma}{E} = \frac{a}{\sqrt{E}} \oplus \frac{b}{E} \oplus c, \tag{5.4}$$

where a is the sampling term, b the noise term, and c the constant term. The sampling term is a function of the absorber material, active material, and thickness of the

sampling layers while the noise term is due to pileup and electronic noise which is determined from calibration runs of the ATLAS detector. At large E, the constant term, which depends on the uninstrumented regions of the calorimeter, limits the performance of the EM calorimeter. Assuming that a and b in Equation (5.4) are well-known, corrections to the energy resolution in MC are taken as energy-independent constants β:

$$\frac{\sigma_{\text{data}}}{E_{\text{data}}} = \frac{\sigma_{\text{MC}}}{E_{\text{MC}}} \oplus \beta. \tag{5.5}$$

Like the energy scale correction, *energy smearing* factors are binned in electron η and are provided by the EGamma group [93]. They are determined by fitting a Breit-Wigner function convoluted with a Crystal Ball function to the $Z \to ee$ invariant mass spectrum in data and in MC. The parameters of the Breit-Wigner function are fixed but the width parameter of the Crystal Ball function is allowed to vary. For a given η bin, the smearing factor β is determined from the difference between the data fit and the MC fit. In Figure 5.3, the effect the energy smearing factors have on the predicted dielectron invariant mass distribution can be seen. These correction factors have the effect of widening the MC Z-peak indicating that the simulated resolution was originally too narrow.

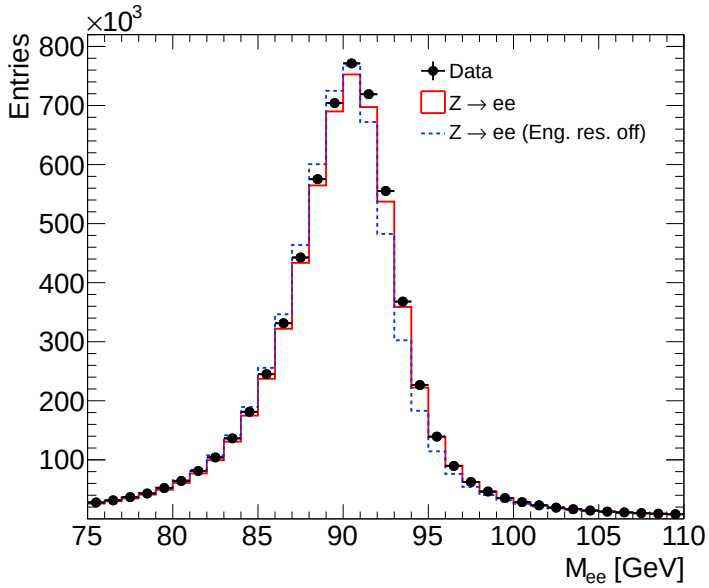

Figure 5.3: Invariant mass distributions measured from data and predicted by Monte Carlo with and without energy resolution corrections applied. The corrections widen the Z-peak in MC improving the agreement between data and MC.

5.4 Efficiency Scale Factors

The probability of an energy cluster belonging to a true electron being reconstructed and identified as an electron and passing an event filter trigger is known as the electron *efficiency*, often denoted as ϵ. It is the product of three independent efficiencies:

$$\epsilon = \epsilon^{\text{reco}} \epsilon^{\text{id}} \epsilon^{\text{trig}}, \tag{5.6}$$

where ϵ^{reco}, ϵ^{id}, and ϵ^{trig} are the reconstruction, identification, and trigger efficiencies. The reconstruction efficiency is the probability the energy cluster found in the EM calorimeter is reconstructed as a candidate electron. The identification efficiency is the probability that the reconstructed electron satisfies a particular (loose, medium, or tight) electron identification criteria. As for the trigger efficiency, it is the probability the electron, in addition to being reconstructed and identified as an electron, also satisfies some EF trigger. Mathematically, they are defined as

$$\epsilon^{\text{reco}} = \frac{N^{\text{reco}}}{N^{\text{clust}}}, \qquad \epsilon^{\text{id}} = \frac{N^{\text{id}}}{N^{\text{reco}}}, \qquad \epsilon^{\text{trig}} = \frac{N^{\text{trig}}}{N^{\text{id}}}, \tag{5.7}$$

where N^{clust} is the number of EM clusters found in some clean, unbiased sample of electrons and N^{reco} is the number of candidate electrons in the same sample that are reconstructed. Moreover, N^{id} is the number of reconstructed electrons that pass the identification requirement and N^{trig} is the number of reconstructed electrons that satisfy both identification and trigger cuts.

Efficiencies are determined using a data-driven technique called the *tag-and-probe method* [94]. This method involves the selection of dielectron events having an invariant mass near the mass of the Z, e.g. $80 < M_{ee} < 100$ GeV. One of these electrons, the *tag*, must pass very strict requirements ensuring with high probability that the object is in fact an electron. Such stringent cuts are used to reduce the background contamination from processes other than $Z \to ee$. The second object, known as the *probe*, is likely to be the second electron of the $Z \to ee$ decay. Having a set of probes, they are then used to determine N^{clust}, N^{reco}, N^{id}, and N^{trig} which are substituted into Equation (5.7) to give ϵ^{reco}, ϵ^{id}, and ϵ^{trig}.

The reconstruction, identification, and trigger efficiencies simulated in MC differ slightly from those measured in data. To mitigate these differences, corrections known as *scale factors* are applied to MC electrons. From data and MC efficiency

measurements, scale factors for each of the three efficiencies can be determined as

$$s^{\text{reco}} = \frac{\epsilon^{\text{reco}}_{\text{data}}}{\epsilon^{\text{reco}}_{\text{MC}}}, \quad s^{\text{id}} = \frac{\epsilon^{\text{id}}_{\text{data}}}{\epsilon^{\text{id}}_{\text{MC}}}, \quad s^{\text{trig}} = \frac{\epsilon^{\text{trig}}_{\text{data}}}{\epsilon^{\text{trig}}_{\text{MC}}}, \tag{5.8}$$

and the total scale factor s is simply their product:

$$s = s^{\text{reco}} s^{\text{id}} s^{\text{trig}}. \tag{5.9}$$

For each electron in an event, the Monte Carlo event weight must be multiplied by its corresponding scale factor. In a Drell-Yan event, which has two electrons in the final state, the MC weight would need to be multipled by two scale factors:

$$w_{\text{MC}} \longrightarrow s_1 s_2 w_{\text{MC}}, \tag{5.10}$$

where s_1 and s_2 are the scale factors of the two electrons. The EGamma group provides the scale factors required for this analysis in two-dimensional bins of electron p_T and $|\eta|$ which are illustrated in Figure 5.4 along with their uncertainties.

5.5 Charge Misidentification

There are two definitions of charge misidentification, one for data and one for MC simulation. For data, the charge is said to be misidentified if the charge of an electron before entering the detector does not equal the charge that is measured. Similarly, a charge misidentification occurs in MC if the charge of a generated electron is different from the charge after reconstruction. In either case, charge misidentification is the result of an electromagnetic energy cluster being matched to a track that does not belong to the electron or a track that does indeed belong to the electron but has been mismeasured. The probability of charge misidentification in data and MC is measured by the EGamma group [95] using the same tag and probe method used to determine the efficiencies. Again, a sample of $Z \to ee$ events are selected in data and MC by requiring the invariant mass of the event to be near the Z mass. The rate of charge misidentification is determined by comparing the number of dielectron pairs with the same electric charge to the number of oppositely charged pairs. Plotted in Figure 5.5 are the rates found in data and MC in bins of electron η.

As Figure 5.5 shows, the probability of charge misidentification differs in data and MC, especially at high $|\eta|$ values. To correct this, reconstructed electrons in MC are

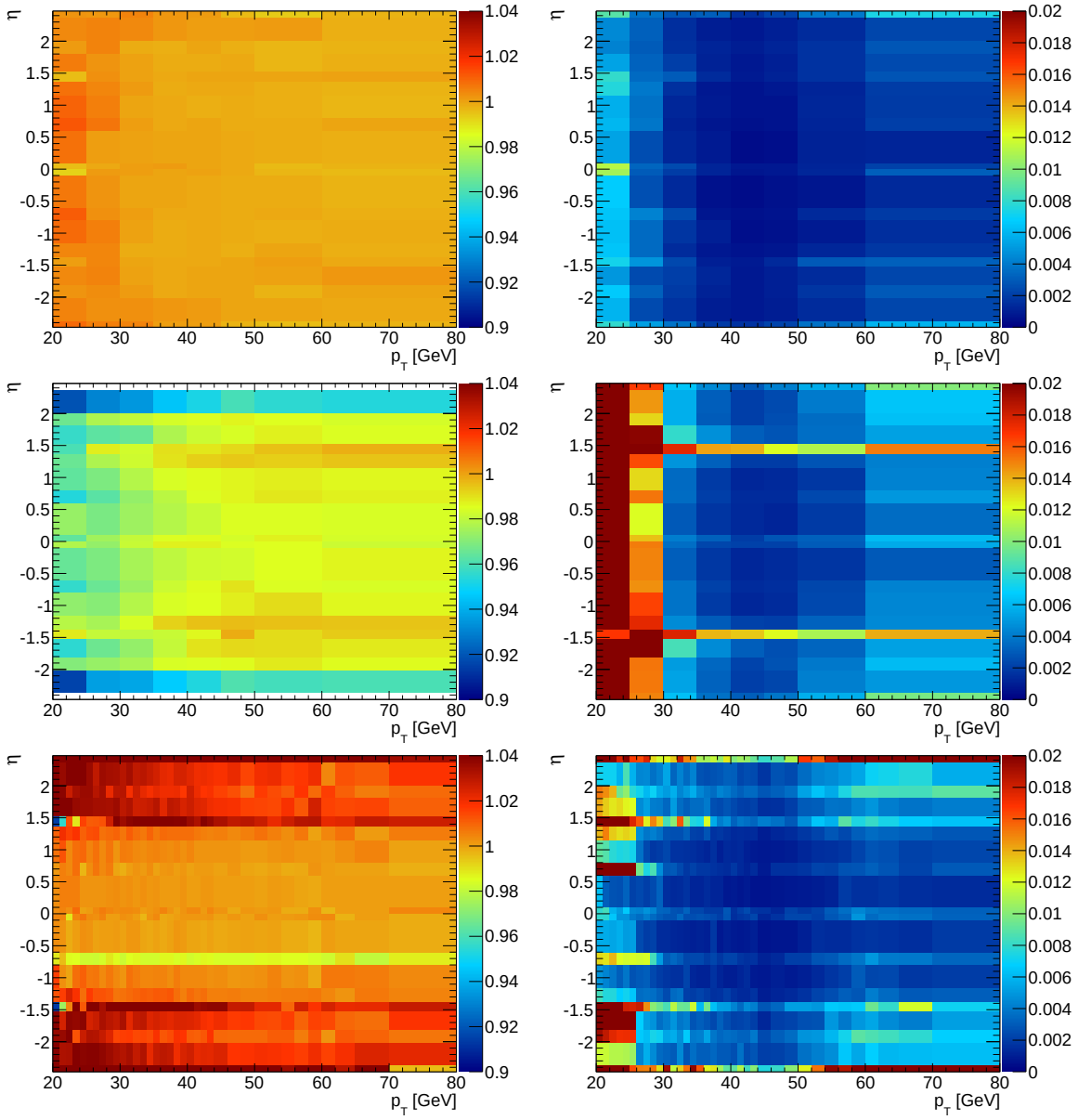

Figure 5.4: EGamma efficiency scale factors (left) and their corresponding absolute uncertainties (right). These two-dimensional plots corresponds to reconstruction (top), medium identification (middle), and trigger (bottom) scale factors. The EF trigger requires two electrons with $p_T > 12$ GeV that satisfy loose identification per event.

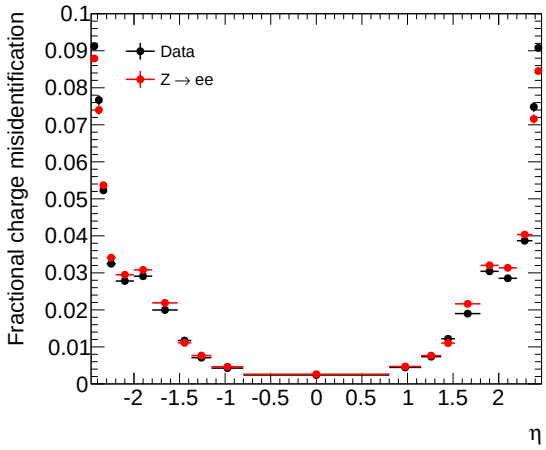

Figure 5.5: Charge misidentification rates in data and MC plotted as a function of electron η.

artificially switched from being negatively to positively charged or vice versa such that the misidentification rate matches the rate in data.

Chapter 6

Methodology

The principal measurement of this dissertation is a three-dimensional differential cross-section of neutral current Drell-Yan production, $q\bar{q} \rightarrow Z/\gamma^* \rightarrow e^-e^+$, from proton-proton collisions (see Equation (2.36)):

$$\frac{d^3\sigma}{dM_{ee}d|y_{ee}|d\cos\theta^*},$$

where M_{ee} is the dielectron invariant mass; $|y_{ee}|$ is the absolute rapidity; and θ^* is the polar angle in the Collins-Soper frame. The measurement is made in a finite region in kinematic phase space known as the *fiducial volume* which is defined as

$$46 < M_{ee} < 200 \text{ GeV}, \quad |\eta^e| < 2.4, \quad p_T^e > 20 \text{ GeV}.$$

Various analytical and statistical techniques are used to obtain a precision measurement of the three-dimensional cross-section. In this chapter, these techniques are introduced.

6.1 Measurement Overview

The differential cross-section is calculated using the following equation:

$$\left(\frac{d^3\sigma}{dM_{ee}d|y_{ee}|d\cos\theta^*}\right)_{\ell mn} = C_{\ell mn}\frac{M^{ijk}_{\ell mn}(N^{\text{sig}}_{ijk} - N^{\text{bkg}}_{ijk})}{\mathcal{L}(\delta M_{ee})_\ell(\delta|y_{ee}|)_m(\delta\cos\theta^*)_n}, \tag{6.1}$$

for i, j, k and $\ell, m, n = 1, 2, 3, ...$, where

- i, j, and k are bin indices corresponding to M_{ee}, $|y_{ee}|$, and $\cos\theta^*$ bins, respectively, at reconstruction-level;

- ℓ, m, and n are bin indices corresponding to M_{ee}, $|y_{ee}|$, and $\cos\theta^*$ bins, respectively, at generator-level;
- N_{ijk}^{sig} is the number of candidate Drell-Yan or signal events found in data;
- N_{ijk}^{bkg} is the estimated number of background events;
- $M_{\ell mn}^{ijk}$ is a matrix determined from MC which converts the measurement from reconstruction-level to generator- or more specifically dressed-level;
- $\mathcal{L}$ is the integrated luminosity of the data set;
- $(\delta M_{ee})_\ell$, $(\delta|y_{ee}|)_m$, and $(\delta\cos\theta^*)_n$ are bin widths in the three dimensions of interest;
- $C_{\ell mn}$ is a correction factor used to correct the measurement from dressed- to Born-level.

First the number N^{sig} of candidate Drell-Yan events in the data set must be determined and binned in M_{ee}, $|y_{ee}|$, and $\cos\theta^*$. Then the number N^{bkg} of background events must be estimated and subtracted from the signal events. Using signal Monte Carlo, matrix $\boldsymbol{M}$ is constructed and used to reverse the measurement from being a reconstruction-level quantity to generator-level one. Dividing by the known integrated luminosity $\mathcal{L}$ of the dataset and the set bin widths δM_{ee}, $\delta|y_{ee}|$, and $\delta\cos\theta^*$, the three-dimensional differential cross-section at dressed-level is obtained. In a final step, the correction factor C is used to convert the differential cross-section from dressed- to Born-level which is the lepton definition used by most parton distribution function fitting groups.

6.1.1 Binning

The cross-section measurement is binned in M_{ee}, $|y_{ee}|$, and $\cos\theta^*$ as follows:

- $M_{ee} = [46, 66, 80, 91, 102, 116, 150, 200]$ GeV,
- $|y_{ee}| = [0.0, 0.2, 0.4, 0.6, 0.8, 1.0, 1.2, 1.4, 1.6, 1.8, 2.0, 2.2, 2.4]$,
- $\cos\theta^* = [-1.0, -0.7, -0.4, 0.0, 0.4, 0.7, 1.0]$,

which shows the bin edges in each of the three dimensions. There are 7 bins in M_{ee}, 12 in $|y_{ee}|$, and 6 in $\cos\theta^*$ for a total of $7 \times 12 \times 6 = 504$ analysis bins.

When an electron pair has a true invariant mass in one M_{ee} bin and a reconstructed mass in another, a *bin migration* has occurred. Due mainly to detector resolution effects, the act of taking a measurement can cause bin migrations which primarily affect energy measurements like M_{ee} while angular quantities such as $|y_{ee}|$ and $\cos\theta^*$ are typically less affected. To illustrate this, two-dimensional Monte Carlo distributions of M_{ee}, $|y_{ee}|$, and $\cos\theta^*$ are plotted in Figure 6.1. The horizontal axis corresponds to reconstructed while the vertical axis corresponds to generated values of M_{ee}, $|y_{ee}|$, and $\cos\theta^*$. With perfect resolution, these plots would be completely diagonal; however, having finite resolution, the generated values – which are estimates of the true values – are smeared across several reconstructed bins. Note that the least diagonal of the three plots is the invariant mass distribution.

By setting the widths of the M_{ee} bins to be wider than the distance of migration, the number of bin migrations may be minimized. This is the reason for the M_{ee} binning that is used. The fine binning in $|y_{ee}|$ is important for any future parton distribution function analyses using this measurement. Given that $x \propto e^{\pm y_{ee}}$, PDF behaviour as a function of x depends strongly on rapidity, so a large number of measurements in $|y_{ee}|$ is required to reveal as much PDF information as possible. Finally, the $\cos\theta^*$ binning is split at zero which separates forward from backward events, vital to the asymmetry measurement central to this dissertation.

Purity is used to quantify the amount of bin migrations that have occurred across the measurement phase space. Estimated using signal MC, purity P_{ijk} is defined as the number $N_{ijk}^{\text{gen+rec}}$ of events generated and reconstructed in three-dimensional bin ijk divided by the number N_{ijk}^{rec} of events generated anywhere but reconstructed in ijk:

$$P_{ijk} = \frac{N_{ijk}^{\text{gen+rec}}}{N_{ijk}^{\text{rec}}}, \qquad i, j, k = 1, 2, 3, ... \tag{6.2}$$

In Figure 6.2, the expected purity in each of the three-dimensional analysis bins are shown. Note that the purity is poorest in the M_{ee} bins below the Z-peak, namely $M_{ee} \in [66, 80]$ and $[80, 91]$ GeV, due to large migrations of electron pairs from the resonance to lower invariant masses.

To ensure an adequate number of events in each of the 504 bins, a decision was made to exclude bins with fewer than 25 reconstructed signal MC events from the

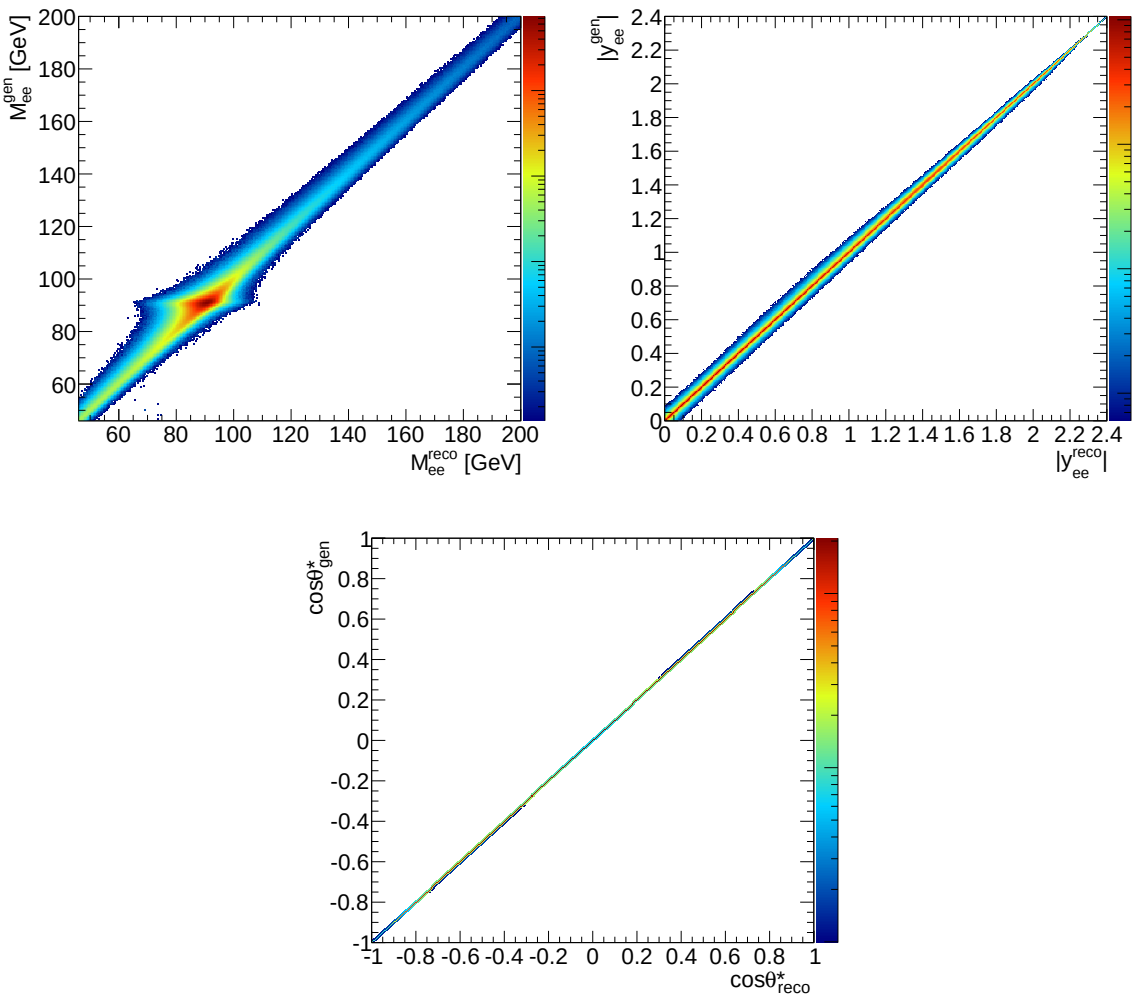

Figure 6.1: Two-dimensional reconstructed versus generated M_{ee}, $|y_{ee}|$, and $\cos\theta^*$ distributions. The z-axes have arbitrary units and are set to log-scale.

measurement. This restriction makes certain that the statistical uncertainty on the number of signal events in the remaining bins is not too large. Figure 6.3 shows the bins rejected from the analysis which are labelled with a "1." These bins are discarded from the measurement only after running through the full analysis chain.

In order to simplify and optimize the measurement process, each of the analysis bins is assigned a unique bin number from 1 to 504. The assignment pattern can be seen in Table 6.1. Starting from the first bin in each of the three dimensions, the six $\cos\theta^*$ bins are iterated through followed by those in $|y_{ee}|$ then M_{ee}. Rather than binning the data in a three-dimensional histogram (which may not be very intuitive), the data is instead binned in a single one-dimensional histogram with 504 bins greatly simplifying many of the technical aspects of this three-dimensional measurement.

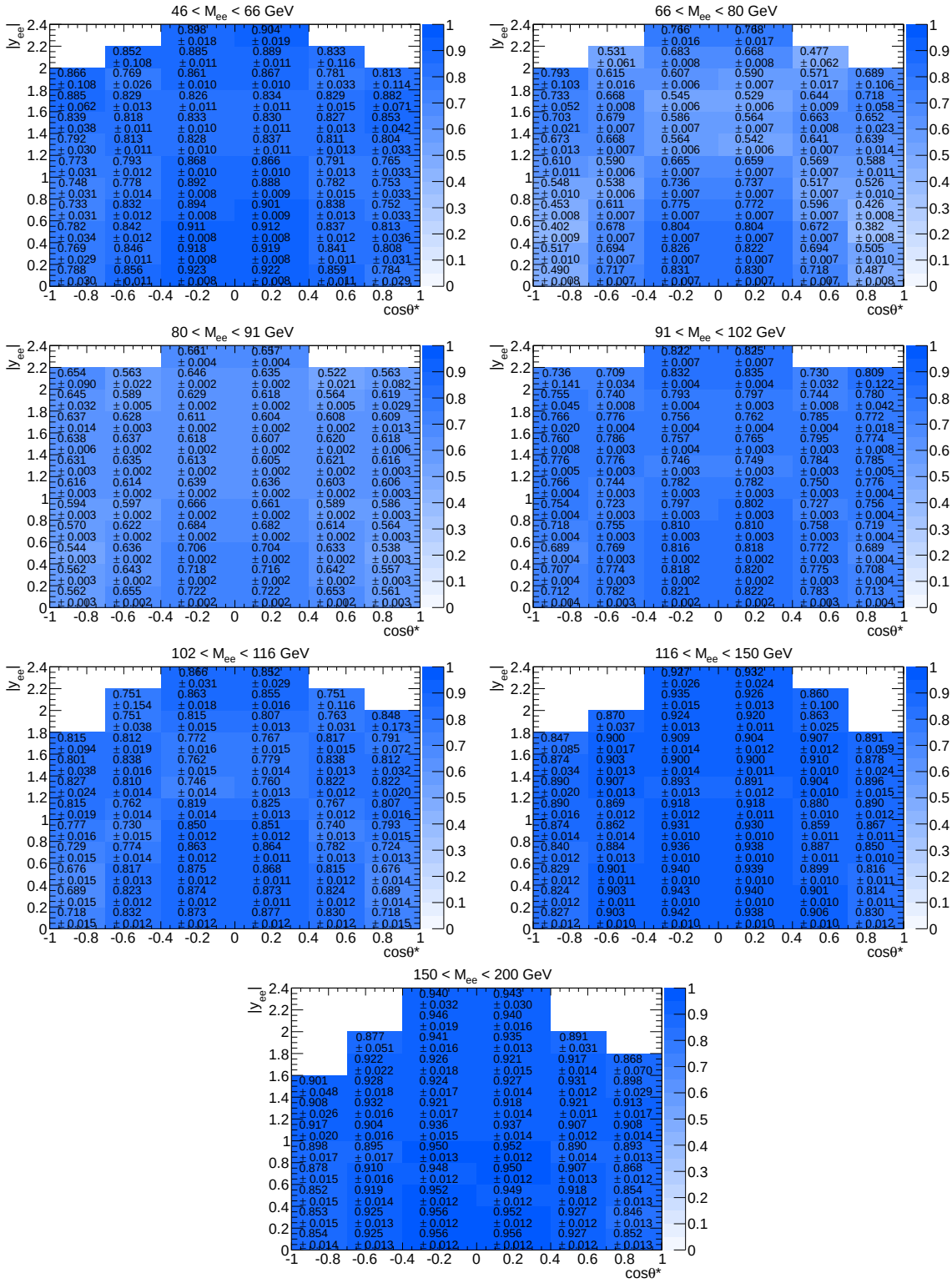

Figure 6.2: Purity in each of the three-dimensional analysis bins.

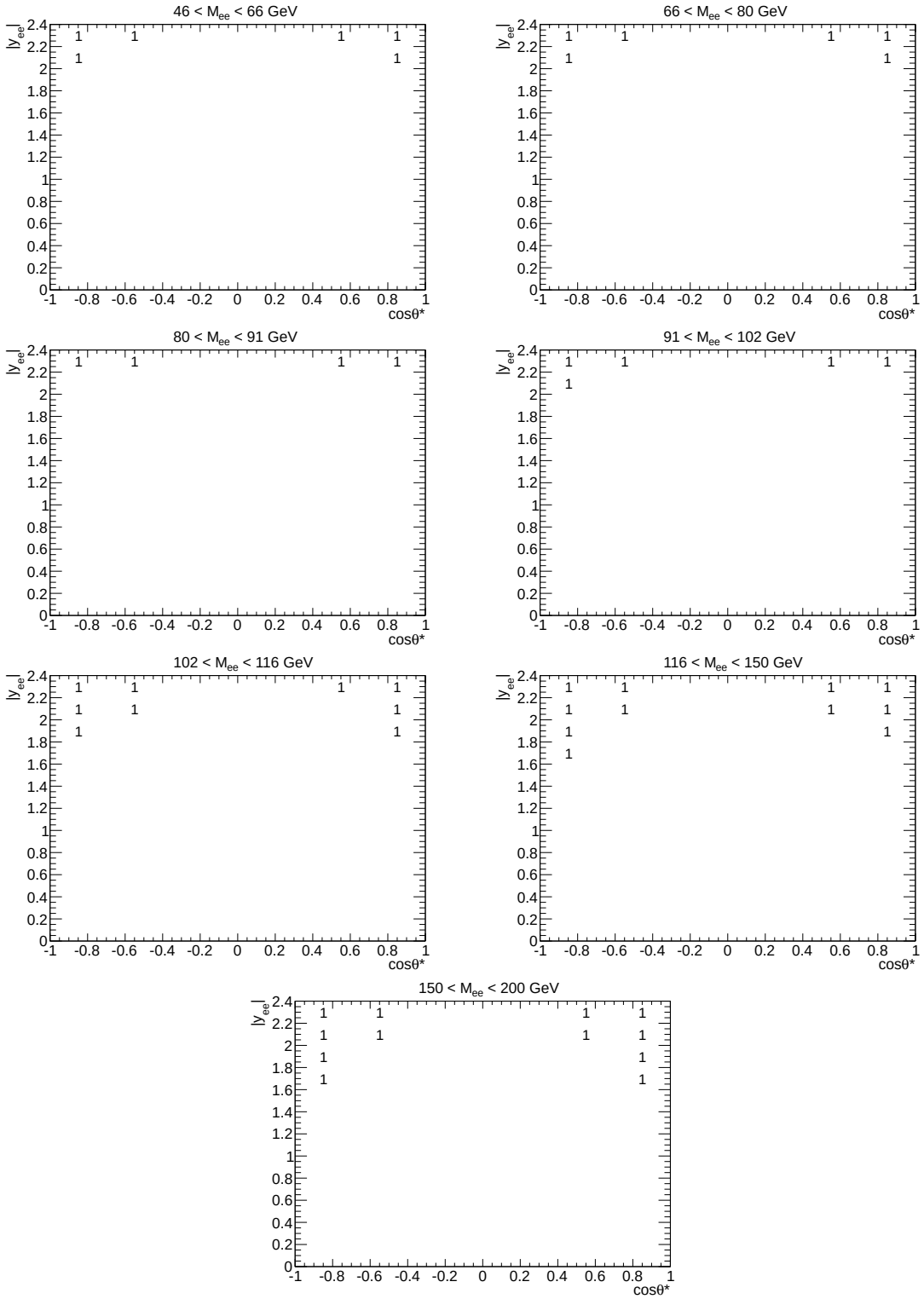

Figure 6.3: Rejected analysis bins. In the bins with an entry of "1," the expected number of signal events is less than 25. For this reason, these bins are eventually excluded from the analysis.

Analysis bin	$\cos\theta^*$		$\lvert y_{ee}\rvert$		M_{ee}	
1	−1.0	−0.7	0.0	0.2	46	66
2	−0.7	−0.4	0.0	0.2	46	66
3	−0.4	0.0	0.0	0.2	46	66
4	0.0	0.4	0.0	0.2	46	66
5	0.4	0.7	0.0	0.2	46	66
6	0.7	1.0	0.0	0.2	46	66
7	−1.0	−0.7	0.2	0.4	46	66
8	−0.7	−0.4	0.2	0.4	46	66
9	−0.4	0.0	0.2	0.4	46	66
10	0.0	0.4	0.2	0.4	46	66
11	0.4	0.7	0.2	0.4	46	66
12	0.7	1.0	0.2	0.4	46	66
⋮	⋮	⋮	⋮	⋮	⋮	⋮
73	−1.0	−0.7	0.0	0.2	66	80
74	−0.7	−0.4	0.0	0.2	66	80
75	−0.4	0.0	0.0	0.2	66	80
76	0.0	0.4	0.0	0.2	66	80
77	0.4	0.7	0.0	0.2	66	80
78	0.7	1.0	0.0	0.2	66	80
⋮	⋮	⋮	⋮	⋮	⋮	⋮
499	−1.0	−0.7	2.2	2.4	150	200
500	−0.7	−0.4	2.2	2.4	150	200
501	−0.4	0.0	2.2	2.4	150	200
502	0.0	0.4	2.2	2.4	150	200
503	0.4	0.7	2.2	2.4	150	200
504	0.7	1.0	2.2	2.4	150	200

Table 6.1: Analysis binning used in the three-dimensional cross-section measurement. Each three-dimensional bin is assigned a unique bin number from 1 to 504. The six $\cos\theta^*$ bins are iterated through, followed by $|y_{ee}|$, and finally M_{ee}.

6.2 Principle of Unfolding

In a collider experiment, the true value of a physical observable is generally different from its measured value as the measurement is typically affected by detector effects such as the electron efficiency and the energy resolution of the EM calorimeter. To illustrate, suppose $\vec{X} = [X_1, X_2, ..., X_m]$ is a histogram of true values of some observable with m bins. This histogram would be obtained using a perfect detector that measures particles with 100% efficiency and infinite resolution. Using the ATLAS detector, however, suppose these true observables are reconstructed and distributed

into histogram $\vec{Y} = [Y_1, Y_2, ..., Y_n]$ which consists of n bins. The relationship between $\vec{X}$ and $\vec{Y}$ is

$$\boldsymbol{R}\vec{X} = \vec{Y}, \tag{6.3}$$

where $\boldsymbol{R}$ is known as the *response matrix*, a two-dimensional $m \times n$ matrix. The elements R_{ji} of this matrix can be interpreted as the probability that true value X_i is measured as Y_j. The response matrix can be approximated using Monte Carlo which contains both generated and reconstructed events. Generator-level quantities are theoretical predictions of true values while the reconstructed quantities in MC are estimates of what is measured from experiment.

If there were no uncertainties on measurements Y_j, then true values X_i can simply be obtained by inverting $\boldsymbol{R}$ and performing the following calculation:

$$\vec{X} = \boldsymbol{R}^{-1}\vec{Y}, \tag{6.4}$$

where $\boldsymbol{R}^{-1} = \boldsymbol{M}$, the matrix presented in Equation (6.1). The resultant histogram is often referred to as an *unfolded* histogram. Unfolded histograms are comparable not only to theoretical predictions, but to results from other experiments as well.

This method of unfolding results in very large errors on the unfolded histogram when the measurements have uncertainties. There are a number of techniques used to unfold data in the presence of uncertainties. Two popular unfolding methods used in experimental particle physics are *bin-by-bin* and *Bayesian unfolding*. Both methods, in addition to unfolding the measurement, treat bin-to-bin correlations in their own unique way. Bin-by-bin and Bayesian unfolding are introduced in the following text.

6.2.1 Bin-by-bin Unfolding

The simpler of the two, bin-by-bin unfolding reduces the $m \times n$ response matrix into a diagonal $n \times n$ matrix. Let $\vec{x} = [x_1, x_2, ..., x_m]$ and $\vec{y} = [y_1, y_2, ..., y_n]$ be the Monte Carlo equivalents of $\vec{X}$ and $\vec{Y}$. The bin-by-bin response matrix $\boldsymbol{R}$ is defined as

$$R_{ii} = \frac{y_i}{x_i}, \qquad i = 1, 2, ..., n. \tag{6.5}$$

The elements of $\boldsymbol{R}^{-1}$, the inverted response matrix, are bin-by-bin correction factors

computed as

$$R_{ii}^{-1} = \frac{x_i}{y_i}. \tag{6.6}$$

The unfolded measurement is obtained by simply multiplying the elements of $\vec{Y}$ by the correction factors:

$$X_i = \left(\frac{x_i}{y_i}\right) Y_i. \tag{6.7}$$

The bin-by-bin method relies heavily on Monte Carlo being able to describe the data well. Mismodelling at event generation, reconstruction, or both will produce incorrect correction factors thus introducing a bias to the unfolded results. Moreover, since the bin-by-bin response matrix is diagonal, this method of unfolding does not correct for possible bin migrations nor does it account for correlations across measurement bins. For these reasons, bin-by-bin unfolding is typically only used in measurements that are unaffected by bin migrations.

6.2.2 Bayesian Unfolding

Bayesian unfolding [96, 97] is based on Bayes' theorem which states that having measured y_j, the conditional probability $P(x_i \,|\, y_j)$ that its corresponding generated value is x_i is given by

$$P(x_i \,|\, y_j) = \frac{P(y_j \,|\, x_i) P(x_i)}{P(y_j)}. \tag{6.8}$$

According to Bayes' theorem, this probability depends on the prior probability $P(x_i)$ of generating x_i, the probability $P(y_j)$ of measuring y_j, and the likelihood $P(y_j \,|\, x_i)$ of measuring y_j after generating x_i. The two-dimensional object $P(y_j \,|\, x_i)$ is in fact the response matrix R_{ji} which, along with $P(x_i)$ and $P(y_j)$, can be computed using signal MC. Calculated using Bayes' theorem, the probability $P(x_i \,|\, y_j)$ is the inverted response matrix,

$$R_{ij}^{-1} = P(x_i \,|\, y_j), \tag{6.9}$$

required to unfold the measurement from reconstruction- to generator-level:

$$X_i = R_{ij}^{-1} Y_j. \tag{6.10}$$

In Bayesian unfolding, three modifications to Equation (6.10) are made to account for effects that are not encoded in $\boldsymbol{R}^{-1}$. Histogram Y_j may contain events that were originally outside the fiducial volume of interest but after reconstruction migrated inside. The number of such events can be estimated using signal MC by selecting a set of reconstructed events that were generated anywhere and a set generated within the fiducial volume. Their difference reveals the number of in-migrations that have occurred which are then subtracted from Y_j.

When an event generated within the fiducial volume is reconstructed outside, an out-migration has occurred. Events that undergo out-migrations must be included in the measurement since they were originally a part of the fiducial volume. By adding overflow and underflow bins to $\vec{Y}$ and $\boldsymbol{R}$, the number of out-migrations can be quantified and corrected for.

The third and final modification accounts for the efficiency that was described in Section 5.4. Some Drell-Yan events may not be reconstructed due to inefficiencies associated with reconstruction, identification, and triggering and again, signal MC is used to provide an estimate of this effect. The ratio of the number of generated events that have a reconstruction-level counterpart to the number of generated events with or without a counterpart equals the efficiency ϵ. To account for the losses due to efficiency effects, ϵ is introduced to Equation (6.10):

$$X_i = \frac{1}{\epsilon_i} R_{ij}^{-1} Y_j, \tag{6.11}$$

where, by definition, $\epsilon \neq 0$.

The inverted response matrix depends on the choice of prior $P(x_i)$ which – if mis-modelled – could bias X_i. To minimize this bias, an iterative unfolding approach is taken whereby after each application of Bayes' theorem, the prior is replaced by the probability

$$P(X_i) = \frac{X_i}{\sum_{i=0}^{m} X_i} \tag{6.12}$$

and $\boldsymbol{R}^{-1}$ is re-solved for and used to unfold the measurement. With a new unfolded measurement, $P(X_i)$ can again be updated and the process repeated. By iterating in this way, the dependency on the predicted true spectrum from Monte Carlo is minimized. Additional iterations can, however, cause the statistical uncertainty on the unfolded measurement to increase. A balance needs to be struck between reducing

the uncertainty while minimizing the reliance of the measurement on the signal MC.

Unlike bin-by-bin unfolding, Bayesian unfolding takes into account correlations across measurement bins making it a good option for measurements with low bin purity. A covariance matrix on the unfolded measurement can be computed by randomly varying MC histograms x_i and y_j by their uncertainties to produce *toys*. Using these toys, $\boldsymbol{R}^{-1}$ is recomputed and the measurement unfolded. The process is repeated many times to produce a set of X_i which are then used to calculate the covariance matrix. This method of uncertainty estimation is known as the *toy method*.

6.3 Uncertainty Propagation

In the process of measuring $\frac{d^3\sigma}{dM_{ee}d|y_{ee}|d\cos\theta^*}$, uncertainties (described in Chapter 8) are introduced which must be propagated to the final unfolded differential cross-section. Three methods of propagation are used in this analysis; they are the *offset*, *combined toy*, and *bootstrap* methods.

6.3.1 Offset Method

The offset method is a simple way of estimating bin-to-bin correlated uncertainties by symmetrizing them about some nominal measurement X. In addition to X, it requires the measurement to be repeated twice for each source of uncertainty, once varying the source up by one standard deviation and again down by one standard deviation. Respectively, these yield X^+ and X^- which are then substituted into the following equation:

$$\delta = \frac{X^+ - X^-}{2}, \tag{6.13}$$

which is taken as the systematic uncertainty due to the source in question. The advantage of the offset method is in its simplicity but its major drawback is uncertainties may be over-estimated since correlations are not taken into account.

6.3.2 Combined Toy Monte Carlo Method

The combined toy method [98] involves running a set of pseudo-experiments where the entire measurement is remade varying some parameter whose uncertainty is being estimated. Typically, the toy method is used for the propagation of uncorrelated

uncertainties; however, the *combined* toy method treats the bin-to-bin correlated and uncorrelated components of the uncertainty simultaneously.

Uncertainties due to efficiency scale factors, used in this analysis to correct the efficiencies in MC to better resemble those in data, are estimated using the combined toy method. Each scale factor s has a total uncertainty comprised of a systematic component δs^{cor} that is correlated across all measurement bins, an uncorrelated systematic component s^{uncor}, and a statistical component δs^{stat}:

$$s \pm \delta s^{\text{cor}} \pm \delta s^{\text{uncor}} \pm \delta s^{\text{stat}}. \tag{6.14}$$

The observable of interest is remeasured using a toy scale factor s^{toy} in which the correlated, uncorrelated, and statistical components are varied according to

$$s^{\text{toy}} = s + \sum_{c=1}^{C} \delta s_c^{\text{cor}} \text{Gaus}(0, 1; c) + \text{Gaus}(0, \delta s_0), \tag{6.15}$$

where $c = 1, 2, 3, .., C$ are the sources of uncertainty that contribute to δs^{cor}; the function $\text{Gaus}(\mu, \sigma_\mu; c)$ is a Gaussian probability distribution with mean μ and standard deviation σ_μ constructed for each source c; $\text{Gaus}(0, \delta s_0)$ is a Gaussian centred at 0 with standard deviation δs_0 defined as the quadrature sum of δs^{uncor} and δs^{stat}. Note that for each toy and source c, the Gaussian factor in the second term in Equation (6.15) is the same across all bins, in contrast to the Gaussian factor in the third term which is toy and bin independent.

With N toy scale factors s^{toy}, N measurements of X_i^{toy} can be produced. The uncertainty on the nominal measurement X due to the use of scale factor s is taken as the standard deviation of the toy measurements:

$$\delta = \sqrt{\frac{1}{N-1} \sum_{i=1}^{N} (X_i^{\text{toy}} - \bar{X}^{\text{toy}})}, \tag{6.16}$$

where $\bar{X}^{\text{toy}}$ is the average toy measurement.

The combined toy method allows a large number of correlated uncertainty sources to be varied while simultaneously varying their uncorrelated and statistical components of the source. Without it, the offset method would need to be used for each correlated source varying the uncorrelated uncertainty and again varying the statistical uncertainty. In total, $2C$ offset uncertainties would need to be calculated. By using the combined toy method, $2C$ uncertainties are reduced to a single uncertainty.

6.3.3 Bootstrap Method

This analysis uses the bootstrap method [99] to calculate improved estimates of the statistical uncertainties due to the limited sample sizes of the data set and MC samples. Let $Z = \{Z_1, Z_2, ..., Z_{n-1}, Z_n\}$ be some sample of events which may be measured from data or from signal or background Monte Carlo. In the bootstrap method, Z is resampled to produce a new sample B known as a *bootstrap replica*. Events from Z are chosen at random and populated into B and after each draw the value is put back into the sampling pool or *replaced* and can be selected again. An example bootstrap replica could look like

$$B = \{Z_1, Z_1, Z_3, ..., Z_{n-1}\}. \tag{6.17}$$

Note that since the entries are selected at random, some values that are in Z may be absent from B, such as event Z_2 in the example above.

In practice, the bootstrap method is implemented with the use of a Poisson probability distribution function with a mean of 1. A random number is drawn from this Poisson distribution for each of the entries of Z and used to weight its corresponding entry. For example, suppose the numbers drawn are

$$P = \{2, 0, 1, ..., 1, 0\}; \tag{6.18}$$

then the resulting bootstrap replica is

$$\begin{aligned} B &= P \cdot Z \\ &= \{2, 0, 1, ..., 1, 0\} \cdot \{Z_1, Z_2, Z_3, ..., Z_{n-1}, Z_n\} \\ &= \{Z_1, Z_1, Z_3, ..., Z_{n-1}\}. \end{aligned} \tag{6.19}$$

Repeating this process N times yields N bootstrap replicas where N should be greater than the number of analysis bins [99]. The original sample Z and the replicas B are each then used to measure observable X. The statistical uncertainty on $X(Z)$, measured from the original sample, is estimated as the standard deviation of the replica measurements:

$$\delta = \sqrt{\frac{1}{N-1}\sum_{i=1}^{N}(X(B_i) - \overline{X}(B))^2}, \tag{6.20}$$

where $\overline{X}(B)$ is the average value obtained from the N replicas.

Chapter 7

Measurement

In this chapter, the measurement of $\frac{d^3\sigma}{dM_{ee}d|y_{ee}|d\cos\theta^*}$ using the 2012 ATLAS data set is discussed and presented in detail. The selection of Drell-Yan or signal events is described first followed by an in depth discussion on the background estimation. The measurement is then unfolded and the cross-section calculated. The material presented in this and the remaining chapters of this dissertation represent the original research done.

7.1 Event Selection

To obtain a sample of Drell-Yan events from the data, a set of requirements known as the *signal selection* is applied. The signal selection is designed such that the events that pass its requirements are highly likely to contain two electrons from Z/γ^* decay. Signal selection is applied not only to the data but all Monte Carlo samples as well. Distributions required for unfolding, such as the response matrix, are constructed using signal MC events that satisfy the signal selection and many of the major backgrounds are estimated using the MC background events that pass the selection.

Signal selection begins by requiring all events to be listed in the good runs list[1] ensuring that the LHC and ATLAS detector were operating in stable conditions. Events must pass the event filter trigger EF_2e12Tvh_loose1[2] which requires two

[1]Data only. This is not a requirement for MC events.

[2]The "T" in the trigger name indicates that the transverse energy threshold of its L1 seed was increased for the 2012 run while the "vh" denotes that calorimeter shower shape requirements were imposed at L1. In 2012, a re-optimization of electron identification criteria was performed for L2 triggers. Event filters whose L2 seeds were improved have "loose1," "medium1," or "tight1" in their names [100].

candidate electrons with transverse energy greater than 12 GeV, both of which must satisfy loose identification. Next, events must not be flagged for noise bursts or data integrity errors in the LAr calorimeters and each event is required to have at least one primary vertex with three or more tracks emanating from it.

Electron candidates in the events are required to have been reconstructed using the sliding window method and to have passed object quality requirements [101]. Kinematic cuts are then applied to the electrons, requiring pseudorapidity $|\eta^e| < 2.4$ excluding the transition region, $1.37 < |\eta^e| < 1.52$, between the EM barrel and end-caps, and transverse momentum $p_T^e > 20$ GeV. They are also required to satisfy medium electron identification which reduces the background more effectively than loose identification while being more efficient than tight identification.

Next, events must not contain more than two electrons satisfying the electron requirements listed above. This cut is designed to increase the signal-to-background ratio since the Drell-Yan process produces exactly two electrons in the final state. Electron pairs or Z/γ^* bosons are then constructed in events with two electrons that pass the electron cuts. The two must possess an invariant mass in the range $46 < M_{ee} < 200$ GeV and have opposite electric charges. Electron pairs satisfying all these requirements are used in this measurement.

A summary of the selection requirements and the number of events at each stage of signal selection for data and signal MC can be seen in Table 7.1. Also shown are the absolute and relative efficiencies of each of the cuts applied. Note that there are initially about 694 million data events and after signal selection, approximately 6.739 million remain to be used for analysis. Monte Carlo, however, predicts that 6.636 million Drell-Yan events should remain after selection. This difference in yields is assumed to be background events that are present in data but not in signal MC.

7.2 Background Estimation

The signal selection requirements described in Section 7.1 reject the majority of background events. Some will remain because the signatures left in the detector by some background processes closely resemble those of the dielectron final state of interest. A combination of MC simulation and data-driven techniques is used to estimate the background.

Recall that the background contribution from the processes depicted in Section 2.3.1 as Feynman diagrams are estimated using the MC samples listed in Tables 4.3

Requirement	N_{data}	$\epsilon^{\text{abs}}_{\text{data}}$ [%]	$\epsilon^{\text{rel}}_{\text{data}}$[%]	N_{MC}	$\epsilon^{\text{abs}}_{\text{MC}}$[%]	$\epsilon^{\text{rel}}_{\text{MC}}$[%]
Good runs list	6.943e×10^8	100.0	100.0	4.063e×10^7	100.0	100.0
Trigger	2.708e×10^7	3.900	3.900	1.078e×10^7	26.53	26.53
LAr event quality	2.702e×10^7	3.892	99.79	1.078e×10^7	26.53	100.0
Vertex with ≥ 3 tracks	2.695e×10^7	3.881	99.72	1.071e×10^7	26.35	99.31
Sliding window	2.654e×10^7	3.822	98.47	1.069e×10^7	26.31	99.85
Electron object quality	2.637e×10^7	3.799	99.39	1.063e×10^7	26.15	99.40
$\lvert\eta^e\rvert < 2.4$	2.613e×10^7	3.763	99.06	1.053e×10^7	25.92	99.10
Exclude $1.37 < \lvert\eta^e\rvert < 1.52$	2.215e×10^7	3.190	84.77	9.523e×10^6	23.44	90.43
$p^e_T > 20$ GeV	1.117e×10^7	1.609	50.44	7.946e×10^6	19.56	83.45
Medium identification	6.970e×10^6	1.004	62.40	6.849e×10^6	16.85	86.19
Maximum two electrons	6.968e×10^6	1.004	99.96	6.847e×10^6	16.85	99.98
$46 < M_{ee} < 200$ GeV	6.813e×10^6	0.981	97.77	6.727e×10^6	16.56	98.25
Opposite electric charge	6.739e×10^6	0.971	98.91	6.636e×10^6	16.33	98.65

Table 7.1: Number of events in data and signal Monte Carlo at different stages of the signal selection. Efficiency ϵ^{abs} shows the percentage of events remaining after each cut with respect to the initial number of events in the GRL and efficiency ϵ^{rel} shows the percentage of events with respect to the previous selection requirement.

and 4.4. The signal selection is applied to each of the listed Monte Carlo samples and the resulting sample is normalized to the integrated luminosity of the data. Summing together the signal selected, normalized background MC samples provides an estimate of the Monte Carlo background. The remaining background, known as the multijet background, is estimated using a data-driven technique known as the *template method*.

7.2.1 The Template Method

The template method is based on extracting a data sample dominated by multijet events by applying a set of requirements that preferentially selects them. Such a selection, which often requires objects to fail electron identification cuts, is known as the *template selection* and the resulting sample is typically referred to as the *template sample*. A discriminating variable is then required to calculate a normalization factor to scale the template sample to the expected number of multijet events contaminating the signal data sample.

A common choice of discriminating variable is *electron isolation*. An energy cluster deposited by an electron in the EM calorimeter has a large concentration of energy at the barycentre and smaller deposits in the surrounding cells. The same cannot be said for a jet which deposits a significant amount of its energy outside the barycentre.

Exploiting this knowledge, electron isolation is defined as

$$E_T Cone\Delta R = E_T^{\Delta R} - E_T^{5\times 7}, \tag{7.1}$$

where $E_T^{\Delta R}$ is the transverse cluster energy measured inside a cone of radius ΔR and $E_T^{5\times 7}$ is the transverse energy measured in a rectangle of area $5\Delta\eta \times 7\Delta\phi = 5(0.025) \times 7(0.025)$ centred about the cluster barycentre. Electrons are expected to have smaller values of $E_T Cone\Delta R$ than jets. In Figure 7.1 is a diagram illustrating this definition.

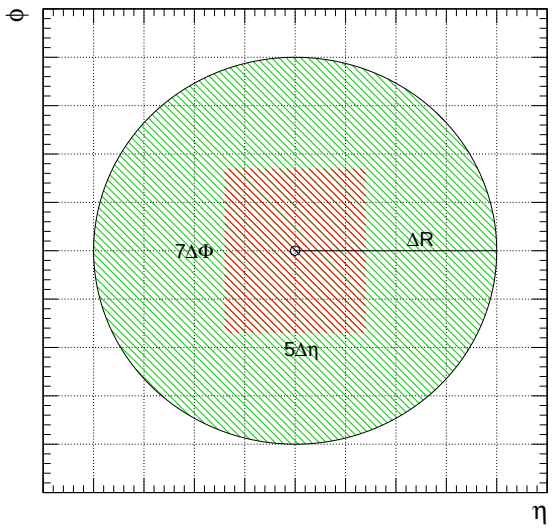

Figure 7.1: Cross-section of an isolation cone of radius ΔR with a $5\Delta\eta \times 7\Delta\phi$ box around the barycentre of the energy cluster.

This analysis opts to use the relative isolation, $E_T Cone\Delta R/E_T$, where the electron isolation is divided by the transverse energy E_T of the electron[3] as the discriminating variable. Illustrations of $E_T Cone\Delta R/E_T$ distributions of data, and signal and background MC can be seen in Figure 7.2. Also plotted is a multijet enriched template distribution which, after deriving the appropriate normalization factor, can be scaled down to obtain an estimate of the multijet background in the data. A vertical line is drawn in Figure 7.2, to the left of which is the electron dominated *peak* region and to the right is the multijet rich *tail* region. The value of $E_T Cone\Delta R/E_T$ where this separation is made varies but a general rule is that in the tail region, the difference

[3] $E_T = E\cos\theta$ where E is measured from the electron energy cluster and θ from the track. See Section 5.1 for full details.

between the number of data and signal MC events should be greater than the number of signal MC events. An equivalent statement would be the number of multijet events should be greater than the number of signal MC events in the tail region.

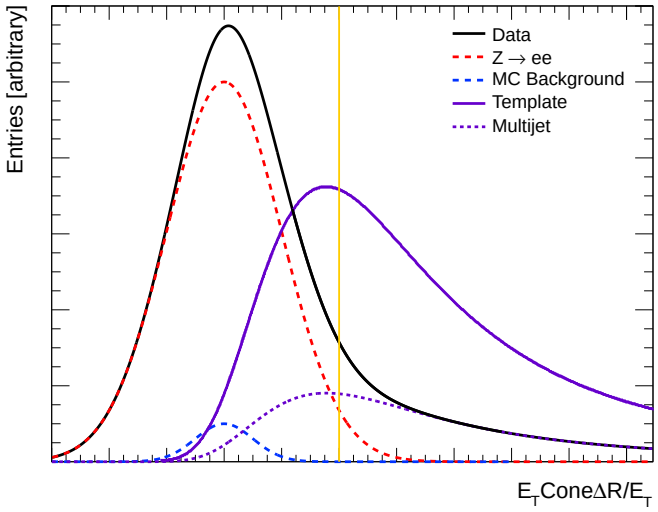

Figure 7.2: Diagram of relative isolation distributions for data, signal and background MC, and the (multijet) template. The electrons from the signal and background MC are expected to be more isolated than jets. The template scaled by a normalization factor yields an estimate of the multijet background.

To derive an equation that can be used to determine the template normalization λ, the signal and template selections are applied to the data and the signal and background MC. Considering first the samples of events obtained from signal selection, it is assumed that what remains after subtracting the signal and background MC events from the data is the number of multijet events present in the data. This statement should be true for all values of relative isolation but only the tail region, where the expected number of multijet events is dominant, will be used in the following derivation. Mathematically, this statement is

$$n_{\mathrm{sig}}^{\mathrm{data}} - \rho\, n_{\mathrm{sig}}^{\mathrm{Zee}} - n_{\mathrm{sig}}^{\mathrm{bkg}} = n_{\mathrm{sig}}^{\mathrm{multijet}}, \tag{7.2}$$

where $n_{\mathrm{sig}}^{\mathrm{data}}$ is the number of data signal events in the tail region; $n_{\mathrm{sig}}^{\mathrm{Zee}}$ and $n_{\mathrm{sig}}^{\mathrm{bkg}}$ are the signal and background MC events that pass signal selection, respectively; and $n_{\mathrm{sig}}^{\mathrm{multijet}}$ is the number of multijet events. The factor ρ is defined as the signal MC normalization whose purpose will be explained a little later on but for now it is set to 1.

Now the template samples are considered. The number $n_{\text{temp}}^{\text{multijet}}$ of multijet events in the template sample is obtained by performing template selection on the data set and subtracting the contributions from signal and background MC:

$$n_{\text{temp}}^{\text{data}} - \rho\, n_{\text{temp}}^{\text{Zee}} - n_{\text{temp}}^{\text{bkg}} = n_{\text{temp}}^{\text{multijet}}, \tag{7.3}$$

where $n_{\text{temp}}^{\text{data}}$ is the number of data template events and $n_{\text{temp}}^{\text{Zee}}$ and $n_{\text{temp}}^{\text{bkg}}$ are the MC events that satisfy the template requirements, all measured in the tail region.

The shapes of $n_{\text{sig}}^{\text{multijet}}$ and $n_{\text{temp}}^{\text{multijet}}$ distributed in $E_T Cone\Delta R/E_T$ should be the same up to a constant factor λ, the template normalization. Therefore, the following relation can be written:

$$n_{\text{sig}}^{\text{multijet}} = \lambda\, n_{\text{temp}}^{\text{multijet}}. \tag{7.4}$$

Substituting Equations (7.2) and (7.3) into Equation (7.4) yields an expression that can be used to solve for λ:

$$\lambda = \frac{n_{\text{sig}}^{\text{data}} - \rho\, n_{\text{sig}}^{\text{Zee}} - n_{\text{sig}}^{\text{bkg}}}{n_{\text{temp}}^{\text{data}} - \rho\, n_{\text{temp}}^{\text{Zee}} - n_{\text{temp}}^{\text{bkg}}} \tag{7.5}$$

Let $N_{\text{temp}}^{\text{multijet}}$ denote the total number – not just those found in the tail region – of multijet events found in the template selected data. This quantity is determined as follows:

$$N_{\text{temp}}^{\text{multijet}} = N_{\text{temp}}^{\text{data}} - \rho\, N_{\text{temp}}^{\text{Zee}} - N_{\text{temp}}^{\text{bkg}}, \tag{7.6}$$

where the uppercase N's correspond to the total numbers (in contrast to the lowercase n's which correspond to the tail numbers). If Equation (7.4) holds true for the tail region then it should also be true for the entire region. Therefore, the number of multijet events in the signal data (the quantity of interest) is

$$N_{\text{sig}}^{\text{multijet}} = \lambda\, N_{\text{temp}}^{\text{multijet}}. \tag{7.7}$$

Now is a good time to explain the ρ factor in Equations (7.2) and (7.3). Having an estimate of the multijet background, the signal MC normalization is retroactively set to

$$\rho = \frac{N_{\text{sig}}^{\text{data}} - N_{\text{sig}}^{\text{bkg}} - N_{\text{sig}}^{\text{multijet}}}{N_{\text{sig}}^{\text{Zee}}} \tag{7.8}$$

and Equations (7.5) and (7.7) are re-evaluated using this new ρ. The factor is designed to reduce the dependency of the template method on the normalization or more specifically the theoretical cross-section of the signal Monte Carlo which may not possess sufficient high order corrections required to accurately describe the data. This iterative procedure ends when the absolute difference between two consecutive values of ρ is less than 0.1%. Having given a general outline, the specifics of the template method used in this analysis are discussed below.

Template Selection

The template selection shares many of the same cuts that are used for signal selection in order to help ensure that the relative isolation shapes of $N_{\text{temp}}^{\text{multijet}}$ and $N_{\text{sig}}^{\text{multijet}}$ are similar. The following differences exist between the two selections:

- For the template selection, the final state objects must have the same electric charge rather than opposite charge. Requiring both objects to possess the same charge reduces the signal contamination in the template sample.
- Instead of requiring the physics objects to satisfy medium identification as in signal selection, template selection requires them to pass loose identification. Hadronic jets are more likely to pass loose than medium identification thus increasing the likelihood that the events remaining after template selection are indeed multijet events.
- In addition to loose identification, template selected objects must fail medium identification. Jets are very likely to fail the stricter medium and tight identification requirements.

The resulting template selected events binned in M_{ee} and $\cos\theta^*$ can be seen in Figure 7.3. The invariant mass distribution is mostly smooth as expected, taking the shape of an exponential decay. In $\cos\theta^*$, the distribution is symmetric about zero which is again expected since QCD processes do not violate parity.

Template Normalization

Having two data sets, one rich in signal events and the other multijet events, the discriminating variable used to determine the normalization is the relative isolation variable $E_T Cone20/E_T$ which uses a cone of radius $\Delta R = 0.20$. In both signal

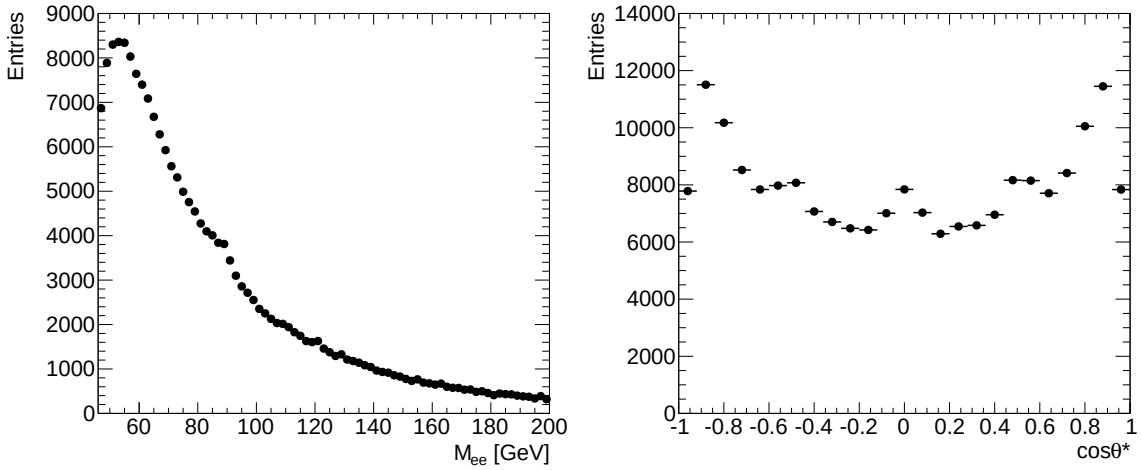

Figure 7.3: M_{ee} and $\cos\theta^*$ distributions of the selected template events.

and template events, there are a pair of objects which may be one of the following: a pair of electrons, an electron and a jet misidentified as an electron, or two jets faking electrons. Instead of using both objects, only the object with the smaller $E_T Cone20/E_T$, i.e. the more isolated of the two, is used in the λ-calculations. It is more probable for an electron cluster to be poorly isolated than it is for a jet EM clusters to be well-isolated. Therefore, if the maximum $E_T Cone20/E_T$ of the two objects were to be used, the tail region of the distribution would be highly contaminated with real electrons, degrading the results of the template method.

For each of the 504 analysis bins, a factor of λ must be calculated in order to obtain a complete estimate of the multijet background. Given the large number of analysis bins, both signal and template events are limited, particularly in bins corresponding to high M_{ee}. Since the template distribution in $\cos\theta^*$ is symmetric about zero, as shown in Figure 7.3, the multijet background in a negative $\cos\theta^*$ bin should equal the background in its positive counterpart. The template events in a negative $\cos\theta^*$ bin are summed with those in the corresponding positive bin hence doubling the number of events available in each bin which greatly improves the reliability of the template method.

In Figure 7.4, $E_T Cone20/E_T$ distributions used to perform the λ-calculations are shown for six analysis bins. These plots, which are binned versions of the one shown in Figure 7.2, show the signal data distribution along with the signal ($Z \to ee$) MC prediction. The template selected data and the estimated multijet background are shown as well. The sum of the signal MC with the MC and multijet backgrounds

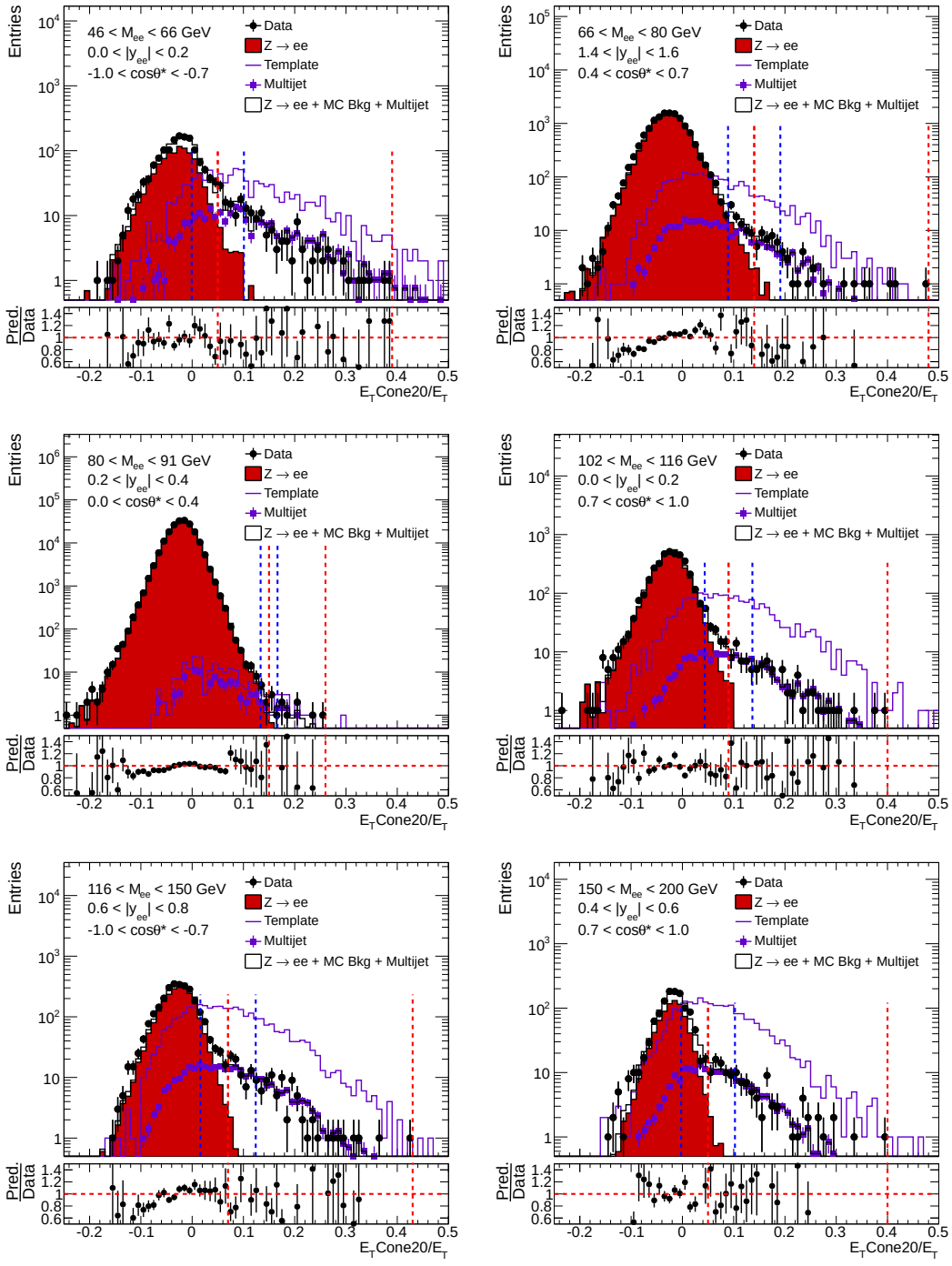

Figure 7.4: Relative isolation distributions for several three-dimensional analysis bins. Shown are the data and signal MC histograms obtained from signal selection along with the template distribution and corresponding multijet estimate. The prediction or sum of the signal MC and total background is plotted as well and its ratio with the data is shown in the bottom panels of these plots. The dashed vertical lines are explained in the text.

constitutes a full model of the data. A comparison in the form of a ratio between the model prediction and the data is given in each of the lower panels of Figure 7.4. As expected, in the low mass bins, $M_{ee} \in [46, 66]$ and $[66, 80]$ GeV, there is a large multijet background hence the long tails. At the Z-peak, $M_{ee} \in [80, 91]$ and $[91, 102]$ GeV, the multijet background is negligible as Z events dominate in this region. Away from the peak, $M_{ee} \in [102, 116]$, $[116, 150]$, and $[150, 200]$ GeV, the multijet background is again a sizable fraction of the signal data.

The multijet estimate depends on where the tail region begins and where it ends. The right edge of the region is set to $E_T Cone20/E_T = 0.05$. If there is no signal data in this bin then the closest bin to the left that has a non-zero number of events is taken as the maximum of the tail region. The left edge is determined by starting at the right edge and is moved leftward until the difference between the number of signal data and MC events is a factor of 1.5 larger than the signal MC events:

$$n_{\text{sig}}^{\text{data}} - n_{\text{sig}}^{\text{Zee}} > 1.5\, n_{\text{sig}}^{\text{Zee}}. \tag{7.9}$$

This requirement helps ensure that the tail region has more multijet than signal events. The tail region is shown in Figure 7.4 marked by the dashed vertical red lines. These plots show that most tail regions are in an approximate range of $0.1 < E_T Cone20/E_T < 0.5$ except for the analysis bins that correspond to the Z-peak where the tail region is much shorter.

Note that with the settings described above, for nearly all 504 calculations of λ, only two or three iterations are required to satisfy the condition that the difference between two successive ρ values must be less than 0.1%.

Multijet Background Uncertainty

An uncertainty must be assigned to the estimated multijet background. The following sources of uncertainty are considered and evaluated as described.

1. A statistical component of the multijet uncertainty is estimated using the bootstrap method. The signal and template data samples are resampled producing $N = 50$ replica distributions and for each replica, template fits are repeated in the 504 analysis bins. For a given analysis bin, the standard deviation of the results from the 50 replicas is taken as the statistical uncertainty on the multijet

background:

$$\delta^{\text{stat}} = \sqrt{\frac{1}{N-1}\sum_{i=1}^{N}(N_{\text{sig},i}^{\text{multijet}} - \overline{N}_{\text{sig}}^{\text{multijet}})},$$

where $\bar{N}_{\text{sig}}^{\text{multijet}}$ is the mean multijet estimate from the 50 bootstrap replicas.

2. A systematic component results from the choice of the tail region. By either widening this region or narrowing it, the estimate may change. The nominal left edge of the region is shifted to the left by 15% of the length of the original window to give a systematic variation on the left edge position:

$$I_{\text{left}}^{\text{wide}} = I_{\text{left}}^{\text{nom}} - 0.15(I_{\text{right}} - I_{\text{left}}^{\text{nom}}),$$

where $I_{\text{left}}^{\text{nom}}$ is the $E_T Cone20/E_T$ value of the nominal left edge and I_{right} is the right edge of the tail region which is fixed. Using this widened tail region, λ-calculations are performed to give a new estimate $N_{\text{sig}}^{\text{multijet}+}$. Conversely, the nominal left edge is shifted to the right by 15% of the original window yielding a new left edge position:

$$I_{\text{left}}^{\text{nar}} = I_{\text{left}}^{\text{nom}} + 0.15(I_{\text{right}} - I_{\text{left}}^{\text{nom}}).$$

Using this narrowed tail region, the calculations are redone to give $N_{\text{sig}}^{\text{multijet}-}$. The maximum difference between these varied estimates and the nominal one is taken as the systematic uncertainty due to the choice of tail region:

$$\delta^{\text{tail}} = \max\left(N_{\text{sig}}^{\text{multijet}+} - N_{\text{sig}}^{\text{multijet}},\, N_{\text{sig}}^{\text{multijet}-} - N_{\text{sig}}^{\text{multijet}}\right).$$

The varied left edges of the tail region can be seen in Figure 7.4 represented by the dashed blue lines.

3. Another systematic component of the uncertainty is due to the shape of the template distributions which depends on the template selection used. To account for this, the selection is varied by removing the electric charge requirement while all other template selection cuts are left unchanged. Relative isolation histograms of data from both the nominal and varied template selections can be seen in

Figure 7.5. By removing the charge requirement an influx of well-isolated signal appears to have contaminated the template sample. The difference between the multijet background estimated using the nominal selection and the estimate, $\tilde{N}_{\rm sig}^{\rm multijet}$, from the varied selection is taken as a systematic uncertainty:

$$\delta^{\rm shape} = \tilde{N}_{\rm sig}^{\rm multijet} - N_{\rm sig}^{\rm multijet}. \tag{7.10}$$

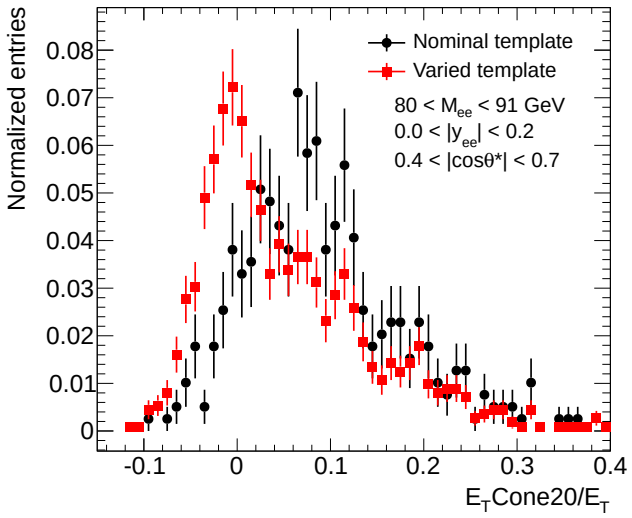

Figure 7.5: A systematic uncertainty is obtained by using a different template selection. Relative isolation distributions from the nominal and varied selections, in which the same sign charge requirement is removed, are shown.

A subset of the three-dimensional multijet background results along with the statistical and total uncertainties represented by the error bars and purple band, respectively, can be seen in Figure 7.6. The lower panels in these plots show the fraction of multijet background in the signal selected data. In the off-peak M_{ee} bins, the multijet background is sizable, as much as 20%, while at the Z-peak the background is negligible. As the figure shows, the total uncertainty on the multijet background is conservative being as large as 100% in some low statistics bins.

7.2.2 Summary

In Table 7.2 is the estimated number of background events for several illustrative regions in the measurement phase space. Below the Z-peak, $M_{ee} \in [46, 66]$ and $[66, 80]$

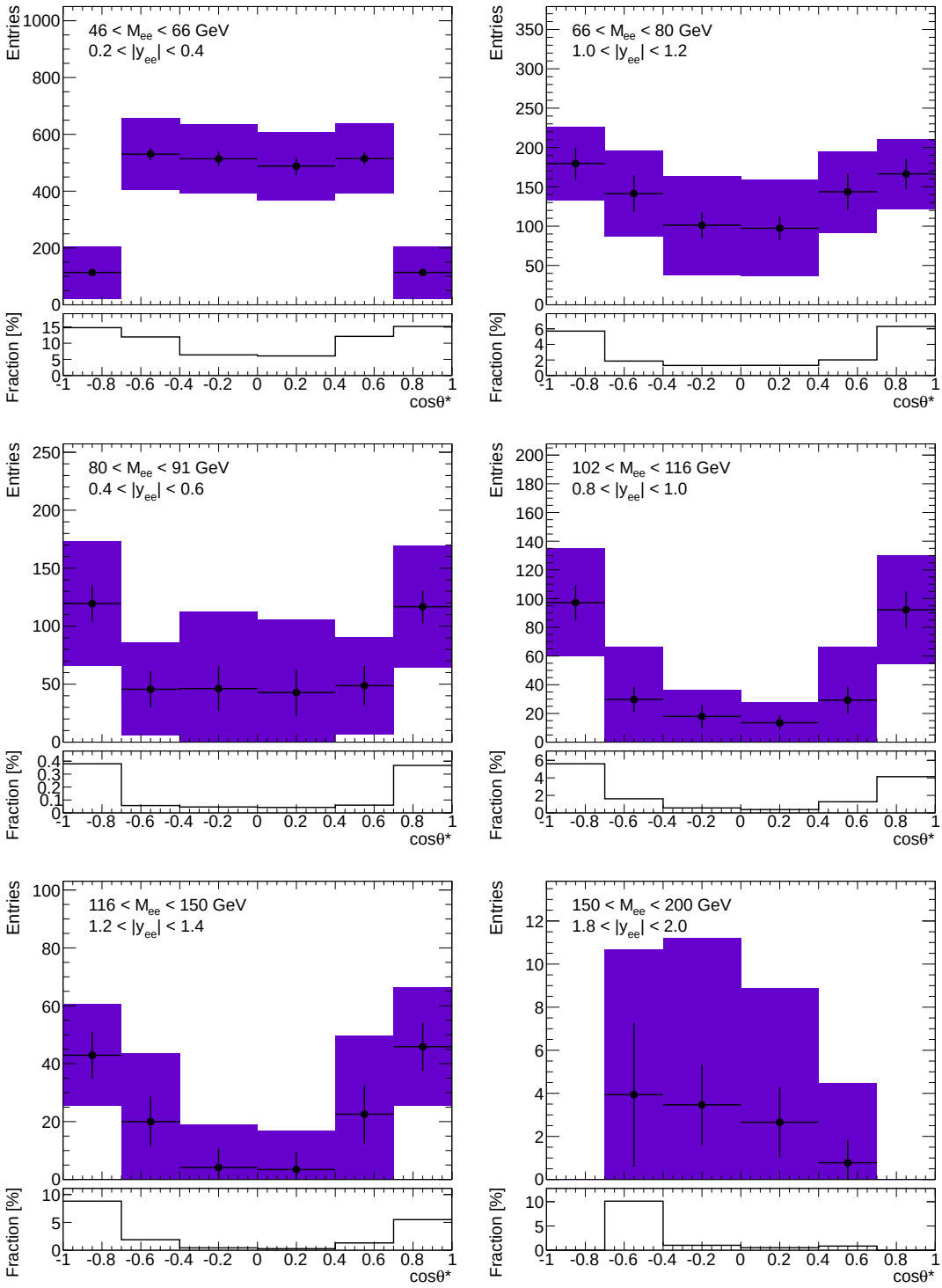

Figure 7.6: Multijet background plotted in bins of $\cos\theta^*$ for several different invariant mass and rapidity ranges. Both the statistical (error bars) and total (error band) uncertainties are shown. The fraction of multijet events in the signal data is shown in the bottom panels of the plots.

Bin	M_{ee} [GeV]	$\lvert y_{ee}\rvert$	$\cos\theta^*$	Data	$Z/\gamma^* \to ee$	$Z/\gamma^* \to \tau\tau$	$\gamma\gamma$	Diboson	$W \to \ell\nu$	Top	Multijet	Prediction
1	46, 66	0.0, 0.2	−1.0, −0.7	802	479	27	13	10	7	120	134	790
2	46, 66	0.0, 0.2	−0.7, −0.4	4439	3540	235	13	82	0	116	538	4524
3	46, 66	0.0, 0.2	−0.4, 0.0	8043	6727	428	26	127	40	170	497	8014
4	46, 66	0.0, 0.2	0.0, +0.4	8050	6665	362	27	135	41	167	514	7910
5	46, 66	0.0, 0.2	+0.4, +0.7	4311	3426	109	15	83	10	118	528	4291
6	46, 66	0.0, 0.2	+0.7, +1.0	787	480	24	11	9	12	117	126	781
85	66, 80	0.4, 0.6	−1.0, −0.7	2743	2380	0	7	16	16	66	125	2610
86	66, 80	0.4, 0.6	−0.7, −0.4	7894	7202	86	19	41	6	87	184	7625
87	66, 80	0.4, 0.6	−0.4, 0.0	9507	8929	147	24	42	24	128	106	9400
88	66, 80	0.4, 0.6	0.0, +0.4	9463	8523	73	23	42	18	128	105	8913
89	66, 80	0.4, 0.6	+0.4, +0.7	7614	6691	53	17	42	8	86	195	7091
90	66, 80	0.4, 0.6	+0.7, +1.0	2670	2293	7	7	15	8	66	128	2523
175	80, 91	1.0, 1.2	−1.0, −0.7	39685	38773	0	51	15	0	36	121	38997
176	80, 91	1.0, 1.2	−0.7, −0.4	68577	68039	2	73	21	8	32	96	68272
177	80, 91	1.0, 1.2	−0.4, 0.0	73632	70713	6	117	14	16	54	62	70982
178	80, 91	1.0, 1.2	0.0, +0.4	73946	71193	0	118	14	9	50	68	71452
179	80, 91	1.0, 1.2	+0.4, +0.7	70518	69382	0	73	17	7	33	95	69607
180	80, 91	1.0, 1.2	+0.7, +1.0	40664	39985	0	52	16	0	40	126	40218
271	91, 102	1.8, 2.0	−1.0, −0.7	224	199	0	3	0	0	1	0	202
272	91, 102	1.8, 2.0	−0.7, −0.4	5925	5718	0	15	1	0	5	0	5738
273	91, 102	1.8, 2.0	−0.4, 0.0	34612	33955	0	50	6	30	13	0	34054
274	91, 102	1.8, 2.0	0.0, +0.4	36966	36171	8	55	7	8	13	1	36262
275	91, 102	1.8, 2.0	+0.4, +0.7	6820	6471	0	12	1	0	5	0	6489
276	91, 102	1.8, 2.0	+0.7, +1.0	258	229	0	3	0	0	1	0	232
313	102, 116	0.8, 1.0	−1.0, −0.7	1734	1547	0	8	19	10	44	97	1725
314	102, 116	0.8, 1.0	−0.7, −0.4	1841	1732	0	8	9	2	43	30	1824
315	102, 116	0.8, 1.0	−0.4, 0.0	3158	3060	14	13	10	53	66	18	3235
316	102, 116	0.8, 1.0	0.0, +0.4	3530	3355	0	15	12	0	61	14	3456
317	102, 116	0.8, 1.0	+0.4, +0.7	2304	2141	7	10	9	10	39	29	2246
318	102, 116	0.8, 1.0	+0.7, +1.0	2230	1968	0	8	15	3	46	92	2133
415	116, 150	1.8, 2.0	−1.0, −0.7	2	3	0	0	0	0	1	0	4
416	116, 150	1.8, 2.0	−0.7, −0.4	152	108	0	2	2	0	6	25	144
417	116, 150	1.8, 2.0	−0.4, 0.0	1018	893	0	8	6	7	19	64	998
418	116, 150	1.8, 2.0	0.0, +0.4	1310	1245	2	10	8	5	19	51	1340
419	116, 150	1.8, 2.0	+0.4, +0.7	282	242	0	5	2	9	8	25	291
420	116, 150	1.8, 2.0	+0.7, +1.0	13	7	0	0	0	0	1	0	8
463	150, 200	1.0, 1.2	−1.0, −0.7	293	186	0	11	9	0	51	38	295
464	150, 200	1.0, 1.2	−0.7, −0.4	401	301	0	6	9	10	50	10	385
465	150, 200	1.0, 1.2	−0.4, 0.0	439	368	0	6	5	0	51	7	436
466	150, 200	1.0, 1.2	0.0, +0.4	559	445	0	6	7	17	48	5	528
467	150, 200	1.0, 1.2	+0.4, +0.7	656	541	0	12	8	10	48	9	627
468	150, 200	1.0, 1.2	+0.7, +1.0	493	376	0	18	12	5	54	31	495

Table 7.2: Yields from data, signal and background MC, and the multijet background. The final column is the prediction (signal plus background) which is comparable to data.

GeV, the largest backgrounds are due to $Z/\gamma^* \to \tau\tau$, top, and multijet processes. At the peak itself, $M_{ee} \in [80, 91]$ and $[91, 102]$ GeV, all backgrounds are negligible and Drell-Yan production overwhelmingly dominates. Finally, in the high mass bins, $M_{ee} \in [102, 116]$, $[116, 150]$, and $[150, 200]$ GeV, the background mostly consists of top and multijet events. Table 7.2 also gives the number of signal data and MC events. Summing together the background estimates and the signal MC yields a complete prediction of the data. As can be seen from this table, the predicted number of events closely matches the observed number having at worst a 10% difference.

7.3 Control Plots

With complete estimates of the MC and multijet backgrounds, it is possible to compare these estimates together with the signal MC to the data for a variety of kinematic observables and ranges in phase space. Electron p_T^e and η^e distributions are shown in Figure 7.7. In Figure 7.8 are control plots of the observables of interest, M_{ee}, $|y_{ee}|$, and $\cos\theta^*$ along with the dielectron transverse momentum P_T^{ee}. These are reconstruction-level distributions of signal events where the Monte Carlo and multijet backgrounds are combined with the signal MC to form a complete prediction of the data. A ratio comparing the prediction to the data is shown in each of the lower panels of the plots. The shaded band in the ratio corresponds to the quadrature sum of the dominant systematic uncertainties which include the following (a complete description of the uncertainties is given in Chapter 8): energy calibration and resolution, efficiency scale factors, charge misidentification, and the multijet background estimation. These uncertainties account for more than 90% of the total systematic uncertainty. The error bars correspond to the Poisson statistical uncertainties of the data and prediction, added in quadrature.

Control plots separated into different regions of kinematic phase space are shown in Figures 7.9 and 7.10. These show electron p_T^e and η^e distributions split into three M_{ee} regions, $46 < M_{ee} < 66$, $80 < M_{ee} < 91$, and $116 < M_{ee} < 150$ GeV, and two $|y_{ee}|$ regions, $|y_{ee}| < 1.0$ (Figure 7.9) and $|y_{ee}| > 1.0$ (Figure 7.10). In Figure 7.11 are dielectron plots of y_{ee} and $\cos\theta^*$ in the same three invariant mass regions listed above. Finally, in Figure 7.12 are dielectron P_T^{ee} distributions for each of the M_{ee} and $|y_{ee}|$ regions. These regions were chosen to illustrate the size and shape of the signal and background at various M_{ee} and $|y_{ee}|$ ranges and to highlight some of the systematic effects at different regions in phase space. For most observables and regions in space,

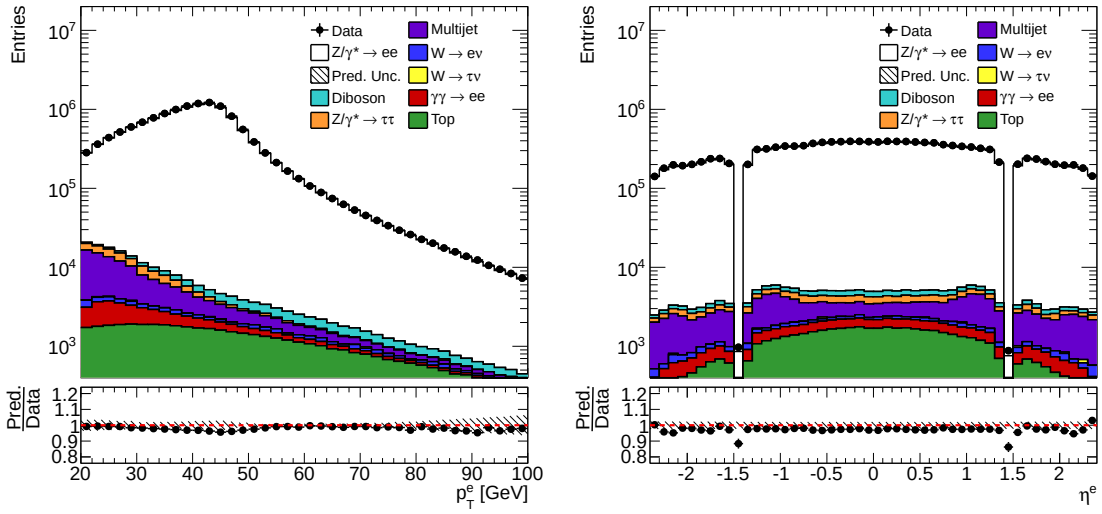

Figure 7.7: Distributions of electron transverse momentum and pseudorapidity. The expected signal and background estimates are summed and compared to the data measurement. The shaded band in the ratio panel corresponds to the dominant systematic uncertainties summed in quadrature while the error bars are the statistical uncertainties on the data and prediction.

the prediction is consistent with the measurement.

Some discrepancies between data and prediction can be seen in the M_{ee} control plot in Figure 7.8 despite the energy scale and smearing corrections applied. These discrepancies are however accounted for by the scale and smearing uncertainties. As for the other two observables of interest, the prediction plotted in $|y_{ee}|$ and $\cos\theta^*$ shows good agreement with data. It might be noted that the $\cos\theta^*$ control plots all appear symmetric about zero. An imbalance between the number of events with $\cos\theta^* > 0$ and $\cos\theta^* < 0$ or a forward-backward asymmetry is not apparent in these distributions due to one of two effects. Events with an invariant mass near the Z-peak, which dominates the data sample, exhibit negligible forward-backward asymmetry. Secondly, for events with small $|y_{ee}|$ the q cannot be distinguished from the $\bar{q}$ leading to a dilution of the forward-backward asymmetry. Both effects were previously discussed in Section 2.3.

The largest differences between data and prediction occur in the Z transverse momentum distributions, around $P_T^{ee} > 80$ GeV for $80 < M_{ee} < 91$ GeV in Figure 7.12. This is not surprising given the transverse momentum of the Z is highly dependent on QCD effects which are difficult to model accurately.

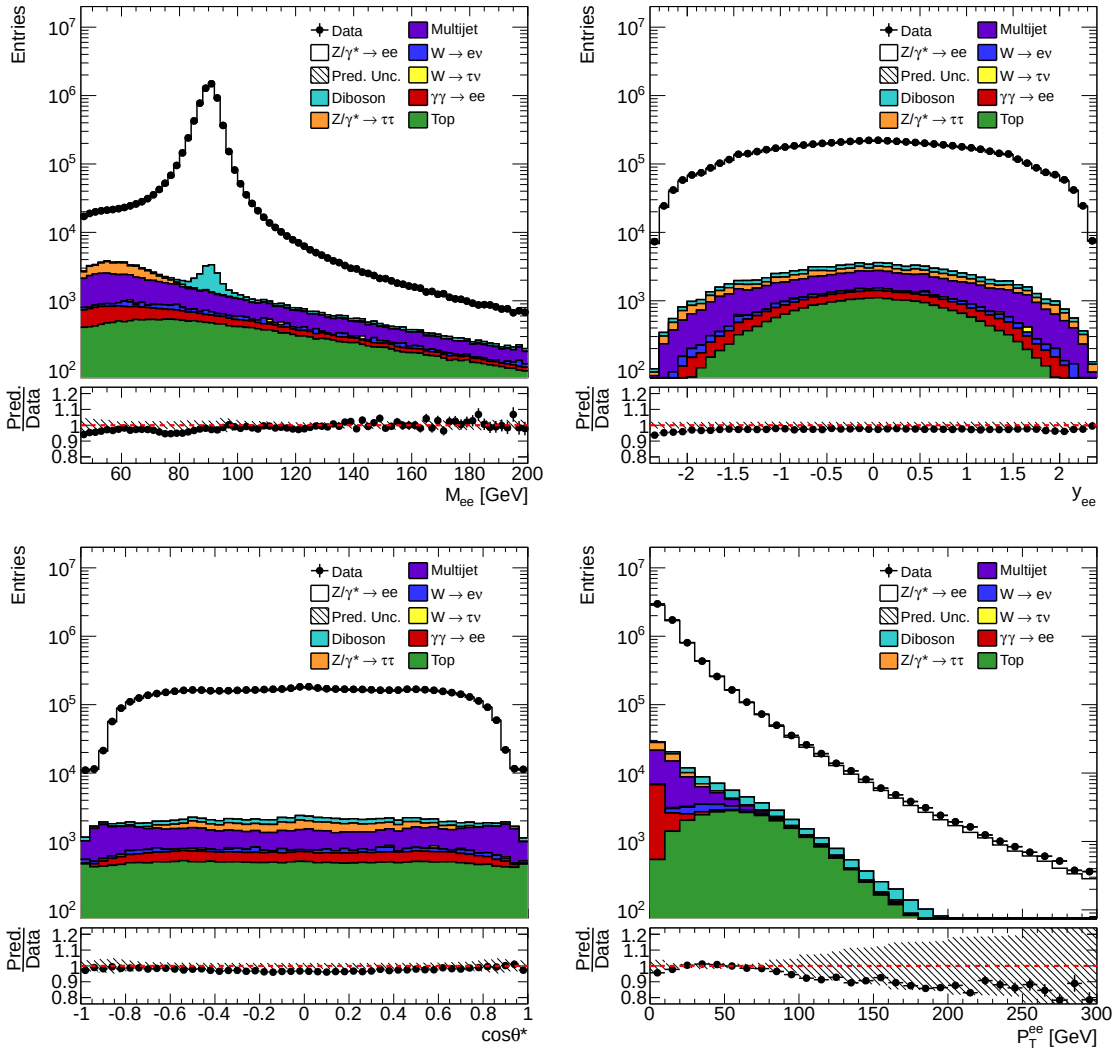

Figure 7.8: Distributions of dielectron invariant mass, rapidity, $\cos\theta^*$, and transverse momentum.

7.4 Unfolding

Due to significant bin migrations which lead to low bin purities about the Z-peak, Bayesian unfolding must be used to unfold the measurement to generator-level. Recall that at generator-level, three lepton definitions exist (see Section 4.3.1): Born, bare, and dressed. Since dressed and reconstructed leptons are similarly defined[4], the measurement is unfolded to dressed-level as it is more efficient unfolding to something that resembles the measured objects than something more different.

[4]Both objects are defined as having a large energy core with smaller surrounding energy deposits.

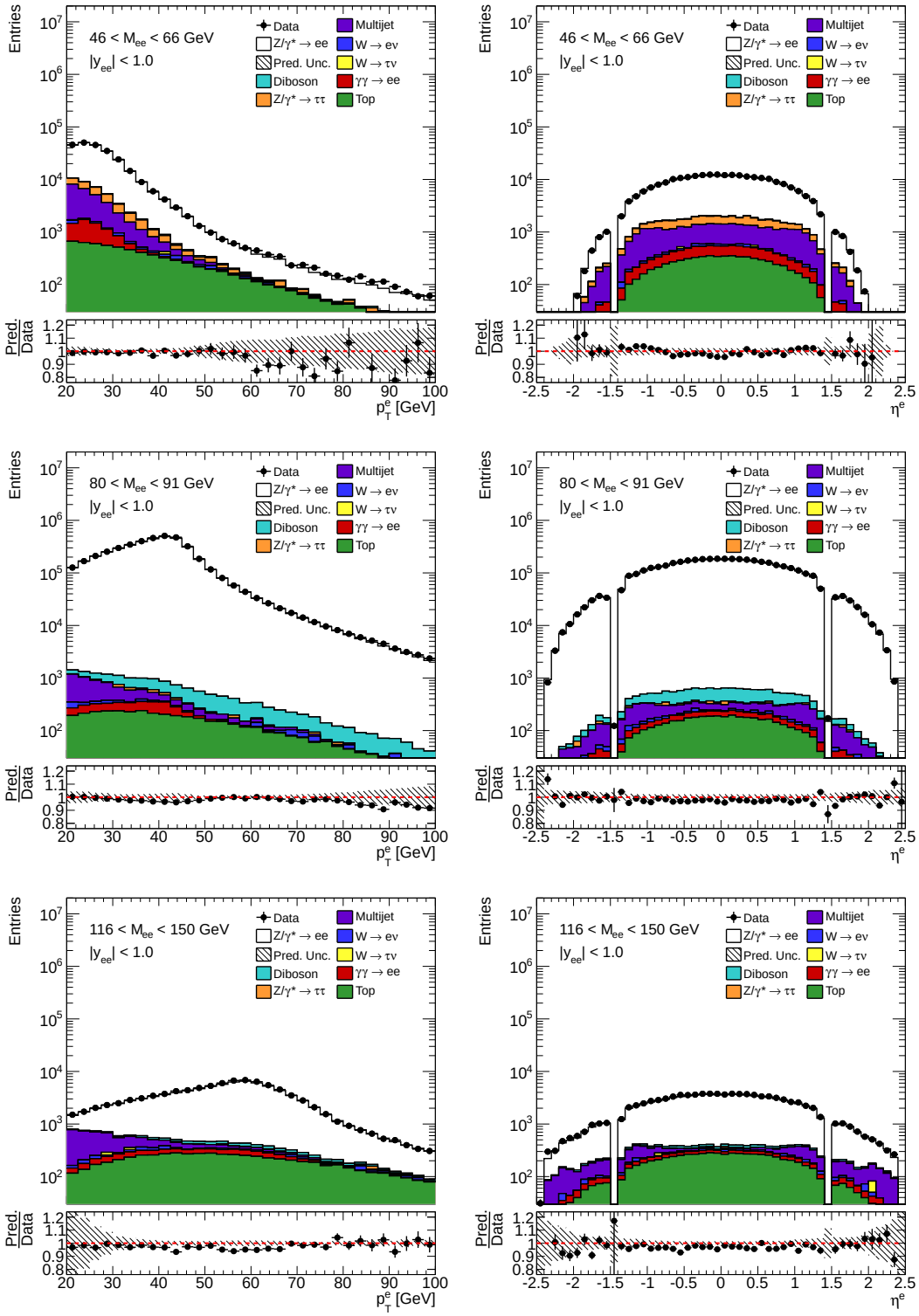

Figure 7.9: Electron p_T^e and η^e distributions for $|y_{ee}| < 1.0$ and $M_{ee} \in [46, 66]$, $[80, 91]$, and $[116, 150]$ GeV.

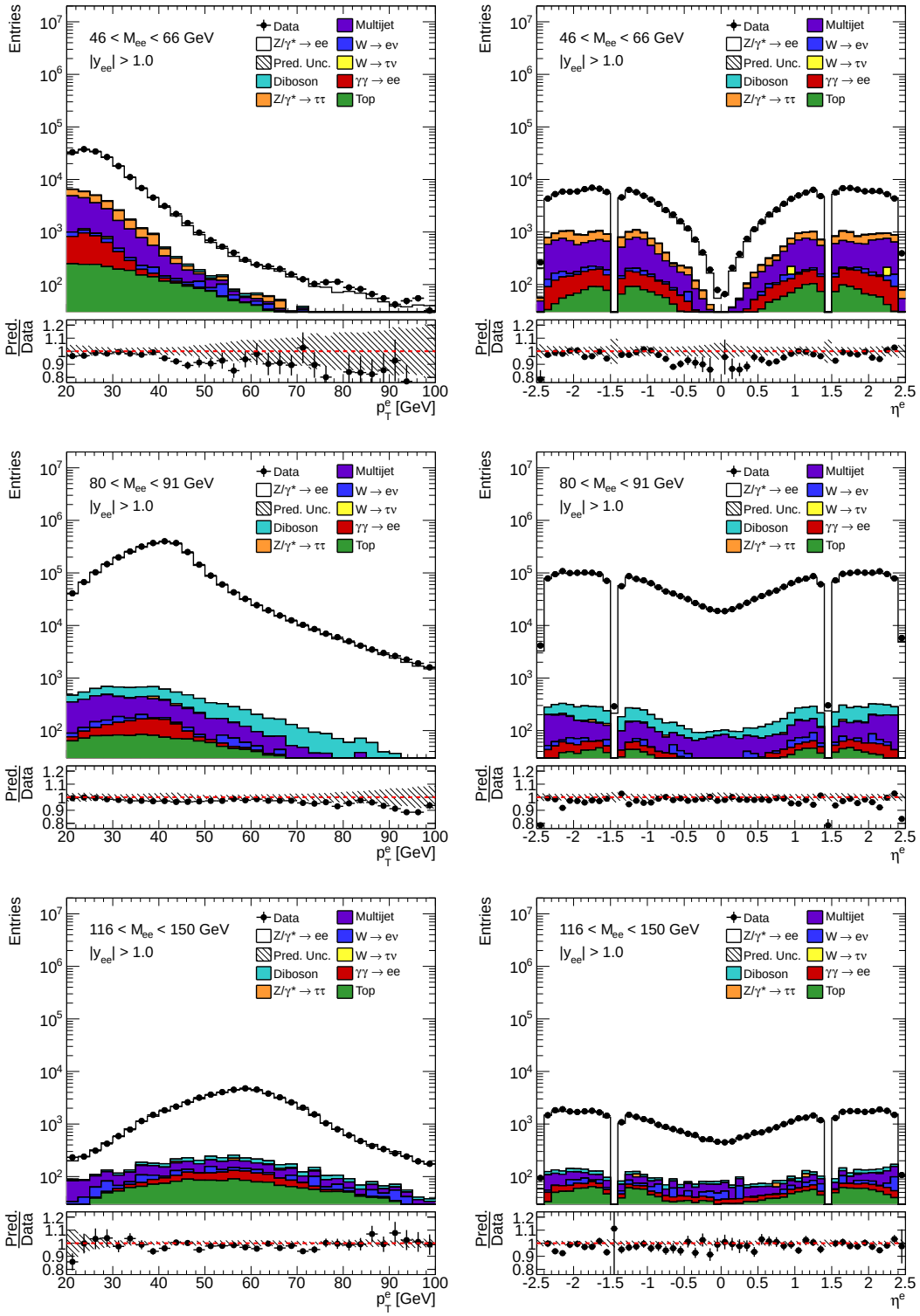

Figure 7.10: Electron p_T^e and η^e distributions for $|y_{ee}| > 1.0$ and $M_{ee} \in [46, 66]$, $[80, 91]$, and $[116, 150]$ GeV.

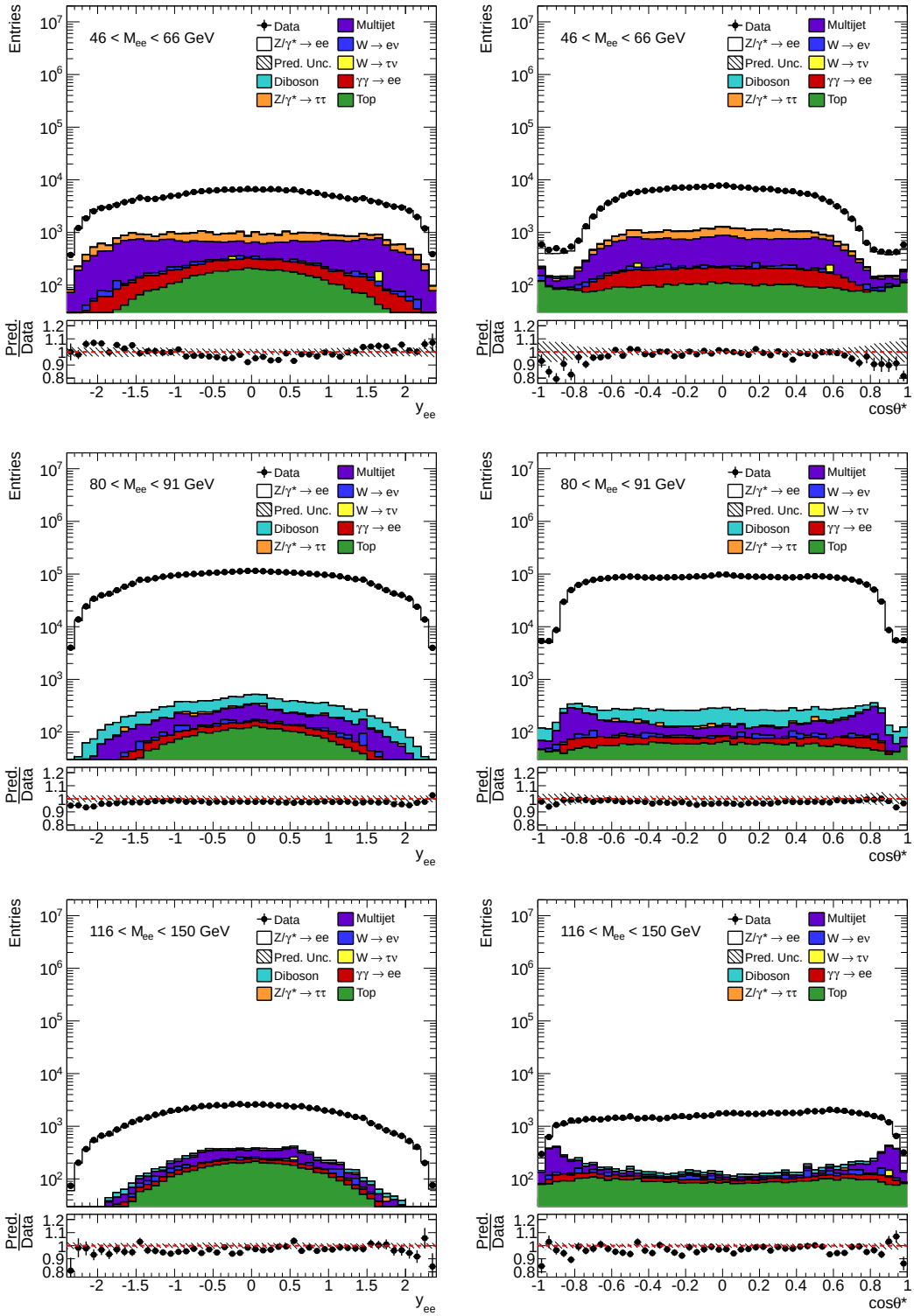

Figure 7.11: Dielectron y_{ee} and $\cos\theta^*$ distributions for $M_{ee} \in [46, 66]$, $[80, 91]$, and $[116, 150]$ GeV.

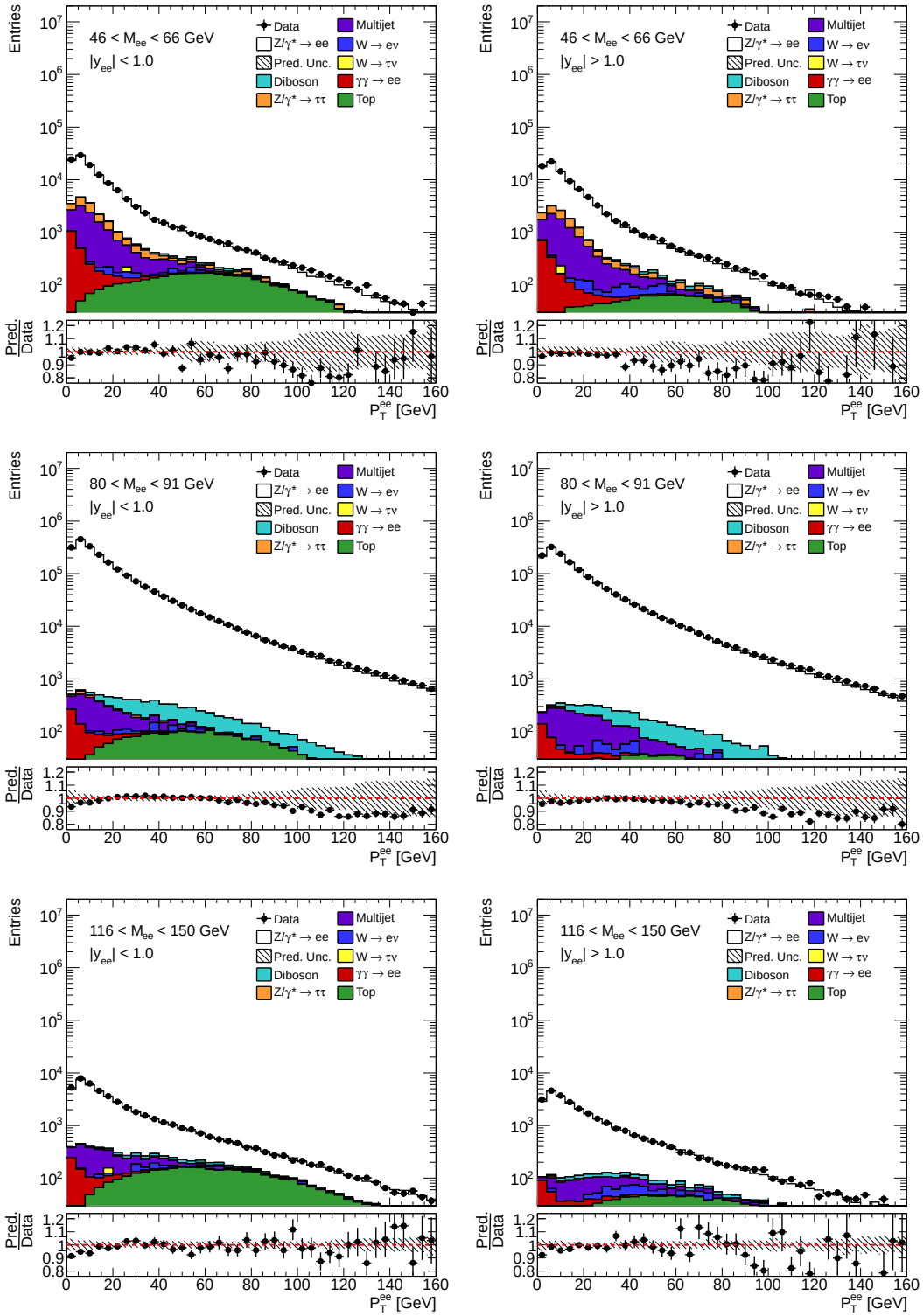

Figure 7.12: Dielectron P_T^{ee} distributions for $|y_{ee}| < 1.0$ and $|y_{ee}| > 1.0$ and $M_{ee} \in [46, 66]$, $[80, 91]$, and $[116, 150]$ GeV.

To compute the inverted response matrix and unfold this measurement, software called RooUnfold [102] is used which requires, in addition to the data itself, three objects as input all of which are computed using signal MC:

1. A response matrix, a two-dimensional array of probabilities describing the likelihood a dressed Drell-Yan electron-positron pair generated in some analysis bin is reconstructed in each of the analysis bins.

2. A histogram of generated Drell-Yan events at dressed-level within the fiducial volume of interest which represents the target distribution (also known as the prior);

3. A histogram of reconstructed Drell-Yan events, the signal MC equivalent of the background subtracted data measurement.

These are exactly the objects described in Section 6.2.2 required to perform Bayesian unfolding. Object 1 in the list above is $P(y_j \,|\, x_i)$ while objects 2 and 3 are used to account for the events that were originally outside but after reconstruction migrated inside the fiducial volume and the unmeasured events due to detector efficiency ϵ effects, respectively. The data is unfolded to whichever lepton definition is used to construct objects 1 and 2; by using dressed Drell-Yan pairs, the data is unfolded to dressed-level. RooUnfold gives the option of performing multiple iterations of Bayesian unfolding in order to reduce the dependency of the data on signal MC. This analysis uses two iterations of unfolding.

Two example response matrices can be seen in Figure 7.13. The vertical axis corresponds to generated values of M_{ee} calculated using dressed electrons while the horizontal axis corresponds to reconstructed values. It should be noted that these matrices span a range of $26 < M_{ee} < 250$ GeV, larger than the range of interest, $46 < M_{ee} < 200$ GeV. The additional bins $M_{ee} \in [26, 46]$ and $[200, 250]$ GeV have been included in the measurement to account for events that have true invariant mass inside the range $46 < M_{ee} < 200$ GeV but after reconstruction are found outside. These bins are treated as though they were a part of the fiducial volume. Full background estimations are performed in these bins and after unfolding, the mass range is truncated and the results measured in these two extra bins are left out of the final results.

For an event generated in one of the nine M_{ee}^{gen} bins, the probability of being reconstructed in each of the nine M_{ee}^{reco} bins is given by these response matrices. As

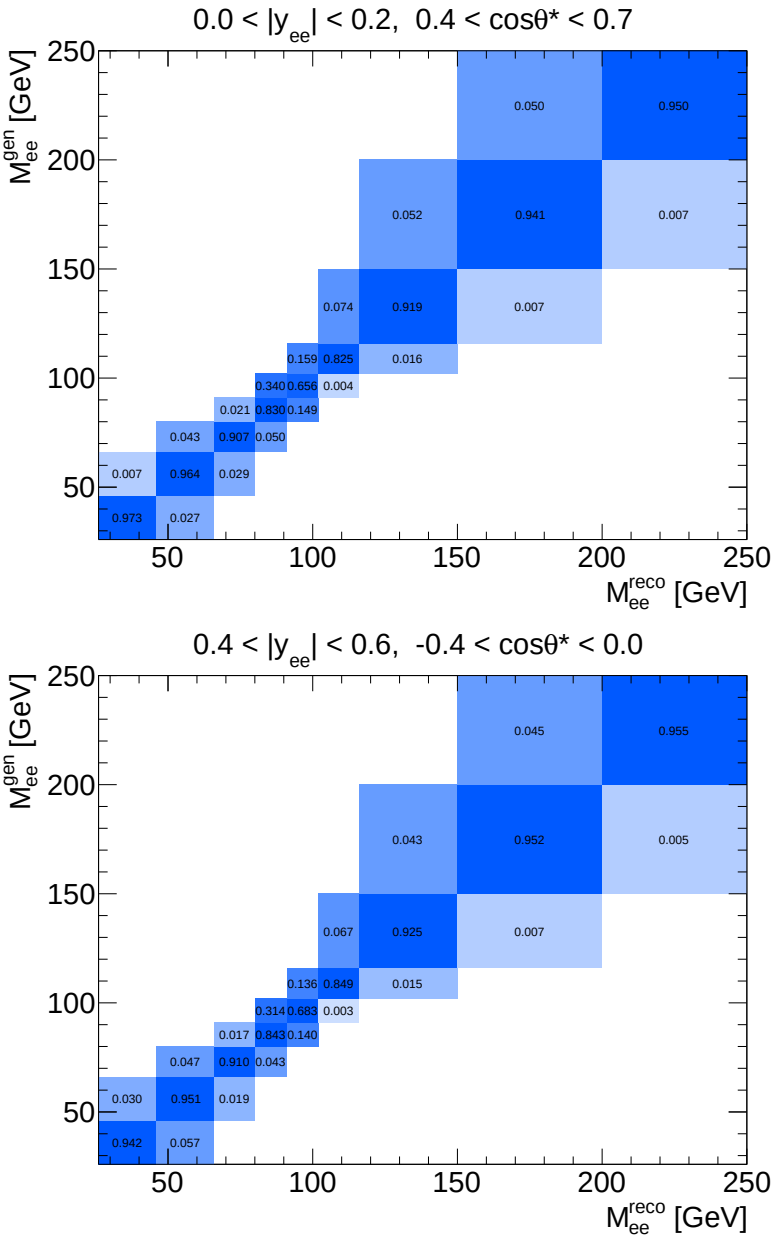

Figure 7.13: Invariant mass response matrices. The vertical axis corresponds to dressed-level invariant mass while the horizontal axis corresponds to reconstructed invariant mass.

a sanity check, the probabilities corresponding to each M_{ee}^{gen} bin do in fact sum to 1. Note that they are nearly diagonal indicating that most dielectron pairs inhabit the same bin after both generation and reconstruction. It can also be seen that in cases where significant migrations do occur, they tend to favour lower invariant mass values. This phenomenon is due to photon emission which, if radiated sufficiently far

from the high energy core of the electron, may not be included in the reconstructed electron. Photons excluded in this way cause generated values of M_{ee} to be smeared after reconstruction with a bias towards lower invariant mass values. The mass bins at the Z-peak, $M_{ee} \in [80, 91]$ and $[91, 102]$ GeV, are affected the most by this.

To illustrate the unfolding process, the operations presented in Equation (6.1) are performed here. In the top row of Figure 7.14 are two example invariant mass distributions of data along with the expected signal and the MC and multijet backgrounds binned three-dimensionally. Subtracting the total background from the data gives the estimated number of Drell-Yan events in data which can be seen in bottom row of the figure.

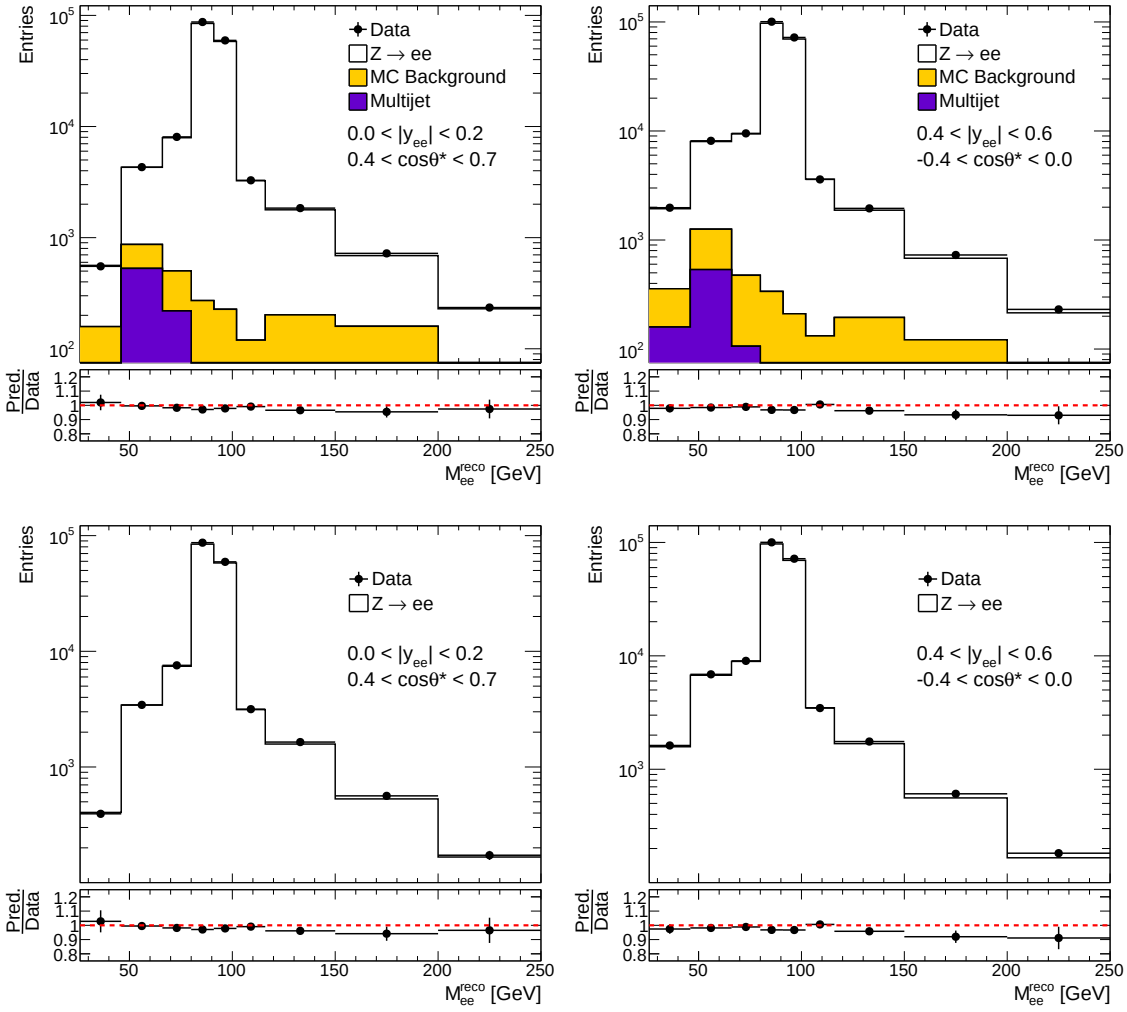

Figure 7.14: Invariant mass distributions of data with the expected background levels (top) and with the total background subtracted (bottom).

The top row of Figure 7.15 shows the invariant mass distributions unfolded to generator-level, or more specifically to dressed-level. As stated earlier, the additional invariant mass bins have now been removed from the measurement. Differential cross-sections are obtained by simply dividing the unfolded distributions by $\mathcal{L} = 20.1$ fb^{-1} and bin widths δM_{ee}, $\delta|y_{ee}|$, and $\delta \cos\theta^*$ which are shown in the bottom row of Figure 7.15.

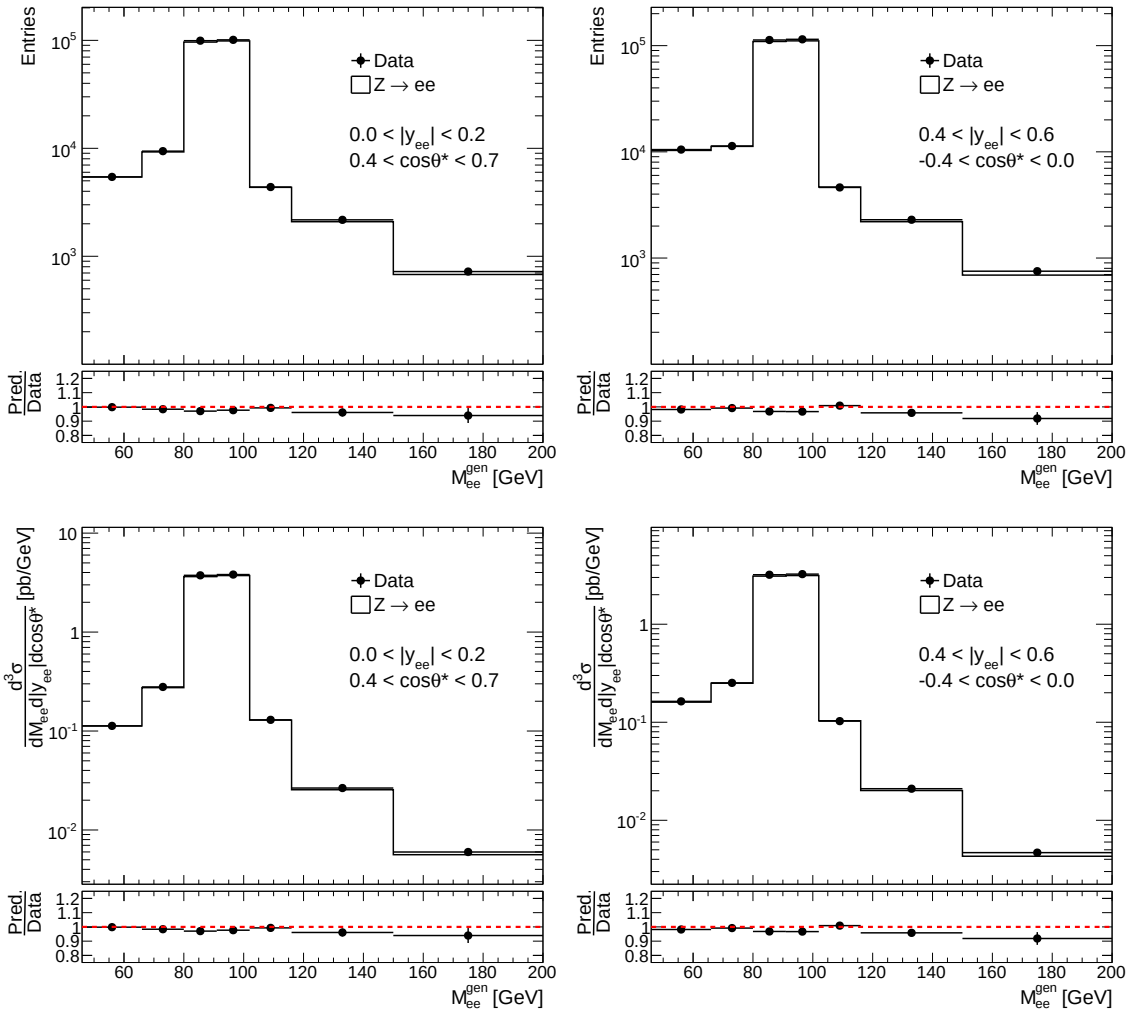

Figure 7.15: Unfolded invariant mass distributions at dressed-level (top) and their corresponding three-dimensional differential cross-sections (bottom).

As a final step in the cross-section calculation, the dressed-level cross-sections are

corrected to Born-level using bin-dependent correction factors, defined as

$$C_i = \frac{N_i^{\text{Born}}}{N_i^{\text{dressed}}}, \quad i = 1, 2, 3, ..., 504, \tag{7.11}$$

where N^{Born} is the number of Born and N^{dressed} is the number of dressed events; and i is the analysis bin index. These correction factors are calculated using signal MC by first selecting Born electron-positron pairs. The electron and positron must satisfy kinematic cuts $p_T^e > 20$ GeV and $|\eta^e| < 2.4$ and their invariant mass must be in the range $46 < M_{ee} < 200$ GeV. The pairs are binned into the 504 analysis bins producing N^{Born}. In order to obtain N^{dressed}, the process is repeated using dressed electron-positron pairs. Two example distributions of the correction can be seen in Figure 7.16. Note that below the Z-peak, the corrections deviate from unity the most since, by definition, dressed leptons have a lower invariant mass than their Born counterparts.

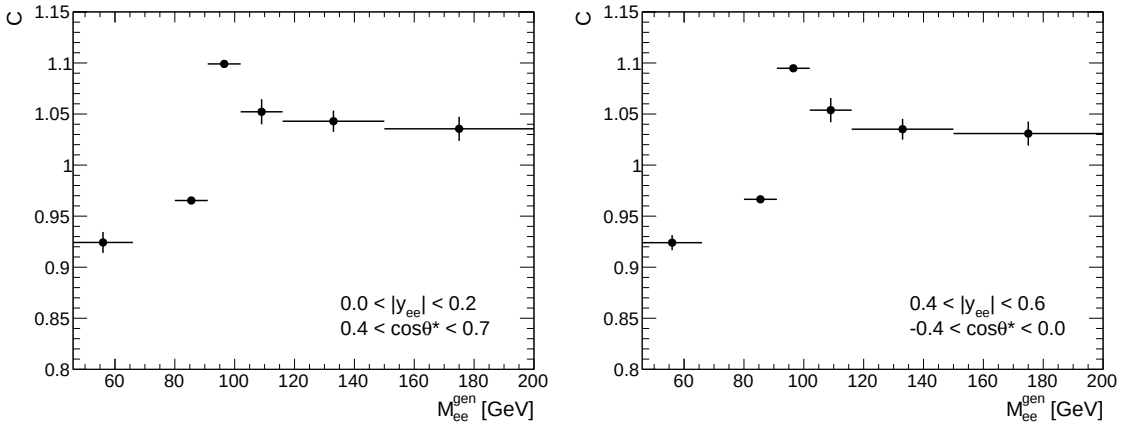

Figure 7.16: Correction factors used to correct to Born-level.

Multiplying $\frac{d^3\sigma}{dM_{ee}d|y_{ee}|d\cos\theta^*}$ at dressed-level by these correction factors gives the Born differential cross-sections of interest which are illustrated in Figure 7.17. This analysis reports the measurement at Born-level since most PDF groups perform their fits on Born quantities.

The unfolding process (and the subsequent cross-section calculation) has been illustrated here for two example M_{ee} histograms, response matrices, and so on. As mentioned previously, in practice, unfolding is performed on a single one-dimensional histogram of the data consisting of $9 \times 12 \times 6 = 648$ bins (where again two extra M_{ee} bins have been appended to the ends of the nominal mass range) using a 648×648

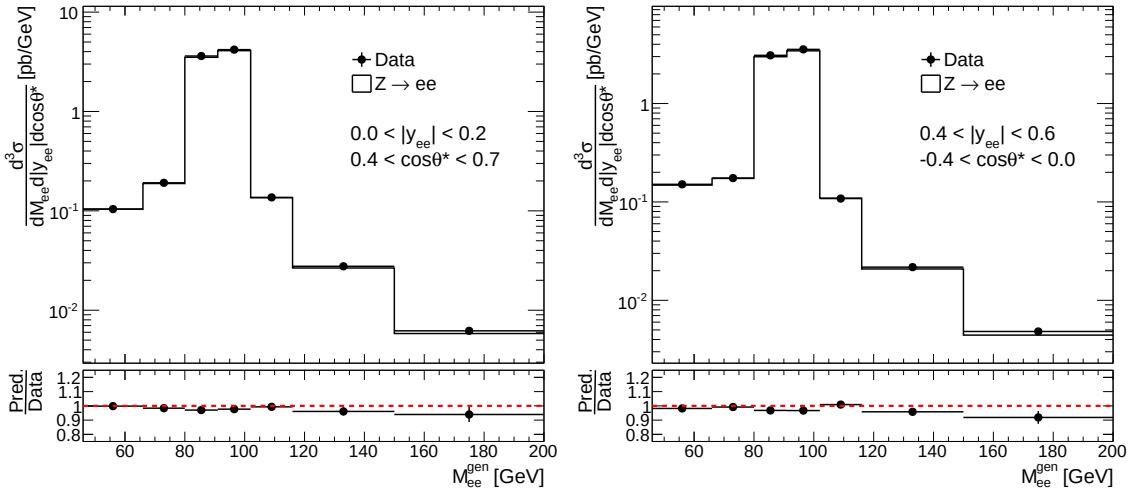

Figure 7.17: Born-level three-dimensional differential cross-sections, the quantity central to this analysis.

response matrix. Unfolding a single histogram is not only practical but also allows resolution effects in $|y_{ee}|$ and $\cos\theta^*$ to be corrected for as well. This histogram and the response matrix provide no intuitive physical value hence are not shown in this dissertation.

Chapter 8

Uncertainties

This measurement is subject to statistical and systematic uncertainties which must be estimated. Random, uncorrelated fluctuations in the measurement due to the finite sample sizes of the data set and Monte Carlo samples result in statistical uncertainties. Systematic uncertainties are reproducible uncertainties that are categorized into two types: experimental and theoretical. Sources of experimental uncertainties come from the measurement apparatus while theoretical uncertainties are due to imperfect physics models or inputs from other experiments. In this chapter, the major sources of uncertainties on the three-dimensional differential cross-section are listed and their treatments described. A summary of the uncertainties considered and their effect on the measurement will be presented.

8.1 Statistical Uncertainties

The measurement is affected by the following statistical uncertainties.

Data

The 2012 data set has a finite number of events leading to a statistical uncertainty on the differential cross-section measurement. The size of this statistical uncertainty is estimated using the bootstrap method [99] which was introduced in Section 6.3.3. A thousand bootstrap replicas are produced and each replica is unfolded using the nominal response matrix and the generated and reconstructed distributions described in Section 7.4 as inputs to RooUnfold. The statistical uncertainty on the differential

cross-section due to the size of the data set is taken as the standard deviation of the 1000 replicas.

Signal Monte Carlo

Like the data set, the signal MC samples used in this analysis have a limited number of events which also leads to a statistical uncertainty on the measurement. The inputs to RooUnfold are constructed using signal MC; therefore, uncertainties on these input distributions have an effect on the unfolded data measurement. To estimate the size of this uncertainty, 1000 bootstrap replicas of the response matrix and the generated and reconstructed distributions are produced. The nominal data measurement is unfolded using these sets of inputs and the standard deviation of the resulting 1000 unfolded data distributions is taken as the statistical uncertainty due to the finite size of the signal MC sample.

Background Monte Carlo

The background Monte Carlo samples are used to estimate several of the major background processes. Having a finite number of events, these samples introduce statistical uncertainties on the differential cross-section measurement. For each background sample, 1000 bootstrap replicas are produced and in turn are subtracted from the data while keeping the other background MC estimates fixed. The background subtracted data is then unfolded, once for each of the 1000 replicas. The standard deviation of the 1000 unfolded cross-sections is the statistical uncertainty due to the sample in question.

Multijet Background

The final statistical uncertainty comes from the multijet background estimate. As described in Section 7.2.1, 50 bootstrap replicas of the signal and template distributions are produced for each of the analysis bins. The template method is then performed 50 times using these replicas, and the results of which are subtracted from the data yielding 50 background subtracted measurements. The standard deviation of the 50 unfolded distributions is taken as the statistical component of the multijet background uncertainty.

8.2 Systematic Uncertainties

The following systematic uncertainties are considered in this measurement.

Luminosity

A constant uncertainty of 1.9% [62] is assigned to the integrated luminosity of the data set. Typically this uncertainty is not included in the systematic uncertainty that is illustrated in plots and quoted in tables. To account for the luminosity uncertainty, it must be added in quadrature to the reported systematic uncertainty.

Background Monte Carlo

In addition to a statistical component, the background MC samples also have a systematic uncertainty due to imperfect knowledge of the cross-sections σ^{bkg} used to normalize the Monte Carlo samples to the integrated luminosity of the data. The event weights used to normalize the samples take the form

$$w_{\text{MC}} = \frac{\sigma^{\text{bkg}}\epsilon^{\text{filter}}\mathcal{L}}{N^{\text{evt}}}, \tag{8.1}$$

where ϵ^{filter} is the filter efficiency and N^{evt} is the number of events in a given sample. An uncertainty on σ^{bkg} leads to an uncertainty on w_{MC} which affects the final measurement. To estimate the uncertainty due to background MC cross-sections, each of the samples is normalized using its cross-section varied up and down by its uncertainty $\delta\sigma^{\text{bkg}}$,

$$w_{\text{MC}+} = \frac{(\sigma^{\text{bkg}} + \delta\sigma^{\text{bkg}})\epsilon^{\text{filter}}\mathcal{L}}{N^{\text{evt}}}, \qquad w_{\text{MC}-} = \frac{(\sigma^{\text{bkg}} - \delta\sigma^{\text{bkg}})\epsilon^{\text{filter}}\mathcal{L}}{N^{\text{evt}}}. \tag{8.2}$$

The analysis is performed as usual using $w_{\text{MC}+}$ and again with $w_{\text{MC}-}$. The offset (see Section 6.3.1) between these two results is taken as the uncertainty on the measurement due to σ^{bkg}. All background cross-sections and their uncertainties are listed in Tables 4.3 and 4.4.

Multijet Background

The multijet background estimate shifted up and down by its systematic uncertainty (see Section 7.2.1) are used in background subtraction and the resulting distribu-

tions are unfolded. The offset between these unfolded cross-sections is taken as the systematic uncertainty from the multijet background.

Electron Energy Scale

Energy scale factors α are applied to electrons in data to correct for some of the residual differences with MC electrons. These scale factors have numerous sources $c = 1, 2, 3, ...$ of uncertainty [93, 103] which, for example, include inner detector and EM calorimeter material identification uncertainties. The effect of these uncertainties on the measurement is estimated using signal MC (as recommended by the EGamma group) rather than data.

RooUnfold inputs are produced using energy scale corrections with one of the sources shifted up and again down by its uncertainty $\delta\alpha_c$. The data is unfolded using these modified input distributions and the total systematic uncertainty due to the energy scale corrections is the sum of the offsets from all sources added in quadrature:

$$\delta = \left[\left(\frac{\sigma^{\delta\alpha_1+} - \sigma^{\delta\alpha_1-}}{2} \right)^2 + \left(\frac{\sigma^{\delta\alpha_2+} - \sigma^{\delta\alpha_2-}}{2} \right)^2 + ... \right], \tag{8.3}$$

where $\sigma^{\delta\alpha_1\pm}$ is the three-dimensional differential cross-section of interest calculated using energy scale corrections shifted up or down by the uncertainty of source $c = 1$ and similarly for the other terms in Equation (8.3).

Electron Energy Resolution

In addition to the scale corrections, energy resolution corrections are applied to Monte Carlo electrons. Its sources of systematic uncertainty include the sampling term a in the expression for energy resolution (Equation (5.4)) and the simulation of pileup [93, 103]. Similar to the energy scale systematic, RooUnfold input distributions are produced using modified energy resolution corrections in which one of its sources is varied up or down by its uncertainty and the data is unfolded. The offset between the upward and downward shifts is the uncertainty due to that source and the total uncertainty due to the energy resolution corrections is the quadrature sum of the offsets from all sources.

Efficiency

Reconstruction, identification, and trigger scale factors are used to correct the efficiency in MC to the efficiency observed in data. These scale factors have statistical and bin-to-bin correlated and uncorrelated uncertainty components. The combined toy method, described in Section 6.3.2, is used to estimate the uncertainty on the final cross-section. For each of the three scale factors used in this analysis, a set of 1000 combined toys are produced simultaneously varying their statistical, correlated, and uncorrelated parts. For each toy, a set of RooUnfold input distributions are produced and used to unfold the measurement. A thousand unfolded differential cross-sections are obtained and their standard deviation is taken as the uncertainty due to the scale factor under study.

Charge Misidentification

The signal selection requires the two electrons to be opposite in electric charge making this measurement sensitive to the misidentification of the electron charge. Corrections are applied to the signal MC such that the frequency of charge misidentification in MC matches data. A systematic uncertainty on these corrections results from the uncertainties associated with the tag and probe method [91]. The corrections are varied up and down by their uncertainties with each shift producing a set of RooUnfold inputs. The offset between the two resulting cross-section measurements is taken as the uncertainty due to the use of the charge misidentification corrections.

k-Factor

The k-factors used to reweight signal MC events from NLO to NNLO in QCD and to include additional higher order EW corrections have asymmetric uncertainties. Their sources of uncertainty include the PDFs and the electroweak and QCD input parameters used to calculate these k-factors. RooUnfold inputs are constructed using both the up and down variations and the data is unfolded for both cases. The offset between the two results is the k-factor systematic uncertainty.

Z Boson Transverse Momentum

Modelling of the Z boson or dielectron transverse momentum, P_T^{ee}, spectrum is known to be difficult as it depends heavily on the accurate modelling of QCD processes.

The discrepancy between the P_T^{ee} spectra observed in data and simulated in MC is accounted for by assigning a systematic uncertainty to the final cross-section measurement. To determine such an uncertainty, event weights are calculated as

$$w_{P_T^{ee}\,i} = \frac{N_i^{\text{data}} - N_i^{\text{bkg}}}{N_i^{\text{Zee}}}, \quad i = 1, 2, 3, ..., \tag{8.4}$$

where N^{data} is the number of signal selected events in data; and N^{Zee} and N^{bkg} are the expected number of signal events and the estimated number of background events, respectively, in P_T^{ee} bin i. These weights are then applied to the signal MC at generator-level. The reweighted signal MC distribution at reconstruction-level, which now closely resembles the data because of the weights, is then unfolded using the nominal RooUnfold inputs. The difference between this unfolded cross-section and the unfolded data is taken as the uncertainty due to Z boson P_T^{ee} modelling.

Parton Distribution Functions

The signal MC samples used in this analysis were generated using the central CT10 NLO PDF [74]. In addition to the central set, 52 orthogonal error sets in which 1 of 26 PDF fitting parameter has been varied either positively or negatively by its uncertainty have also been produced. To propagate the uncertainty on the CT10 PDF to the measurement, signal MC events are reweighted 52 times, once for each error set. RooUnfold input parameters are produced for each reweighted sample and used to unfold the data. Following the CT10 recommended procedure, the following formula is used to quantify the PDF uncertainty on the unfolded differential cross-section [104]:

$$\delta = \frac{1}{2}\sqrt{\sum_{i=1}^{26}(\sigma_{2i-1} - \sigma_{2i})^2}, \tag{8.5}$$

where σ_{2i-1} and σ_{2i} are the unfolded differential cross-section measurements obtained from the up and down variations of PDF fitting parameter i, respectively.

8.3 Summary

The uncertainties considered in this analysis are summarized in Table 8.1 which gives the source name, the method used to estimate it, and its type indicating whether

it is correlated or uncorrelated across analysis bins. In Figures 8.2 to 8.8, the percent uncertainties relative to $\frac{d^3\sigma}{dM_{ee}d|y_{ee}|d\cos\theta^*}$ are plotted in bins of $\cos\theta^*$ for all three-dimensional analysis bins.

Source	Method	Type
Data statistics	Bootstrap	Uncorrelated
Signal MC statistics	Bootstrap	Uncorrelated
Background MC statistics	Bootstrap	Uncorrelated
Multijet background statistics	Bootstrap	Uncorrelated
Background MC cross-sections	Offset	Correlated
Multijet background systematics	Offset	Correlated
Electron energy scale	Offset	Correlated
Electron energy resolution	Offset	Correlated
Electron reconstruction efficiency	Combined toy	Correlated
Electron identification efficiency	Combined toy	Correlated
Electron trigger efficiency	Combined toy	Correlated
Charge misidentification	Offset	Correlated
k-factor	Offset	Correlated
Z boson P_T	Offset	Correlated
PDF	Error sets	Correlated

Table 8.1: Summary of the systematic uncertainties affecting the measurement and their method of evaluation and type, correlated or uncorrelated across analysis bins.

The total uncertainty, defined as the quadrature sum of each of the individual uncertainties is also shown in these figures. As can be seen, the total uncertainty varies as a function of all three observables of interest. Typically, the total uncertainty is larger in the extremal bins of $\cos\theta^*$, namely $\cos\theta^* \in [-1.0, -0.7]$ and $[0.7, 1.0]$, than in the central bins. Along the $|y_{ee}|$-dimension, the total uncertainty generally increases as $|y_{ee}|$ increases. And in M_{ee}, the measurement is most precise in the Z-peak bins, $M_{ee} \in [80, 91]$ and $[91, 102]$ GeV, while the total uncertainty is more than a factor of two larger in the off-peak bins.

For the bins at the extremities of the fiducial volume, data statistics is consistently a dominate uncertainty. This is unsurprising given the large number of bins associated with this analysis. A similar statement applies to the signal MC despite the samples being very large. The statistical uncertainties from the background MC samples and the multijet estimate vary proportionally with the statistical uncertainty of the data.

In bins $M_{ee} \in [80, 91]$ and $[91, 102]$ GeV, the uncertainty due to the electron energy scale calibration is sizable. This is expected given the sensitivity of the Z-peak to

changes in energy scale. The effect of applying a small shift to α on the peak can be seen in Figure 8.1 (left). The maximum of the distribution is shifted to a higher M_{ee} value when α is increased and conversely, to a lower value when α is decreased. For a fixed value of M_{ee}, these variations result in sizable differences between the nominal and varied distributions which is a measure of the energy scale uncertainty. Note that a similar though less drastic effect is observed when the energy resolution smearing factors β are varied as shown in Figure 8.1 (right).

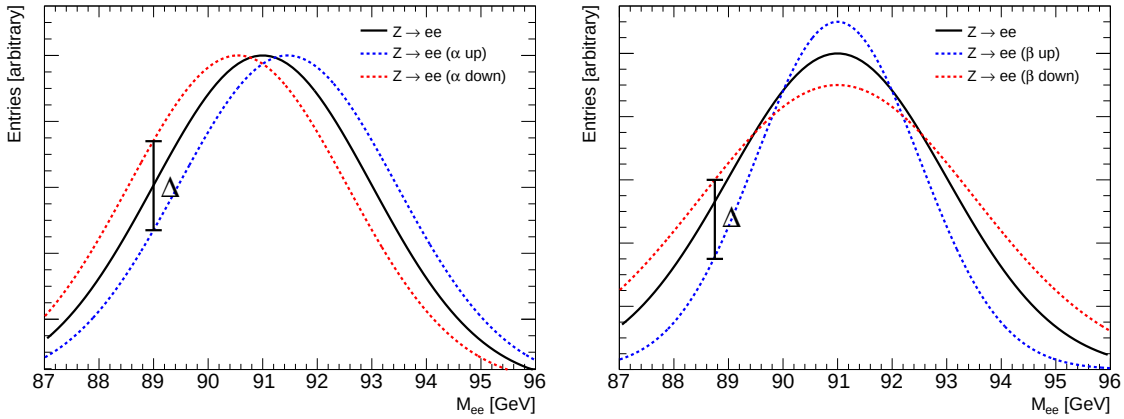

Figure 8.1: The effect of varying the energy scale α (left) and resolution smearing β (right) factors. Shifting α results in an overall shift of the invariant mass distribution which significantly affects the estimated uncertainty. A similar effect occurs when increasing and decreasing the amount of energy smearing applied.

While the reconstruction and trigger scale factor uncertainties are mostly negligible, the uncertainty from identification scale factors is a dominant uncertainty. This uncertainty is particularly large at low mass and at the Z-peak as seen in Figures 8.2 to 8.5. The high mass bins are in general populated by high energy electron pairs which are typically easier to identify as indeed electrons leading to a smaller uncertainty at high mass.

The multijet systematic uncertainty is strongly correlated with the data statistical uncertainty. This is unsurprising given how dependent the template method is on having a large sample of data with which to work. In the extremal invariant mass bins, $M_{ee} \in [46, 66]$ and $[150, 200]$ GeV, and rapidity bins, $|y_{ee}| \in [2.0, 2.2]$ and $[2.2, 2.4]$, where data statistics are low, the multijet systematic is a dominant uncertainty.

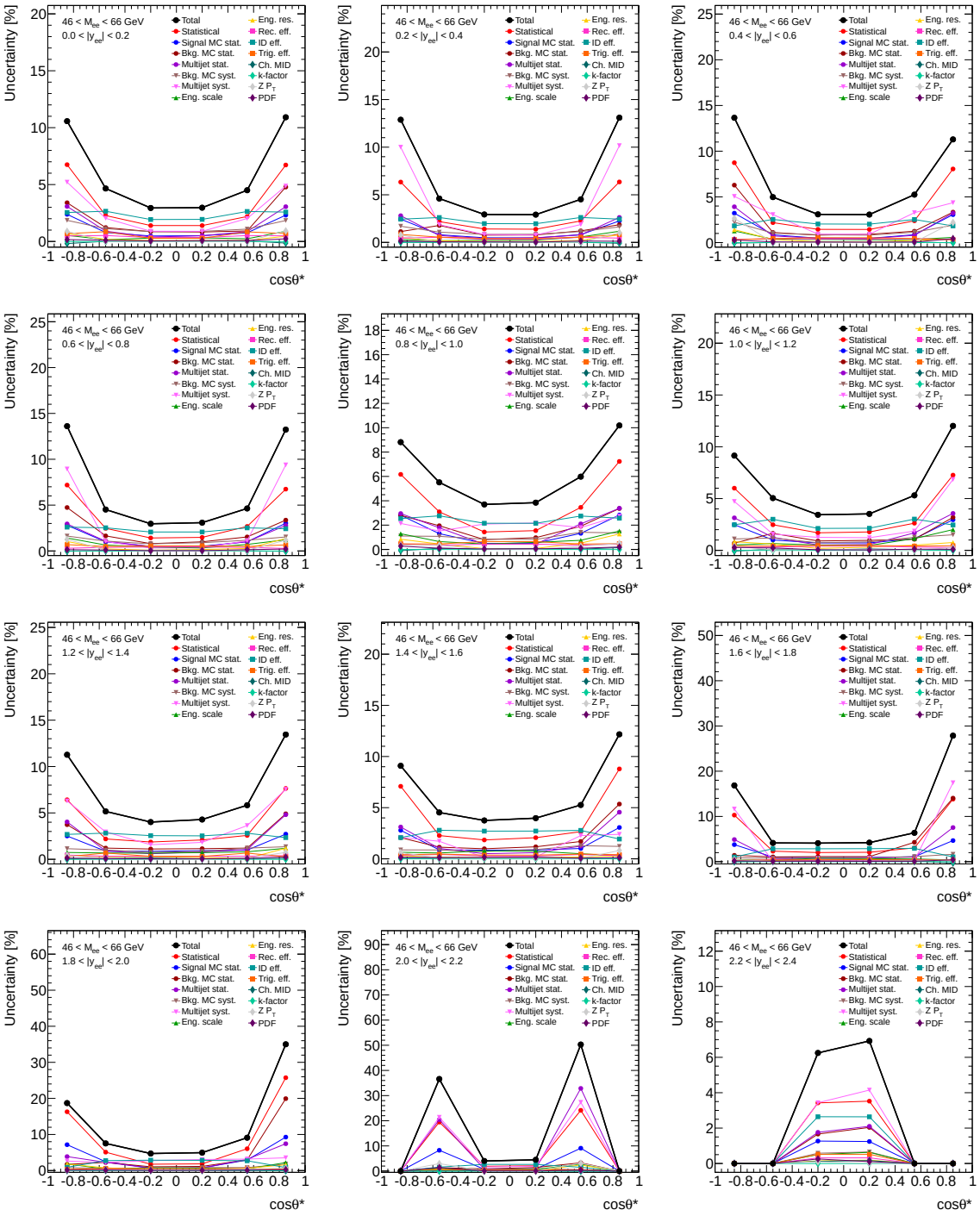

Figure 8.2: Uncertainties propagated to $\frac{d^3\sigma}{dM_{ee}d|y_{ee}|d\cos\theta^*}$ for invariant mass bin $M_{ee} \in [46, 66]$ GeV and for the entire rapidity range of interest, $0.0 < |y_{ee}| < 2.4$.

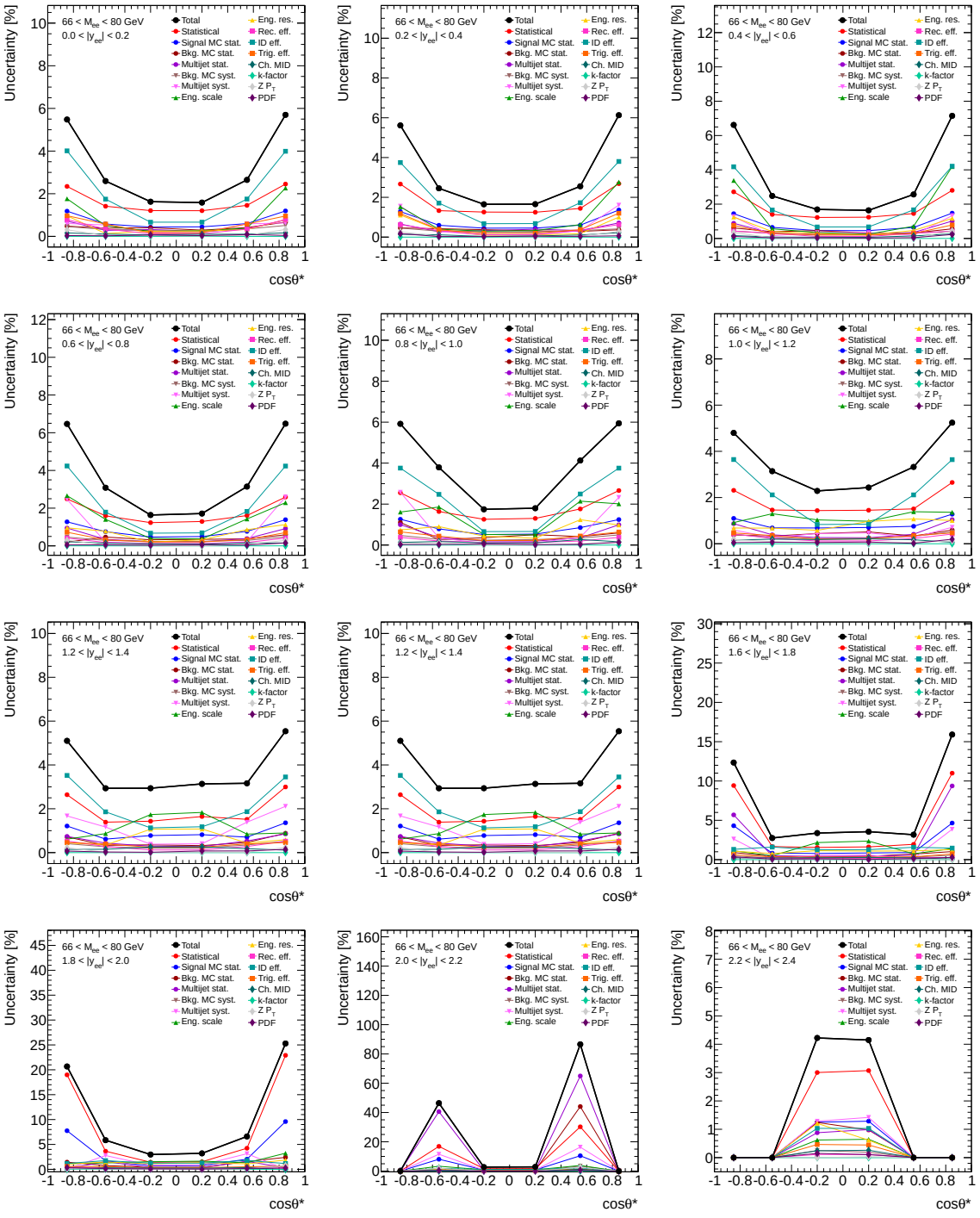

Figure 8.3: Uncertainties propagated to $\frac{d^3\sigma}{dM_{ee}d|y_{ee}|d\cos\theta^*}$ for invariant mass bin $M_{ee} \in [66, 80]$ GeV and for the entire rapidity range of interest, $0.0 < |y_{ee}| < 2.4$.

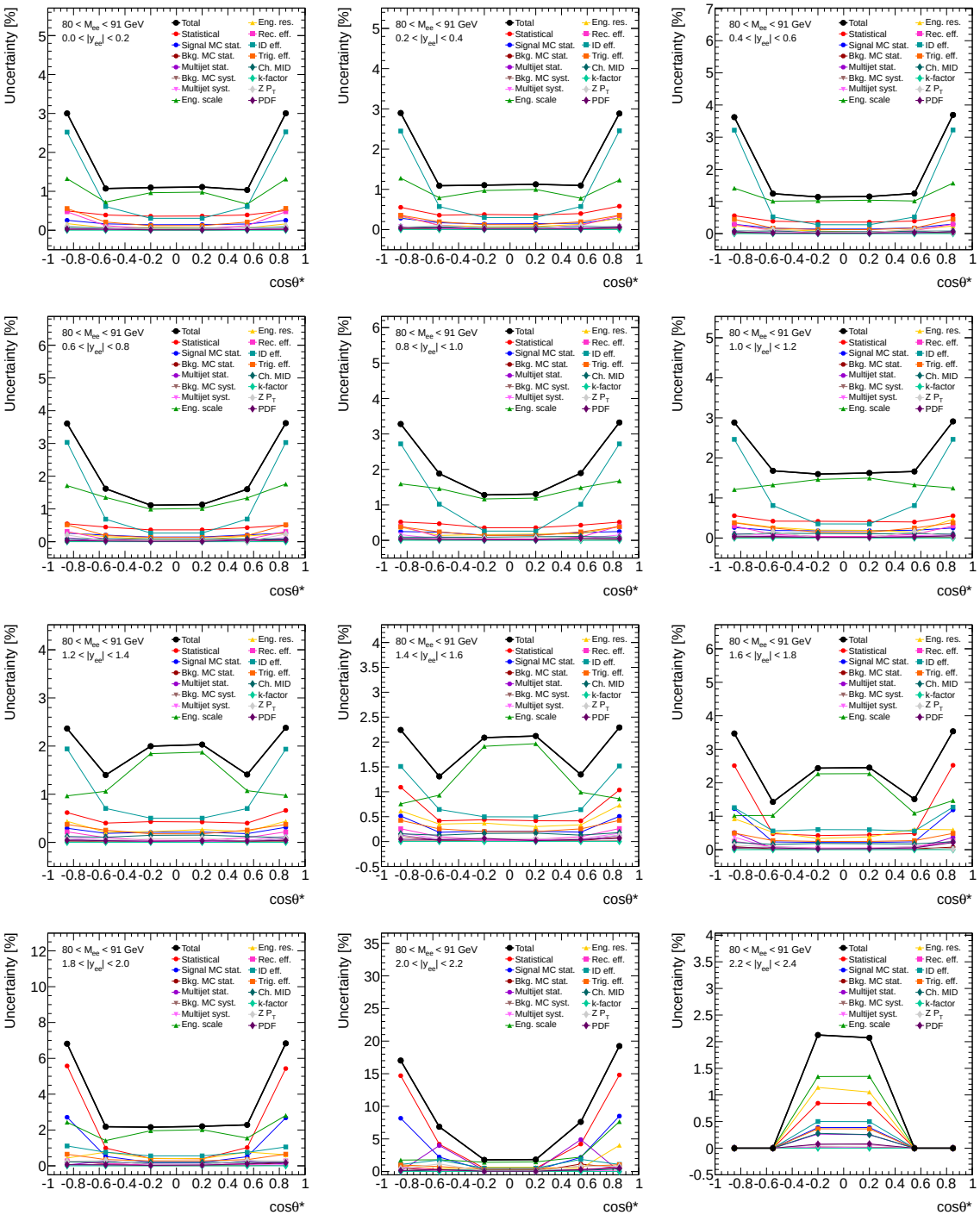

Figure 8.4: Uncertainties propagated to $\frac{d^3\sigma}{dM_{ee}d|y_{ee}|d\cos\theta^*}$ for invariant mass bin $M_{ee} \in [80, 91]$ GeV and for the entire rapidity range of interest, $0.0 < |y_{ee}| < 2.4$.

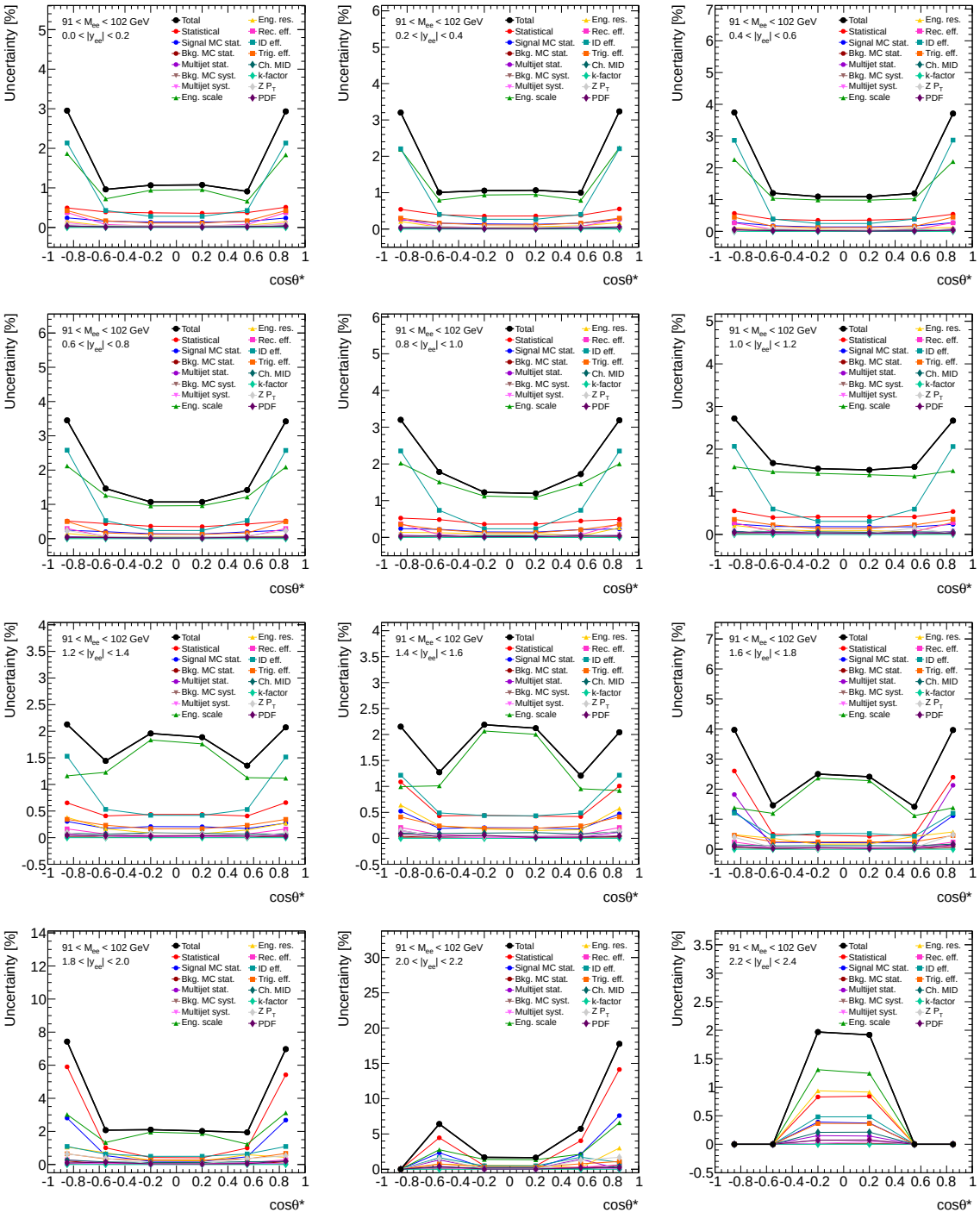

Figure 8.5: Uncertainties propagated to $\frac{d^3\sigma}{dM_{ee}d|y_{ee}|d\cos\theta^*}$ for invariant mass bin $M_{ee} \in [91, 102]$ GeV and for the entire rapidity range of interest, $0.0 < |y_{ee}| < 2.4$.

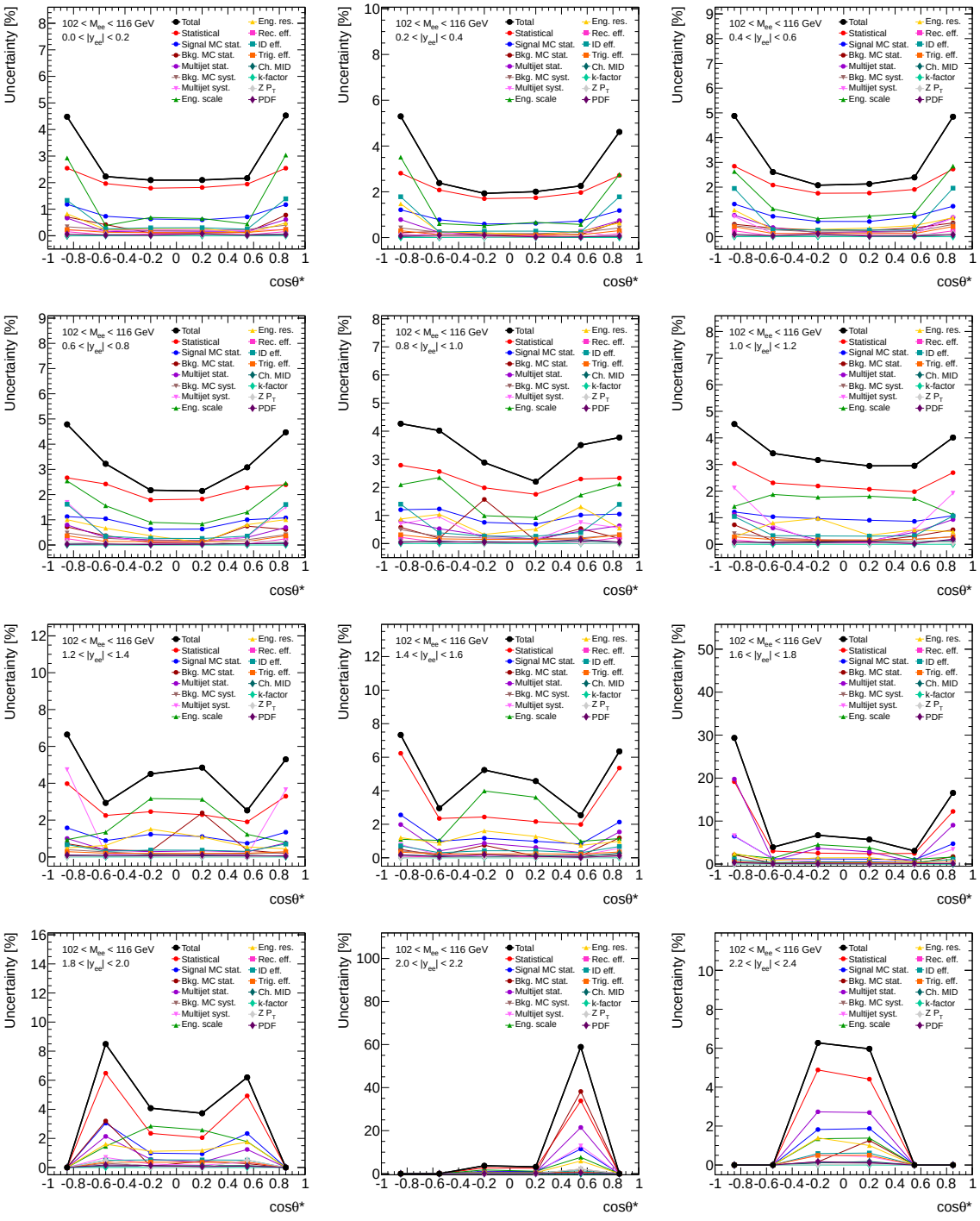

Figure 8.6: Uncertainties propagated to $\frac{d^3\sigma}{dM_{ee}d|y_{ee}|d\cos\theta^*}$ for invariant mass bin $M_{ee} \in [102, 116]$ GeV and for the entire rapidity range of interest, $0.0 < |y_{ee}| < 2.4$.

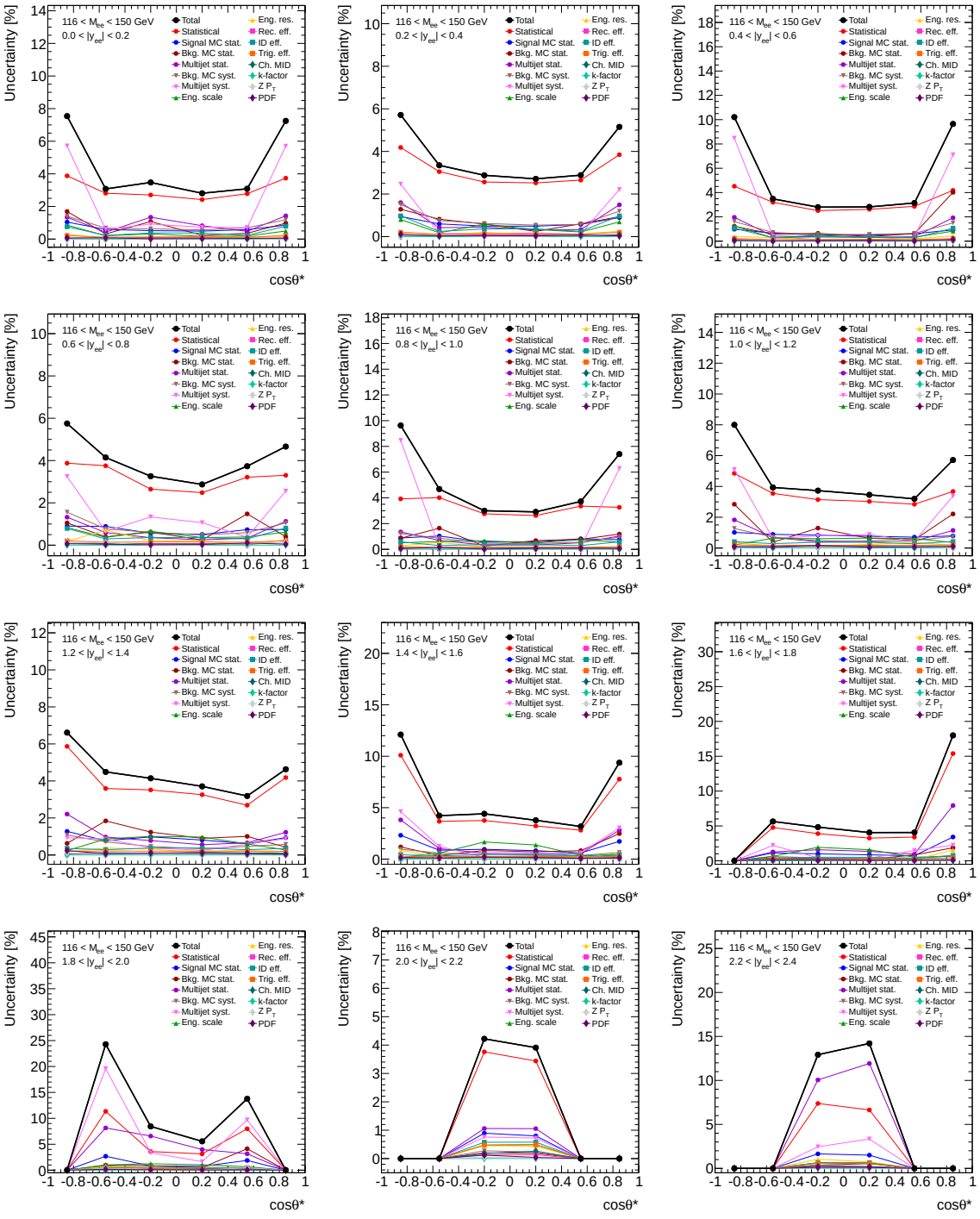

Figure 8.7: Uncertainties propagated to $\frac{d^3\sigma}{dM_{ee}d|y_{ee}|d\cos\theta^*}$ for invariant mass bin $M_{ee} \in [116, 150]$ GeV and for the entire rapidity range of interest, $0.0 < |y_{ee}| < 2.4$.

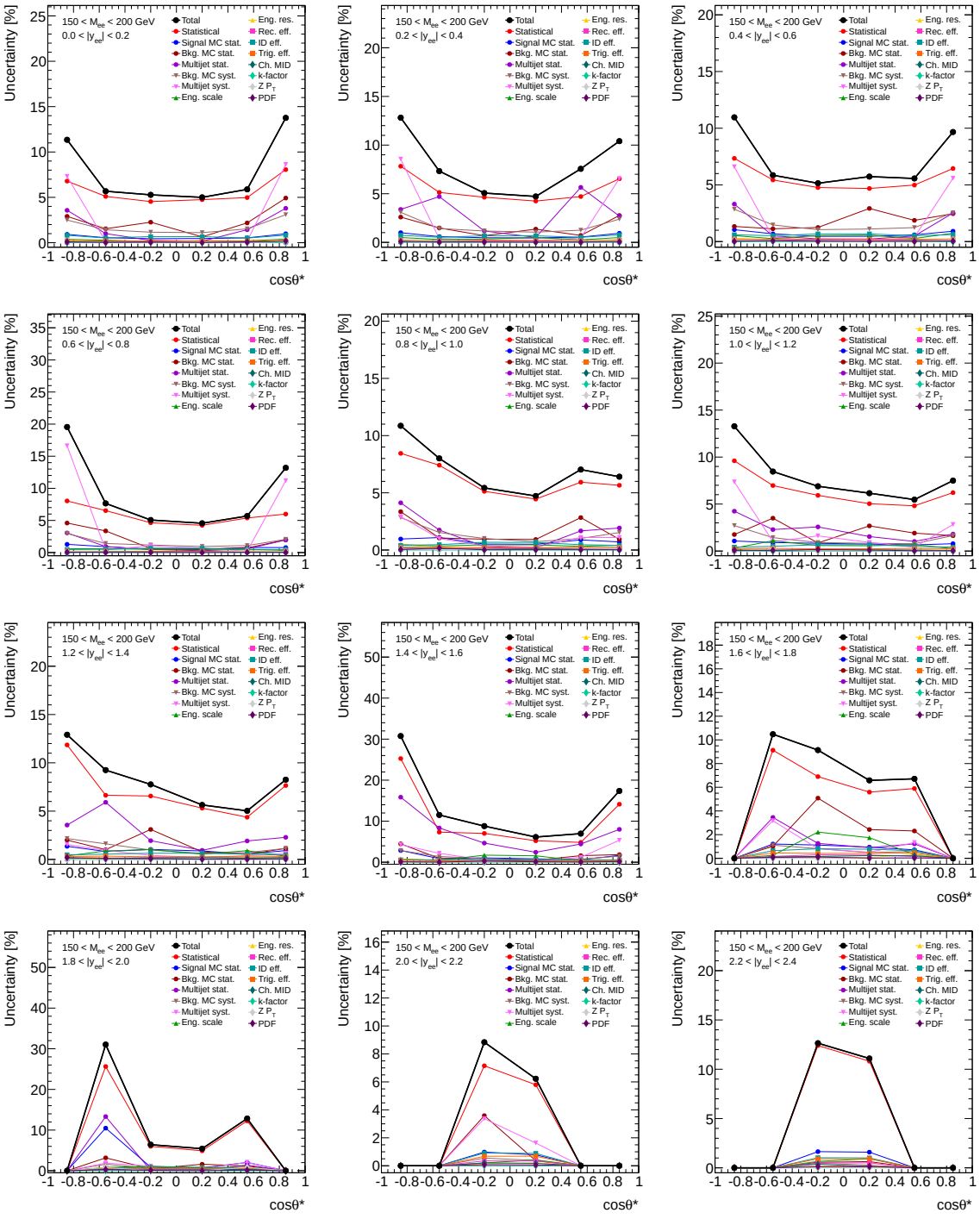

Figure 8.8: Uncertainties propagated to $\frac{d^3\sigma}{dM_{ee}d|y_{ee}|d\cos\theta^*}$ for invariant mass bin $M_{ee} \in [150, 200]$ GeV and for the entire rapidity range of interest, $0.0 < |y_{ee}| < 2.4$.

Chapter 9

Results

In this chapter, the three-dimensional differential cross-section result is presented and compared to a theoretical prediction produced using the POWHEG signal Monte Carlo. The cross-section measurement is then used to calculate the forward-backward asymmetry in bins of M_{ee} and $|y_{ee}|$ and again, the result is compared to the signal MC prediction. Finally, using the MCFM program, cross-section calculations are produced with several different parton distribution functions and values of the weak mixing angle θ_{W}. These theoretical calculations are compared with the cross-section and asymmetry measurements.

9.1 Differential Cross-Section Measurement

Expressed as a mathematical equation in Equation (2.36) and described as a measurement in Equation (6.1), the differential cross-section of interest is

$$\frac{d^3\sigma}{dM_{ee}d|y_{ee}|d\cos\theta^*},$$

at Born-level and in a fiducial volume defined by the following kinematic requirements on the dielectron invariant mass and electron pseudorapidity and transverse momentum:

$$46 < M_{ee} < 200 \text{ GeV}, \quad |\eta^e| < 2.4, \quad p_T^e > 20 \text{ GeV}.$$

The measurement of this differential cross-section has been made and its uncertainties evaluated as detailed in the previous chapters. In Figures 9.1 to 9.7 are the measured cross-section values for every three-dimensional bin of this analysis save for those that

have been rejected due to a lack of expected signal (see Section 6.1.1). Figure 9.1 corresponds to invariant mass bin $M_{ee} \in [46, 66]$ GeV, Figure 9.2 to $M_{ee} \in [66, 80]$ GeV, and so on. In each figure, there are twelve plots corresponding to the twelve $|y_{ee}|$ bins. The measurement is presented in bins of $\cos\theta^*$ which is the dimension that illustrates the forward-backward asymmetric behaviour of Drell-Yan events. For each estimated cross-section value, its statistical and total uncertainties and a theoretical prediction at NNLO in QCD and NLO in EW generated with POWHEG are also shown. In each plot is a lower panel where the ratio of prediction to data is drawn. The error bars on the ratio correspond to the statistical uncertainty of the data and the prediction, added in quadrature, while the error band represents the total measurement uncertainty symmetrized about unity.

The asymmetry of Drell-Yan events is clearly visible in these figures which show an imbalance between the cross-sections of forward ($\cos\theta^* > 0$) and backward ($\cos\theta^* < 0$) events. The amount of asymmetry varies from M_{ee} bin to M_{ee} bin and in general increases as $|y_{ee}|$ increases. The reasons for this behaviour will be discussed later on in this chapter, after presenting the forward-backward asymmetry measurement results.

Most analysis bins, in particular those at the Z-peak, show good agreement between data and prediction. This is not unexpected given the level of sophistication of the signal MC. The k-factors used in this analysis enhance the signal MC to include higher order QCD and EW corrections while theoretical systematic uncertainties from the PDFs and the Z transverse momentum shape account for most remaining differences between the data and prediction.

The total uncertainty on the cross-section measurement varies as a function of M_{ee} with the bins at the Z-peak being the most precise. At the peak, where the number of signal events is quite sizable and the background negligible, the total uncertainty ranges from 1 to 5% which is dominated by systematics. In the off-peak regions, the measurement uncertainties are larger ranging between 5 and 15% in most of the analysis bins. This uncertainty is driven by the statistical uncertainty which is the dominant uncertainty for bins at the extremal values of M_{ee} and $|y_{ee}|$. To provide a sense of the magnitudes of the individual uncertainties in different regions of kinematic phase space, Table 9.1 is presented. In this table, six $\cos\theta^*$ distributions of the cross-section in select M_{ee} and $|y_{ee}|$ bins are given with a full breakdown of the uncertainties from all the sources considered. A less detailed table of the results in all 504 analysis bins can be seen in Table A.1 of Appendix A.

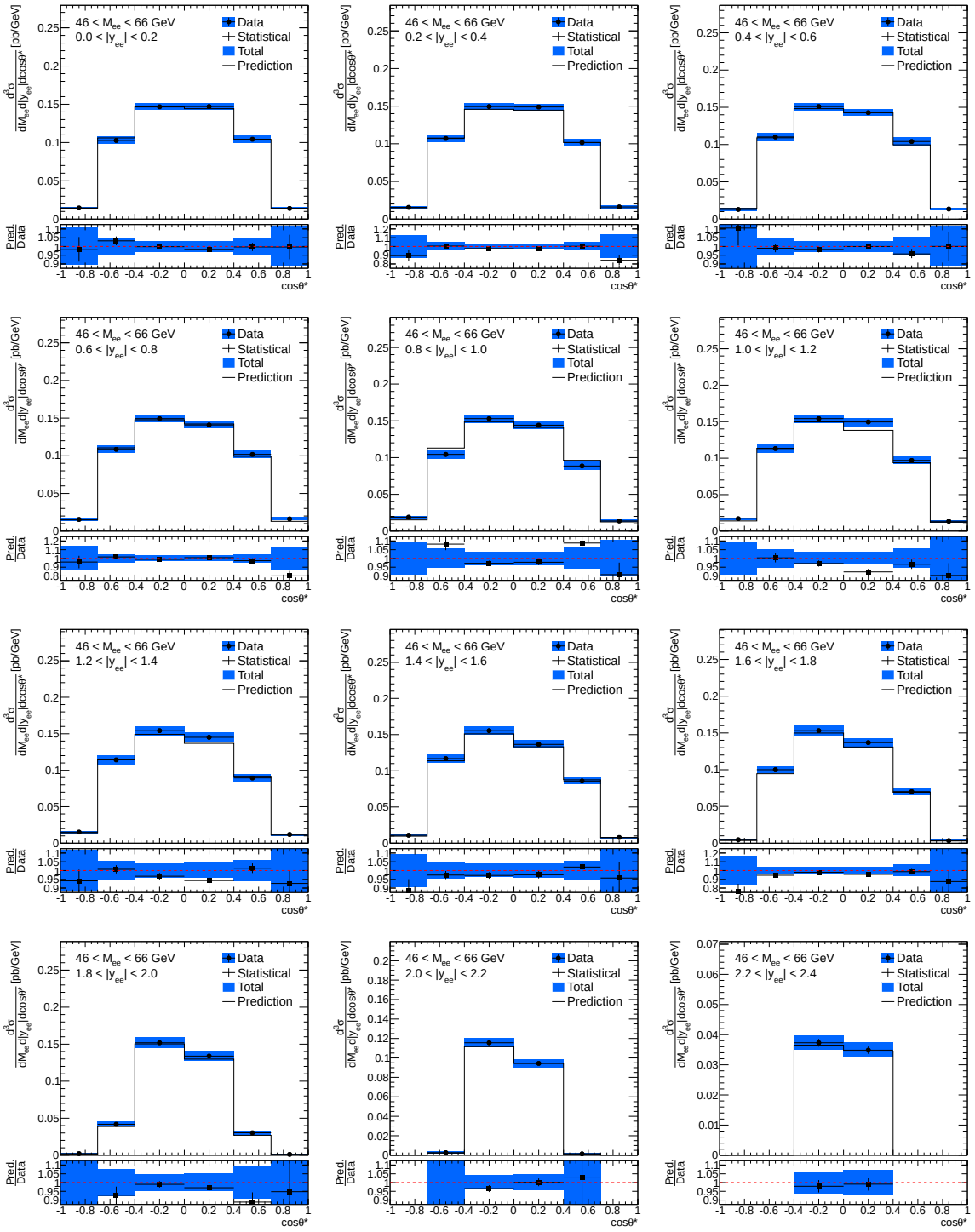

Figure 9.1: Three-dimensional differential cross-section $\frac{d^3\sigma}{dM_{ee}d|y_{ee}|d\cos\theta^*}$ results for invariant mass bin $M_{ee} \in [46, 66]$ GeV and for the entire rapidity range of interest, $0.0 < |y_{ee}| < 2.4$.

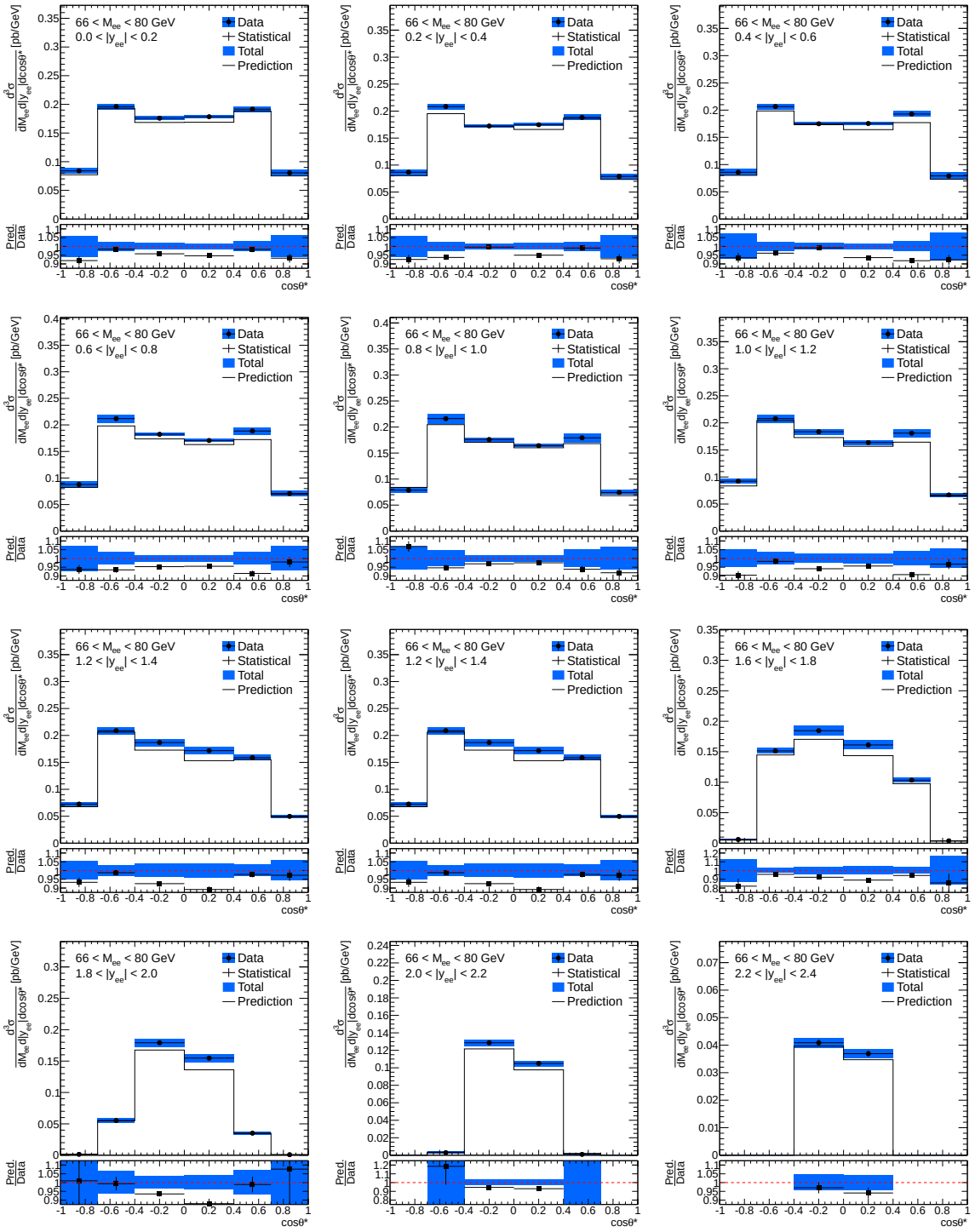

Figure 9.2: Three-dimensional differential cross-section $\frac{d^3\sigma}{dM_{ee}d|y_{ee}|d\cos\theta^*}$ results for invariant mass bin $M_{ee} \in [66, 80]$ GeV and for the entire rapidity range of interest, $0.0 < |y_{ee}| < 2.4$.

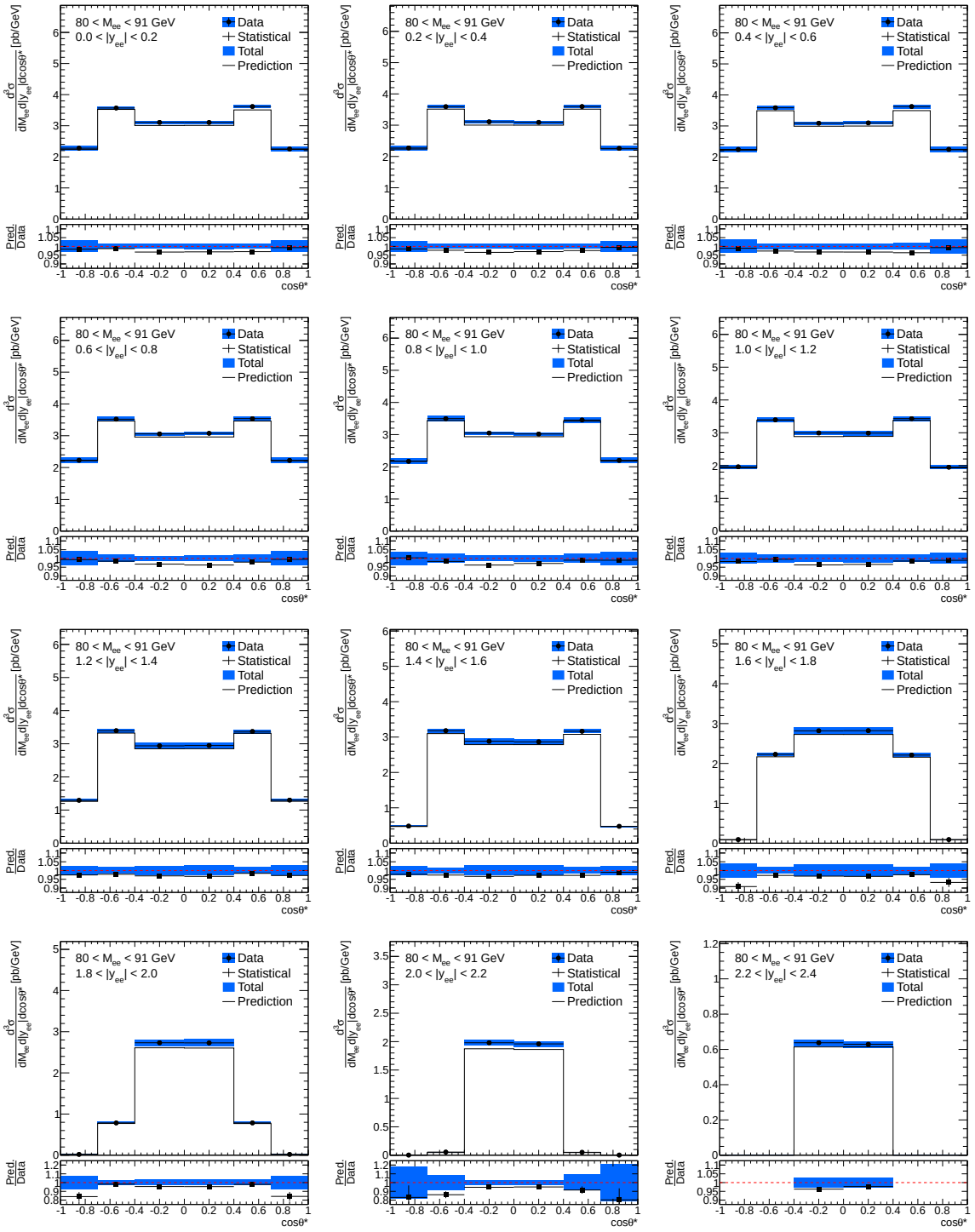

Figure 9.3: Three-dimensional differential cross-section $\frac{d^3\sigma}{dM_{ee}d|y_{ee}|d\cos\theta^*}$ results for invariant mass bin $M_{ee} \in [80, 91]$ GeV and for the entire rapidity range of interest, $0.0 < |y_{ee}| < 2.4$.

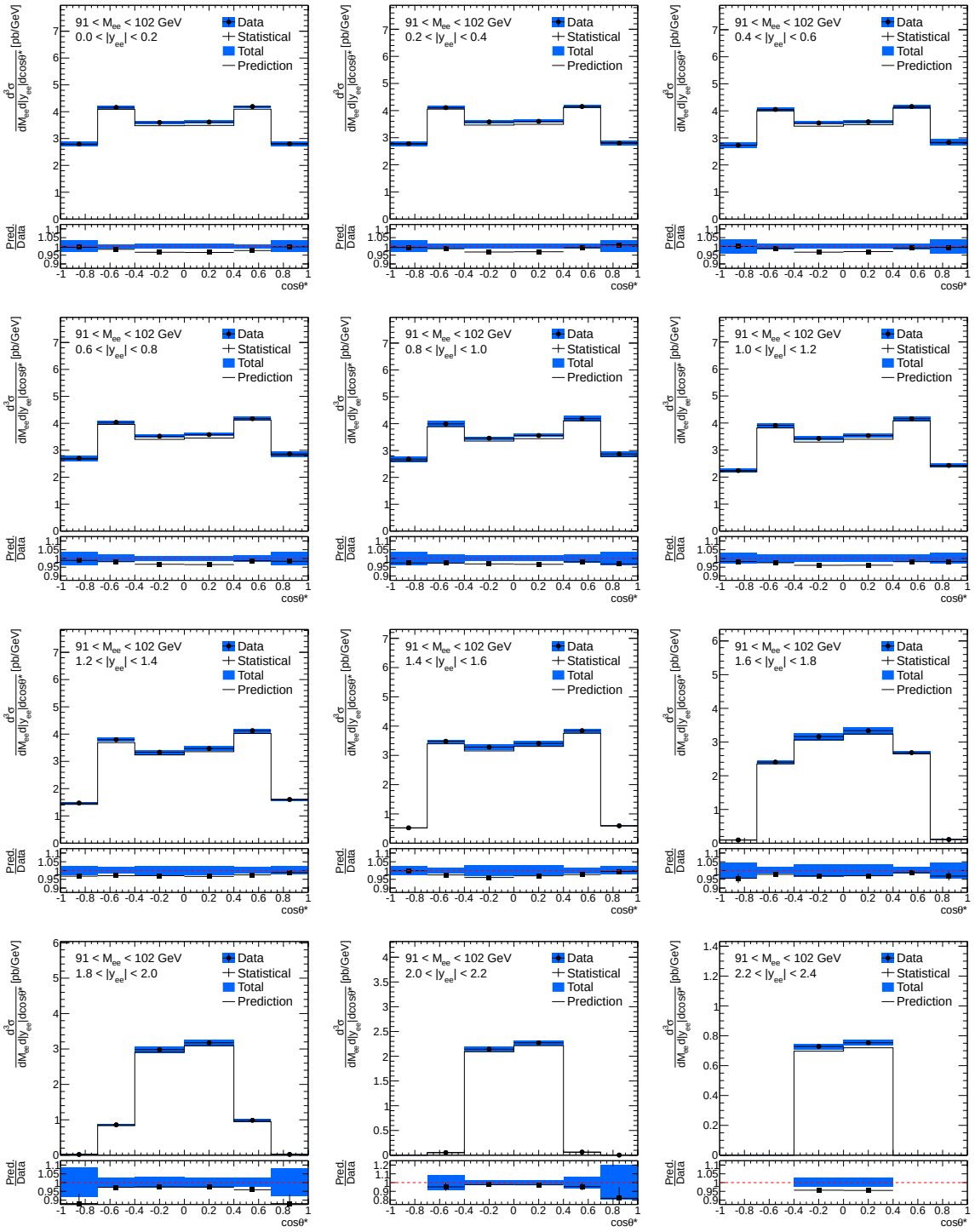

Figure 9.4: Three-dimensional differential cross-section $\frac{d^3\sigma}{dM_{ee}d|y_{ee}|d\cos\theta^*}$ results for invariant mass bin $M_{ee} \in [91, 102]$ GeV and for the entire rapidity range of interest, $0.0 < |y_{ee}| < 2.4$.

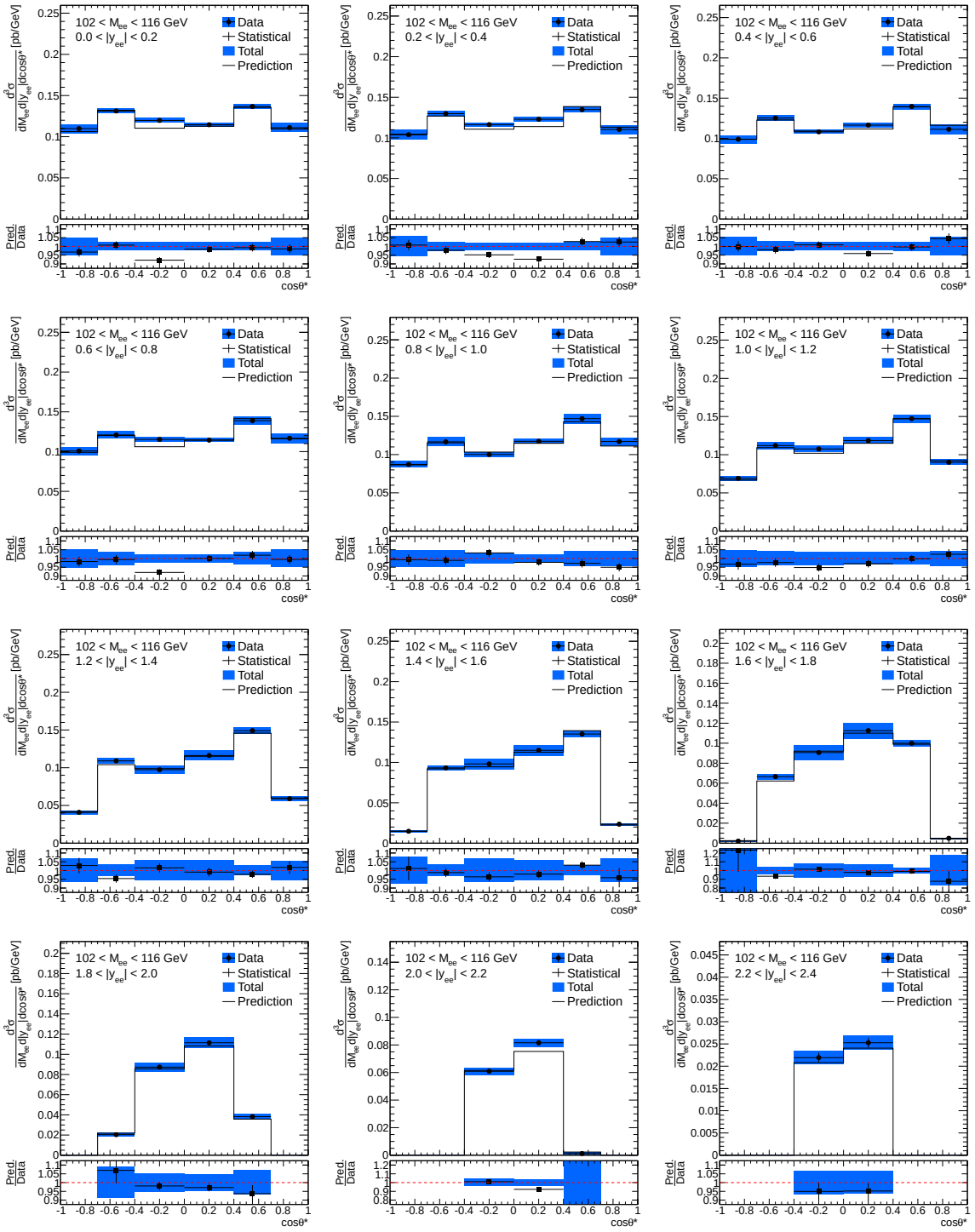

Figure 9.5: Three-dimensional differential cross-section $\frac{d^3\sigma}{dM_{ee}d|y_{ee}|d\cos\theta^*}$ results for invariant mass bin $M_{ee} \in [102, 116]$ GeV and for the entire rapidity range of interest, $0.0 < |y_{ee}| < 2.4$.

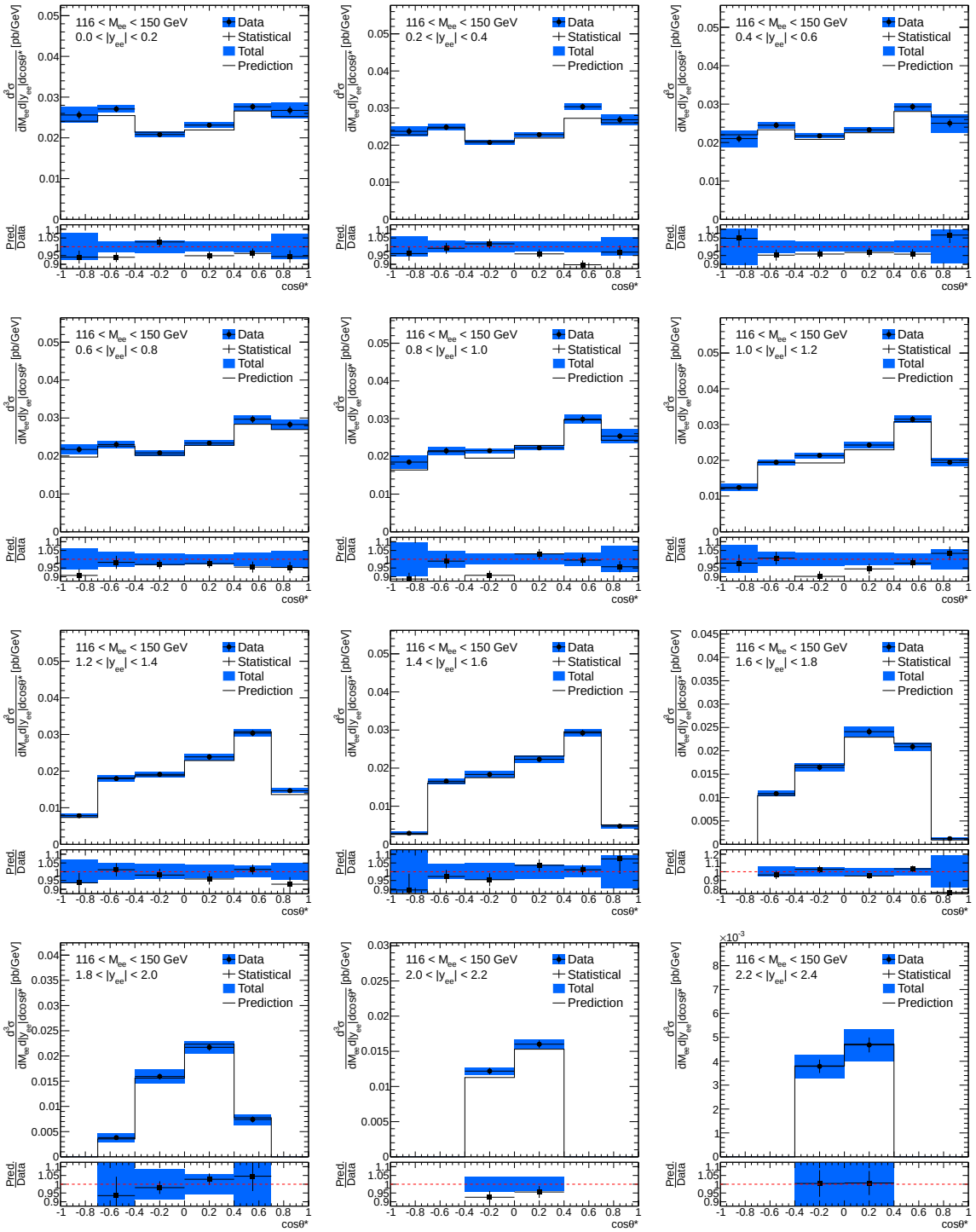

Figure 9.6: Three-dimensional differential cross-section $\frac{d^3\sigma}{dM_{ee}d|y_{ee}|d\cos\theta^*}$ results for invariant mass bin $M_{ee} \in [116, 150]$ GeV and for the entire rapidity range of interest, $0.0 < |y_{ee}| < 2.4$.

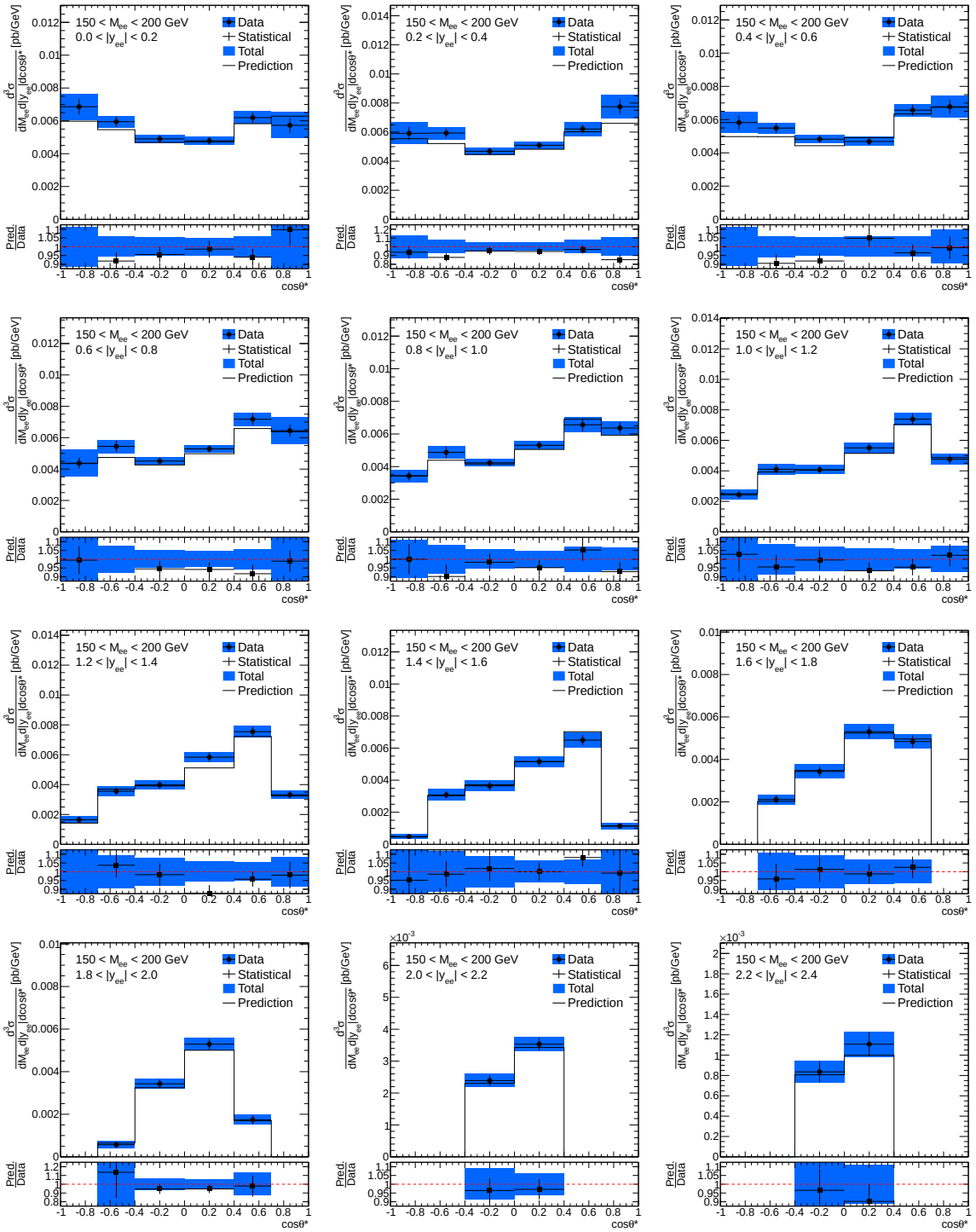

Figure 9.7: Three-dimensional differential cross-section $\frac{d^3\sigma}{dM_{ee}d|y_{ee}|d\cos\theta^*}$ results for invariant mass bin $M_{ee} \in [150, 200]$ GeV and for the entire rapidity range of interest, $0.0 < |y_{ee}| < 2.4$.

Bin	M_{ee} [GeV]	$\lvert y_{ee}\rvert$	$\cos\theta^*$	σ [pb/GeV]	$\delta^{\text{stat}}_{\text{unc}}$ [%]	$\delta^{\text{sig}}_{\text{unc}}$ [%]	$\delta^{\text{bkg}}_{\text{unc}}$ [%]	$\delta^{\text{mj}}_{\text{unc}}$ [%]	$\delta^{\text{bkg}}_{\text{cor}}$ [%]	$\delta^{\text{mj}}_{\text{cor}}$ [%]	$\delta^{\text{scale}}_{\text{cor}}$ [%]	$\delta^{\text{res}}_{\text{cor}}$ [%]	$\delta^{\text{rec}}_{\text{cor}}$ [%]	$\delta^{\text{id}}_{\text{cor}}$ [%]	$\delta^{\text{trig}}_{\text{cor}}$ [%]	$\delta^{\text{chmid}}_{\text{cor}}$ [%]	$\delta^{\text{kfac}}_{\text{cor}}$ [%]	$\delta^{\text{zpt}}_{\text{cor}}$ [%]	$\delta^{\text{pdf}}_{\text{cor}}$ [%]	δ^{tot} [%]
1	46, 66	0.0, 0.2	−1.0, −0.7	1.45×10^{-2}	6.7	2.4	3.4	3.1	1.9	5.2	0.5	0.7	0.5	2.5	0.7	0.2	0.0	0.9	0.2	10.6
2	46, 66	0.0, 0.2	−0.7, −0.4	1.03×10^{-1}	2.3	0.8	1.2	0.9	1.1	2.0	0.2	0.2	0.5	2.7	0.9	0.0	0.0	0.0	0.1	4.7
3	46, 66	0.0, 0.2	−0.4, 0.0	1.47×10^{-1}	1.4	0.5	0.9	0.4	0.9	0.9	0.3	0.1	0.3	1.9	0.3	0.0	0.0	0.0	0.0	2.9
4	46, 66	0.0, 0.2	0.0, +0.4	1.47×10^{-1}	1.4	0.5	0.8	0.5	0.9	0.9	0.3	0.1	0.3	1.9	0.3	0.0	0.0	0.0	0.1	3.0
5	46, 66	0.0, 0.2	+0.4, +0.7	1.04×10^{-1}	2.2	0.8	0.9	0.9	1.1	2.0	0.2	0.1	0.5	2.6	0.8	0.0	0.0	0.0	0.1	4.5
6	46, 66	0.0, 0.2	+0.7, +1.0	1.40×10^{-2}	6.7	2.3	4.8	3.1	1.8	4.9	0.9	0.5	0.5	2.6	0.7	0.1	0.0	0.9	0.2	10.9
85	66, 80	0.4, 0.6	−1.0, −0.7	8.58×10^{-2}	2.7	1.4	0.6	0.9	0.4	1.3	3.4	1.2	0.4	4.2	0.8	0.2	0.0	0.3	0.1	6.6
86	66, 80	0.4, 0.6	−0.7, −0.4	2.07×10^{-1}	1.4	0.6	0.4	0.3	0.3	0.2	0.6	0.4	0.3	1.7	0.3	0.1	0.0	0.0	0.0	2.5
87	66, 80	0.4, 0.6	−0.4, 0.0	1.75×10^{-1}	1.2	0.5	0.5	0.2	0.3	0.3	0.3	0.3	0.1	0.7	0.2	0.1	0.0	0.0	0.0	1.7
88	66, 80	0.4, 0.6	0.0, +0.4	1.75×10^{-1}	1.2	0.5	0.3	0.2	0.2	0.3	0.3	0.2	0.1	0.7	0.2	0.1	0.0	0.0	0.0	1.6
89	66, 80	0.4, 0.6	+0.4, +0.7	1.93×10^{-1}	1.5	0.6	0.3	0.3	0.3	0.2	0.7	0.5	0.3	1.7	0.3	0.1	0.0	0.0	0.0	2.6
90	66, 80	0.4, 0.6	+0.7, +1.0	7.92×10^{-2}	2.8	1.5	0.6	1.0	0.4	1.3	4.2	1.2	0.4	4.2	0.8	0.3	0.0	0.4	0.2	7.1
175	80, 91	1.0, 1.2	−1.0, −0.7	1.96	0.6	0.3	0.0	0.1	0.0	0.1	1.2	0.4	0.3	2.5	0.4	0.1	0.0	0.0	0.0	2.9
176	80, 91	1.0, 1.2	−0.7, −0.4	3.39	0.4	0.2	0.0	0.0	0.0	0.1	1.3	0.3	0.1	0.8	0.3	0.1	0.0	0.2	0.0	1.7
177	80, 91	1.0, 1.2	−0.4, 0.0	2.99	0.4	0.2	0.0	0.0	0.0	0.0	1.5	0.2	0.0	0.4	0.1	0.1	0.0	0.0	0.0	1.6
178	80, 91	1.0, 1.2	0.0, +0.4	2.99	0.4	0.2	0.0	0.0	0.0	0.0	1.5	0.2	0.0	0.4	0.1	0.1	0.0	0.0	0.0	1.6
179	80, 91	1.0, 1.2	+0.4, +0.7	3.43	0.4	0.2	0.0	0.0	0.0	0.1	1.3	0.1	0.1	0.8	0.3	0.1	0.0	0.2	0.0	1.7
180	80, 91	1.0, 1.2	+0.7, +1.0	1.95	0.6	0.3	0.0	0.1	0.0	0.1	1.2	0.5	0.3	2.5	0.4	0.1	0.0	0.0	0.1	2.9
271	91, 102	1.8, 2.0	−1.0, −0.7	2.10×10^{-2}	5.9	2.8	0.2	0.0	0.1	0.0	3.0	1.1	0.3	1.1	0.6	0.3	0.0	0.6	0.1	7.4
272	91, 102	1.8, 2.0	−0.7, −0.4	8.59×10^{-1}	1.0	0.5	0.0	0.1	0.0	0.1	1.3	0.7	0.1	0.6	0.3	0.2	0.0	0.4	0.1	2.1
273	91, 102	1.8, 2.0	−0.4, 0.0	2.98	0.4	0.2	0.0	0.0	0.0	0.0	2.0	0.3	0.0	0.5	0.3	0.1	0.0	0.0	0.0	2.1
274	91, 102	1.8, 2.0	0.0, +0.4	3.18	0.4	0.2	0.0	0.0	0.0	0.0	1.9	0.2	0.0	0.5	0.3	0.1	0.0	0.0	0.0	2.0
275	91, 102	1.8, 2.0	+0.4, +0.7	9.86×10^{-1}	1.0	0.5	0.0	0.1	0.0	0.0	1.2	0.6	0.1	0.6	0.3	0.2	0.0	0.4	0.1	1.9
276	91, 102	1.8, 2.0	+0.7, +1.0	2.36×10^{-2}	5.4	2.7	0.2	0.0	0.0	0.0	3.1	0.4	0.3	1.1	0.7	0.2	0.0	0.5	0.2	7.0
313	102, 116	0.8, 1.0	−1.0, −0.7	8.71×10^{-2}	2.8	1.2	0.6	0.8	0.5	0.7	2.1	0.9	0.2	1.4	0.3	0.1	0.0	0.1	0.0	4.3
314	102, 116	0.8, 1.0	−0.7, −0.4	1.17×10^{-1}	2.6	1.2	0.2	0.5	0.2	0.9	2.3	1.0	0.0	0.4	0.2	0.0	0.0	0.1	0.1	4.0
315	102, 116	0.8, 1.0	−0.4, 0.0	1.00×10^{-1}	2.0	0.8	1.6	0.3	0.2	0.2	1.0	0.3	0.1	0.3	0.1	0.1	0.0	0.0	0.0	2.9
316	102, 116	0.8, 1.0	0.0, +0.4	1.17×10^{-1}	1.8	0.7	0.1	0.2	0.2	0.1	0.9	0.5	0.1	0.3	0.1	0.0	0.0	0.1	0.1	2.2
317	102, 116	0.8, 1.0	+0.4, +0.7	1.47×10^{-1}	2.3	1.0	0.5	0.4	0.2	0.7	1.7	1.3	0.0	0.4	0.2	0.1	0.0	0.0	0.1	3.5
318	102, 116	0.8, 1.0	+0.7, +1.0	1.17×10^{-1}	2.3	1.0	0.2	0.6	0.3	0.6	2.1	0.6	0.2	1.4	0.3	0.0	0.0	0.0	0.1	3.8
391	116, 150	1.0, 1.2	−1.0, −0.7	1.24×10^{-2}	4.8	1.0	2.8	1.8	1.3	5.1	0.2	0.4	0.1	0.4	0.2	0.1	0.0	0.0	0.1	8.0
392	116, 150	1.0, 1.2	−0.7, −0.4	1.94×10^{-2}	3.5	0.9	0.4	0.7	0.7	0.6	0.6	0.1	0.1	0.3	0.2	0.1	0.0	0.2	0.1	3.9
393	116, 150	1.0, 1.2	−0.4, 0.0	2.14×10^{-2}	3.1	0.8	1.3	0.4	0.5	0.8	0.6	0.1	0.1	0.4	0.2	0.1	0.0	0.0	0.2	3.7
394	116, 150	1.0, 1.2	0.0, +0.4	2.43×10^{-2}	3.0	0.8	0.6	0.5	0.4	0.9	0.6	0.2	0.1	0.4	0.2	0.1	0.0	0.1	0.0	3.5
395	116, 150	1.0, 1.2	+0.4, +0.7	3.15×10^{-2}	2.8	0.7	0.5	0.5	0.5	0.4	0.6	0.4	0.1	0.3	0.2	0.1	0.0	0.1	0.1	3.2
396	116, 150	1.0, 1.2	+0.7, +1.0	1.94×10^{-2}	3.7	0.8	2.2	1.1	0.8	3.4	0.4	0.2	0.1	0.4	0.2	0.1	0.0	0.0	0.1	5.7
463	150, 200	1.0, 1.2	−1.0, −0.7	2.43×10^{-3}	9.6	1.1	1.8	4.2	2.7	7.4	0.3	0.2	0.1	0.4	0.3	0.1	0.0	0.0	0.1	13.3
464	150, 200	1.0, 1.2	−0.7, −0.4	4.11×10^{-3}	7.0	0.9	3.5	2.3	1.4	1.0	1.1	0.2	0.1	0.5	0.3	0.0	0.0	0.2	0.1	8.5
465	150, 200	1.0, 1.2	−0.4, 0.0	4.07×10^{-3}	5.9	0.8	0.9	2.6	0.9	1.6	0.6	0.1	0.2	0.7	0.2	0.1	0.0	0.0	0.2	6.9
466	150, 200	1.0, 1.2	0.0, +0.4	5.51×10^{-3}	5.0	0.7	2.7	1.5	0.8	0.9	0.6	0.1	0.2	0.7	0.2	0.1	0.0	0.1	0.1	6.2
467	150, 200	1.0, 1.2	+0.4, +0.7	7.39×10^{-3}	4.8	0.7	1.9	1.0	0.8	0.4	0.7	0.2	0.1	0.5	0.3	0.1	0.0	0.1	0.0	5.5
468	150, 200	1.0, 1.2	+0.7, +1.0	4.76×10^{-3}	6.2	0.8	1.6	1.8	1.6	2.8	0.3	0.2	0.1	0.4	0.3	0.0	0.0	0.1	0.0	7.5

Table 9.1: A selection of the three-dimensional differential cross-section results tabulated for several illustrative analysis bins. The results are at Born-level and all uncertainties are in units of percent.

9.2 Forward-Backward Asymmetry

Forward-backward asymmetry is measured in bins of M_{ee} and $|y_{ee}|$ using the triple-differential cross-section measurement. It is defined as

$$A_{\mathrm{FB}} = \frac{\sum_{i=1}^{3} \frac{d^3\sigma_i}{dM_{ee}d|y_{ee}|d\cos\theta^*} - \sum_{j=1}^{3} \frac{d^3\sigma_j}{dM_{ee}d|y_{ee}|d\cos\theta^*}}{\sum_{i=1}^{3} \frac{d^3\sigma_i}{dM_{ee}d|y_{ee}|d\cos\theta^*} + \sum_{j=1}^{3} \frac{d^3\sigma_j}{dM_{ee}d|y_{ee}|d\cos\theta^*}}, \tag{9.1}$$

where index i runs over the positive, $\cos\theta^* \in [0.0, 0.4]$, $[0.4, 0.7]$, and $[0.7, 1.0]$, and index j runs over the negative, $\cos\theta^* \in [0.0, -0.4]$, $[-0.4, -0.7]$, and $[-0.7, -1.0]$, $\cos\theta^*$ bins.

The cross-section uncertainties are propagated to A_{FB} source by source with correlated and uncorrelated sources being treated differently. To simplify the notation, let $\sigma = \frac{d^3\sigma}{dM_{ee}d|y_{ee}|d\cos\theta^*}$. Correlated uncertainties are propagated from the differential cross-section measurement to A_{FB} as

$$\delta^{\mathrm{cor}} = A_{\mathrm{FB}}^{\mathrm{cor}} - A_{\mathrm{FB}}, \tag{9.2}$$

where $A_{\mathrm{FB}}^{\mathrm{cor}}$ is defined as

$$A_{\mathrm{FB}}^{\mathrm{cor}} = \frac{\sum_{i=1}^{3}(\sigma_i + \delta\sigma_i^{\mathrm{cor}}) - \sum_{j=1}^{3}(\sigma_j + \delta\sigma_j^{\mathrm{cor}})}{\sum_{i=1}^{3}(\sigma_i + \delta\sigma_i^{\mathrm{cor}}) + \sum_{j=1}^{3}(\sigma_j + \delta\sigma_j^{\mathrm{cor}})}. \tag{9.3}$$

In other words, for each source of correlated uncertainty $\delta\sigma^{\mathrm{cor}}$, $A_{\mathrm{FB}}^{\mathrm{cor}}$ is calculated by using the nominal three-dimensional cross-section σ shifted by $\delta\sigma^{\mathrm{cor}}$.

For the uncorrelated uncertainties, such as the data statistical uncertainty, the uncertainty is calculated as

$$\delta^{\mathrm{uncor}} = \sqrt{\sum_{i=1}^{3}\left(\frac{dA_{\mathrm{FB}}}{d\sigma_i}\delta\sigma_i^{\mathrm{uncor}}\right)^2 + \sum_{j=1}^{3}\left(\frac{dA_{\mathrm{FB}}}{d\sigma_j}\delta\sigma_j^{\mathrm{uncor}}\right)^2}, \tag{9.4}$$

where $\delta\sigma^{\mathrm{uncor}}$ is the corresponding uncorrelated uncertainty on the cross-section mea-

surement. The derivatives in Equation (9.4) work out to be

$$\frac{dA_{\rm FB}}{d\sigma_i} = 2\frac{\sum_{j=1}^{3}\sigma_j}{\left(\sum_{i=1}^{3}\sigma_i + \sum_{j=1}^{3}\sigma_j\right)^2}, \qquad \frac{dA_{\rm FB}}{d\sigma_j} = -2\frac{\sum_{i=1}^{3}\sigma_i}{\left(\sum_{i=1}^{3}\sigma_i + \sum_{j=1}^{3}\sigma_j\right)^2}. \tag{9.5}$$

The total uncertainty on $A_{\rm FB}$ is simply the correlated and uncorrelated uncertainties added in quadrature:

$$\delta^{\rm tot} = \sqrt{\sum(\delta^{\rm cor})^2 + \sum(\delta^{\rm uncor})^2}. \tag{9.6}$$

The forward-backward asymmetry uncertainty is dominated by the statistical uncertainty from the data. Correlated uncertainties, especially those from the electron energy scale and resolution corrections are significantly reduced when propagating them from the cross-section to the $A_{\rm FB}$ measurement. If a correlated uncertainty does not depend significantly on the sign of $\cos\theta^*$, i.e. $\delta\sigma_i^{\rm cor} \approx \delta\sigma_j^{\rm cor} = \delta\sigma^{\rm cor}$, then Equation (9.2) can be approximated as follows:

$$\begin{aligned}\delta^{\rm cor} &= \frac{\sum_{i=1}^{3}(\sigma_i + \delta\sigma_i^{\rm cor}) - \sum_{j=1}^{3}(\sigma_j + \delta\sigma_j^{\rm cor})}{\sum_{i=1}^{3}(\sigma_i + \delta\sigma_i^{\rm cor}) + \sum_{j=1}^{3}(\sigma_j + \delta\sigma_j^{\rm cor})} - \frac{\sum_{i=1}^{3}\sigma_i - \sum_{j=1}^{3}\sigma_j}{\sum_{i=1}^{3}\sigma_i + \sum_{j=1}^{3}\sigma_j} \\ &\approx \frac{\sum_{i=1}^{3}\sigma_i - \sum_{j=1}^{3}\sigma_j}{\sum_{i=1}^{3}\sigma_i + \sum_{j=1}^{3}\sigma_j + 2\delta\sigma^{\rm cor}} - \frac{\sum_{i=1}^{3}\sigma_i - \sum_{j=1}^{3}\sigma_j}{\sum_{i=1}^{3}\sigma_i + \sum_{j=1}^{3}\sigma_j}.\end{aligned} \tag{9.7}$$

Correlated systematic uncertainties that are symmetric in $\cos\theta^*$ approximately cancel in the difference of ratios. This reduction in uncertainty is particularly significant for the electron energy scale systematic which is one of the dominant uncertainties on the cross-section measurement.

The measured and predicted forward-backward asymmetry can be seen in Figures 9.8 and 9.9 as a function of M_{ee} for each of the twelve $|y_{ee}|$ analysis bins. In the lower panels of the plots, differences between the measurement and prediction are shown. A table of the measured $A_{\rm FB}$ values with the associated statistical, systematic, and total uncertainties is given in Table A.2 of Appendix A. The shape of $A_{\rm FB}$ is consistent with the theory presented in Section 2.3. At low invariant mass, the

Drell-Yan process is mediated primarily by the virtual photon γ^* with non-negligible contributions from Z/γ^* interference which results in forward-backward asymmetry. At the Z-peak, the Drell-Yan process is dominated by Z exchange resulting in negligible forward-backward asymmetry; hence at $M_{ee} \approx M_Z$, the asymmetry is nearly zero. At high mass, interference effects contribute once again leading to large values of A_{FB}. The sign of A_{FB}, which is negative below the peak and positive above, is due to its dependence on $1/(M_{ee}^2 - M_Z^2)$. A dilution effect can be clearly seen in the A_{FB} plot corresponding to the rapidity range $0.0 < |y_{ee}| < 0.2$ where the measured A_{FB} is nearly zero in all mass bins. As $|y_{ee}|$ increases, the measurement becomes increasingly sensitive to A_{FB} effects. This increased sensitivity appears to halt for $2.0 < |y_{ee}| < 2.2$ and $2.2 < |y_{ee}| < 2.4$ which in fact show a decrease in overall A_{FB}. This feature is due to the kinematic cut of $|\eta^e| < 2.4$ applied to the electrons. If this cut were not applied, events with electrons having $|\eta^e| \geq 2.4$ would predominantly fill these two rapidity regions and the general trend of A_{FB} increasing with $|y_{ee}|$ would be preserved.

9.3 Additional Theoretical Predictions

To conclude the analysis, theoretical predictions produced using MCFM (Monte Carlo for FeMtobarn processes) [105] are compared with the differential cross-section and forward-backward asymmetry results. MCFM is a standalone computer program – independent from the ATLAS framework – that is capable of calculating cross-sections of proton-proton collisions to NLO accuracy in QCD. Comparisons between MCFM predictions and the measurement may reveal regions in kinematic phase space where the data can be sufficiently described with only NLO in QCD theoretical predictions.

MCFM allows the user to choose the parton distribution functions used in the calculations. PDF sets CT10, MSTW2008 [106], HERAPDF15 [35], NNPDF23 [107], and ATLAS-epWZ12 [108] are used as inputs to the cross-section calculations. A small subset of the results are plotted in Figure 9.10. For these calculations, the electroweak parameters were set to the values listed in Table 9.2.

In a majority of the analysis bins, the MCFM predictions appear to be consistent with each other implying that the PDF sets used are consistent with one another. As for data comparisons, in the low mass bin $M_{ee} \in [46, 66]$ GeV and in polar angle bins $\cos\theta^* \in [-1, -0.7]$ and $[0.7, 1.0]$, there are large differences between the MCFM predictions and data. At low dielectron mass, $M_{ee} \approx 2\, p_T^e$ implying that the electron

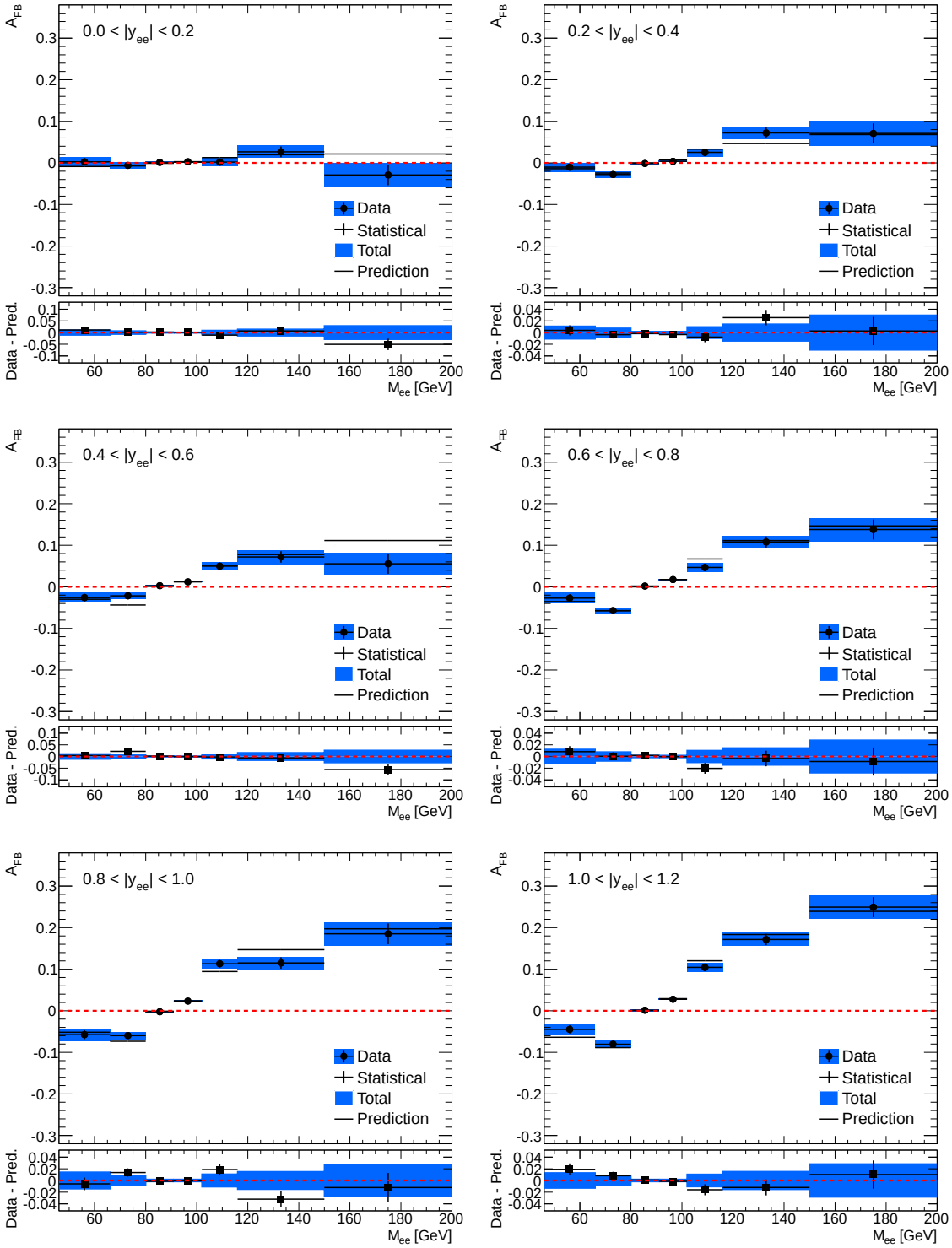

Figure 9.8: Forward-backward asymmetry results plotted as a function of M_{ee} for $0.0 < |y_{ee}| < 1.2$.

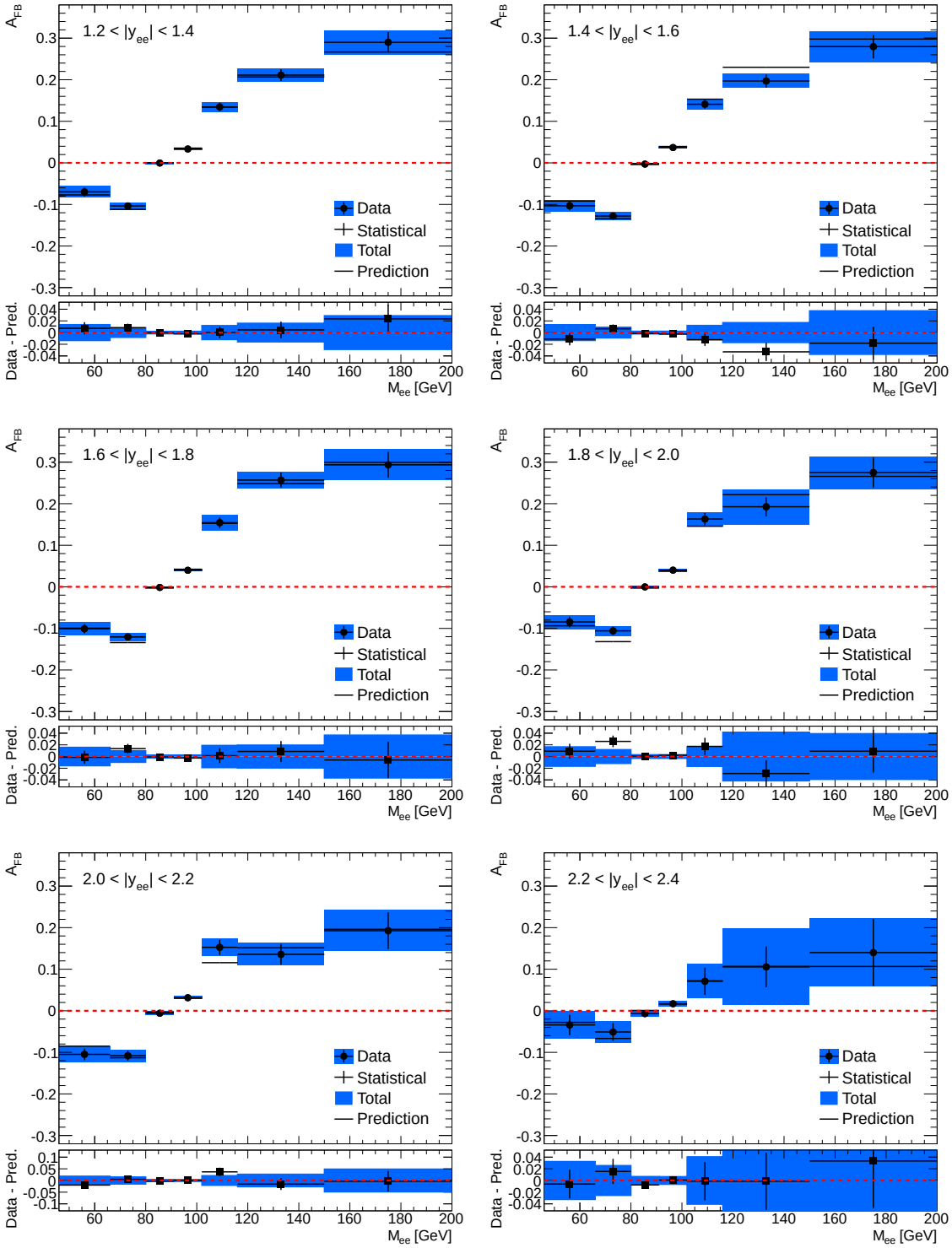

Figure 9.9: Forward-backward asymmetry results plotted as a function of M_{ee} for $1.2 < |y_{ee}| < 2.4$.

and positron are produced back-to-back at LO. Due to this kinematic restriction [109] the first order contribution to the cross-section in this region of phase space is the NLO term. MCFM, which calculates up to NLO, will of course struggle to model what is observed at low mass where the NNLO term plays a bigger role. The signal Monte Carlo, also plotted in Figure 9.10, is NNLO in QCD and NLO in EW hence is able to accurately describe the data at low M_{ee}. These findings are consistent with past analyses [76, 109] which found that at low invariant mass, NNLO QCD calculations provide a significantly better description of the data than NLO predictions. At higher invariant masses, the impact of radiative corrections on the cross-section decreases and as a result, MCFM predictions in general show agreement with the data.

Parameter	Value
Z mass (M_Z)	91.1876 GeV
W mass (M_W)	80.398 GeV
Z decay width (Γ_Z)	2.4952 GeV
W decay width (Γ_W)	2.1054 GeV
top quark mass (m_t)	173.2 GeV
Higgs mass (M_H)	126 GeV
Fermi coupling constant (G_F)	1.16639×10^{-5} GeV^{-2}
Weak mixing angle ($\sin^2\theta_{\mathrm{W}}$)	0.2312

Table 9.2: The MCFM electroweak parameters used in the theory calculations.

Finally, the measured A_{FB} is compared to the MCFM calculations in Figure 9.11 which shows A_{FB} as a function of M_{ee} in 6 of the 12 rapidity bins of this analysis. Note that the CT10 parton distribution functions were used for these predictions. Three sets of MCFM calculations were made for this comparison; in each instance, the value of the weak mixing angle was varied to one of the following values:

$$\sin^2\theta_{\mathrm{W}} = 0.2312, \qquad \sin^2\theta^{-}_{\mathrm{W}} = 0.225, \qquad \sin^2\theta^{+}_{\mathrm{W}} = 0.240.$$

The nominal value of 0.2312 is the default of MCFM which is varied to 0.225 and 0.240 to illustrate the effect θ_{W} has on A_{FB}. Despite their simplicity, the majority of the MCFM predicted values are consistent with the measured ones. While the measured A_{FB} in most M_{ee} bins have sizable uncertainties making them insensitive to small changes in θ_{W}, the same cannot be said for the bins near M_Z. Forward-backward asymmetry measurements in these bins provide the best data for the extraction of a measurement of θ_{W}. Such an extraction is beyond the scope of this dissertation but represents a possible continuation of this analysis.

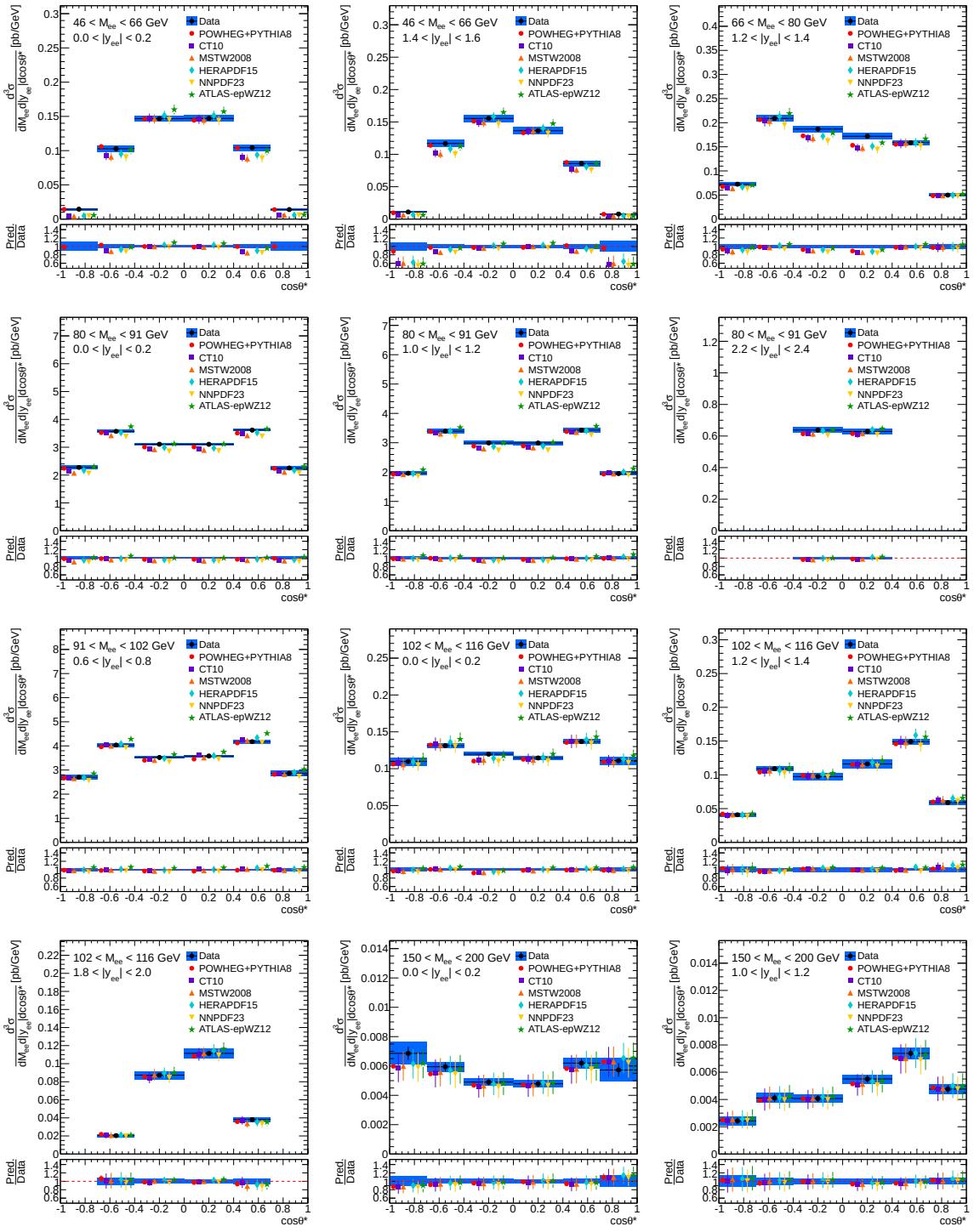

Figure 9.10: Differential cross-section distributions of data and theory predictions. The data is compared with the signal MC (POWHEG+PYTHIA8) and MCFM calculations using several popular PDF sets.

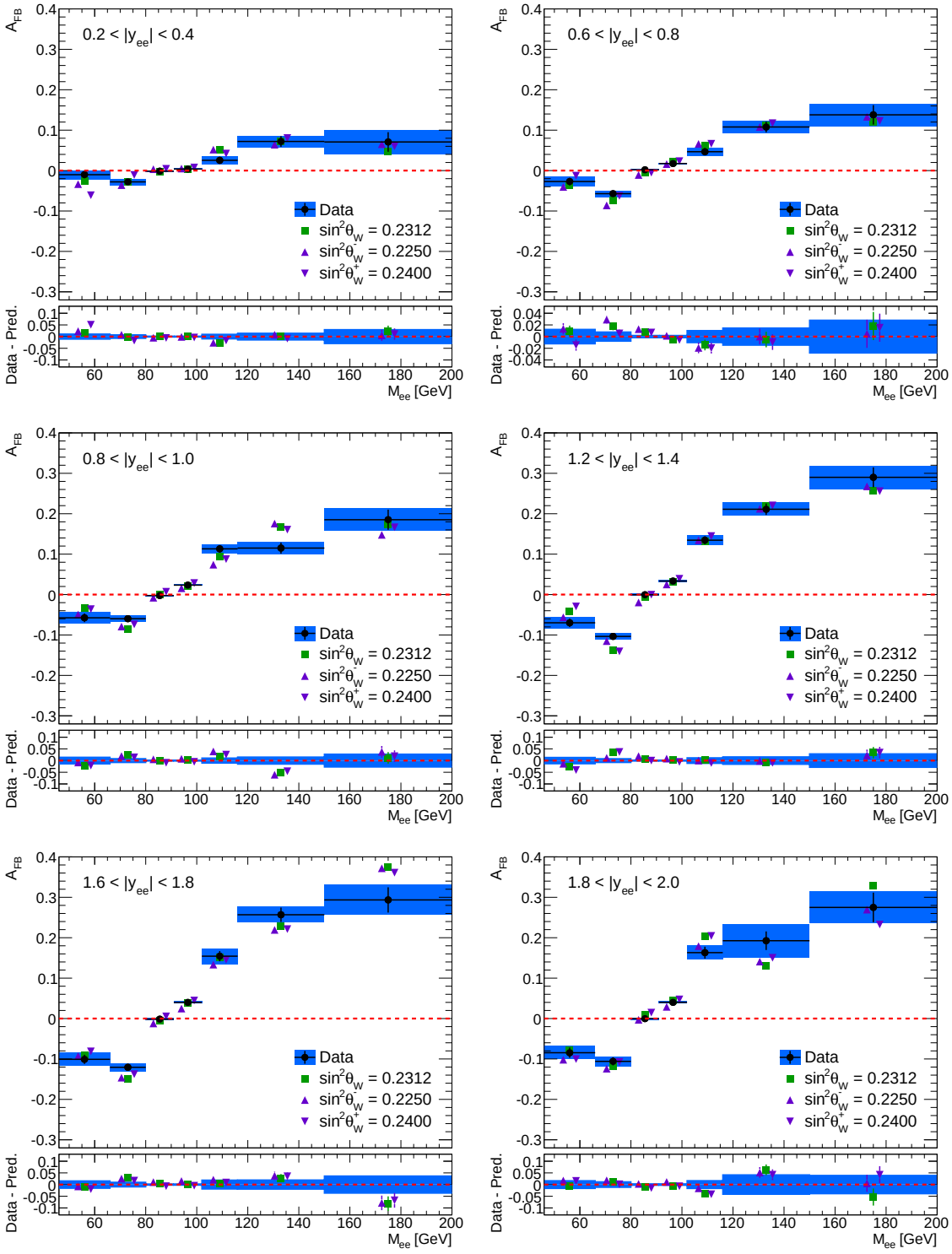

Figure 9.11: Forward-backward asymmetry measured in data and predicted by MCFM where values of $\sin^2\theta_{\mathrm{W}} = 0.2312$ (nominal), 0.2250 (lower), and 0.2400 (upper) were used to produce the predictions.

Chapter 10

Conclusions

Measurement of a three-dimensional differential cross-section of Drell-Yan production, $q\bar{q} \to Z/\gamma^* \to e^-e^+$, in proton-proton collisions at the LHC was performed. Collected in 2012, the ATLAS data set used in this analysis has an integrated luminosity of $\mathcal{L} = 20.1$ fb^{-1} and a proton-proton centre-of-mass energy of $\sqrt{s} = 8$ TeV. The measurement was binned in dielectron invariant mass M_{ee}, absolute rapidity $|y_{ee}|$, and cosine of the polar angle θ^* in the Collins-Soper frame.

The differential cross-section measurement was compared to an NLO theoretical prediction from the Monte Carlo generator POWHEG enhanced to NNLO in QCD and to include higher order EW corrections by reweighting the events with k-factors calculated using the software FEWZ. In nearly all measurement bins, data and theory were found to be consistent with each other.

The differential cross-section result can be used to improve on existing measurements of the parton distribution functions, which have an M_{ee} and y_{ee} dependency, of the proton. PDFs play a vital role in ATLAS, specifically in the production of ATLAS Monte Carlo simulations which are used to study detector performance, to test theoretical models, and to estimate background yields. It is of great importance that PDFs are well-measured as the alternative may hinder potential physics results at the LHC such as the discovery of a new particle.

Forward-backward asymmetry A_{FB} arises in Drell-Yan events from the parity violating nature of electroweak interactions. Integrating over $\cos\theta^* > 0$ and $\cos\theta^* < 0$, the differential cross-section measurement was used to obtain a measurement of A_{FB}. An interesting result in its own right, A_{FB} can be used to extract a measurement of the weak mixing angle θ_{W}, a fundamental parameter of the Standard Model.

Appendix A

Tables of Results

Bin	M_{ee} [GeV]		$\lvert y_{ee}\rvert$		$\cos\theta^*$		σ [pb/GeV]	δ^{stat} [%]	δ^{syst} [%]	δ^{tot} [%]
1	46	66	0.0	0.2	−1.0	−0.7	1.45×10^{-2}	6.7	8.1	10.6
2	46	66	0.0	0.2	−0.7	−0.4	1.03×10^{-1}	2.3	4.1	4.7
3	46	66	0.0	0.2	−0.4	0.0	1.47×10^{-1}	1.4	2.6	2.9
4	46	66	0.0	0.2	0.0	+0.4	1.47×10^{-1}	1.4	2.6	3.0
5	46	66	0.0	0.2	+0.4	+0.7	1.04×10^{-1}	2.2	3.9	4.5
6	46	66	0.0	0.2	+0.7	+1.0	1.40×10^{-2}	6.7	8.6	10.9
7	46	66	0.2	0.4	−1.0	−0.7	1.55×10^{-2}	6.3	11.2	12.9
8	46	66	0.2	0.4	−0.7	−0.4	1.07×10^{-1}	2.2	4.1	4.6
9	46	66	0.2	0.4	−0.4	0.0	1.49×10^{-1}	1.4	2.6	2.9
10	46	66	0.2	0.4	0.0	+0.4	1.49×10^{-1}	1.4	2.6	2.9
11	46	66	0.2	0.4	+0.4	+0.7	1.02×10^{-1}	2.3	3.9	4.5
12	46	66	0.2	0.4	+0.7	+1.0	1.61×10^{-2}	6.3	11.5	13.1
13	46	66	0.4	0.6	−1.0	−0.7	1.29×10^{-2}	8.7	10.5	13.7
14	46	66	0.4	0.6	−0.7	−0.4	1.10×10^{-1}	2.2	4.5	5.0
15	46	66	0.4	0.6	−0.4	0.0	1.51×10^{-1}	1.4	2.7	3.1
16	46	66	0.4	0.6	0.0	+0.4	1.43×10^{-1}	1.4	2.7	3.1
17	46	66	0.4	0.6	+0.4	+0.7	1.04×10^{-1}	2.4	4.7	5.2
18	46	66	0.4	0.6	+0.7	+1.0	1.35×10^{-2}	8.1	7.9	11.3
19	46	66	0.6	0.8	−1.0	−0.7	1.55×10^{-2}	7.2	11.6	13.6
20	46	66	0.6	0.8	−0.7	−0.4	1.09×10^{-1}	2.5	3.8	4.5
21	46	66	0.6	0.8	−0.4	0.0	1.49×10^{-1}	1.4	2.6	3.0
22	46	66	0.6	0.8	0.0	+0.4	1.41×10^{-1}	1.5	2.7	3.1
23	46	66	0.6	0.8	+0.4	+0.7	1.02×10^{-1}	2.7	3.8	4.6
24	46	66	0.6	0.8	+0.7	+1.0	1.62×10^{-2}	6.7	11.4	13.2
25	46	66	0.8	1.0	−1.0	−0.7	1.90×10^{-2}	6.2	6.3	8.8
26	46	66	0.8	1.0	−0.7	−0.4	1.04×10^{-1}	3.1	4.6	5.5
27	46	66	0.8	1.0	−0.4	0.0	1.53×10^{-1}	1.4	3.4	3.7
28	46	66	0.8	1.0	0.0	+0.4	1.44×10^{-1}	1.5	3.5	3.8
29	46	66	0.8	1.0	+0.4	+0.7	8.85×10^{-2}	3.5	4.9	6.0
30	46	66	0.8	1.0	+0.7	+1.0	1.38×10^{-2}	7.2	7.2	10.2

Bin	M_{ee} [GeV]		$\lvert y_{ee}\rvert$		$\cos\theta^*$		σ [pb/GeV]	δ^{stat} [%]	δ^{syst} [%]	δ^{tot} [%]
31	46	66	1.0	1.2	−1.0	−0.7	1.69×10^{-2}	6.0	6.9	9.1
32	46	66	1.0	1.2	−0.7	−0.4	1.13×10^{-1}	2.5	4.4	5.0
33	46	66	1.0	1.2	−0.4	0.0	1.54×10^{-1}	1.7	3.0	3.4
34	46	66	1.0	1.2	0.0	+0.4	1.50×10^{-1}	1.8	3.0	3.5
35	46	66	1.0	1.2	+0.4	+0.7	9.69×10^{-2}	2.6	4.6	5.3
36	46	66	1.0	1.2	+0.7	+1.0	1.35×10^{-2}	7.3	9.6	12.0
37	46	66	1.2	1.4	−1.0	−0.7	1.52×10^{-2}	6.4	9.3	11.3
38	46	66	1.2	1.4	−0.7	−0.4	1.14×10^{-1}	2.2	4.7	5.2
39	46	66	1.2	1.4	−0.4	0.0	1.54×10^{-1}	1.9	3.6	4.0
40	46	66	1.2	1.4	0.0	+0.4	1.45×10^{-1}	2.1	3.7	4.3
41	46	66	1.2	1.4	+0.4	+0.7	8.95×10^{-2}	2.6	5.2	5.8
42	46	66	1.2	1.4	+0.7	+1.0	1.19×10^{-2}	7.6	11.1	13.5
43	46	66	1.4	1.6	−1.0	−0.7	1.10×10^{-2}	7.1	5.7	9.1
44	46	66	1.4	1.6	−0.7	−0.4	1.17×10^{-1}	2.3	3.9	4.5
45	46	66	1.4	1.6	−0.4	0.0	1.55×10^{-1}	1.8	3.3	3.8
46	46	66	1.4	1.6	0.0	+0.4	1.36×10^{-1}	2.1	3.4	4.0
47	46	66	1.4	1.6	+0.4	+0.7	8.58×10^{-2}	2.7	4.5	5.3
48	46	66	1.4	1.6	+0.7	+1.0	7.89×10^{-3}	8.8	8.4	12.2
49	46	66	1.6	1.8	−1.0	−0.7	4.67×10^{-3}	10.3	13.3	16.9
50	46	66	1.6	1.8	−0.7	−0.4	1.00×10^{-1}	2.3	3.4	4.1
51	46	66	1.6	1.8	−0.4	0.0	1.53×10^{-1}	2.0	3.6	4.1
52	46	66	1.6	1.8	0.0	+0.4	1.37×10^{-1}	2.1	3.7	4.2
53	46	66	1.6	1.8	+0.4	+0.7	7.02×10^{-2}	3.0	5.6	6.4
54	46	66	1.6	1.8	+0.7	+1.0	3.45×10^{-3}	13.8	24.2	27.9
55	46	66	1.8	2.0	−1.0	−0.7	2.15×10^{-3}	16.3	9.2	18.7
56	46	66	1.8	2.0	−0.7	−0.4	4.18×10^{-2}	5.1	5.5	7.5
57	46	66	1.8	2.0	−0.4	0.0	1.52×10^{-1}	1.8	4.4	4.7
58	46	66	1.8	2.0	0.0	+0.4	1.34×10^{-1}	1.8	4.6	5.0
59	46	66	1.8	2.0	+0.4	+0.7	3.03×10^{-2}	6.0	6.8	9.1
60	46	66	1.8	2.0	+0.7	+1.0	1.16×10^{-3}	25.7	23.7	35.0
61	46	66	2.0	2.2	−1.0	−0.7	-	-	-	-
62	46	66	2.0	2.2	−0.7	−0.4	2.62×10^{-3}	19.5	31.0	36.6
63	46	66	2.0	2.2	−0.4	0.0	1.16×10^{-1}	1.9	3.5	4.0
64	46	66	2.0	2.2	0.0	+0.4	9.44×10^{-2}	2.1	4.0	4.5
65	46	66	2.0	2.2	+0.4	+0.7	1.40×10^{-3}	24.1	44.1	50.3
66	46	66	2.0	2.2	+0.7	+1.0	-	-	-	-
67	46	66	2.2	2.4	−1.0	−0.7	-	-	-	-
68	46	66	2.2	2.4	−0.7	−0.4	-	-	-	-
69	46	66	2.2	2.4	−0.4	0.0	3.73×10^{-2}	3.4	5.2	6.2
70	46	66	2.2	2.4	0.0	+0.4	3.49×10^{-2}	3.5	6.0	6.9
71	46	66	2.2	2.4	+0.4	+0.7	-	-	-	-
72	46	66	2.2	2.4	+0.7	+1.0	-	-	-	-
73	66	80	0.0	0.2	−1.0	−0.7	8.40×10^{-2}	2.3	5.0	5.5
74	66	80	0.0	0.2	−0.7	−0.4	1.96×10^{-1}	1.4	2.2	2.6
75	66	80	0.0	0.2	−0.4	0.0	1.76×10^{-1}	1.2	1.1	1.6
76	66	80	0.0	0.2	0.0	+0.4	1.78×10^{-1}	1.2	1.0	1.6
77	66	80	0.0	0.2	+0.4	+0.7	1.92×10^{-1}	1.5	2.2	2.6
78	66	80	0.0	0.2	+0.7	+1.0	8.06×10^{-2}	2.5	5.1	5.7

Bin	M_{ee} [GeV]		$\lvert y_{ee}\rvert$		$\cos\theta^*$		σ [pb/GeV]	δ^{stat} [%]	δ^{syst} [%]	δ^{tot} [%]
79	66	80	0.2	0.4	−1.0	−0.7	8.67×10^{-2}	2.7	4.9	5.6
80	66	80	0.2	0.4	−0.7	−0.4	2.08×10^{-1}	1.3	2.1	2.5
81	66	80	0.2	0.4	−0.4	0.0	1.72×10^{-1}	1.3	1.1	1.6
82	66	80	0.2	0.4	0.0	+0.4	1.75×10^{-1}	1.2	1.1	1.7
83	66	80	0.2	0.4	+0.4	+0.7	1.88×10^{-1}	1.4	2.1	2.6
84	66	80	0.2	0.4	+0.7	+1.0	7.91×10^{-2}	2.7	5.5	6.1
85	66	80	0.4	0.6	−1.0	−0.7	8.58×10^{-2}	2.7	6.0	6.6
86	66	80	0.4	0.6	−0.7	−0.4	2.07×10^{-1}	1.4	2.0	2.5
87	66	80	0.4	0.6	−0.4	0.0	1.75×10^{-1}	1.2	1.2	1.7
88	66	80	0.4	0.6	0.0	+0.4	1.75×10^{-1}	1.2	1.1	1.6
89	66	80	0.4	0.6	+0.4	+0.7	1.93×10^{-1}	1.5	2.1	2.6
90	66	80	0.4	0.6	+0.7	+1.0	7.92×10^{-2}	2.8	6.6	7.1
91	66	80	0.6	0.8	−1.0	−0.7	8.78×10^{-2}	2.5	6.0	6.5
92	66	80	0.6	0.8	−0.7	−0.4	2.12×10^{-1}	1.6	2.6	3.1
93	66	80	0.6	0.8	−0.4	0.0	1.82×10^{-1}	1.2	1.1	1.6
94	66	80	0.6	0.8	0.0	+0.4	1.71×10^{-1}	1.3	1.1	1.7
95	66	80	0.6	0.8	+0.4	+0.7	1.88×10^{-1}	1.6	2.7	3.1
96	66	80	0.6	0.8	+0.7	+1.0	7.08×10^{-2}	2.6	5.9	6.5
97	66	80	0.8	1.0	−1.0	−0.7	7.86×10^{-2}	2.6	5.3	5.9
98	66	80	0.8	1.0	−0.7	−0.4	2.16×10^{-1}	1.6	3.4	3.8
99	66	80	0.8	1.0	−0.4	0.0	1.76×10^{-1}	1.3	1.2	1.7
100	66	80	0.8	1.0	0.0	+0.4	1.64×10^{-1}	1.3	1.2	1.8
101	66	80	0.8	1.0	+0.4	+0.7	1.79×10^{-1}	1.8	3.7	4.1
102	66	80	0.8	1.0	+0.7	+1.0	7.42×10^{-2}	2.7	5.3	5.9
103	66	80	1.0	1.2	−1.0	−0.7	9.22×10^{-2}	2.3	4.2	4.8
104	66	80	1.0	1.2	−0.7	−0.4	2.08×10^{-1}	1.5	2.8	3.1
105	66	80	1.0	1.2	−0.4	0.0	1.84×10^{-1}	1.4	1.8	2.3
106	66	80	1.0	1.2	0.0	+0.4	1.64×10^{-1}	1.5	2.0	2.4
107	66	80	1.0	1.2	+0.4	+0.7	1.81×10^{-1}	1.5	3.0	3.3
108	66	80	1.0	1.2	+0.7	+1.0	6.68×10^{-2}	2.7	4.5	5.2
109	66	80	1.2	1.4	−1.0	−0.7	7.25×10^{-2}	2.6	4.4	5.1
110	66	80	1.2	1.4	−0.7	−0.4	2.09×10^{-1}	1.4	2.6	2.9
111	66	80	1.2	1.4	−0.4	0.0	1.87×10^{-1}	1.4	2.6	2.9
112	66	80	1.2	1.4	0.0	+0.4	1.72×10^{-1}	1.6	2.7	3.1
113	66	80	1.2	1.4	+0.4	+0.7	1.59×10^{-1}	1.5	2.8	3.2
114	66	80	1.2	1.4	+0.7	+1.0	4.98×10^{-2}	3.0	4.7	5.5
115	66	80	1.4	1.6	−1.0	−0.7	2.72×10^{-2}	4.4	4.2	6.1
116	66	80	1.4	1.6	−0.7	−0.4	2.09×10^{-1}	1.5	2.3	2.8
117	66	80	1.4	1.6	−0.4	0.0	1.85×10^{-1}	1.5	2.5	2.9
118	66	80	1.4	1.6	0.0	+0.4	1.62×10^{-1}	1.5	2.7	3.1
119	66	80	1.4	1.6	+0.4	+0.7	1.46×10^{-1}	1.7	2.5	3.1
120	66	80	1.4	1.6	+0.7	+1.0	1.81×10^{-2}	5.0	7.3	8.8
121	66	80	1.6	1.8	−1.0	−0.7	6.07×10^{-3}	9.4	8.0	12.3
122	66	80	1.6	1.8	−0.7	−0.4	1.51×10^{-1}	1.7	2.2	2.7
123	66	80	1.6	1.8	−0.4	0.0	1.85×10^{-1}	1.5	3.0	3.4
124	66	80	1.6	1.8	0.0	+0.4	1.61×10^{-1}	1.6	3.2	3.6
125	66	80	1.6	1.8	+0.4	+0.7	1.03×10^{-1}	1.9	2.5	3.2
126	66	80	1.6	1.8	+0.7	+1.0	3.87×10^{-3}	11.0	11.5	15.9

Bin	M_{ee} [GeV]		$\lvert y_{ee}\rvert$		$\cos\theta^*$		σ [pb/GeV]	δ^{stat} [%]	δ^{syst} [%]	δ^{tot} [%]
127	66	80	1.8	2.0	−1.0	−0.7	1.46×10^{-3}	19.0	8.2	20.7
128	66	80	1.8	2.0	−0.7	−0.4	5.53×10^{-2}	3.6	4.6	5.9
129	66	80	1.8	2.0	−0.4	0.0	1.79×10^{-1}	1.4	2.6	3.0
130	66	80	1.8	2.0	0.0	+0.4	1.55×10^{-1}	1.5	2.8	3.2
131	66	80	1.8	2.0	+0.4	+0.7	3.52×10^{-2}	4.2	5.1	6.6
132	66	80	1.8	2.0	+0.7	+1.0	8.35×10^{-4}	22.9	10.7	25.3
133	66	80	2.0	2.2	−1.0	−0.7	-	-	-	-
134	66	80	2.0	2.2	−0.7	−0.4	2.99×10^{-3}	16.9	43.2	46.4
135	66	80	2.0	2.2	−0.4	0.0	1.29×10^{-1}	1.7	2.1	2.7
136	66	80	2.0	2.2	0.0	+0.4	1.05×10^{-1}	1.7	2.3	2.9
137	66	80	2.0	2.2	+0.4	+0.7	9.95×10^{-4}	30.2	81.1	86.6
138	66	80	2.0	2.2	+0.7	+1.0	-	-	-	-
139	66	80	2.2	2.4	−1.0	−0.7	-	-	-	-
140	66	80	2.2	2.4	−0.7	−0.4	-	-	-	-
141	66	80	2.2	2.4	−0.4	0.0	4.09×10^{-2}	3.0	3.0	4.2
142	66	80	2.2	2.4	0.0	+0.4	3.69×10^{-2}	3.1	2.8	4.1
143	66	80	2.2	2.4	+0.4	+0.7	-	-	-	-
144	66	80	2.2	2.4	+0.7	+1.0	-	-	-	-
145	80	91	0.0	0.2	−1.0	−0.7	2.28	0.5	3.0	3.0
146	80	91	0.0	0.2	−0.7	−0.4	3.57	0.4	1.0	1.1
147	80	91	0.0	0.2	−0.4	0.0	3.11	0.4	1.0	1.1
148	80	91	0.0	0.2	0.0	+0.4	3.11	0.4	1.0	1.1
149	80	91	0.0	0.2	+0.4	+0.7	3.62	0.4	1.0	1.0
150	80	91	0.0	0.2	+0.7	+1.0	2.25	0.5	3.0	3.0
151	80	91	0.2	0.4	−1.0	−0.7	2.27	0.6	2.8	2.9
152	80	91	0.2	0.4	−0.7	−0.4	3.59	0.4	1.0	1.1
153	80	91	0.2	0.4	−0.4	0.0	3.11	0.4	1.0	1.1
154	80	91	0.2	0.4	0.0	+0.4	3.09	0.4	1.1	1.1
155	80	91	0.2	0.4	+0.4	+0.7	3.60	0.4	1.0	1.1
156	80	91	0.2	0.4	+0.7	+1.0	2.26	0.6	2.8	2.9
157	80	91	0.4	0.6	−1.0	−0.7	2.24	0.6	3.6	3.6
158	80	91	0.4	0.6	−0.7	−0.4	3.59	0.4	1.2	1.2
159	80	91	0.4	0.6	−0.4	0.0	3.09	0.4	1.1	1.1
160	80	91	0.4	0.6	0.0	+0.4	3.10	0.4	1.1	1.2
161	80	91	0.4	0.6	+0.4	+0.7	3.63	0.4	1.2	1.2
162	80	91	0.4	0.6	+0.7	+1.0	2.25	0.6	3.6	3.7
163	80	91	0.6	0.8	−1.0	−0.7	2.23	0.5	3.6	3.6
164	80	91	0.6	0.8	−0.7	−0.4	3.52	0.4	1.6	1.6
165	80	91	0.6	0.8	−0.4	0.0	3.06	0.4	1.1	1.1
166	80	91	0.6	0.8	0.0	+0.4	3.08	0.4	1.1	1.1
167	80	91	0.6	0.8	+0.4	+0.7	3.54	0.4	1.5	1.6
168	80	91	0.6	0.8	+0.7	+1.0	2.22	0.5	3.6	3.6
169	80	91	0.8	1.0	−1.0	−0.7	2.17	0.5	3.2	3.3
170	80	91	0.8	1.0	−0.7	−0.4	3.50	0.5	1.8	1.9
171	80	91	0.8	1.0	−0.4	0.0	3.05	0.4	1.2	1.3
172	80	91	0.8	1.0	0.0	+0.4	3.02	0.4	1.3	1.3
173	80	91	0.8	1.0	+0.4	+0.7	3.45	0.4	1.8	1.9
174	80	91	0.8	1.0	+0.7	+1.0	2.20	0.5	3.3	3.3

Bin	M_{ee} [GeV]		$\lvert y_{ee}\rvert$		$\cos\theta^*$		σ [pb/GeV]	δ^{stat} [%]	δ^{syst} [%]	δ^{tot} [%]
175	80	91	1.0	1.2	−1.0	−0.7	1.96	0.6	2.8	2.9
176	80	91	1.0	1.2	−0.7	−0.4	3.39	0.4	1.6	1.7
177	80	91	1.0	1.2	−0.4	0.0	2.99	0.4	1.5	1.6
178	80	91	1.0	1.2	0.0	+0.4	2.99	0.4	1.6	1.6
179	80	91	1.0	1.2	+0.4	+0.7	3.43	0.4	1.6	1.7
180	80	91	1.0	1.2	+0.7	+1.0	1.95	0.6	2.9	2.9
181	80	91	1.2	1.4	−1.0	−0.7	1.29	0.6	2.3	2.4
182	80	91	1.2	1.4	−0.7	−0.4	3.40	0.4	1.3	1.4
183	80	91	1.2	1.4	−0.4	0.0	2.94	0.4	2.0	2.0
184	80	91	1.2	1.4	0.0	+0.4	2.95	0.4	2.0	2.0
185	80	91	1.2	1.4	+0.4	+0.7	3.37	0.4	1.4	1.4
186	80	91	1.2	1.4	+0.7	+1.0	1.30	0.7	2.3	2.4
187	80	91	1.4	1.6	−1.0	−0.7	4.82×10^{-1}	1.1	2.0	2.2
188	80	91	1.4	1.6	−0.7	−0.4	3.18	0.4	1.2	1.3
189	80	91	1.4	1.6	−0.4	0.0	2.88	0.4	2.0	2.1
190	80	91	1.4	1.6	0.0	+0.4	2.87	0.4	2.1	2.1
191	80	91	1.4	1.6	+0.4	+0.7	3.16	0.4	1.3	1.3
192	80	91	1.4	1.6	+0.7	+1.0	4.77×10^{-1}	1.0	2.0	2.3
193	80	91	1.6	1.8	−1.0	−0.7	9.02×10^{-2}	2.5	2.4	3.5
194	80	91	1.6	1.8	−0.7	−0.4	2.23	0.5	1.3	1.4
195	80	91	1.6	1.8	−0.4	0.0	2.82	0.4	2.4	2.4
196	80	91	1.6	1.8	0.0	+0.4	2.82	0.4	2.4	2.5
197	80	91	1.6	1.8	+0.4	+0.7	2.21	0.5	1.4	1.5
198	80	91	1.6	1.8	+0.7	+1.0	9.02×10^{-2}	2.5	2.5	3.5
199	80	91	1.8	2.0	−1.0	−0.7	2.01×10^{-2}	5.6	3.9	6.8
200	80	91	1.8	2.0	−0.7	−0.4	7.84×10^{-1}	1.0	1.9	2.2
201	80	91	1.8	2.0	−0.4	0.0	2.73	0.4	2.1	2.2
202	80	91	1.8	2.0	0.0	+0.4	2.73	0.4	2.2	2.2
203	80	91	1.8	2.0	+0.4	+0.7	7.85×10^{-1}	1.0	2.0	2.3
204	80	91	1.8	2.0	+0.7	+1.0	2.06×10^{-2}	5.4	4.2	6.8
205	80	91	2.0	2.2	−1.0	−0.7	2.58×10^{-3}	14.7	8.6	17.0
206	80	91	2.0	2.2	−0.7	−0.4	5.55×10^{-2}	4.2	5.4	6.9
207	80	91	2.0	2.2	−0.4	0.0	1.98	0.5	1.7	1.8
208	80	91	2.0	2.2	0.0	+0.4	1.96	0.5	1.8	1.8
209	80	91	2.0	2.2	+0.4	+0.7	5.15×10^{-2}	4.2	6.3	7.6
210	80	91	2.0	2.2	+0.7	+1.0	2.65×10^{-3}	14.8	12.3	19.2
211	80	91	2.2	2.4	−1.0	−0.7	-	-	-	-
212	80	91	2.2	2.4	−0.7	−0.4	-	-	-	-
213	80	91	2.2	2.4	−0.4	0.0	6.38×10^{-1}	0.8	2.0	2.1
214	80	91	2.2	2.4	0.0	+0.4	6.29×10^{-1}	0.8	1.9	2.1
215	80	91	2.2	2.4	+0.4	+0.7	-	-	-	-
216	80	91	2.2	2.4	+0.7	+1.0	-	-	-	-
217	91	102	0.0	0.2	−1.0	−0.7	2.79	0.5	2.9	3.0
218	91	102	0.0	0.2	−0.7	−0.4	4.16	0.4	0.9	1.0
219	91	102	0.0	0.2	−0.4	0.0	3.60	0.4	1.0	1.1
220	91	102	0.0	0.2	0.0	+0.4	3.61	0.4	1.0	1.1
221	91	102	0.0	0.2	+0.4	+0.7	4.19	0.4	0.8	0.9
222	91	102	0.0	0.2	+0.7	+1.0	2.81	0.5	2.9	2.9

Bin	M_{ee} [GeV]		$\lvert y_{ee}\rvert$		$\cos\theta^*$		σ [pb/GeV]	δ^{stat} [%]	δ^{syst} [%]	δ^{tot} [%]
223	91	102	0.2	0.4	−1.0	−0.7	2.78	0.5	3.2	3.2
224	91	102	0.2	0.4	−0.7	−0.4	4.11	0.4	0.9	1.0
225	91	102	0.2	0.4	−0.4	0.0	3.58	0.4	1.0	1.1
226	91	102	0.2	0.4	0.0	+0.4	3.60	0.4	1.0	1.1
227	91	102	0.2	0.4	+0.4	+0.7	4.15	0.4	0.9	1.0
228	91	102	0.2	0.4	+0.7	+1.0	2.80	0.6	3.2	3.2
229	91	102	0.4	0.6	−1.0	−0.7	2.73	0.6	3.7	3.7
230	91	102	0.4	0.6	−0.7	−0.4	4.05	0.4	1.1	1.2
231	91	102	0.4	0.6	−0.4	0.0	3.55	0.3	1.0	1.1
232	91	102	0.4	0.6	0.0	+0.4	3.60	0.4	1.0	1.1
233	91	102	0.4	0.6	+0.4	+0.7	4.16	0.4	1.1	1.2
234	91	102	0.4	0.6	+0.7	+1.0	2.83	0.5	3.7	3.7
235	91	102	0.6	0.8	−1.0	−0.7	2.70	0.5	3.4	3.5
236	91	102	0.6	0.8	−0.7	−0.4	4.03	0.4	1.4	1.5
237	91	102	0.6	0.8	−0.4	0.0	3.52	0.4	1.0	1.1
238	91	102	0.6	0.8	0.0	+0.4	3.58	0.3	1.0	1.1
239	91	102	0.6	0.8	+0.4	+0.7	4.17	0.4	1.4	1.4
240	91	102	0.6	0.8	+0.7	+1.0	2.87	0.5	3.4	3.4
241	91	102	0.8	1.0	−1.0	−0.7	2.68	0.5	3.2	3.2
242	91	102	0.8	1.0	−0.7	−0.4	3.99	0.5	1.7	1.8
243	91	102	0.8	1.0	−0.4	0.0	3.46	0.4	1.2	1.2
244	91	102	0.8	1.0	0.0	+0.4	3.56	0.4	1.1	1.2
245	91	102	0.8	1.0	+0.4	+0.7	4.19	0.4	1.7	1.7
246	91	102	0.8	1.0	+0.7	+1.0	2.87	0.5	3.2	3.2
247	91	102	1.0	1.2	−1.0	−0.7	2.24	0.6	2.7	2.7
248	91	102	1.0	1.2	−0.7	−0.4	3.91	0.4	1.6	1.7
249	91	102	1.0	1.2	−0.4	0.0	3.43	0.4	1.5	1.5
250	91	102	1.0	1.2	0.0	+0.4	3.54	0.4	1.5	1.5
251	91	102	1.0	1.2	+0.4	+0.7	4.16	0.4	1.5	1.6
252	91	102	1.0	1.2	+0.7	+1.0	2.43	0.5	2.6	2.7
253	91	102	1.2	1.4	−1.0	−0.7	1.47	0.7	2.0	2.1
254	91	102	1.2	1.4	−0.7	−0.4	3.80	0.4	1.4	1.4
255	91	102	1.2	1.4	−0.4	0.0	3.33	0.4	1.9	2.0
256	91	102	1.2	1.4	0.0	+0.4	3.47	0.4	1.8	1.9
257	91	102	1.2	1.4	+0.4	+0.7	4.13	0.4	1.3	1.4
258	91	102	1.2	1.4	+0.7	+1.0	1.60	0.7	2.0	2.1
259	91	102	1.4	1.6	−1.0	−0.7	5.22×10^{-1}	1.1	1.9	2.2
260	91	102	1.4	1.6	−0.7	−0.4	3.48	0.4	1.2	1.3
261	91	102	1.4	1.6	−0.4	0.0	3.28	0.4	2.1	2.2
262	91	102	1.4	1.6	0.0	+0.4	3.41	0.4	2.1	2.1
263	91	102	1.4	1.6	+0.4	+0.7	3.84	0.4	1.1	1.2
264	91	102	1.4	1.6	+0.7	+1.0	5.93×10^{-1}	1.0	1.8	2.0
265	91	102	1.6	1.8	−1.0	−0.7	9.49×10^{-2}	2.6	3.0	4.0
266	91	102	1.6	1.8	−0.7	−0.4	2.40	0.5	1.4	1.5
267	91	102	1.6	1.8	−0.4	0.0	3.16	0.5	2.5	2.5
268	91	102	1.6	1.8	0.0	+0.4	3.34	0.4	2.4	2.4
269	91	102	1.6	1.8	+0.4	+0.7	2.69	0.5	1.3	1.4
270	91	102	1.6	1.8	+0.7	+1.0	1.09×10^{-1}	2.4	3.2	4.0

Bin	M_{ee} [GeV]		$\lvert y_{ee}\rvert$		$\cos\theta^*$		σ [pb/GeV]	δ^{stat} [%]	δ^{syst} [%]	δ^{tot} [%]
271	91	102	1.8	2.0	−1.0	−0.7	2.10×10^{-2}	5.9	4.5	7.4
272	91	102	1.8	2.0	−0.7	−0.4	8.59×10^{-1}	1.0	1.8	2.1
273	91	102	1.8	2.0	−0.4	0.0	2.98	0.4	2.1	2.1
274	91	102	1.8	2.0	0.0	+0.4	3.18	0.4	2.0	2.0
275	91	102	1.8	2.0	+0.4	+0.7	9.86×10^{-1}	1.0	1.7	1.9
276	91	102	1.8	2.0	+0.7	+1.0	2.36×10^{-2}	5.4	4.4	7.0
277	91	102	2.0	2.2	−1.0	−0.7	-	-	-	-
278	91	102	2.0	2.2	−0.7	−0.4	5.37×10^{-2}	4.5	4.6	6.4
279	91	102	2.0	2.2	−0.4	0.0	2.14	0.5	1.6	1.7
280	91	102	2.0	2.2	0.0	+0.4	2.27	0.5	1.6	1.6
281	91	102	2.0	2.2	+0.4	+0.7	6.31×10^{-2}	4.0	4.1	5.7
282	91	102	2.0	2.2	+0.7	+1.0	3.34×10^{-3}	14.1	10.8	17.8
283	91	102	2.2	2.4	−1.0	−0.7	-	-	-	-
284	91	102	2.2	2.4	−0.7	−0.4	-	-	-	-
285	91	102	2.2	2.4	−0.4	0.0	7.28×10^{-1}	0.8	1.8	2.0
286	91	102	2.2	2.4	0.0	+0.4	7.53×10^{-1}	0.8	1.7	1.9
287	91	102	2.2	2.4	+0.4	+0.7	-	-	-	-
288	91	102	2.2	2.4	+0.7	+1.0	-	-	-	-
289	102	116	0.0	0.2	−1.0	−0.7	1.10×10^{-1}	2.5	3.7	4.5
290	102	116	0.0	0.2	−0.7	−0.4	1.31×10^{-1}	2.0	1.1	2.2
291	102	116	0.0	0.2	−0.4	0.0	1.20×10^{-1}	1.8	1.1	2.1
292	102	116	0.0	0.2	0.0	+0.4	1.15×10^{-1}	1.8	1.0	2.1
293	102	116	0.0	0.2	+0.4	+0.7	1.37×10^{-1}	1.9	1.0	2.2
294	102	116	0.0	0.2	+0.7	+1.0	1.11×10^{-1}	2.5	3.7	4.5
295	102	116	0.2	0.4	−1.0	−0.7	1.04×10^{-1}	2.8	4.5	5.3
296	102	116	0.2	0.4	−0.7	−0.4	1.30×10^{-1}	2.1	1.2	2.4
297	102	116	0.2	0.4	−0.4	0.0	1.16×10^{-1}	1.7	0.9	1.9
298	102	116	0.2	0.4	0.0	+0.4	1.23×10^{-1}	1.7	1.0	2.0
299	102	116	0.2	0.4	+0.4	+0.7	1.35×10^{-1}	2.0	1.1	2.3
300	102	116	0.2	0.4	+0.7	+1.0	1.10×10^{-1}	2.7	3.7	4.6
301	102	116	0.4	0.6	−1.0	−0.7	9.90×10^{-2}	2.8	4.0	4.9
302	102	116	0.4	0.6	−0.7	−0.4	1.25×10^{-1}	2.1	1.6	2.6
303	102	116	0.4	0.6	−0.4	0.0	1.08×10^{-1}	1.8	1.1	2.1
304	102	116	0.4	0.6	0.0	+0.4	1.16×10^{-1}	1.8	1.2	2.1
305	102	116	0.4	0.6	+0.4	+0.7	1.40×10^{-1}	1.9	1.4	2.4
306	102	116	0.4	0.6	+0.7	+1.0	1.11×10^{-1}	2.7	4.0	4.8
307	102	116	0.6	0.8	−1.0	−0.7	1.01×10^{-1}	2.7	4.0	4.8
308	102	116	0.6	0.8	−0.7	−0.4	1.21×10^{-1}	2.4	2.1	3.2
309	102	116	0.6	0.8	−0.4	0.0	1.15×10^{-1}	1.8	1.2	2.2
310	102	116	0.6	0.8	0.0	+0.4	1.14×10^{-1}	1.8	1.1	2.1
311	102	116	0.6	0.8	+0.4	+0.7	1.39×10^{-1}	2.3	2.1	3.1
312	102	116	0.6	0.8	+0.7	+1.0	1.17×10^{-1}	2.4	3.8	4.5
313	102	116	0.8	1.0	−1.0	−0.7	8.71×10^{-2}	2.8	3.2	4.3
314	102	116	0.8	1.0	−0.7	−0.4	1.17×10^{-1}	2.6	3.1	4.0
315	102	116	0.8	1.0	−0.4	0.0	1.00×10^{-1}	2.0	2.1	2.9
316	102	116	0.8	1.0	0.0	+0.4	1.17×10^{-1}	1.8	1.3	2.2
317	102	116	0.8	1.0	+0.4	+0.7	1.47×10^{-1}	2.3	2.6	3.5
318	102	116	0.8	1.0	+0.7	+1.0	1.17×10^{-1}	2.3	3.0	3.8

Bin	M_{ee} [GeV]		$\lvert y_{ee}\rvert$		$\cos\theta^*$		σ [pb/GeV]	δ^{stat} [%]	δ^{syst} [%]	δ^{tot} [%]
319	102	116	1.0	1.2	−1.0	−0.7	6.91×10^{-2}	3.0	3.4	4.5
320	102	116	1.0	1.2	−0.7	−0.4	1.12×10^{-1}	2.3	2.5	3.4
321	102	116	1.0	1.2	−0.4	0.0	1.07×10^{-1}	2.2	2.3	3.2
322	102	116	1.0	1.2	0.0	+0.4	1.18×10^{-1}	2.1	2.1	2.9
323	102	116	1.0	1.2	+0.4	+0.7	1.47×10^{-1}	2.0	2.2	3.0
324	102	116	1.0	1.2	+0.7	+1.0	9.01×10^{-2}	2.7	3.0	4.0
325	102	116	1.2	1.4	−1.0	−0.7	4.08×10^{-2}	4.0	5.3	6.6
326	102	116	1.2	1.4	−0.7	−0.4	1.09×10^{-1}	2.3	1.9	2.9
327	102	116	1.2	1.4	−0.4	0.0	9.74×10^{-2}	2.5	3.8	4.5
328	102	116	1.2	1.4	0.0	+0.4	1.16×10^{-1}	2.3	4.3	4.9
329	102	116	1.2	1.4	+0.4	+0.7	1.49×10^{-1}	1.9	1.7	2.5
330	102	116	1.2	1.4	+0.7	+1.0	5.89×10^{-2}	3.3	4.1	5.3
331	102	116	1.4	1.6	−1.0	−0.7	1.47×10^{-2}	6.2	3.9	7.3
332	102	116	1.4	1.6	−0.7	−0.4	9.32×10^{-2}	2.3	1.8	3.0
333	102	116	1.4	1.6	−0.4	0.0	9.81×10^{-2}	2.4	4.6	5.2
334	102	116	1.4	1.6	0.0	+0.4	1.15×10^{-1}	2.2	4.0	4.6
335	102	116	1.4	1.6	+0.4	+0.7	1.35×10^{-1}	2.0	1.6	2.5
336	102	116	1.4	1.6	+0.7	+1.0	2.35×10^{-2}	5.4	3.4	6.3
337	102	116	1.6	1.8	−1.0	−0.7	2.05×10^{-3}	19.2	22.2	29.4
338	102	116	1.6	1.8	−0.7	−0.4	6.65×10^{-2}	3.0	2.5	3.9
339	102	116	1.6	1.8	−0.4	0.0	9.07×10^{-2}	2.5	6.2	6.7
340	102	116	1.6	1.8	0.0	+0.4	1.13×10^{-1}	2.4	5.2	5.7
341	102	116	1.6	1.8	+0.4	+0.7	1.00×10^{-1}	2.5	1.8	3.1
342	102	116	1.6	1.8	+0.7	+1.0	4.91×10^{-3}	12.2	11.1	16.6
343	102	116	1.8	2.0	−1.0	−0.7	-	-	-	-
344	102	116	1.8	2.0	−0.7	−0.4	2.04×10^{-2}	6.5	5.5	8.5
345	102	116	1.8	2.0	−0.4	0.0	8.73×10^{-2}	2.3	3.3	4.1
346	102	116	1.8	2.0	0.0	+0.4	1.11×10^{-1}	2.0	3.1	3.7
347	102	116	1.8	2.0	+0.4	+0.7	3.82×10^{-2}	4.9	3.8	6.2
348	102	116	1.8	2.0	+0.7	+1.0	-	-	-	-
349	102	116	2.0	2.2	−1.0	−0.7	-	-	-	-
350	102	116	2.0	2.2	−0.7	−0.4	-	-	-	-
351	102	116	2.0	2.2	−0.4	0.0	6.09×10^{-2}	2.7	2.5	3.7
352	102	116	2.0	2.2	0.0	+0.4	8.16×10^{-2}	2.5	1.9	3.2
353	102	116	2.0	2.2	+0.4	+0.7	1.25×10^{-3}	33.8	48.2	58.9
354	102	116	2.0	2.2	+0.7	+1.0	-	-	-	-
355	102	116	2.2	2.4	−1.0	−0.7	-	-	-	-
356	102	116	2.2	2.4	−0.7	−0.4	-	-	-	-
357	102	116	2.2	2.4	−0.4	0.0	2.19×10^{-2}	4.9	3.9	6.3
358	102	116	2.2	2.4	0.0	+0.4	2.53×10^{-2}	4.4	4.0	6.0
359	102	116	2.2	2.4	+0.4	+0.7	-	-	-	-
360	102	116	2.2	2.4	+0.7	+1.0	-	-	-	-
361	116	150	0.0	0.2	−1.0	−0.7	2.56×10^{-2}	3.9	6.5	7.5
362	116	150	0.0	0.2	−0.7	−0.4	2.71×10^{-2}	2.8	1.2	3.1
363	116	150	0.0	0.2	−0.4	0.0	2.08×10^{-2}	2.7	2.2	3.5
364	116	150	0.0	0.2	0.0	+0.4	2.31×10^{-2}	2.4	1.4	2.8
365	116	150	0.0	0.2	+0.4	+0.7	2.76×10^{-2}	2.8	1.3	3.1
366	116	150	0.0	0.2	+0.7	+1.0	2.67×10^{-2}	3.7	6.2	7.2

Bin	M_{ee} [GeV]		$\lvert y_{ee}\rvert$		$\cos\theta^*$		σ [pb/GeV]	δ^{stat} [%]	δ^{syst} [%]	δ^{tot} [%]
367	116	150	0.2	0.4	−1.0	−0.7	2.37×10^{-2}	4.2	3.9	5.7
368	116	150	0.2	0.4	−0.7	−0.4	2.48×10^{-2}	3.0	1.4	3.3
369	116	150	0.2	0.4	−0.4	0.0	2.07×10^{-2}	2.6	1.3	2.9
370	116	150	0.2	0.4	0.0	+0.4	2.28×10^{-2}	2.5	1.0	2.7
371	116	150	0.2	0.4	+0.4	+0.7	3.04×10^{-2}	2.7	1.1	2.9
372	116	150	0.2	0.4	+0.7	+1.0	2.68×10^{-2}	3.8	3.4	5.2
373	116	150	0.4	0.6	−1.0	−0.7	2.10×10^{-2}	4.5	9.2	10.2
374	116	150	0.4	0.6	−0.7	−0.4	2.45×10^{-2}	3.2	1.4	3.5
375	116	150	0.4	0.6	−0.4	0.0	2.17×10^{-2}	2.5	1.2	2.8
376	116	150	0.4	0.6	0.0	+0.4	2.33×10^{-2}	2.6	1.0	2.8
377	116	150	0.4	0.6	+0.4	+0.7	2.93×10^{-2}	2.9	1.3	3.1
378	116	150	0.4	0.6	+0.7	+1.0	2.50×10^{-2}	4.2	8.7	9.6
379	116	150	0.6	0.8	−1.0	−0.7	2.17×10^{-2}	3.9	4.3	5.8
380	116	150	0.6	0.8	−0.7	−0.4	2.30×10^{-2}	3.8	1.8	4.1
381	116	150	0.6	0.8	−0.4	0.0	2.08×10^{-2}	2.6	1.9	3.3
382	116	150	0.6	0.8	0.0	+0.4	2.34×10^{-2}	2.5	1.4	2.9
383	116	150	0.6	0.8	+0.4	+0.7	2.97×10^{-2}	3.2	1.9	3.7
384	116	150	0.6	0.8	+0.7	+1.0	2.83×10^{-2}	3.3	3.3	4.7
385	116	150	0.8	1.0	−1.0	−0.7	1.85×10^{-2}	3.9	8.8	9.6
386	116	150	0.8	1.0	−0.7	−0.4	2.15×10^{-2}	4.0	2.4	4.7
387	116	150	0.8	1.0	−0.4	0.0	2.15×10^{-2}	2.8	1.2	3.0
388	116	150	0.8	1.0	0.0	+0.4	2.22×10^{-2}	2.6	1.3	2.9
389	116	150	0.8	1.0	+0.4	+0.7	2.99×10^{-2}	3.4	1.6	3.7
390	116	150	0.8	1.0	+0.7	+1.0	2.54×10^{-2}	3.3	6.6	7.4
391	116	150	1.0	1.2	−1.0	−0.7	1.24×10^{-2}	4.8	6.4	8.0
392	116	150	1.0	1.2	−0.7	−0.4	1.94×10^{-2}	3.5	1.7	3.9
393	116	150	1.0	1.2	−0.4	0.0	2.14×10^{-2}	3.1	2.0	3.7
394	116	150	1.0	1.2	0.0	+0.4	2.43×10^{-2}	3.0	1.7	3.5
395	116	150	1.0	1.2	+0.4	+0.7	3.15×10^{-2}	2.8	1.5	3.2
396	116	150	1.0	1.2	+0.7	+1.0	1.94×10^{-2}	3.7	4.4	5.7
397	116	150	1.2	1.4	−1.0	−0.7	7.84×10^{-3}	5.9	3.0	6.6
398	116	150	1.2	1.4	−0.7	−0.4	1.79×10^{-2}	3.6	2.7	4.5
399	116	150	1.2	1.4	−0.4	0.0	1.91×10^{-2}	3.5	2.2	4.1
400	116	150	1.2	1.4	0.0	+0.4	2.39×10^{-2}	3.3	1.8	3.7
401	116	150	1.2	1.4	+0.4	+0.7	3.04×10^{-2}	2.7	1.7	3.2
402	116	150	1.2	1.4	+0.7	+1.0	1.46×10^{-2}	4.2	2.0	4.6
403	116	150	1.4	1.6	−1.0	−0.7	2.90×10^{-3}	10.1	6.7	12.1
404	116	150	1.4	1.6	−0.7	−0.4	1.65×10^{-2}	3.7	2.1	4.2
405	116	150	1.4	1.6	−0.4	0.0	1.83×10^{-2}	3.8	2.3	4.4
406	116	150	1.4	1.6	0.0	+0.4	2.23×10^{-2}	3.2	2.0	3.8
407	116	150	1.4	1.6	+0.4	+0.7	2.92×10^{-2}	2.8	1.5	3.2
408	116	150	1.4	1.6	+0.7	+1.0	4.76×10^{-3}	7.8	5.2	9.4
409	116	150	1.6	1.8	−1.0	−0.7	-	-	-	-
410	116	150	1.6	1.8	−0.7	−0.4	1.08×10^{-2}	4.8	3.0	5.6
411	116	150	1.6	1.8	−0.4	0.0	1.65×10^{-2}	3.9	2.9	4.8
412	116	150	1.6	1.8	0.0	+0.4	2.41×10^{-2}	3.3	2.4	4.1
413	116	150	1.6	1.8	+0.4	+0.7	2.09×10^{-2}	3.4	2.2	4.1
414	116	150	1.6	1.8	+0.7	+1.0	1.22×10^{-3}	15.4	9.3	18.0

Bin	M_{ee} [GeV]		$\lvert y_{ee}\rvert$		$\cos\theta^*$		σ [pb/GeV]	δ^{stat} [%]	δ^{syst} [%]	δ^{tot} [%]
415	116	150	1.8	2.0	−1.0	−0.7	-	-	-	-
416	116	150	1.8	2.0	−0.7	−0.4	3.80×10^{-3}	11.4	21.5	24.3
417	116	150	1.8	2.0	−0.4	0.0	1.59×10^{-2}	3.6	7.6	8.4
418	116	150	1.8	2.0	0.0	+0.4	2.17×10^{-2}	3.1	4.6	5.6
419	116	150	1.8	2.0	+0.4	+0.7	7.41×10^{-3}	8.0	11.2	13.8
420	116	150	1.8	2.0	+0.7	+1.0	-	-	-	-
421	116	150	2.0	2.2	−1.0	−0.7	-	-	-	-
422	116	150	2.0	2.2	−0.7	−0.4	-	-	-	-
423	116	150	2.0	2.2	−0.4	0.0	1.22×10^{-2}	3.8	1.9	4.2
424	116	150	2.0	2.2	0.0	+0.4	1.60×10^{-2}	3.4	1.9	3.9
425	116	150	2.0	2.2	+0.4	+0.7	-	-	-	-
426	116	150	2.0	2.2	+0.7	+1.0	-	-	-	-
427	116	150	2.2	2.4	−1.0	−0.7	-	-	-	-
428	116	150	2.2	2.4	−0.7	−0.4	-	-	-	-
429	116	150	2.2	2.4	−0.4	0.0	3.79×10^{-3}	7.4	10.6	12.9
430	116	150	2.2	2.4	0.0	+0.4	4.68×10^{-3}	6.6	12.6	14.2
431	116	150	2.2	2.4	+0.4	+0.7	-	-	-	-
432	116	150	2.2	2.4	+0.7	+1.0	-	-	-	-
433	150	200	0.0	0.2	−1.0	−0.7	6.86×10^{-3}	6.8	9.1	11.3
434	150	200	0.0	0.2	−0.7	−0.4	5.95×10^{-3}	5.1	2.5	5.7
435	150	200	0.0	0.2	−0.4	0.0	4.90×10^{-3}	4.5	2.7	5.3
436	150	200	0.0	0.2	0.0	+0.4	4.79×10^{-3}	4.7	1.6	5.0
437	150	200	0.0	0.2	+0.4	+0.7	6.20×10^{-3}	5.0	3.1	5.9
438	150	200	0.0	0.2	+0.7	+1.0	5.73×10^{-3}	8.1	11.2	13.8
439	150	200	0.2	0.4	−1.0	−0.7	5.92×10^{-3}	7.8	10.1	12.8
440	150	200	0.2	0.4	−0.7	−0.4	5.93×10^{-3}	5.1	5.2	7.3
441	150	200	0.2	0.4	−0.4	0.0	4.68×10^{-3}	4.6	2.0	5.1
442	150	200	0.2	0.4	0.0	+0.4	5.09×10^{-3}	4.2	2.1	4.7
443	150	200	0.2	0.4	+0.4	+0.7	6.21×10^{-3}	4.7	5.9	7.6
444	150	200	0.2	0.4	+0.7	+1.0	7.75×10^{-3}	6.5	8.1	10.4
445	150	200	0.4	0.6	−1.0	−0.7	5.82×10^{-3}	7.3	8.1	11.0
446	150	200	0.4	0.6	−0.7	−0.4	5.49×10^{-3}	5.4	2.2	5.9
447	150	200	0.4	0.6	−0.4	0.0	4.82×10^{-3}	4.8	1.9	5.1
448	150	200	0.4	0.6	0.0	+0.4	4.68×10^{-3}	4.7	3.3	5.7
449	150	200	0.4	0.6	+0.4	+0.7	6.57×10^{-3}	5.0	2.5	5.6
450	150	200	0.4	0.6	+0.7	+1.0	6.78×10^{-3}	6.4	7.2	9.7
451	150	200	0.6	0.8	−1.0	−0.7	4.38×10^{-3}	8.0	17.8	19.6
452	150	200	0.6	0.8	−0.7	−0.4	5.44×10^{-3}	6.5	4.0	7.7
453	150	200	0.6	0.8	−0.4	0.0	4.51×10^{-3}	4.6	2.0	5.1
454	150	200	0.6	0.8	0.0	+0.4	5.29×10^{-3}	4.2	1.7	4.6
455	150	200	0.6	0.8	+0.4	+0.7	7.18×10^{-3}	5.4	1.8	5.7
456	150	200	0.6	0.8	+0.7	+1.0	6.45×10^{-3}	6.0	11.8	13.2
457	150	200	0.8	1.0	−1.0	−0.7	3.43×10^{-3}	8.4	6.8	10.9
458	150	200	0.8	1.0	−0.7	−0.4	4.87×10^{-3}	7.4	3.0	8.0
459	150	200	0.8	1.0	−0.4	0.0	4.23×10^{-3}	5.1	1.8	5.4
460	150	200	0.8	1.0	0.0	+0.4	5.31×10^{-3}	4.5	1.6	4.7
461	150	200	0.8	1.0	+0.4	+0.7	6.56×10^{-3}	5.9	3.8	7.0
462	150	200	0.8	1.0	+0.7	+1.0	6.36×10^{-3}	5.7	3.0	6.4

Bin	M_{ee} [GeV]		$\lvert y_{ee}\rvert$		$\cos\theta^*$		σ [pb/GeV]	δ^{stat} [%]	δ^{syst} [%]	δ^{tot} [%]
463	150	200	1.0	1.2	−1.0	−0.7	2.43×10^{-3}	9.6	9.2	13.3
464	150	200	1.0	1.2	−0.7	−0.4	4.11×10^{-3}	7.0	4.8	8.5
465	150	200	1.0	1.2	−0.4	0.0	4.07×10^{-3}	5.9	3.5	6.9
466	150	200	1.0	1.2	0.0	+0.4	5.51×10^{-3}	5.0	3.5	6.2
467	150	200	1.0	1.2	+0.4	+0.7	7.39×10^{-3}	4.8	2.6	5.5
468	150	200	1.0	1.2	+0.7	+1.0	4.76×10^{-3}	6.2	4.2	7.5
469	150	200	1.2	1.4	−1.0	−0.7	1.65×10^{-3}	11.9	5.1	12.9
470	150	200	1.2	1.4	−0.7	−0.4	3.56×10^{-3}	6.6	6.4	9.2
471	150	200	1.2	1.4	−0.4	0.0	3.98×10^{-3}	6.6	4.2	7.8
472	150	200	1.2	1.4	0.0	+0.4	5.84×10^{-3}	5.3	1.9	5.6
473	150	200	1.2	1.4	+0.4	+0.7	7.54×10^{-3}	4.4	2.5	5.0
474	150	200	1.2	1.4	+0.7	+1.0	3.32×10^{-3}	7.6	3.1	8.3
475	150	200	1.4	1.6	−1.0	−0.7	4.83×10^{-4}	25.3	17.5	30.8
476	150	200	1.4	1.6	−0.7	−0.4	3.08×10^{-3}	7.3	8.9	11.5
477	150	200	1.4	1.6	−0.4	0.0	3.64×10^{-3}	7.0	5.3	8.8
478	150	200	1.4	1.6	0.0	+0.4	5.16×10^{-3}	5.2	3.2	6.1
479	150	200	1.4	1.6	+0.4	+0.7	6.50×10^{-3}	4.8	5.0	7.0
480	150	200	1.4	1.6	+0.7	+1.0	1.15×10^{-3}	14.1	10.1	17.4
481	150	200	1.6	1.8	−1.0	−0.7	-	-	-	-
482	150	200	1.6	1.8	−0.7	−0.4	2.11×10^{-3}	9.1	5.1	10.5
483	150	200	1.6	1.8	−0.4	0.0	3.43×10^{-3}	6.9	6.0	9.1
484	150	200	1.6	1.8	0.0	+0.4	5.31×10^{-3}	5.6	3.5	6.6
485	150	200	1.6	1.8	+0.4	+0.7	4.84×10^{-3}	5.9	3.2	6.7
486	150	200	1.6	1.8	+0.7	+1.0	-	-	-	-
487	150	200	1.8	2.0	−1.0	−0.7	-	-	-	-
488	150	200	1.8	2.0	−0.7	−0.4	5.68×10^{-4}	25.6	17.5	31.0
489	150	200	1.8	2.0	−0.4	0.0	3.43×10^{-3}	6.0	2.2	6.4
490	150	200	1.8	2.0	0.0	+0.4	5.29×10^{-3}	4.9	2.3	5.4
491	150	200	1.8	2.0	+0.4	+0.7	1.74×10^{-3}	12.3	3.8	12.8
492	150	200	1.8	2.0	+0.7	+1.0	-	-	-	-
493	150	200	2.0	2.2	−1.0	−0.7	-	-	-	-
494	150	200	2.0	2.2	−0.7	−0.4	-	-	-	-
495	150	200	2.0	2.2	−0.4	0.0	2.39×10^{-3}	7.2	5.2	8.8
496	150	200	2.0	2.2	0.0	+0.4	3.53×10^{-3}	5.8	2.3	6.2
497	150	200	2.0	2.2	+0.4	+0.7	-	-	-	-
498	150	200	2.0	2.2	+0.7	+1.0	-	-	-	-
499	150	200	2.2	2.4	−1.0	−0.7	-	-	-	-
500	150	200	2.2	2.4	−0.7	−0.4	-	-	-	-
501	150	200	2.2	2.4	−0.4	0.0	8.36×10^{-4}	12.4	2.4	12.6
502	150	200	2.2	2.4	0.0	+0.4	1.11×10^{-3}	10.8	2.5	11.1
503	150	200	2.2	2.4	+0.4	+0.7	-	-	-	-
504	150	200	2.2	2.4	+0.7	+1.0	-	-	-	-

Table A.1: Summary table of the three-dimensional differential cross-section measurement at Born-level. The relative statistical, systematic, and total uncertainties are also given. A luminosity uncertainty of 1.9% has not been included.

$\lvert y_{ee}\rvert$		M_{ee} [GeV]		A_{FB}	δ^{stat}	δ^{syst}	δ^{tot}
0.0	0.2	46	66	0.0025	0.009	0.007	0.011
0.0	0.2	66	80	−0.0060	0.006	0.004	0.007
0.0	0.2	80	91	0.0012	0.002	0.001	0.002
0.0	0.2	91	102	0.0028	0.002	0.001	0.002
0.0	0.2	102	116	0.0019	0.009	0.004	0.010
0.0	0.2	116	150	0.0266	0.013	0.007	0.014
0.0	0.2	150	200	−0.0291	0.025	0.016	0.029
0.2	0.4	46	66	−0.0102	0.009	0.007	0.011
0.2	0.4	66	80	−0.0280	0.006	0.004	0.008
0.2	0.4	80	91	−0.0014	0.002	0.001	0.002
0.2	0.4	91	102	0.0038	0.002	0.001	0.002
0.2	0.4	102	116	0.0254	0.009	0.004	0.010
0.2	0.4	116	150	0.0721	0.013	0.006	0.015
0.2	0.4	150	200	0.0708	0.024	0.017	0.030
0.4	0.6	46	66	−0.0258	0.009	0.007	0.011
0.4	0.6	66	80	−0.0217	0.007	0.004	0.008
0.4	0.6	80	91	0.0027	0.002	0.001	0.002
0.4	0.6	91	102	0.0121	0.002	0.001	0.002
0.4	0.6	102	116	0.0498	0.009	0.005	0.010
0.4	0.6	116	150	0.0718	0.014	0.009	0.016
0.4	0.6	150	200	0.0554	0.024	0.011	0.027
0.6	0.8	46	66	−0.0271	0.010	0.008	0.012
0.6	0.8	66	80	−0.0572	0.007	0.004	0.008
0.6	0.8	80	91	0.0018	0.002	0.001	0.002
0.6	0.8	91	102	0.0174	0.002	0.001	0.002
0.6	0.8	102	116	0.0467	0.009	0.005	0.010
0.6	0.8	116	150	0.1078	0.013	0.006	0.015
0.6	0.8	150	200	0.1379	0.024	0.015	0.028
0.8	1.0	46	66	−0.0575	0.011	0.009	0.014
0.8	1.0	66	80	−0.0597	0.007	0.004	0.008
0.8	1.0	80	91	−0.0024	0.002	0.001	0.002
0.8	1.0	91	102	0.0233	0.002	0.001	0.002
0.8	1.0	102	116	0.1131	0.009	0.006	0.011
0.8	1.0	116	150	0.1150	0.014	0.007	0.015
0.8	1.0	150	200	0.1852	0.025	0.012	0.028
1.0	1.2	46	66	−0.0447	0.010	0.008	0.013
1.0	1.2	66	80	−0.0805	0.007	0.005	0.008
1.0	1.2	80	91	0.0013	0.002	0.001	0.002
1.0	1.2	91	102	0.0277	0.002	0.001	0.002
1.0	1.2	102	116	0.1044	0.009	0.005	0.011
1.0	1.2	116	150	0.1715	0.014	0.007	0.015
1.0	1.2	150	200	0.2493	0.024	0.015	0.028

$\lvert y_{ee}\rvert$		M_{ee} [GeV]		A_{FB}	δ^{stat}	δ^{syst}	δ^{tot}
1.2	1.4	46	66	−0.0698	0.010	0.009	0.014
1.2	1.4	66	80	−0.1035	0.007	0.004	0.008
1.2	1.4	80	91	−0.0004	0.002	0.001	0.002
1.2	1.4	91	102	0.0334	0.002	0.001	0.002
1.2	1.4	102	116	0.1345	0.010	0.007	0.012
1.2	1.4	116	150	0.2111	0.014	0.007	0.016
1.2	1.4	150	200	0.2901	0.025	0.015	0.029
1.4	1.6	46	66	−0.1032	0.011	0.009	0.014
1.4	1.6	66	80	−0.1279	0.007	0.005	0.009
1.4	1.6	80	91	−0.0030	0.002	0.001	0.002
1.4	1.6	91	102	0.0369	0.002	0.001	0.002
1.4	1.6	102	116	0.1410	0.011	0.006	0.012
1.4	1.6	116	150	0.1970	0.016	0.007	0.017
1.4	1.6	150	200	0.2796	0.028	0.024	0.037
1.6	1.8	46	66	−0.1009	0.011	0.011	0.016
1.6	1.8	66	80	−0.1206	0.008	0.006	0.010
1.6	1.8	80	91	−0.0015	0.002	0.001	0.003
1.6	1.8	91	102	0.0399	0.002	0.001	0.003
1.6	1.8	102	116	0.1543	0.013	0.014	0.019
1.6	1.8	116	150	0.2568	0.018	0.008	0.020
1.6	1.8	150	200	0.2935	0.031	0.019	0.037
1.8	2.0	46	66	−0.0846	0.013	0.011	0.017
1.8	2.0	66	80	−0.1059	0.010	0.006	0.012
1.8	2.0	80	91	−0.0002	0.003	0.002	0.003
1.8	2.0	91	102	0.0401	0.003	0.001	0.003
1.8	2.0	102	116	0.1631	0.015	0.008	0.017
1.8	2.0	116	150	0.1926	0.023	0.035	0.042
1.8	2.0	150	200	0.2749	0.037	0.014	0.039
2.0	2.2	46	66	−0.1048	0.014	0.012	0.018
2.0	2.2	66	80	−0.1080	0.012	0.009	0.015
2.0	2.2	80	91	−0.0059	0.003	0.002	0.004
2.0	2.2	91	102	0.0313	0.003	0.002	0.004
2.0	2.2	102	116	0.1527	0.018	0.010	0.021
2.0	2.2	116	150	0.1358	0.025	0.010	0.027
2.0	2.2	150	200	0.1926	0.044	0.020	0.049
2.2	2.4	46	66	−0.0341	0.025	0.021	0.032
2.2	2.4	66	80	−0.0510	0.021	0.014	0.026
2.2	2.4	80	91	−0.0068	0.006	0.003	0.007
2.2	2.4	91	102	0.0169	0.006	0.003	0.007
2.2	2.4	102	116	0.0710	0.033	0.024	0.041
2.2	2.4	116	150	0.1056	0.049	0.078	0.092
2.2	2.4	150	200	0.1400	0.081	0.012	0.082

Table A.2: Summary table of the forward-backward asymmetry measurement at Born-level. The absolute statistical, systematic, and total uncertainties are also given.

Appendix B

Central-Forward Measurement

In addition to the measurement outlined in the main chapters of this dissertation, a secondary measurement of Drell-Yan production was made by the author of this dissertation using events with one electron measured in the central region ($|\eta| < 2.47$) and one in the forward regions ($2.5 < |\eta| < 4.9$) of the ATLAS detector. An event display of a central-forward dielectron event can be seen in Figure B.1. This measurement was originally done by [110]. Recommendations from the EGamma group were, however, subsequently updated which prompted the need for this measurement to be remade. All results shown in this chapter were produced by the author.

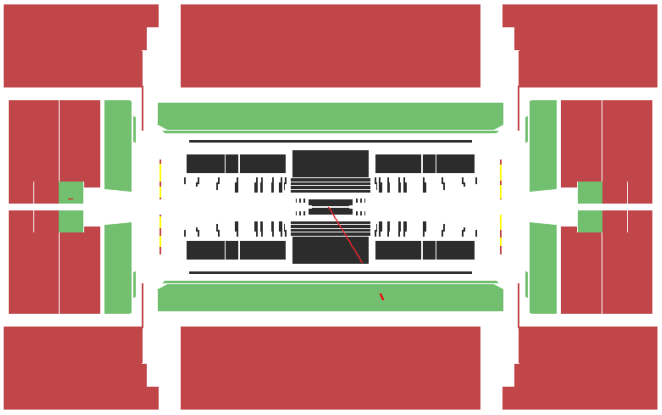

Figure B.1: Cross-sectional display of an ATLAS event with two electrons, one central and one forward, in the final state. Note that there is no track leading to the energy cluster in the FCal on the left-hand side of the ATLAS detector.

Since the inner detector has a coverage of $|\eta| < 2.5$, forward electrons are reconstructed and identified solely using information from the forward calorimeter making

them more challenging to measure than central electrons. The pseudorapidity of the forward electron, however, allows for this measurement to be made up to $|y_{ee}| = 3.6$ in dielectron rapidity making it possible to probe extremal values of x in PDF phase space (see Figure 2.5). Furthermore, at high $|y_{ee}|$ dilution effects decrease as it becomes easier to distinguish the direction of the quark from that of the antiquark making this measurement more sensitive to forward-backward symmetry effects.

The physics goals of the *central-forward* measurement are the same as the *central-central* measurement: to provide data that can be used to improve upon the existing measurements of the PDFs of the proton and the weak mixing angle θ_{W}. In the following sections of this appendix chapter, the central-forward measurement is described in detail.

B.1 Measurement Overview

As in the central-central analysis, the central-forward three-dimensional differential cross-section is measured using the following equation:

$$\left(\frac{d^3\sigma}{dM_{ee}d|y_{ee}|d\cos\theta^*}\right)_{\ell mn} = C_{\ell mn}\frac{M^{ijk}_{\ell mn}(N^{\mathrm{sig}}_{ijk} - N^{\mathrm{bkg}}_{ijk})}{\mathcal{L}(\delta M_{ee})_\ell(\delta|y_{ee}|)_m(\delta\cos\theta^*)_n}, \tag{B.1}$$

for $i, j, k, \ell, m, n = 1, 2, 3, ...$, where

- i, j, and k are bin indices corresponding to M_{ee}, $|y_{ee}|$, and $\cos\theta^*$ bins, respectively, at reconstruction-level;
- ℓ, m, and n are bin indices corresponding to M_{ee}, $|y_{ee}|$, and $\cos\theta^*$ bins, respectively, at generator-level;
- N^{sig}_{ijk} is the number of candidate Drell-Yan or signal events found in data;
- N^{bkg}_{ijk} is the estimated number of background events;
- $M^{ijk}_{\ell mn}$ is a matrix determined from MC which converts the measurement from reconstruction-level to generator- or more specifically dressed-level;
- $\mathcal{L}$ is the integrated luminosity of the data set;
- $(\delta M_{ee})_\ell$, $(\delta|y_{ee}|)_m$, and $(\delta\cos\theta^*)_n$ are bin widths in the three dimensions of interest;

- $C_{\ell mn}$ is a correction factor used to correct the measurement from dressed- to Born-level.

The measurement is made in a fiducial volume defined by the following cuts:

$$66 < M_{ee} < 150\,\text{GeV},\ |\eta^{\text{ctr}}| < 2.4,\ p_T^{\text{ctr}} > 25\,\text{GeV},\ 2.5 < |\eta^{\text{fwd}}| < 4.9,\ p_T^{\text{fwd}} > 20\,\text{GeV},$$

where η^{ctr} and p_T^{ctr} are the pseudorapidity and transverse momentum of the central electron and η^{fwd} and p_T^{fwd} are those of the forward electron.

B.2 Analysis Binning

Requiring a forward electron reduces the number of events available for analysis and the three-dimensional binning chosen reflects this. The following binning is used in the central-forward analysis:

- $M_{ee} = [66, 80, 91, 102, 116, 150]$ GeV,
- $|y_{ee}| = [1.2, 1.6, 2.0, 2.4, 2.8, 3.6]$,
- $\cos\theta^* = [-1.0, -0.7, -0.4, 0.0, 0.4, 0.7, 1.0]$.

With 5 bins in M_{ee}, 5 in $|y_{ee}|$, and 6 in $\cos\theta^*$, there are a total of $5 \times 5 \times 6 = 150$ analysis bins. Note that the invariant mass bins $M_{ee} \in [46, 66]$ and $[150, 200]$ GeV present in the central-central analysis are not included in this analysis due to too few events measured in these bins. Although having fewer and coarser bins in $|y_{ee}|$ than the central-central measurement, the central-forward $|y_{ee}|$ range extends to much larger values. The $\cos\theta^*$ binning is the same in both analyses. As was the case in the central-central measurement, analysis bins with less than 25 expected signal events are rejected from the final measurement.

B.3 Event Selection

Events used in this measurement are required to be listed in the analysis GRL. They must pass at least one of two central electron triggers, one requiring the central electron to have $p_T^{\text{ctr}} > 24$ GeV and satisfy cluster isolation requirements and medium identification and the other requiring $p_T^{\text{ctr}} > 60$ GeV and medium identification.

Events must not be flagged by the LAr calorimeters for noise bursts or data integrity problems. There must be at least one reconstructed primary vertex with three or more associated tracks in each event.

Cuts on the electrons are applied by first requiring that the central electron be reconstructed using the sliding window algorithm and the forward electron using the topological algorithm. Having checked the central electron for object quality, the kinematic cut $|\eta^{\text{ctr}}| < 2.4$ excluding the crack region, $1.37 < |\eta^{\text{ctr}}| < 1.52$, between the EM barrel and end-cap is applied. For the forward electron, a pseudorapidity requirement of $2.5 < |\eta^{\text{fwd}}| < 4.9$ is applied excluding the transition region, $3.00 < |\eta^{\text{fwd}}| < 3.35$, between the end-cap and forward calorimeter. Additionally, the region $2.70 < |\eta^{\text{fwd}}| < 2.80$ is excluded from the measurement due to poor energy calibration. Next, transverse momentum cuts are made which require $p_T^{\text{ctr}} > 25$ GeV and $p_T^{\text{fwd}} > 20$ GeV.

Tight identification is required of the central electron and forward tight identification of the forward electron. These requirements greatly suppress the large multijet background that would otherwise overwhelm the signal. A track isolation cut is made on the central electron requiring the ratio of the transverse momentum measured from the inner detector surrounding the electron in a cone of radius $\Delta R = 0.20$ to its transverse momentum p_T^{ctr} to be less than 0.14: $p_T^{\text{ctr}} Cone20/p_T^{\text{ctr}} < 0.14$.

Finally, electron pairs or Z/γ^* bosons are constructed in events with exactly one central and one forward electron. Their invariant mass must be in the range $66 < M_{ee} < 150$ GeV. Note that no charge requirement can be made on the electron pair without tracking detectors in the forward regions. A summary of the signal selection used in the central-forward measurement is given in Table B.1.

B.4 Forward Electron Energy Corrections

In the process of making this measurement it was discovered that the electron energy scale α and resolution smearing β corrections provided by the EGamma performance group (see Section 5.3) for forward electrons were not sufficient in resolving some of the differences in Monte Carlo and data; e.g. the energy resolution of the simulated FCal was found to be too narrow. To bring the forward electron energy responses into better agreement, a private derivation of energy scale and resolution smearing factors is performed and applied *in addition* to the official recommendations. The additional energy scale α^{fwd} (applied to data) and resolution smearing β^{fwd} (applied

Requirement	N_{data}	$\epsilon^{\text{abs}}_{\text{data}}$ [%]	$\epsilon^{\text{rel}}_{\text{data}}$[%]	N_{MC}	$\epsilon^{\text{abs}}_{\text{MC}}$[%]	$\epsilon^{\text{rel}}_{\text{MC}}$[%]
Good runs list	6.943×10^8	100.0	100.0	3.810×10^7	100.0	100.0
Trigger	2.503×10^8	36.05	36.05	1.375×10^7	36.09	36.09
LAr event quality	2.498×10^8	35.98	99.78	1.375×10^7	36.09	100.0
Vertex with ≥ 3 tracks	2.492×10^8	35.89	99.75	1.366×10^7	35.87	99.37
Reconstruction algorithms	1.813×10^8	26.12	72.78	1.012×10^7	26.57	74.08
Electron object quality	1.806×10^8	26.01	99.59	1.010×10^7	26.52	99.80
$\lvert\eta^{\text{ctr}}\rvert < 2.4$, $2.5 < \lvert\eta^{\text{fwd}}\rvert < 4.9$	1.780×10^8	25.64	98.58	1.004×10^7	26.36	99.40
Exclude $1.37 < \lvert\eta^{\text{ctr}}\rvert < 1.52$	1.674×10^8	24.11	94.04	9.808×10^6	25.75	97.69
Exclude $3.00 < \lvert\eta^{\text{fwd}}\rvert < 3.35$	1.560×10^8	22.47	93.19	9.062×10^6	23.79	92.39
Exclude $2.70 < \lvert\eta^{\text{fwd}}\rvert < 2.80$	1.454×10^8	20.94	93.16	8.431×10^6	22.13	93.04
$p_T^{\text{ctr}} > 25$ GeV	1.426×10^8	20.54	98.09	8.402×10^6	22.06	99.66
$p_T^{\text{fwd}} > 20$ GeV	1.120×10^7	1.613	7.854	1.944×10^6	5.103	23.14
Tight identification	5.972×10^6	0.860	53.33	1.710×10^6	4.490	87.98
Forward tight identification	1.077×10^6	0.155	18.04	1.071×10^6	2.811	62.61
Track isolation	1.066×10^6	0.153	98.91	1.069×10^6	2.805	99.79
One central-forward pair	1.063×10^6	0.153	99.75	1.066×10^6	2.799	99.78
$66 < M_{ee} < 150$ GeV	1.029×10^6	0.148	96.75	1.044×10^6	2.741	97.93

Table B.1: Number of events in data and signal Monte Carlo at different stages of the signal selection. Efficiency ϵ^{abs} shows the percentage of events remaining after each cut with respect to the initial number of events in the GRL and efficiency ϵ^{rel} shows the percentage of events with respect to the previous selection requirement.

to signal MC) corrections are derived in the same bins as the official corrections:

$$\eta^{\text{fwd}} = [\pm2.50, \pm2.60, \pm2.70, \pm2.80, \pm2.90, \pm3.00, \pm3.35, \pm3.60, \pm4.00, \pm4.90].$$

First the energy scale correction is determined. Having applied the official correction (as shown in Equation (5.3)), another factor of $1/(1+\alpha^{\text{fwd}})$ is applied to energies E_{data} measured in data:

$$E^{\text{corr}}_{\text{data}} = \left(\frac{1}{1+\alpha^{\text{fwd}}}\right)\left(\frac{1}{1+\alpha}\right)E_{\text{data}}, \tag{B.2}$$

where α^{fwd} is varied from ±0.0005, ±0.001, 0.0015, ..., to ±0.01, producing 40 new data samples each with a different value of α^{fwd} applied. To illustrate, plots of the first twelve of these data distributions can be seen in Figure B.2 which shows invariant mass distributions where the forward electron has pseudorapidity in the range $-4.90 < \eta^{\text{fwd}} < -4.00$. These distributions are then compared to model predictions (signal MC events plus background) in the range $80 < M_{ee} < 102$ GeV using a χ^2-test statistic [111] that performs a shape comparison of the two. Of the 40 data samples, the one that yields the smallest χ^2 or most closely matches the prediction is taken as

the additional energy scale correction. For the $-4.90 < \eta^{\text{fwd}} < -4.00$ example shown, $\alpha^{\text{fwd}}_{\text{min}} = -0.001$ gives the best fit value, $\chi^2_{\text{min}} = 134.967$. This corresponds to the plot in the second row, first column in Figure B.2. Electrons in $-4.90 < \eta^{\text{fwd}} < -4.00$ therefore have an additional scale of $\alpha^{\text{fwd}}_{\text{min}} = -0.001$ applied.

Having determined and applied the optimal additional energy scale correction, the additional resolution smearing correction is determined. In addition to the EGamma correction (see Equation (5.5)), a smearing is applied in the form of a Gaussian random number centred at the energy of the electron with a relative standard deviation of β^{fwd}:

$$\frac{\sigma_{\text{data}}}{E_{\text{data}}} = \frac{\sigma_{\text{MC}}}{E_{\text{MC}}} \oplus \beta \oplus \beta^{\text{fwd}}. \tag{B.3}$$

The method used here is similar to what was done for the additional scale. In the same η^{fwd} bins, 40 signal MC samples are produced, each having a unique amount of additional Gaussian smearing applied varying from 0.001, 0.002, 0.003, ..., to 0.04. The β^{fwd} value that yields the minimal χ^2 value is taken as the smearing needed to help resolve the differences between data and prediction. Figure B.3 shows twelve (of the 40) invariant mass spectra for $-4.90 < \eta^{\text{fwd}} < -4.00$. The value of β^{fwd} that gives the best agreement, $\chi^2_{\text{min}} = 20.3867$, corresponds to $\beta^{\text{fwd}}_{\text{min}} = 0.034$ shown in the bottom row, middle. Therefore, forward electrons in the range $-4.90 < \eta^{\text{fwd}} < -4.00$ have an additional Gaussian smearing of $\beta^{\text{fwd}}_{\text{min}} = 0.034$ applied.

One source of uncertainty on α^{fwd} and β^{fwd} is determined by finding the values of α^{fwd} and β^{fwd} that give $\chi^2_{\text{min}}+1$. Defining these as $\alpha^{\text{fwd}}_{\text{min}+1}$ and $\beta^{\text{fwd}}_{\text{min}+1}$, the uncertainties are estimated as

$$\delta\alpha^{\text{fwd}}_{\chi^2} = |\alpha^{\text{fwd}}_{\text{min}+1} - \alpha^{\text{fwd}}_{\text{min}}|, \qquad \delta\beta^{\text{fwd}}_{\chi^2} = |\beta^{\text{fwd}}_{\text{min}+1} - \beta^{\text{fwd}}_{\text{min}}|. \tag{B.4}$$

For the $-4.90 < \eta^{\text{fwd}} < -4.00$ example, the 1-sigma values are $\alpha^{\text{fwd}}_{\text{min}+1} = -0.0005$ and $\beta^{\text{fwd}}_{\text{min}+1} = 0.033$; hence

$$\delta\alpha^{\text{fwd}}_{\chi^2} = 0.0005,$$
$$\delta\beta^{\text{fwd}}_{\chi^2} = 0.001.$$

A second source of uncertainty due to the choice of fit region, $80 < M_{ee} < 102$ GeV, is considered. This uncertainty is estimated by varying the range to $76 < M_{ee} < 106$ GeV, widening it, and to $84 < M_{ee} < 88$ GeV, narrowing it, and the usual procedure is followed using these varied fit ranges. The maximum difference between the nominal

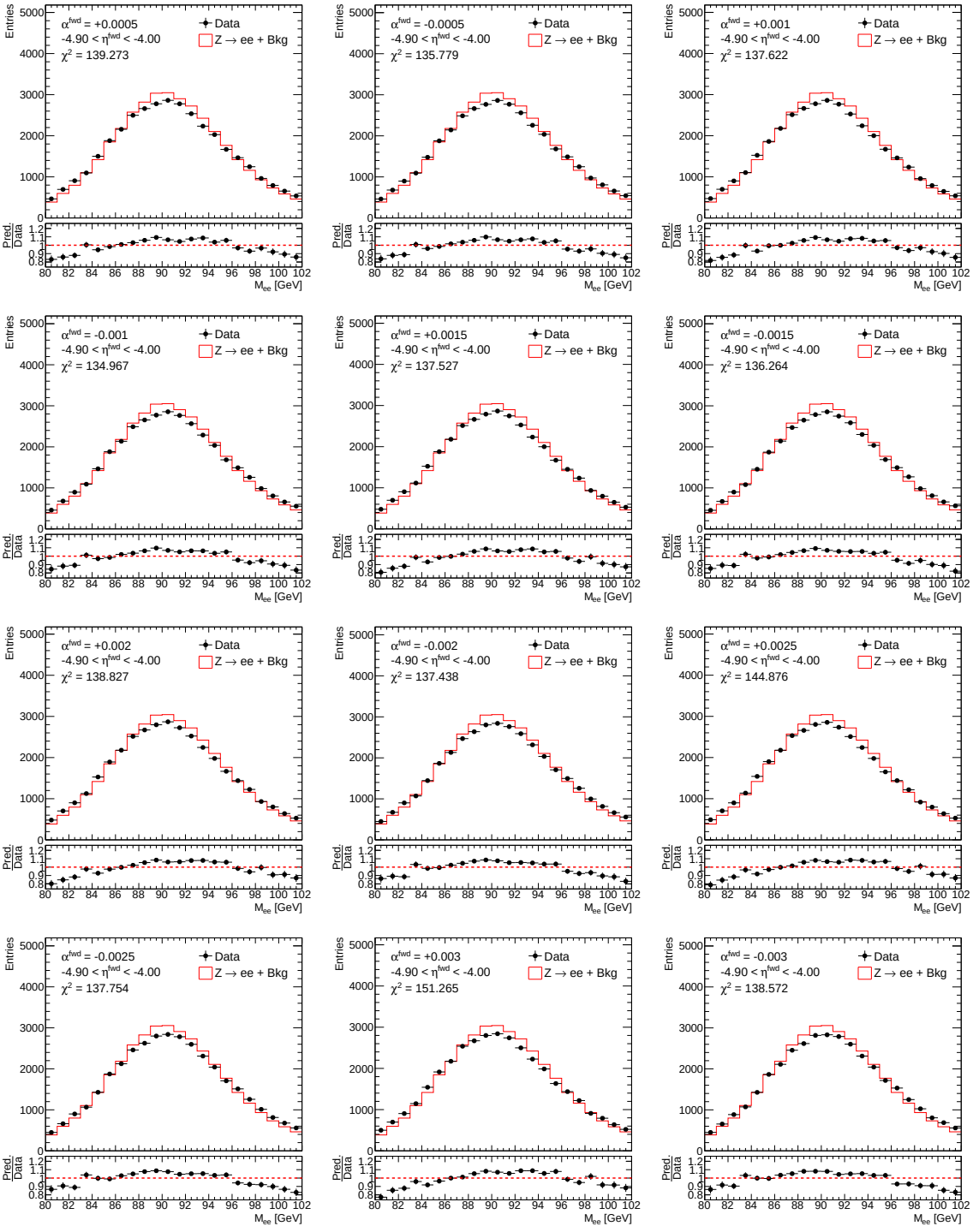

Figure B.2: Data with additional forward electron energy scale corrections applied plotted with model (signal MC plus background) predictions.

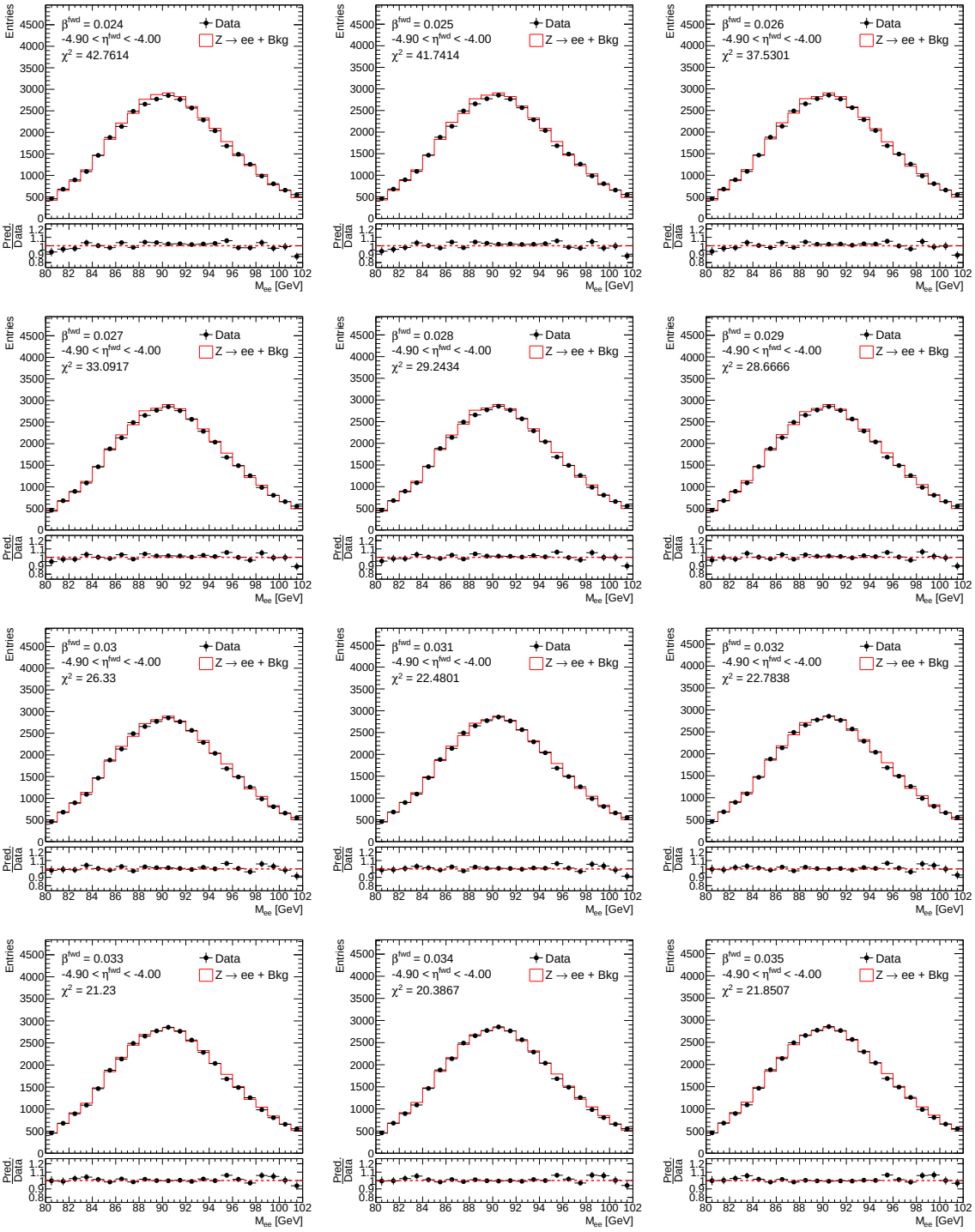

Figure B.3: Signal MC with additional forward electron energy resolution corrections applied plotted with data.

values of $\alpha^{\text{fwd}}_{\text{min}}$ and $\beta^{\text{fwd}}_{\text{min}}$ and the results from widening ($\alpha^{\text{fwd}}_{\text{min}+}$ and $\beta^{\text{fwd}}_{\text{min}+}$) and narrowing ($\alpha^{\text{fwd}}_{\text{min}-}$ and $\beta^{\text{fwd}}_{\text{min}-}$) the mass range are taken as systematic uncertainties:

$$\delta\alpha^{\text{fwd}}_{M_{ee}} = \max(\alpha^{\text{fwd}} - \alpha^{\text{fwd}}_{\text{min}+},\, \alpha^{\text{fwd}} - \alpha^{\text{fwd}}_{\text{min}-}),$$
$$\delta\beta^{\text{fwd}}_{M_{ee}} = \max(\beta^{\text{fwd}} - \beta^{\text{fwd}}_{\text{min}+},\, \beta^{\text{fwd}} - \beta^{\text{fwd}}_{\text{min}-}).$$

In the end, the additional forward electron energy corrections are quoted as

$$\alpha^{\text{fwd}} = \alpha^{\text{fwd}}_{\text{min}} \pm \delta\alpha^{\text{fwd}}_{\chi^2} \pm \delta\alpha^{\text{fwd}}_{M_{ee}},$$
$$\beta^{\text{fwd}} = \beta^{\text{fwd}}_{\text{min}} \pm \delta\beta^{\text{fwd}}_{\chi^2} \pm \delta\beta^{\text{fwd}}_{M_{ee}}.$$

Summarized in Figure B.4 are the private corrections plotted with the EGamma α and β values (top) and their uncertainties (bottom). This plot shows that for most η^{fwd} bins, the corrections derived here are consistent with those from EGamma. A few bins in the β^{fwd} plots show, however, some inconsistencies implying that these bins are under-smeared by the official recommendations.

In a final step, a second set of the energy corrections are determined using the results of the first as inputs. Plotted in Figure B.5 are the scale and smearing factors obtained from the second iteration which show that the results are consistent with zero. Consequently, no further iterations were performed. In the end, both sets of corrections are used in the central-forward measurement. The behaviour of the χ^2_{min} values at each step in the derivation is presented in Table B.2. Following the first column which gives the η^{fwd} bin, the χ^2_{min} values from applying only the EGamma corrections, α^{fwd} to the data, both α^{fwd} to the data and β^{fwd} to the signal MC, and the effect of the second iteration are shown.

Figure B.6 shows invariant mass distributions before and after applying these corrections for the most improved η^{fwd} bins. In addition to ratios of prediction to data, the bottom panels of these plots show uncertainty bands which include the systematics due to the EGamma and private energy corrections, efficiency scale factors, charge misidentification, and multijet background estimation. The bins showing the greatest improvement are $\eta^{\text{fwd}} \in [-2.90, -2.80]$ and $[+2.80, +2.90]$ while the other bins plotted in the figure are moderately improved. In these M_{ee} distributions, it can be seen that the predicted Z-peak without the private corrections is more narrow than the observed peak. This means that the simulated energy resolution is too narrow compared to the resolution of the FCal.

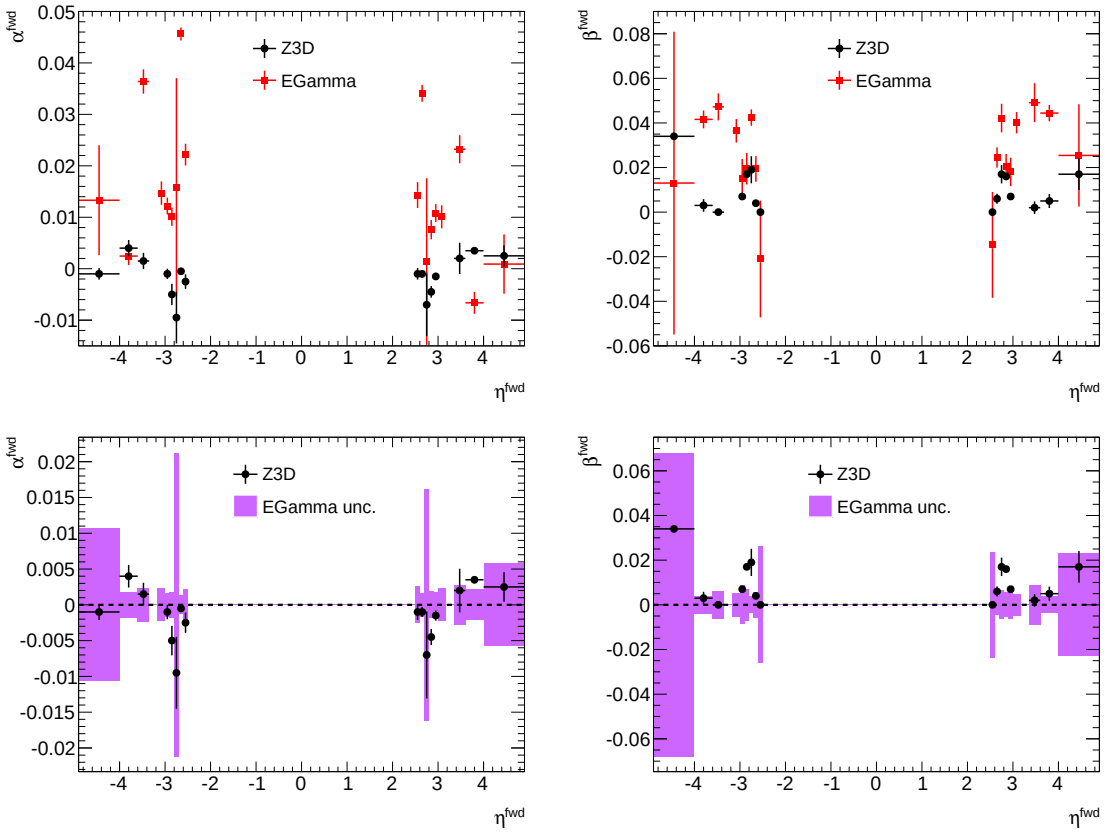

Figure B.4: Additional energy scale and smearing corrections applied to forward electrons. The top row compares the central values obtained here with those derived by EGamma and the bottom set of plots compares the private corrections with the uncertainties on the EGamma corrections.

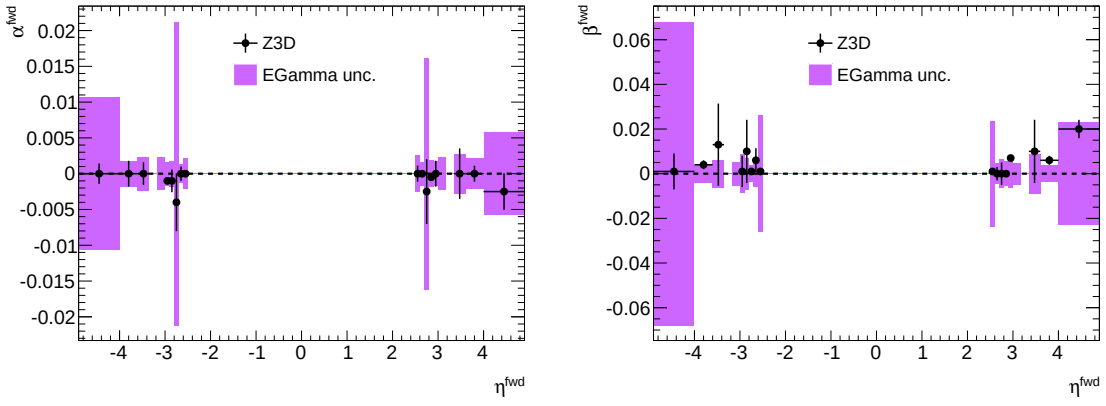

Figure B.5: Second iteration of the additional energy scale and smearing corrections applied to forward electrons. The results in most bins are consistent with zero hence no further iterating was done.

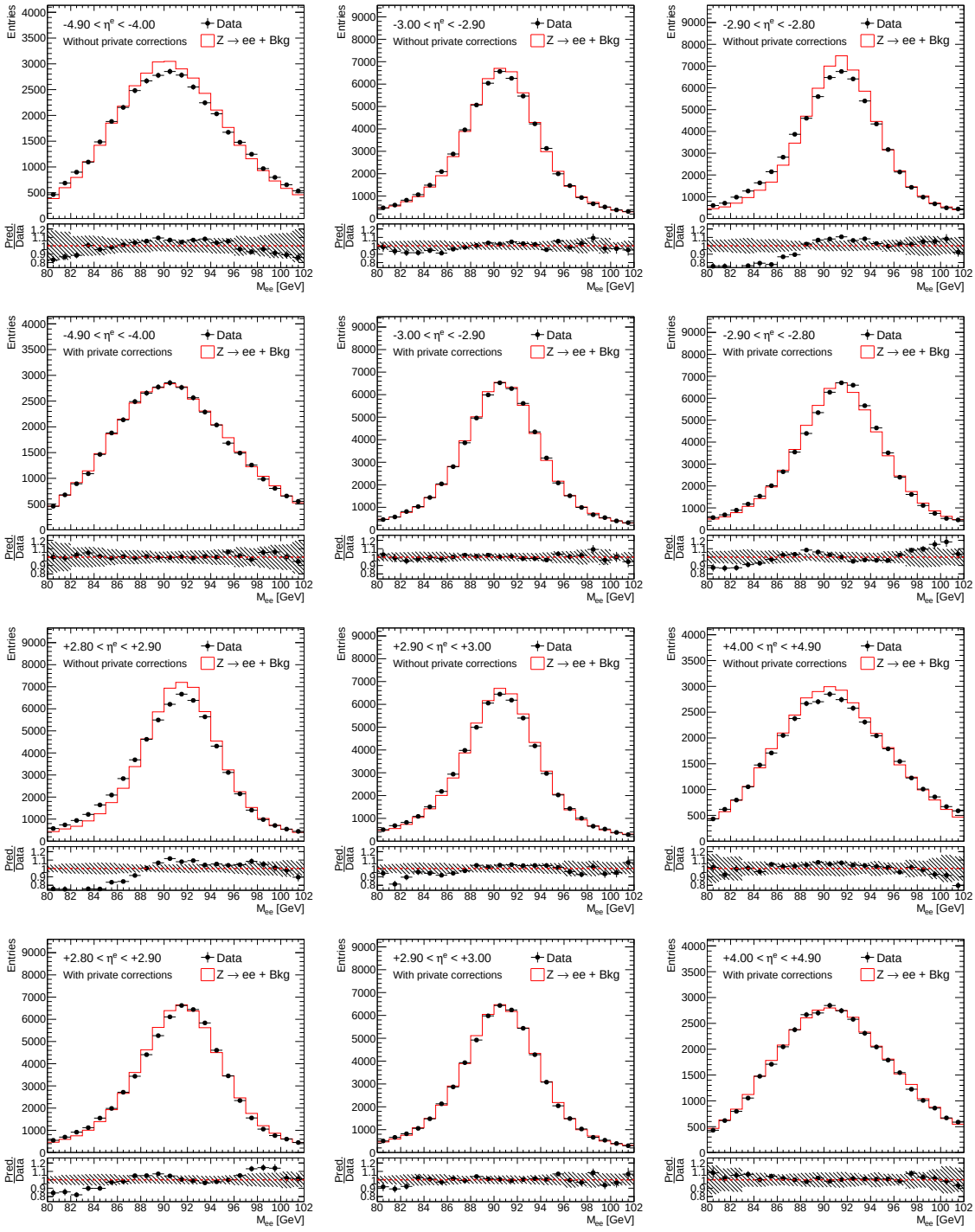

Figure B.6: Invariant mass distributions using only the EGamma corrections (odd numbered rows) and both the EGamma and private corrections (even numbered rows).

η^{fwd} bin	EGamma	α^{fwd} applied	β^{fwd} applied	Second iteration
$-4.90, -4.00$	137.2	134.9	20.4	19.6
$-4.00, -3.60$	90.5	52.8	48.7	46.4
$-3.60, -3.35$	83.6	77.5	77.5	76.0
$-3.00, -2.90$	66.9	55.5	23.8	18.3
$-2.90, -2.80$	583.5	463.5	154.9	149.7
$-2.80, -2.70$	1993.7	1453.9	719.3	625.1
$-2.70, -2.60$	48.3	44.4	23.6	22.3
$-2.60, -2.50$	245.3	214.1	214.1	211.9
$+2.50, +2.60$	94.9	88.3	88.3	87.4
$+2.60, +2.70$	133.5	127.4	80.2	80.2
$+2.70, +2.80$	1172.2	960.3	415.0	404.4
$+2.80, +2.90$	588.8	454.0	167.4	162.9
$+2.90, +3.00$	93.3	79.1	36.6	34.8
$+3.35, +3.60$	133.3	119.5	119.1	118.3
$+3.60, +4.00$	98.5	54.2	36.8	34.0
$+4.00, +4.90$	83.8	80.9	32.3	23.8

Table B.2: χ^2_{min} values from comparisons between data and prediction, applying only the EGamma corrections, the additional scale, the scale and smearing together, and a second iteration.

B.5 Event and Electron Corrections

The pileup, z-vertex, k-factor, and lineshape corrections discussed in Section 4.5 are also applied in the central-forward analysis. Furthermore, the EGamma charge misidentification corrections are applied to signal MC, specifically the simulated central electron. As for energy corrections, EGamma electron energy scale and resolution corrections are applied to data and MC, respectively, along with the private corrections derived specially for this measurement. Finally, reconstruction, tight identification, trigger, isolation, and forward tight identification scale factors [94] are used to match the efficiencies in MC to what is observed in data.

B.6 Background Estimation

Exactly like the central-central analysis, the Monte Carlo background, which is estimated using the samples listed in Tables 4.3 and 4.4, is defined as the background from the processes illustrated as Feynman diagrams in Section 2.3.1. Their contribution to this analysis is estimated by performing signal selection on the samples and

normalizing the resulting histograms to the integrated luminosity of the data. As in the central-central analysis, the remaining multijet background is estimated using the template method.

B.6.1 The Template Method

The same technique described in Section 7.2.1 is used in the central-forward analysis. A template selection is required to obtain a data sample enriched with multijet events and a discriminating variable is needed to determine the template normalization.

Template Selection

The central-forward signal and template selections share many of the same cuts, but the following two differences exist between them:

- The tight identification requirement on the central electron used in signal selection is removed. Instead, it must satisfy medium identification and fail tight.
- The forward electron must fail forward tight identification.

By making these requirements, the data events that pass are likely to contain multijet events along with some non-negligible contamination coming mostly from $Z/\gamma^* \to ee$ and $W \to e\nu$ events. To minimize this contamination, the template selection is also applied to the signal and background Monte Carlo samples and the selected events are subtracted from the data template sample.

In Figure B.7, template events distributed in M_{ee} and $\cos\theta^*$ can be seen. Note that the resulting M_{ee} template distribution is smooth, as expected, with a small bump near the Z-peak coming from the aforementioned $Z/\gamma^* \to ee$ contamination. Also, the $\cos\theta^*$ distribution is symmetric about zero which is expected since multijet events do not exhibit forward-backward asymmetry. This symmetry allows template events in $\cos\theta^*$ bins with the same absolute value to be summed effectively increasing the available statistics two-fold.

Template Normalization

In some bins, it was found that the use of $E_T^{\rm ctr} Cone30/E_T^{\rm ctr}$ of the central electron as the discriminating variable[1] was underestimating the multijet background in many of

[1]The discriminating variable in the central-central analysis uses a cone of radius $\Delta R = 0.20$ while this analysis uses $\Delta R = 0.30$.

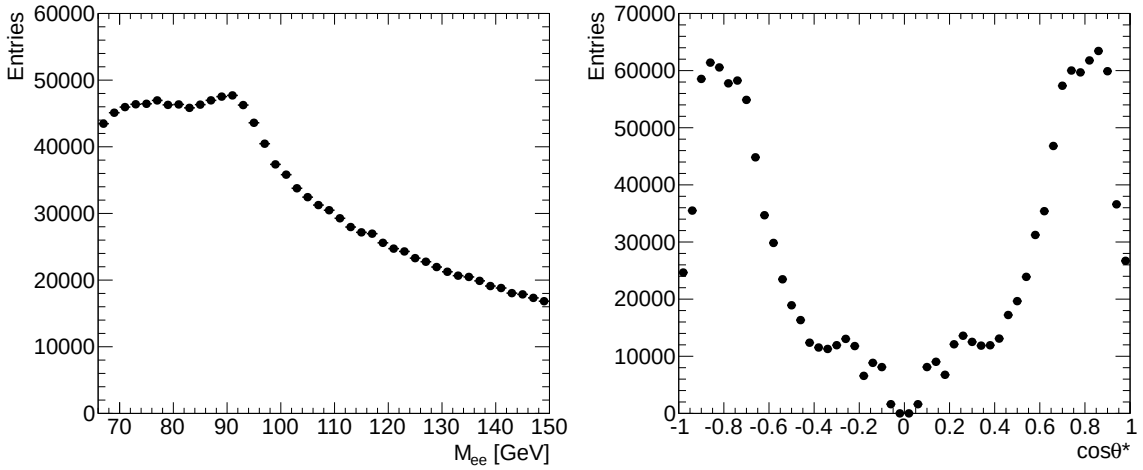

Figure B.7: M_{ee} and $\cos\theta^*$ distributions of the selected template events.

the analysis bins. Too few events were populating the tail regions which resulted in unreliable values of λ. As a solution, the transverse momentum p_T^{fwd} of the forward electron was also used as a discriminating variable. The p_T^{fwd} distribution of electrons has a different shape compared to the transverse momentum distribution of jets which tends to peak at lower values than electrons making p_T^{fwd} a viable discriminating variable. Calculations using $E_T^{\text{ctr}}Cone30/E_T^{\text{ctr}}$ are performed for the Z-peak bins, $M_{ee} \in [80, 91]$ and $[91, 102]$ GeV, while p_T^{fwd} is used for the off-peak bins, $M_{ee} \in [66, 80]$, $[102, 116]$, and $[116, 150]$ GeV.

Several $E_T^{\text{ctr}}Cone30/E_T^{\text{ctr}}$ and p_T^{fwd} plots can be seen in Figures B.8 and B.9, respectively. The tail region in the λ-calculations using $E_T^{\text{ctr}}Cone30/E_T^{\text{ctr}}$ is defined following the scheme described in Section 7.2.1. As for p_T^{fwd}, the left edge of the normalization region is chosen to be the minimum p_T^{fwd} value of 20 GeV. The right edge starts at the largest p_T^{fwd} bin with at least one entry and is moved to the left until a bin with at least ten entries is found. In Figure B.9, the multijet-rich normalization region is enclosed by the dashed vertical red lines.

Multijet Background Uncertainty

The following sources of uncertainties on the multijet background estimate are considered:

1. A statistical component of the uncertainty is evaluated using the bootstrap method. One hundred replicas of the signal and template histograms produced

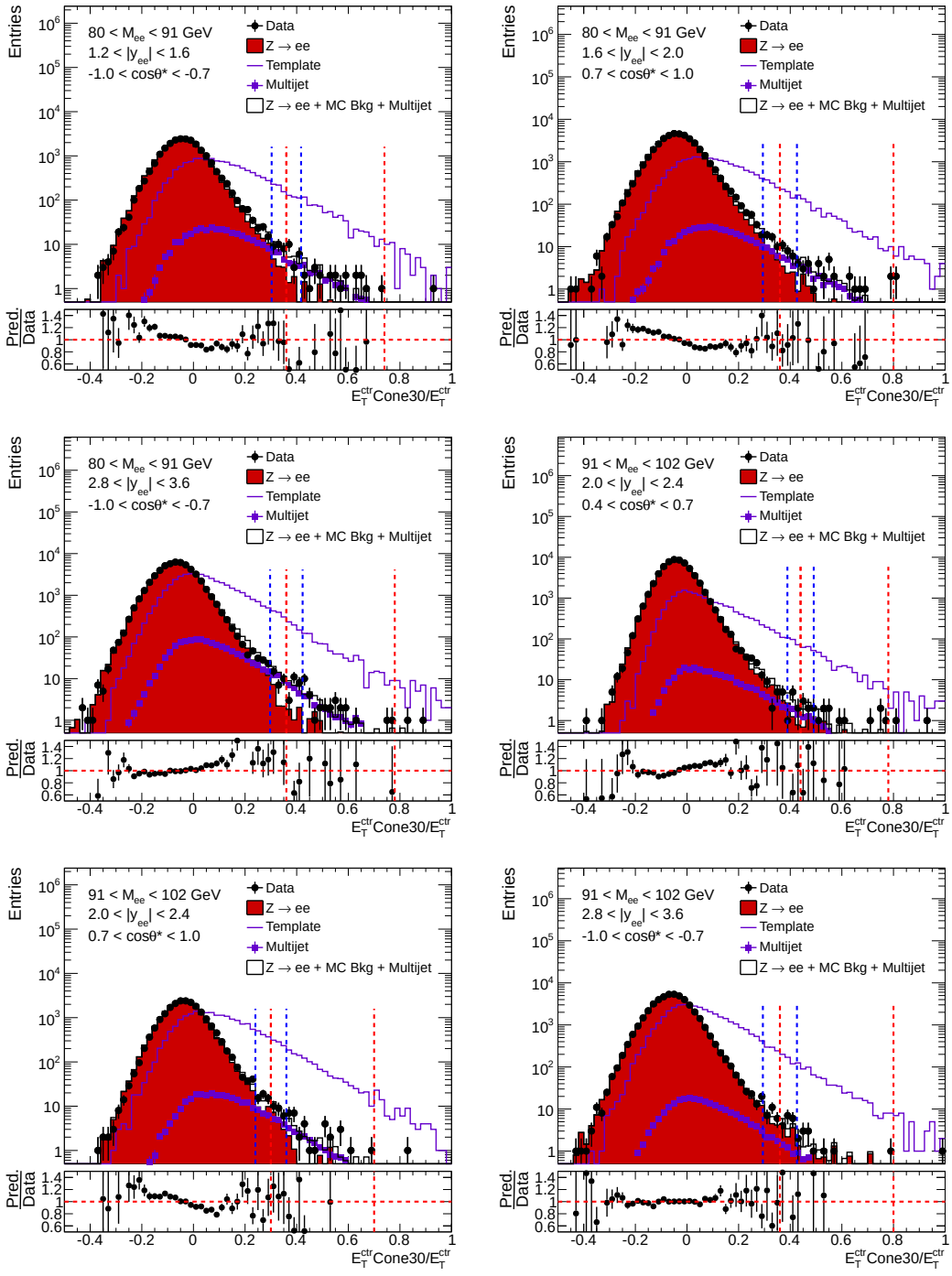

Figure B.8: Relative isolation distributions for several three-dimensional analysis bins. Shown are the data and signal MC histograms obtained from signal selection along with the template distribution and corresponding multijet estimate. The prediction or sum of the signal MC and total background is plotted as well and its ratio with the data is shown in the bottom panels of these plots. The dashed vertical lines are explained in the text.

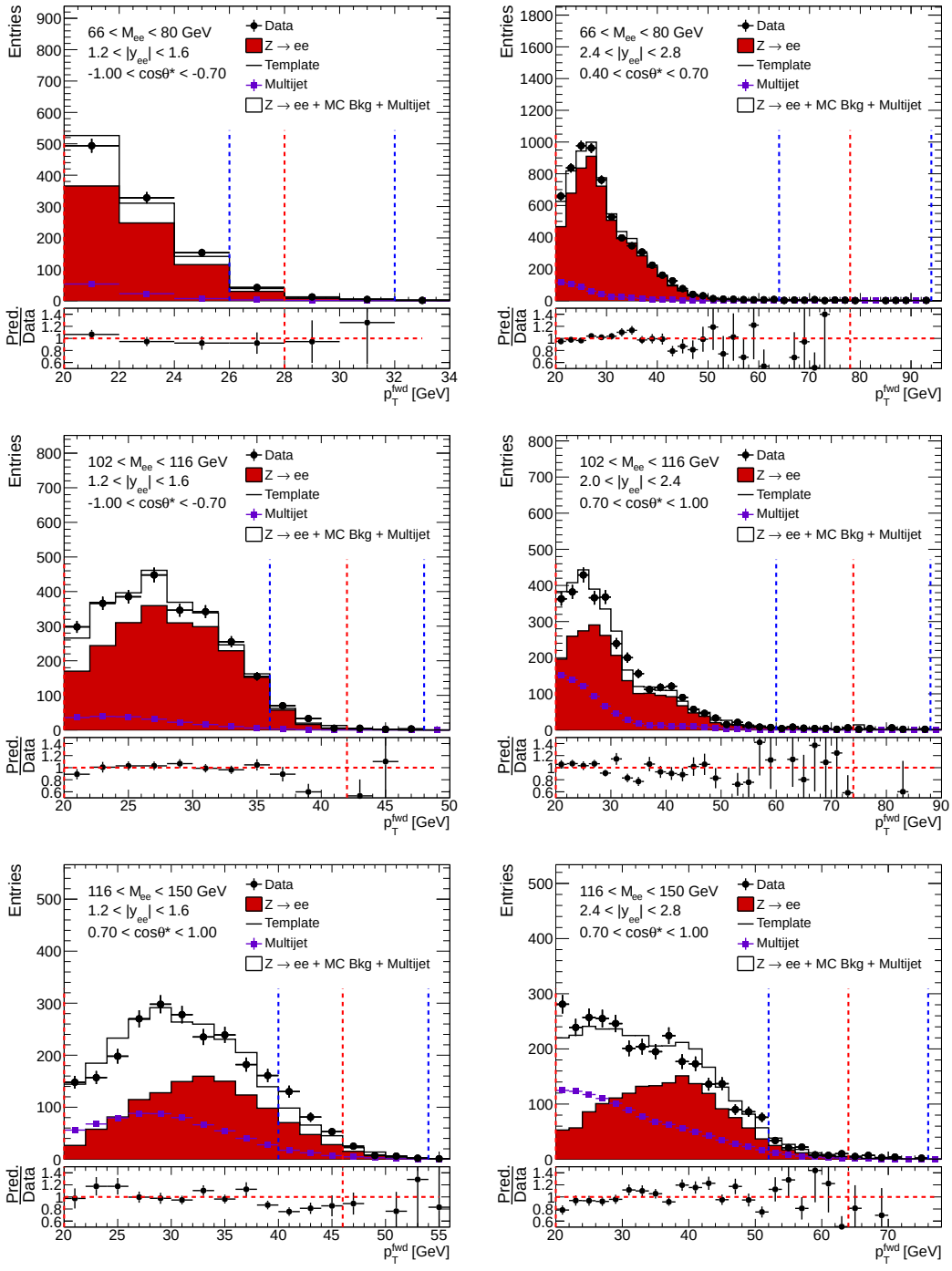

Figure B.9: Transverse momentum distributions for several three-dimensional analysis bins. Shown are the data and signal MC histograms obtained from signal selection along with the template distribution and corresponding multijet estimate. The prediction or sum of the signal MC and total background is plotted as well and its ratio with the data is shown in the bottom panels of these plots. The dashed vertical lines are explained in the text.

by resampling the data. For each replica, λ-calculations are repeated in each of the analysis bins and their standard deviation is taken as the statistical uncertainty.

2. An uncertainty results from the choice of the normalization region. For calculations using $E_T^{\mathrm{ctr}} Cone30/E_T^{\mathrm{ctr}}$ as the discriminating variable, the central-central procedure is used (see Section 7.2.1) to determine the normalization region variations. For p_T^{fwd}, it is the right edge that is varied, once moving it to the left and once moving it to the right [36]. The fit region variations can be seen in Figures B.8 and B.9 represented by the dashed blue lines. The maximum difference between these varied estimates and the nominal multijet estimate is taken as the systematic uncertainty due to the choice of normalization region.

3. Another systematic component is due to the shape of the template selected data. To estimate this uncertainty, the template selection is varied requiring forward electrons to additionally pass forward loose identification. To illustrate, $E_T^{\mathrm{ctr}} Cone30/E_T^{\mathrm{ctr}}$ distributions using the nominal and varied template selections are shown in Figure B.10. The difference between the estimates obtained using the two selections is taken as a systematic.

4. A final systematic is evaluated in the analysis bins that use $E_T^{\mathrm{ctr}} Cone30/E_T^{\mathrm{ctr}}$ as the discriminating variable. The difference between the results obtained using $E_T^{\mathrm{ctr}} Cone30/E_T^{\mathrm{ctr}}$ and $E_T^{\mathrm{ctr}} Cone20/E_T^{\mathrm{ctr}}$ is taken as an uncertainty. An example distribution of $E_T^{\mathrm{ctr}} Cone20/E_T^{\mathrm{ctr}}$ can be seen in Figure B.10.

In Figure B.11, the multijet background binned in $\cos\theta^*$ is plotted for several M_{ee} and $|y_{ee}|$ bins along with their uncertainties. The bottom panels show the fraction of multijet events contaminating the signal selected data. In the off-peak bins, $M_{ee} \in [66, 80]$, $[102, 116]$, and $[116, 150]$ GeV, the multijet background is sizable being on the order of 10% at low invariant mass and as much as 50% at high mass.

B.7 Control Plots

Central and forward electron distributions of p_T^{ctr}, η^{ctr}, p_T^{fwd}, and η^{fwd} are shown in Figure B.12. M_{ee}, $|y_{ee}|$, and $\cos\theta^*$, the kinematic quantities of interest, along with the dielectron transverse momentum P_T^{ee} are illustrated in Figure B.13. These are distributions of signal data at reconstruction-level plotted with a model prediction

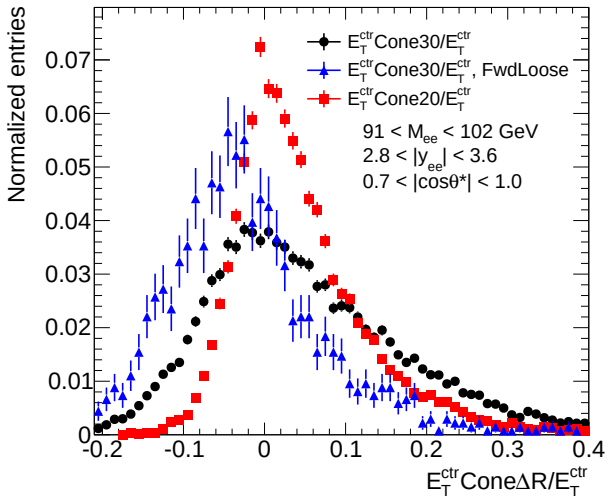

Figure B.10: Systematic uncertainties are obtained by varying the template selection to require forward loose identification (blue) and by using an alternative discriminating variable (red). The nominal template distribution (black) is plotted for reference.

constructed from the signal MC and background estimates. Ratios comparing the prediction with the measurement are shown in the lower panels of these plots. The dominant systematic uncertainties at reconstruction-level are represented by the shaded bands which include uncertainties due to the energy scale and resolution, efficiency scale factors, charge misidentification, and multijet background estimation. The error bars represent the Poisson statistical uncertainty.

Control plots of events separated into different regions in phase space are shown in Figures B.14 to B.16. These include electron p_T^e and η^e distributions split into three dielectron invariant mass regions, $66 < M_{ee} < 80$, $91 < M_{ee} < 102$, and $102 < M_{ee} < 116$ GeV, and two regions in absolute rapidity, $|y_{ee}| < 2.4$ (Figure B.14) and $|y_{ee}| > 2.4$ (Figure B.15). In Figure B.16 are plots of y_{ee} and $\cos\theta^*$ in the same three invariant mass regions listed above.

Most of the control plots show good agreement between data and prediction with the best agreement coming from events in the range $91 < M_{ee} < 102$ GeV. Note that the systematic uncertainty bands are larger in this measurement than they are in the central-central measurement, the main cause being energy scale calibration uncertainties from the forward electrons. Note also that the background contamination is sizable in this analysis with the largest contributions coming from multijet and semileptonically decaying W events. The shapes of the y_{ee} and $\cos\theta^*$ distributions are much different than those of the central-central analysis which are illustrated in Sec-

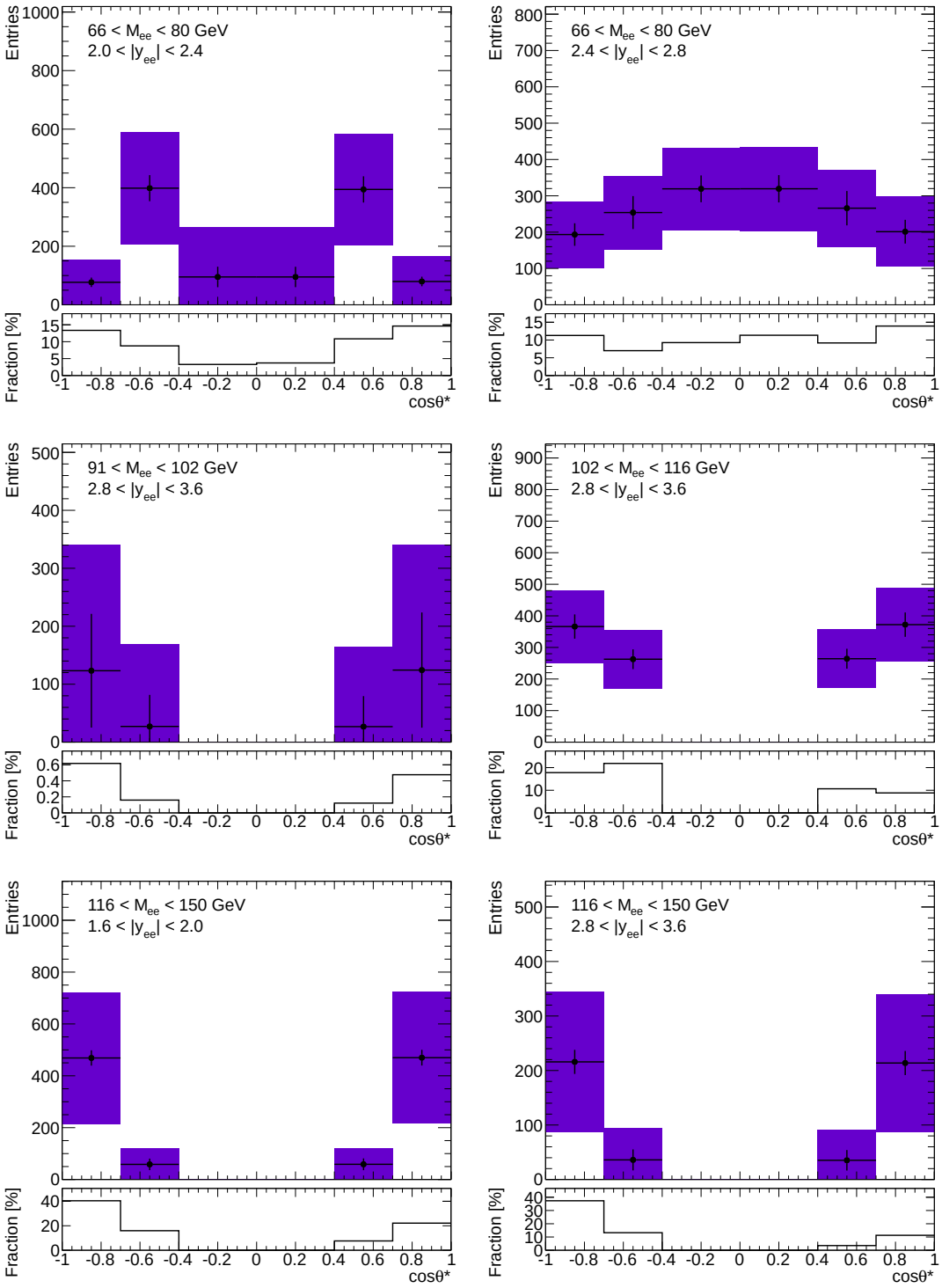

Figure B.11: Multijet background plotted in bins of $\cos\theta^*$ for several different invariant mass and rapidity ranges. Both the statistical (error bars) and total (error band) uncertainties are shown. The fraction of multijet events in the signal data is shown in the bottom panels of the plots.

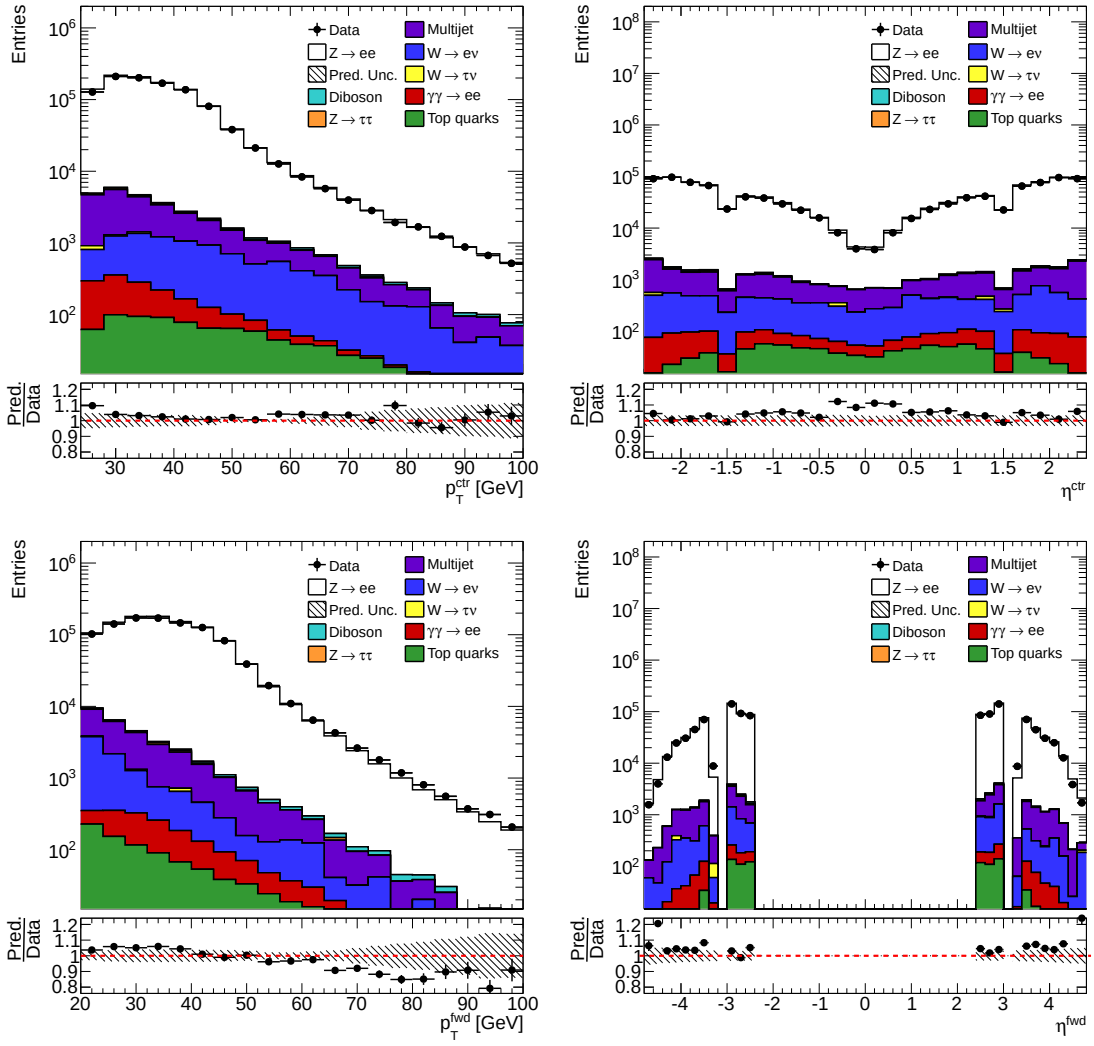

Figure B.12: Distributions of central and forward electron transverse momentum and pseudorapidity. The expected signal and background estimates are summed and compared to the data measurement. The shaded band in the ratio panel corresponds to the dominant systematic uncertainties summed in quadrature while the error bars are the statistical uncertainties on the data and prediction.

tion 7.3. These differences are a result of the forward electron shifting the dielectron system to more extreme values of y_{ee} and $\cos\theta^*$.

B.8 Unfolding

Following the procedure (see Section 7.4) used in the central-central analysis, this measurement is also unfolded to dressed-level using two iterations of RooUnfold's

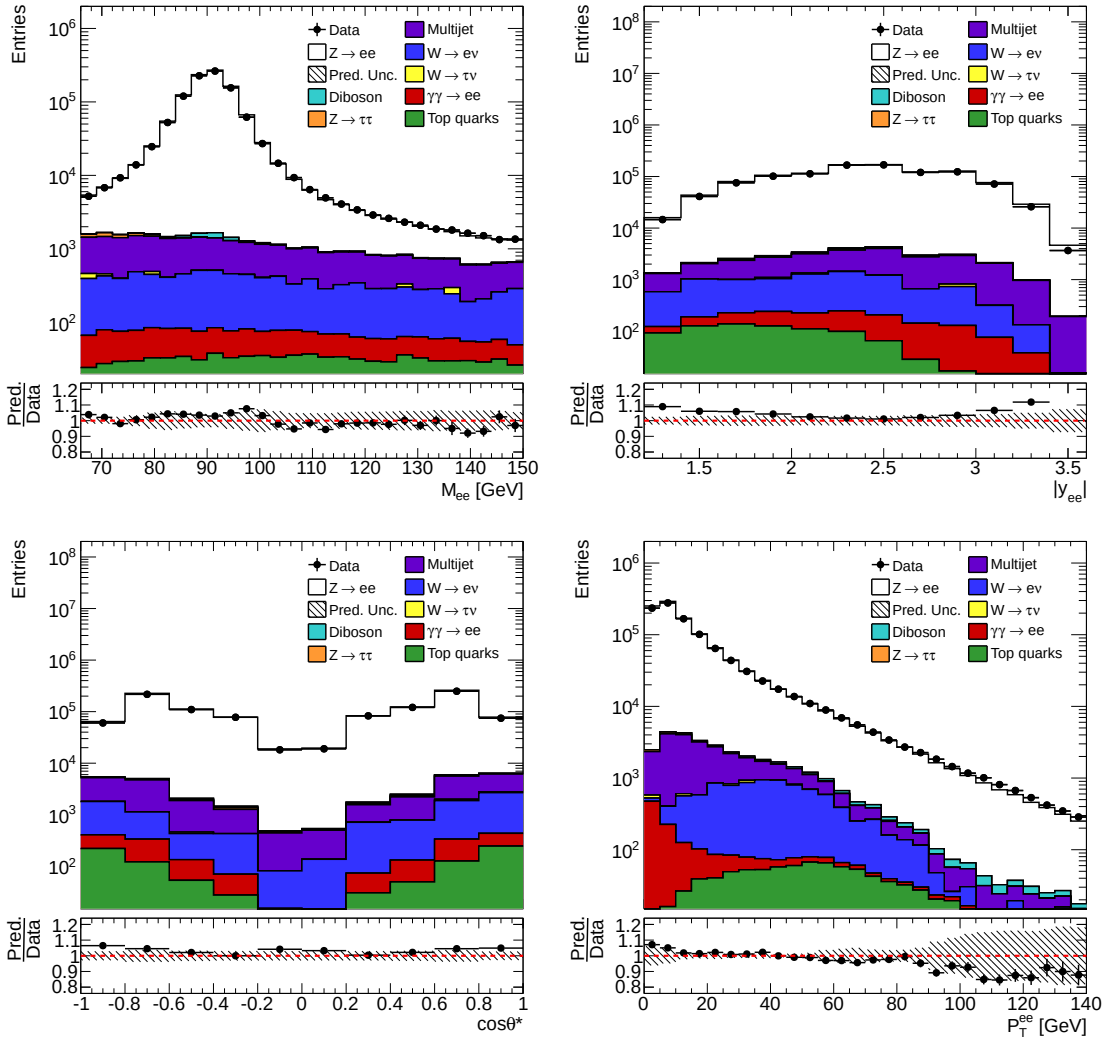

Figure B.13: Distributions of dielectron invariant mass, rapidity, $\cos\theta^*$, and transverse momentum.

implementation of Bayesian unfolding. Unfolding corrects the measurement for efficiency and energy response effects thus taking the measurement from reconstruction-to dressed-level. The results are then corrected to Born-level using bin-by-bin correction factors defined in Equation (7.11). Estimated values of the three-dimensional differential cross-section are obtained by dividing the unfolded distribution by the integrated luminosity of the data, and the bin widths of each of the three dimensions. To complete the differential cross-section measurement, its uncertainties must be estimated.

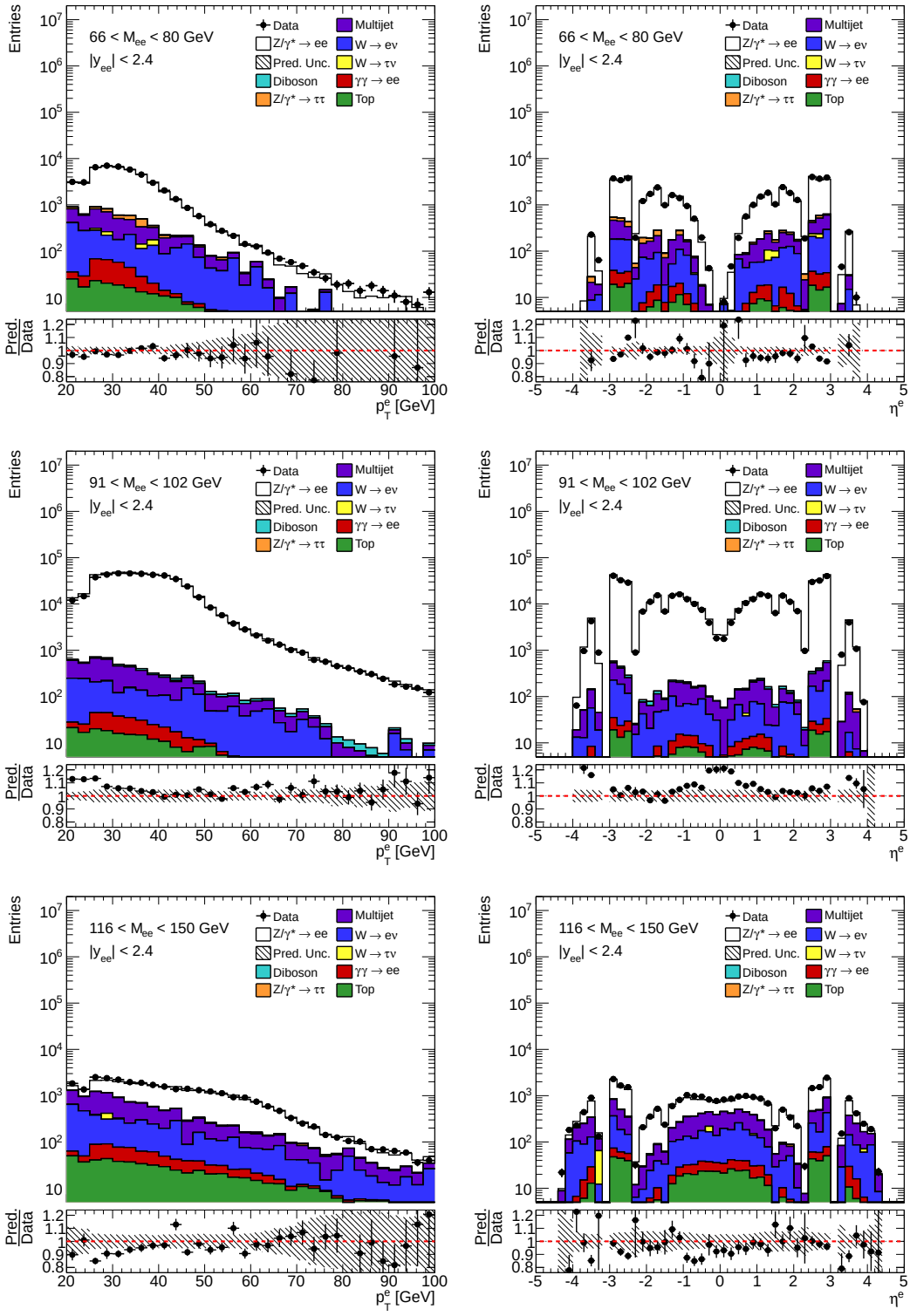

Figure B.14: Electron p_T^e and η^e distributions for $|y_{ee}| < 2.4$ and $M_{ee} \in [66, 80]$, $[91, 102]$, and $[116, 150]$ GeV.

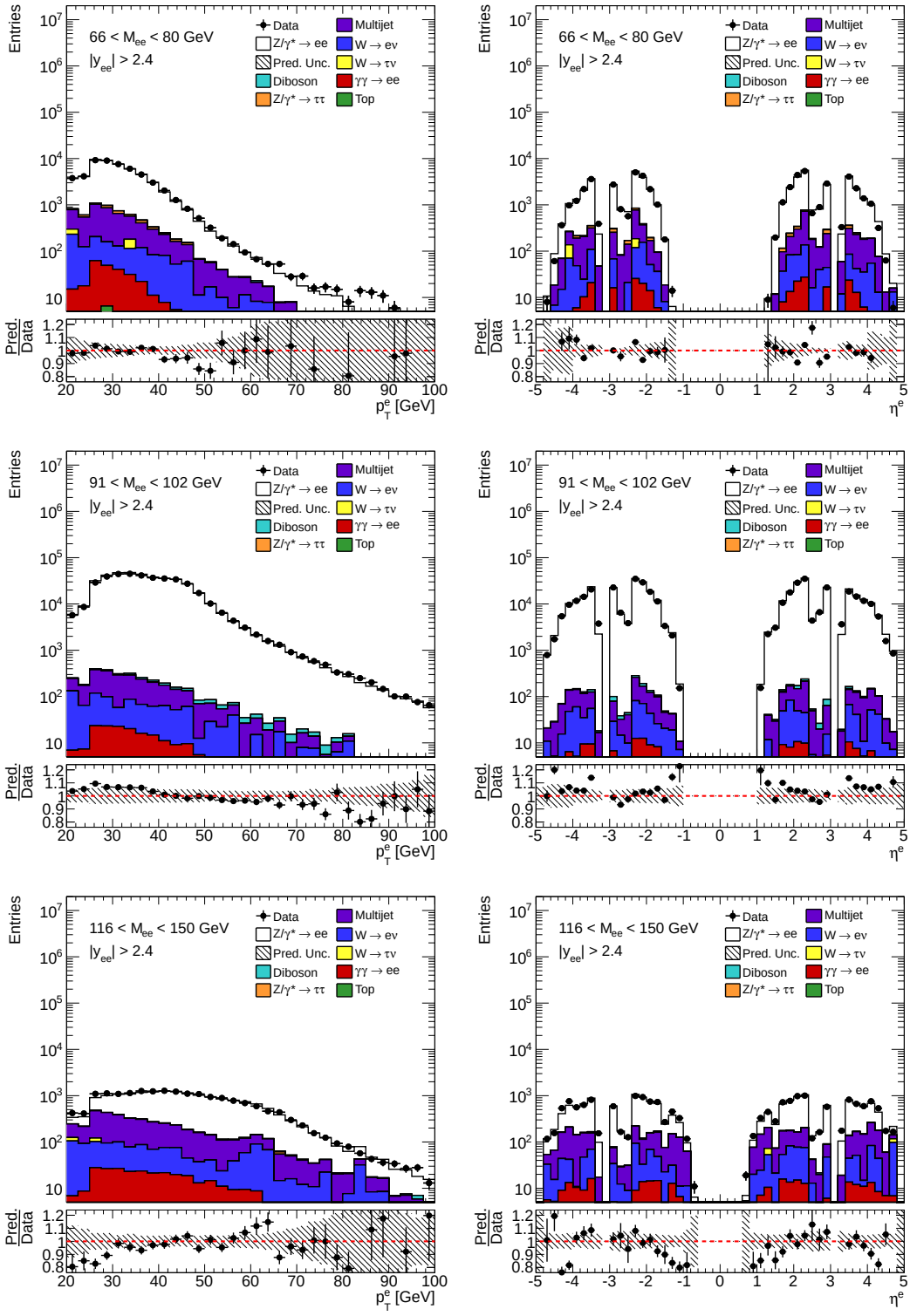

Figure B.15: Electron p_T^e and η^e distributions for $|y_{ee}| > 2.4$ and $M_{ee} \in [66, 80]$, $[91, 102]$, and $[116, 150]$ GeV.

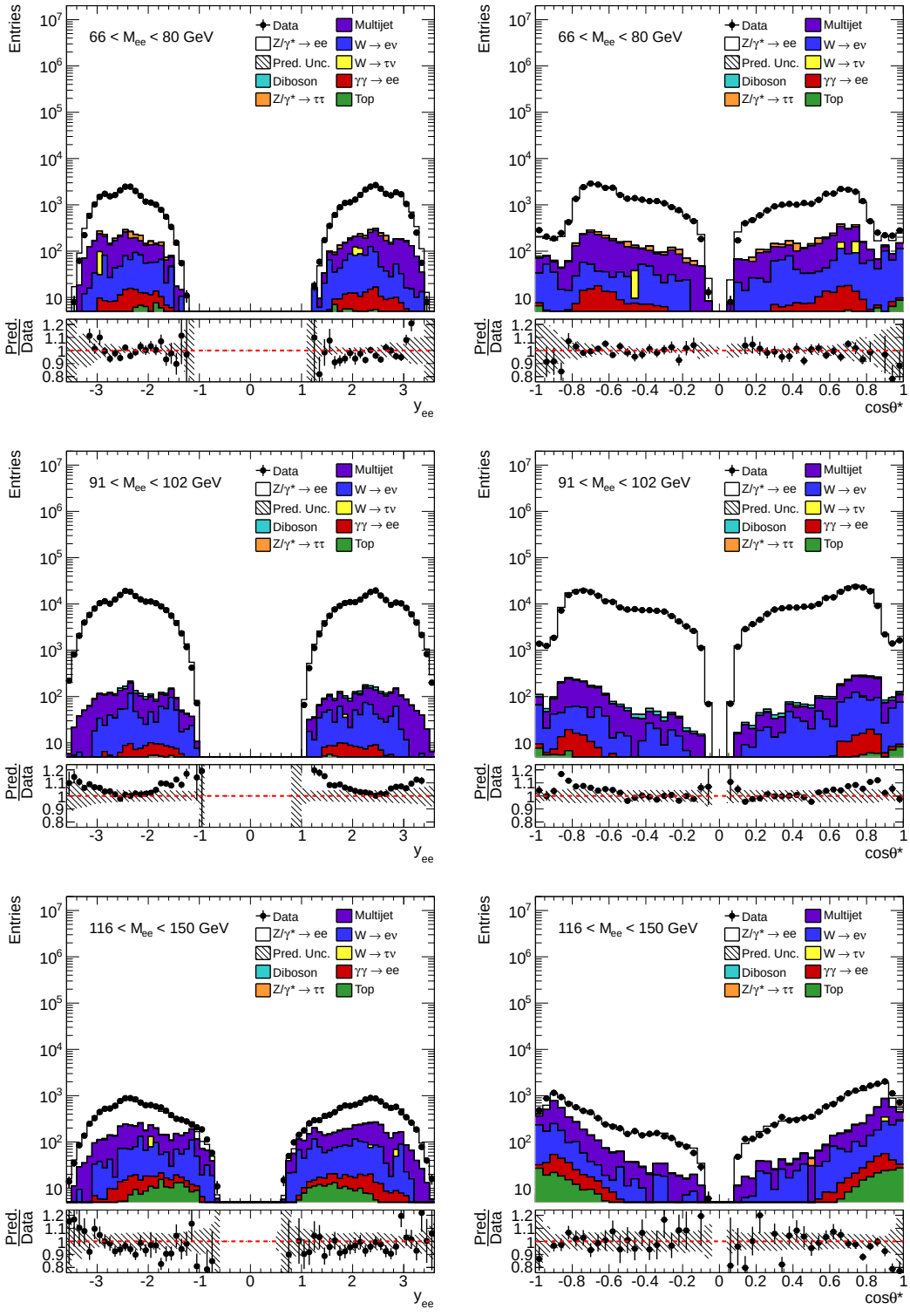

Figure B.16: Dielectron y_{ee} and $\cos\theta^*$ distributions for $M_{ee} \in [66, 80]$, $[91, 102]$, and $[116, 150]$ GeV.

B.9 Uncertainties

The central-forward analysis is affected by many of the same sources of uncertainty present in central-central analysis. The differences include the additional uncertainties associated with the private energy scale and smearing corrections applied to forward electrons. These are propagated to the unfolded cross-section in the same way the uncertainties on the official energy corrections are propagated. Moreover, uncertainties from the use of isolation and forward identification scale factors are treated using the combined toy method. Analogous to Table 8.1 of the central-central measurement, Table B.3 summarizes the uncertainties affecting this measurement.

Source	Method	Type
Data statistics	Bootstrap	Uncorrelated
Signal MC statistics	Bootstrap	Uncorrelated
Background MC statistics	Bootstrap	Uncorrelated
Multijet background statistics	Bootstrap	Uncorrelated
Background MC cross-sections	Offset	Correlated
Multijet background systematics	Offset	Correlated
Electron energy scale	Offset	Correlated
Electron energy resolution	Offset	Correlated
Additional electron energy scale	Offset	Correlated
Additional electron energy resolution	Offset	Correlated
Electron reconstruction efficiency	Combined toy	Correlated
Electron identification efficiency	Combined toy	Correlated
Electron trigger efficiency	Combined toy	Correlated
Electron isolation efficiency	Combined toy	Correlated
Electron forward identification efficiency	Combined toy	Correlated
Charge misidentification	Offset	Correlated
k-factor	Offset	Correlated
Z boson P_T	Offset	Correlated
PDF	Error sets	Correlated

Table B.3: Summary of the systematic uncertainties affecting the central-forward measurement and their method of evaluation and type, correlated or uncorrelated across analysis bins.

Plots of the relative uncertainties from all sources and the total uncertainty, where the individual uncertainties have been added in quadrature, on the differential cross-section are shown in Figures B.17 to B.21. In general, the total uncertainty here is larger than the total uncertainty in the central-central measurement. Electron energy uncertainties, particularly those from the energy scale corrections, are the dominant uncertainties. This is not surprising given that the electromagnetic forward

calorimeters have poorer resolution than the calorimeters in the barrel and end-caps. Note that in the highest M_{ee} bin, $M_{ee} \in [116, 150]$ GeV, where the number of data events is limited, the statistical uncertainty on the data and the uncertainties due to the multijet estimate dominate the total uncertainty.

B.10 Results

The $\frac{d^3\sigma}{dM_{ee}d|y_{ee}|d\cos\theta^*}$ measurement at Born-level is illustrated in Figures B.22 to B.26 along with a theoretical prediction produced using the POWHEG signal MC. In most analysis bins, the theory is consistent with the data as most ratio points are within the 1-sigma error bands which correspond to the total measurement uncertainty while the error bars represent the statistical uncertainties of the prediction and measurement. The shapes of these $\cos\theta^*$ distributions are more asymmetric than those of the central-central measurement (see Figures 9.1 to 9.7). Central-forward events are boosted to more extreme values of $|y_{ee}|$ hence are less affected by dilution. Note that numerous bins, usually $\cos\theta^* \in [-0.4, 0.0]$ and $[0.0, 0.4]$, are empty due to their being rejected from the analysis because of a lack of statistics at reconstruction-level. Though having large uncertainties at the cross-section level, many of these uncertainties are reduced when propagated to the A_{FB} measurement.

Forward-backward asymmetry results (determined using the prescription outlined in Section 9.2) can be seen in Figure B.27 plotted with the prediction from the signal Monte Carlo. The A_{FB} measurement is plotted as a function of M_{ee} for each of the five $|y_{ee}|$ bins. The differences between the data and prediction can be seen in the lower panels of these plots. The agreement between data and prediction is strong, especially at large $|y_{ee}|$ where A_{FB} effects are expected to be at their largest. Comparing these A_{FB} results to their central-central counterparts (see Figures 9.8 and 9.9) it becomes evident that this measurement is far more sensitive to A_{FB}. As stated above, there has been a significant reduction in many of the correlated uncertainties that were dominant in the cross-section measurement, most notably in the M_{ee} bins at the Z-peak.

The central-central and central-forward measurements differ in their uses. Due to its sensitivity to forward-backward asymmetry, the central-forward measurement is expected to yield a better measurement of θ_{W} than the central-central result. However, because of its smaller cross-section uncertainties, the central-central analysis will provide more precise measurements of the PDFs of the proton.

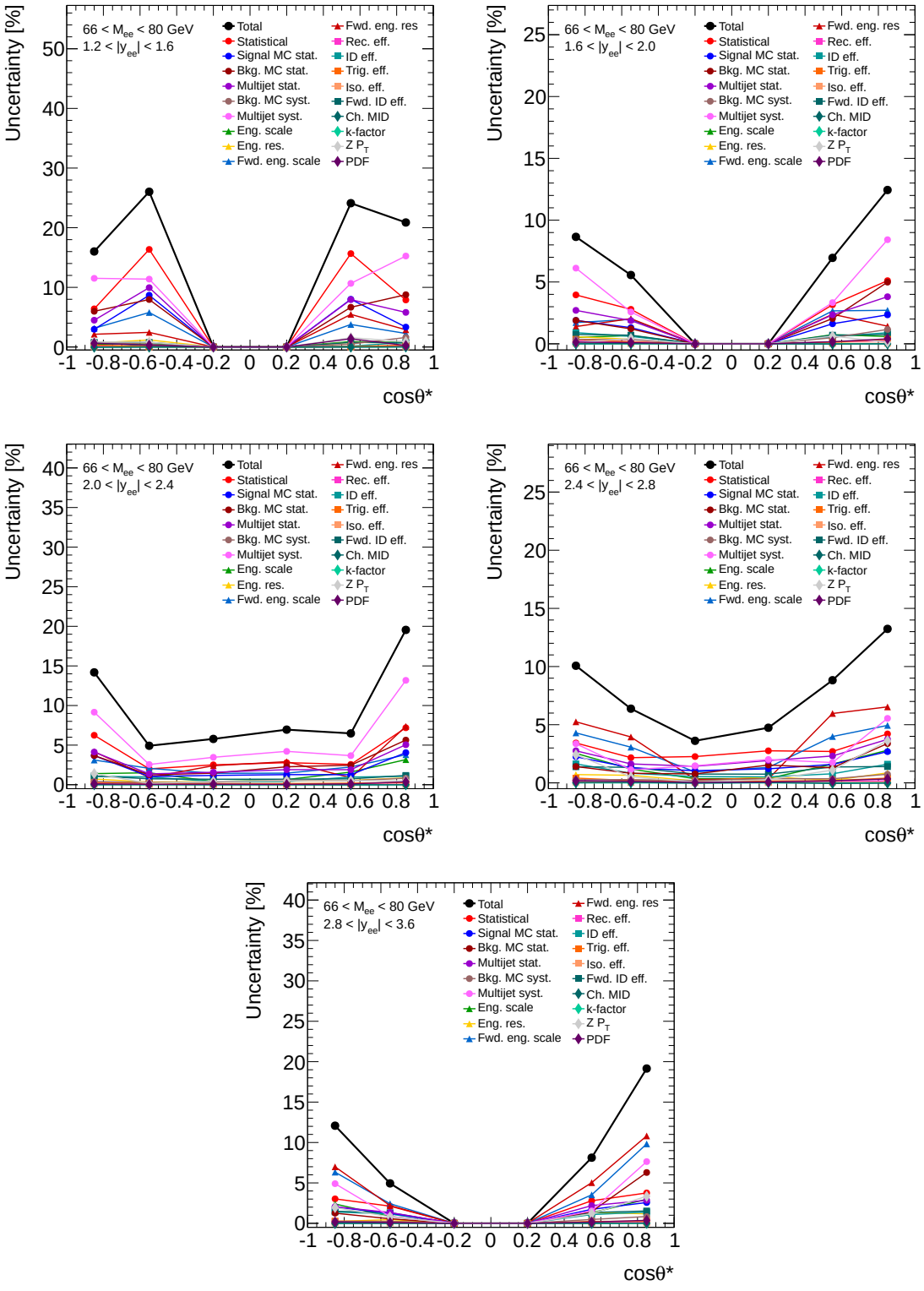

Figure B.17: Uncertainties propagated to $\frac{d^3\sigma}{dM_{ee}d|y_{ee}|d\cos\theta^*}$ for invariant mass bin $M_{ee} \in [66, 80]$ GeV and for the entire rapidity range of interest, $1.2 < |y_{ee}| < 3.6$.

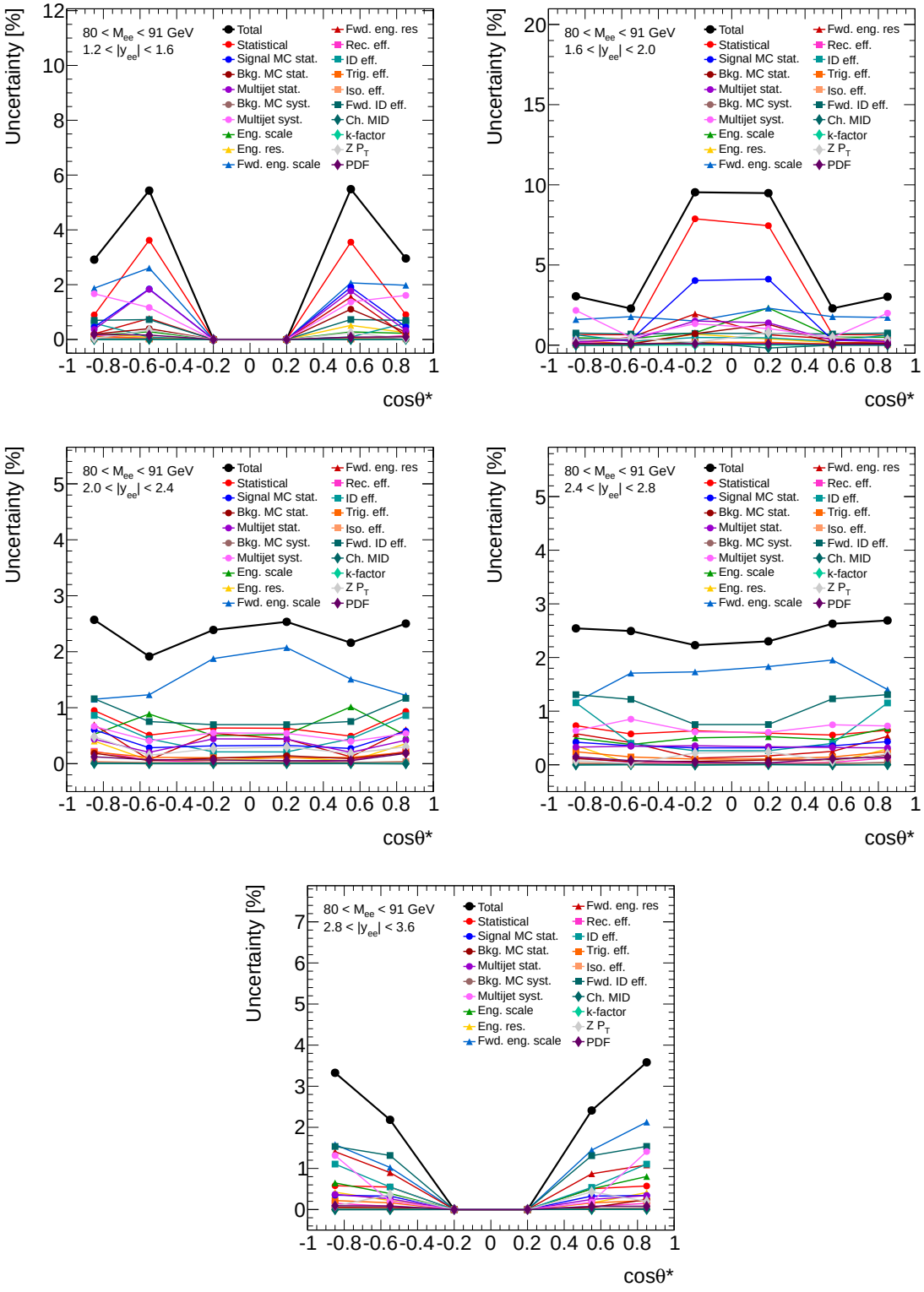

Figure B.18: Uncertainties propagated to $\frac{d^3\sigma}{dM_{ee}d|y_{ee}|d\cos\theta^*}$ for invariant mass bin $M_{ee} \in [80, 91]$ GeV and for the entire rapidity range of interest, $1.2 < |y_{ee}| < 3.6$.

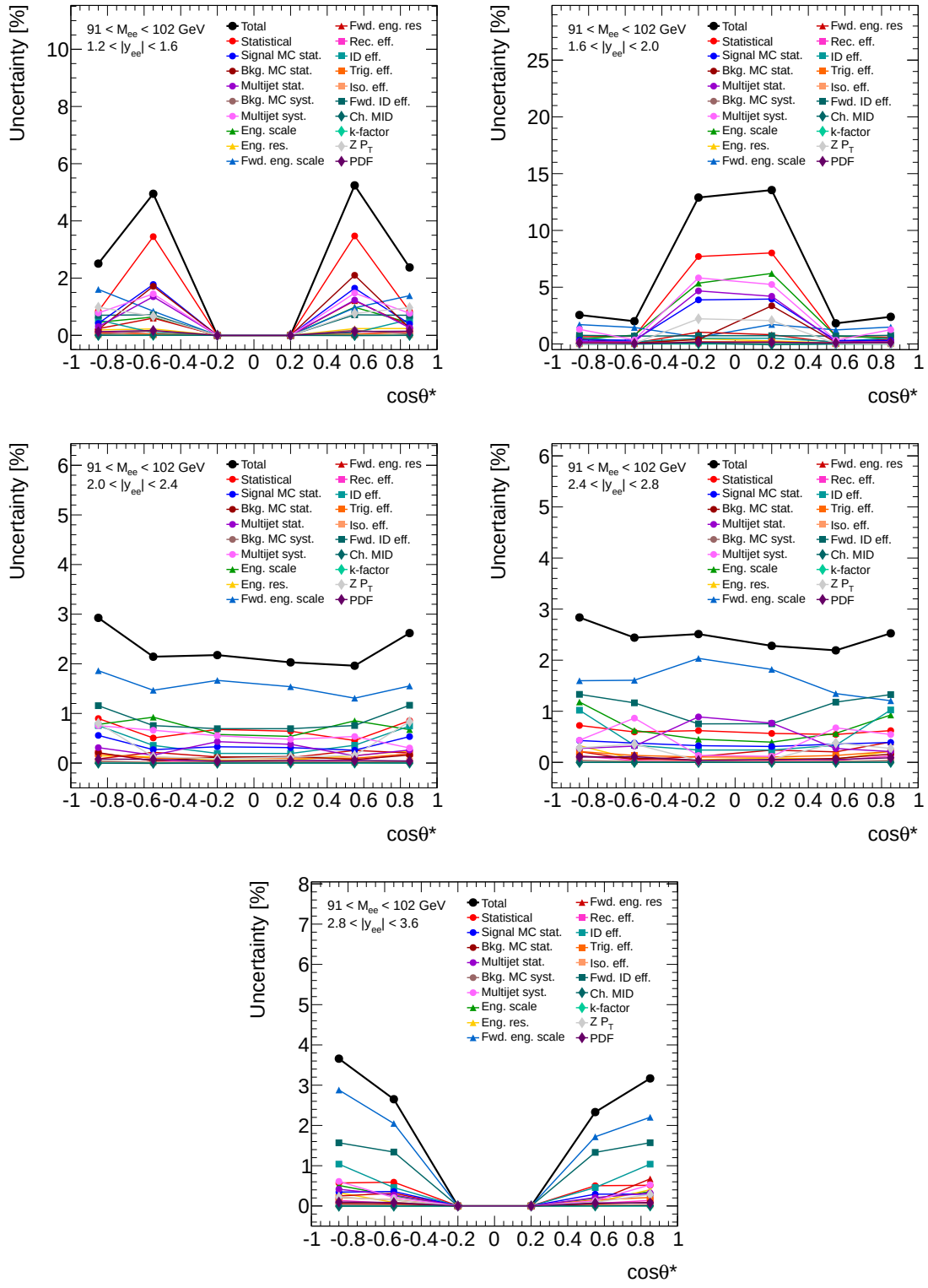

Figure B.19: Uncertainties propagated to $\frac{d^3\sigma}{dM_{ee}d|y_{ee}|d\cos\theta^*}$ for invariant mass bin $M_{ee} \in [91, 102]$ GeV and for the entire rapidity range of interest, $1.2 < |y_{ee}| < 3.6$.

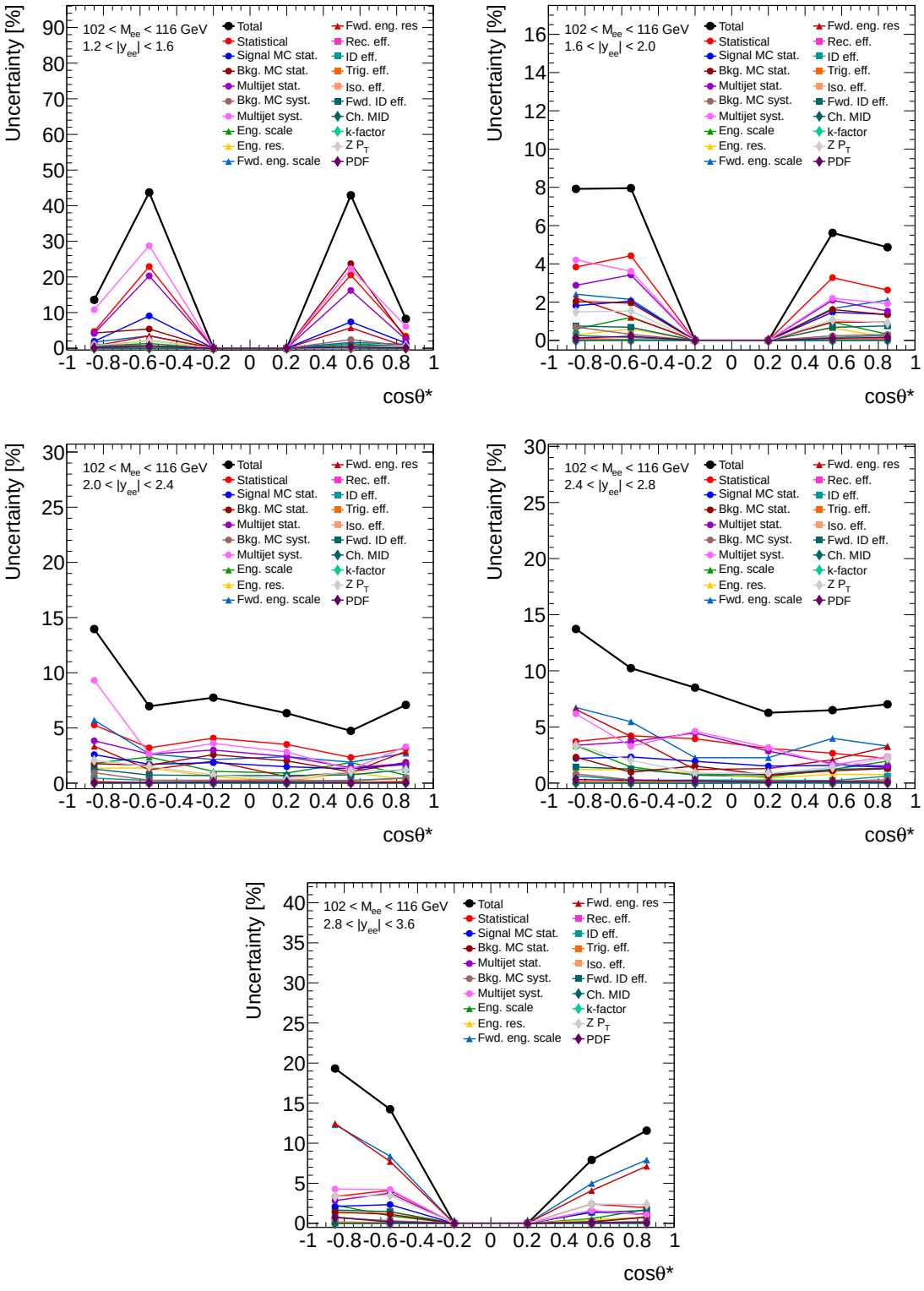

Figure B.20: Uncertainties propagated to $\frac{d^3\sigma}{dM_{ee}d|y_{ee}|d\cos\theta^*}$ for invariant mass bin $M_{ee} \in [102, 116]$ GeV and for the entire rapidity range of interest, $1.2 < |y_{ee}| < 3.6$.

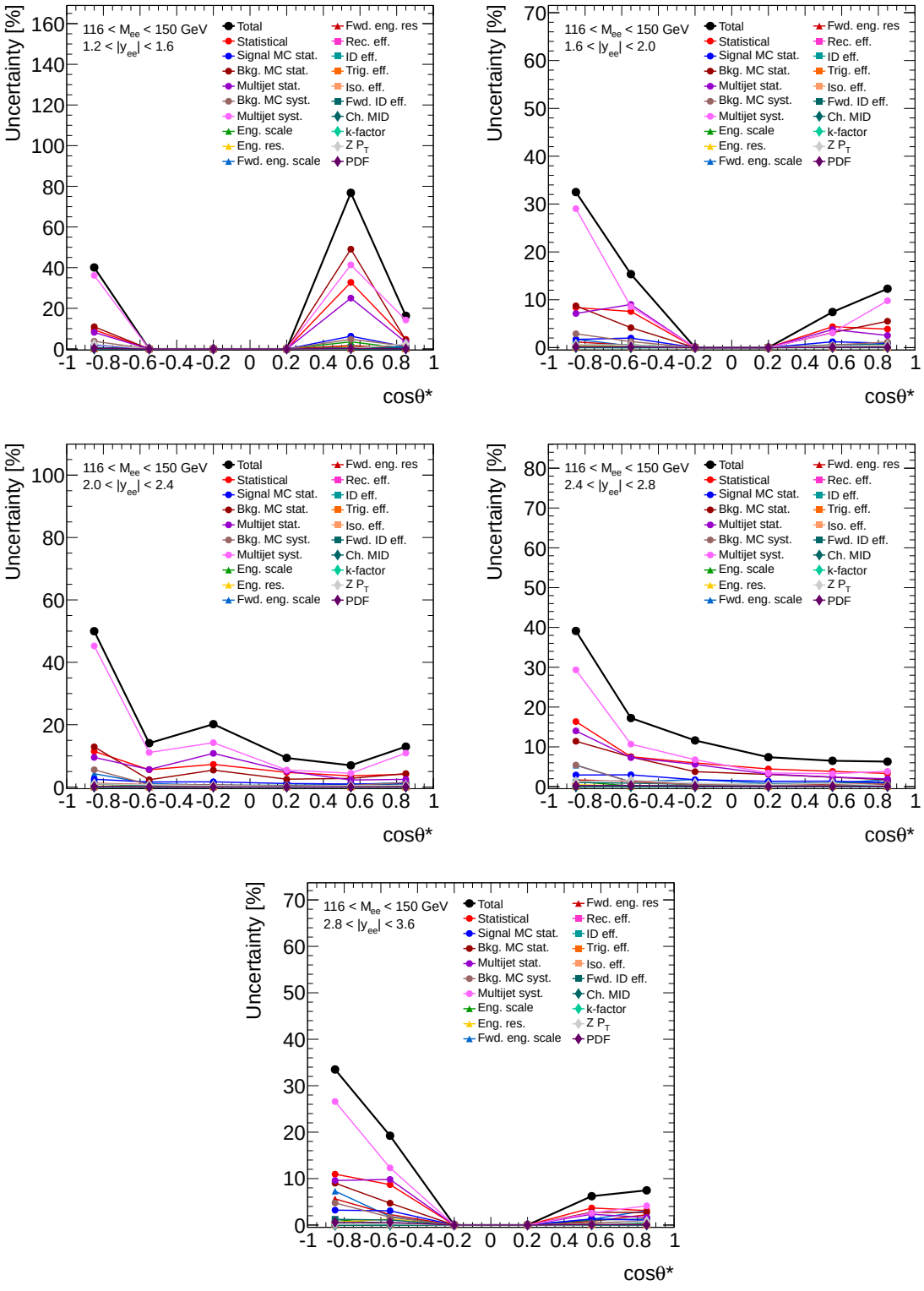

Figure B.21: Uncertainties propagated to $\frac{d^3\sigma}{dM_{ee}d|y_{ee}|d\cos\theta^*}$ for invariant mass bin $M_{ee} \in [116, 150]$ GeV and for the entire rapidity range of interest, $1.2 < |y_{ee}| < 3.6$.

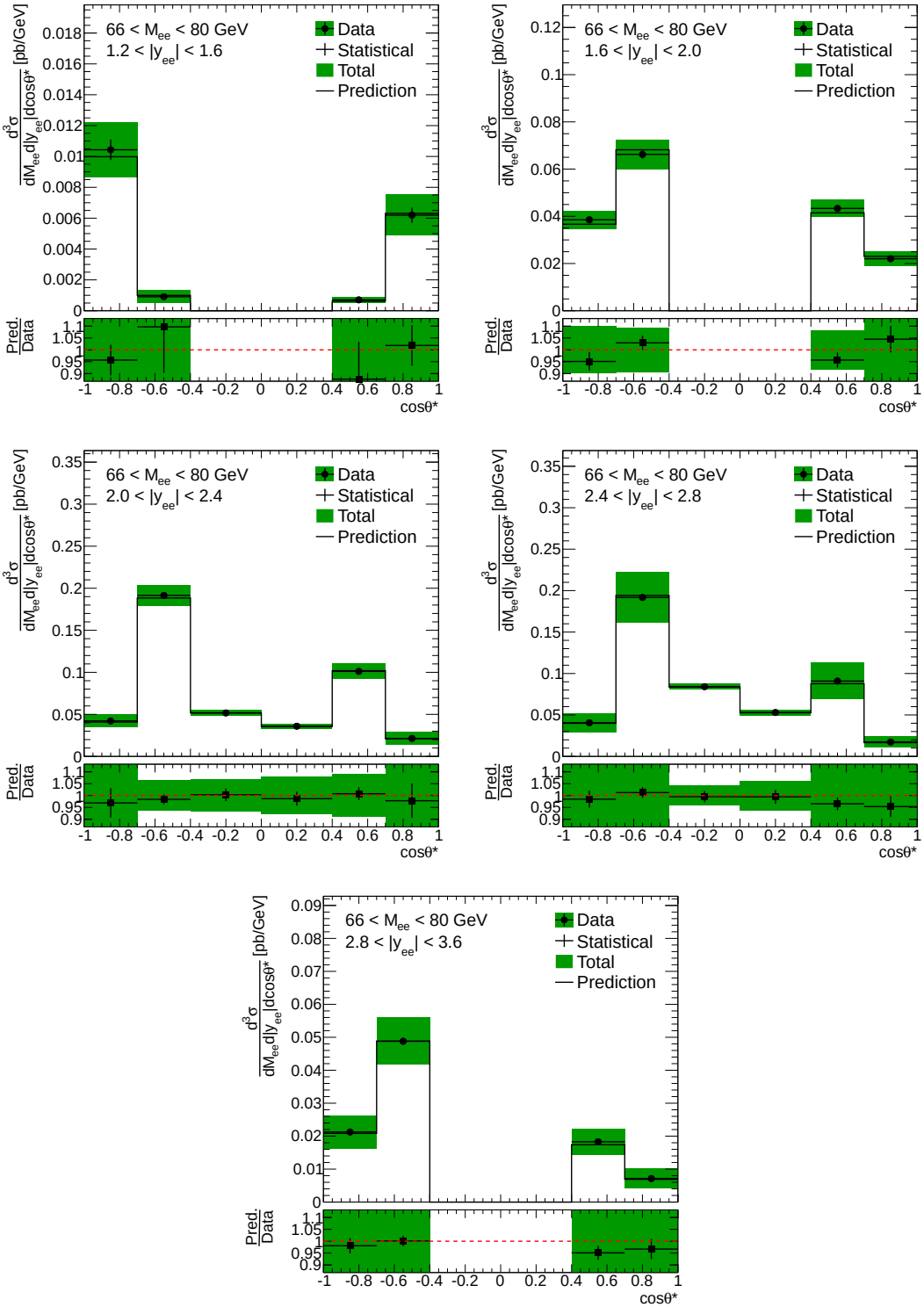

Figure B.22: Three-dimensional differential cross-section $\frac{d^3\sigma}{dM_{ee}d|y_{ee}|d\cos\theta^*}$ results for invariant mass bin $M_{ee} \in [66, 80]$ GeV and for the entire rapidity range of interest, $1.2 < |y_{ee}| < 3.6$.

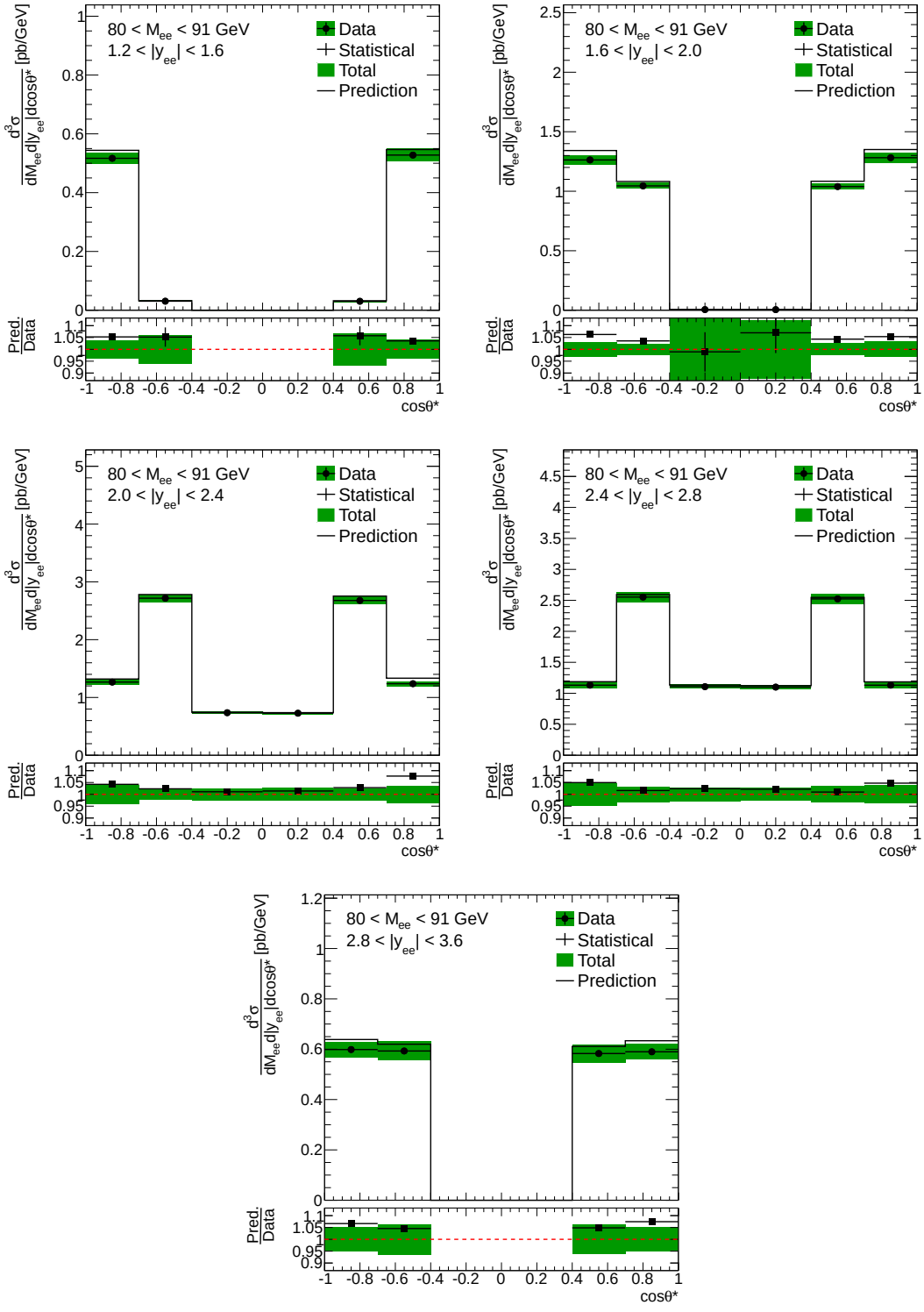

Figure B.23: Three-dimensional differential cross-section $\frac{d^3\sigma}{dM_{ee}d|y_{ee}|d\cos\theta^*}$ results for invariant mass bin $M_{ee} \in [80, 91]$ GeV and for the entire rapidity range of interest, $1.2 < |y_{ee}| < 3.6$.

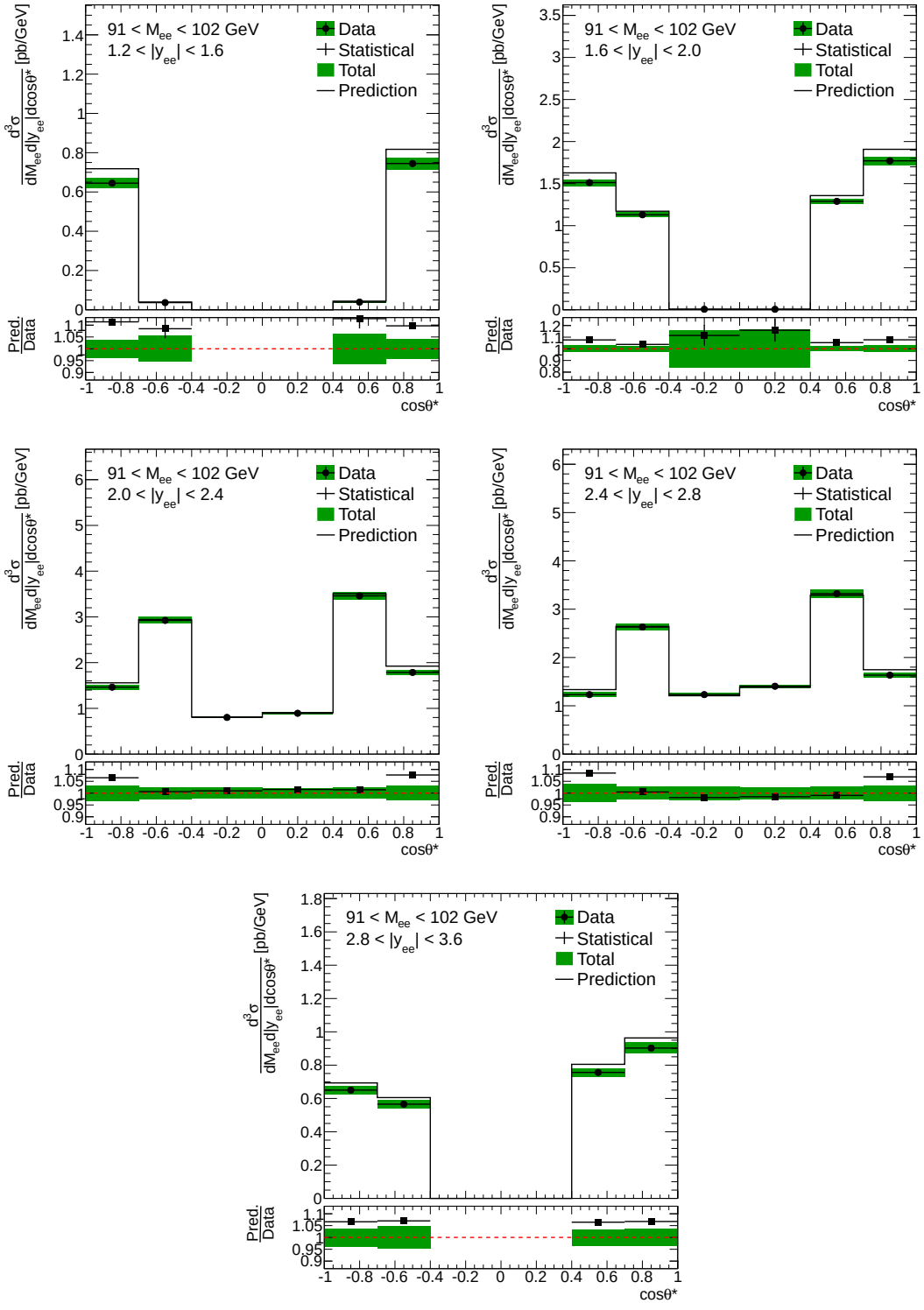

Figure B.24: Three-dimensional differential cross-section $\frac{d^3\sigma}{dM_{ee}d|y_{ee}|d\cos\theta^*}$ results for invariant mass bin $M_{ee} \in [91, 102]$ GeV and for the entire rapidity range of interest, $1.2 < |y_{ee}| < 3.6$.

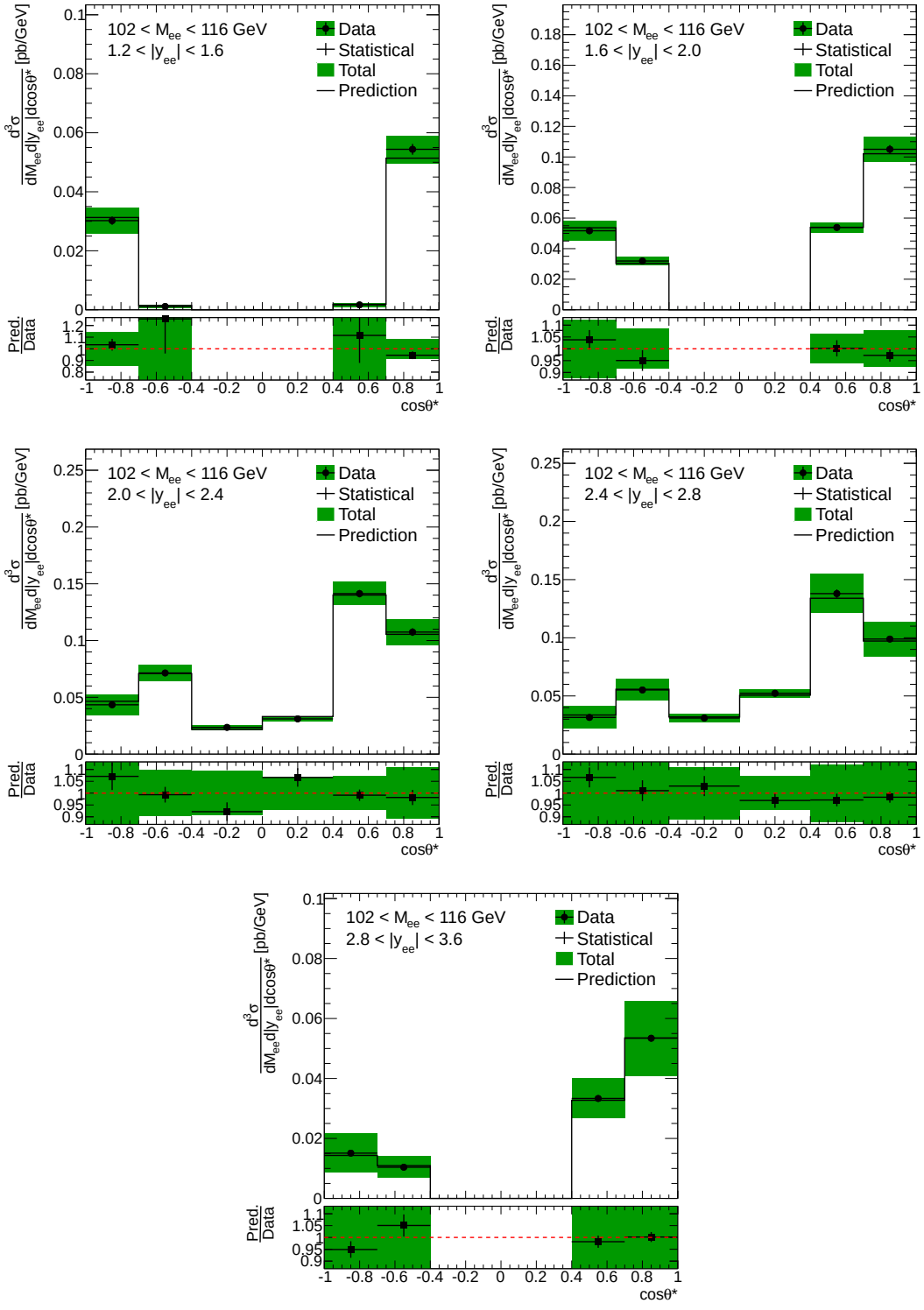

Figure B.25: Three-dimensional differential cross-section $\frac{d^3\sigma}{dM_{ee}d|y_{ee}|d\cos\theta^*}$ results for invariant mass bin $M_{ee} \in [102, 116]$ GeV and for the entire rapidity range of interest, $1.2 < |y_{ee}| < 3.6$.

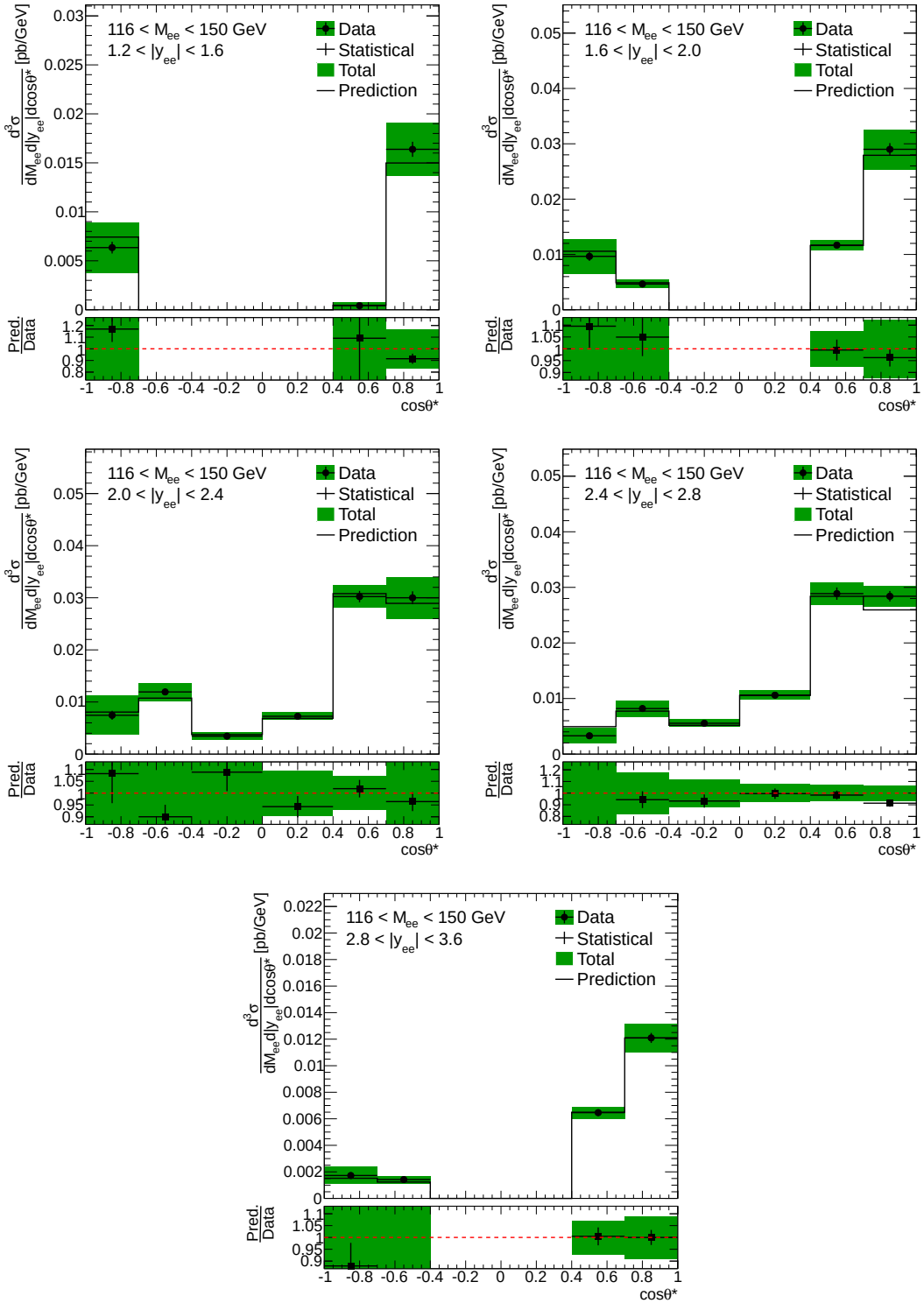

Figure B.26: Three-dimensional differential cross-section $\frac{d^3\sigma}{dM_{ee}d|y_{ee}|d\cos\theta^*}$ results for invariant mass bin $M_{ee} \in [116, 150]$ GeV and for the entire rapidity range of interest, $1.2 < |y_{ee}| < 3.6$.

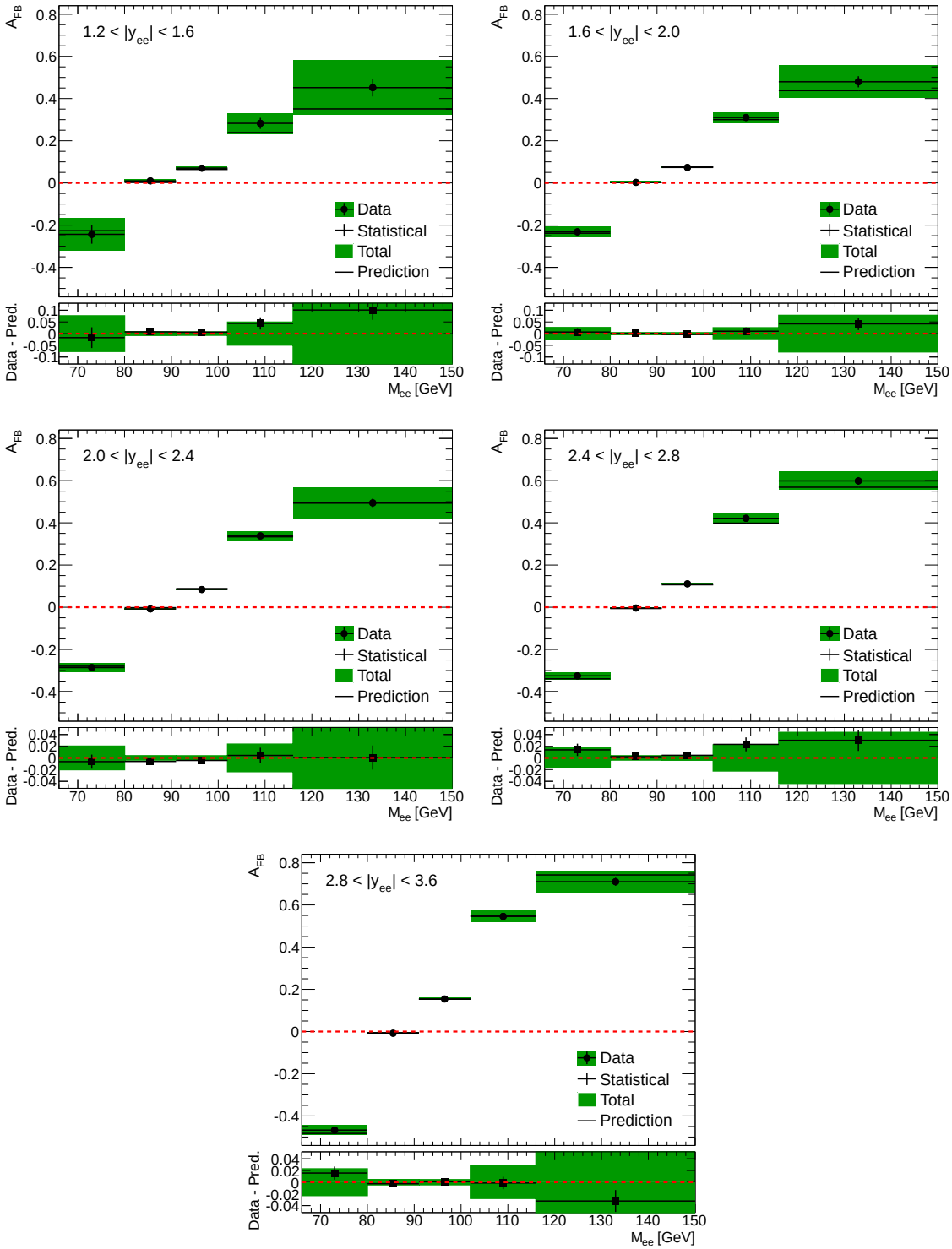

Figure B.27: Forward-backward asymmetry results plotted as a function of M_{ee} for the entire rapidity range of interest, $1.2 < |y_{ee}| < 3.6$.

B.11 Tables of Results

Bin	M_{ee} [GeV]		$\lvert y_{ee}\rvert$		$\cos\theta^*$		σ [pb/GeV]	δ^{stat} [%]	δ^{syst} [%]	δ^{tot} [%]
1	66	80	1.2	1.6	−1.0	−0.7	1.04×10^{-2}	6.4	14.7	16.0
2	66	80	1.2	1.6	−0.7	−0.4	9.07×10^{-4}	16.4	20.2	26.0
3	66	80	1.2	1.6	−0.4	0.0	-	-	-	-
4	66	80	1.2	1.6	0.0	+0.4	-	-	-	-
5	66	80	1.2	1.6	+0.4	+0.7	7.05×10^{-4}	15.7	18.3	24.1
6	66	80	1.2	1.6	+0.7	+1.0	6.19×10^{-3}	7.9	19.3	20.9
7	66	80	1.6	2.0	−1.0	−0.7	3.85×10^{-2}	4.0	7.7	8.7
8	66	80	1.6	2.0	−0.7	−0.4	6.62×10^{-2}	2.8	4.8	5.6
9	66	80	1.6	2.0	−0.4	0.0	-	-	-	-
10	66	80	1.6	2.0	0.0	+0.4	-	-	-	-
11	66	80	1.6	2.0	+0.4	+0.7	4.33×10^{-2}	3.2	6.2	6.9
12	66	80	1.6	2.0	+0.7	+1.0	2.20×10^{-2}	5.1	11.3	12.4
13	66	80	2.0	2.4	−1.0	−0.7	4.22×10^{-2}	6.2	12.7	14.2
14	66	80	2.0	2.4	−0.7	−0.4	1.91×10^{-1}	2.0	4.5	4.9
15	66	80	2.0	2.4	−0.4	0.0	5.17×10^{-2}	2.5	5.2	5.8
16	66	80	2.0	2.4	0.0	+0.4	3.59×10^{-2}	2.8	6.4	7.0
17	66	80	2.0	2.4	+0.4	+0.7	1.01×10^{-1}	2.6	6.0	6.5
18	66	80	2.0	2.4	+0.7	+1.0	2.14×10^{-2}	7.2	18.2	19.5
19	66	80	2.4	2.8	−1.0	−0.7	4.06×10^{-2}	3.4	9.5	10.1
20	66	80	2.4	2.8	−0.7	−0.4	1.92×10^{-1}	2.2	6.0	6.4
21	66	80	2.4	2.8	−0.4	0.0	8.41×10^{-2}	2.3	2.8	3.6
22	66	80	2.4	2.8	0.0	+0.4	5.29×10^{-2}	2.8	3.9	4.7
23	66	80	2.4	2.8	+0.4	+0.7	9.09×10^{-2}	2.7	8.4	8.8
24	66	80	2.4	2.8	+0.7	+1.0	1.74×10^{-2}	4.2	12.6	13.2
25	66	80	2.8	3.6	−1.0	−0.7	2.13×10^{-2}	3.0	11.7	12.1
26	66	80	2.8	3.6	−0.7	−0.4	4.88×10^{-2}	2.1	4.5	4.9
27	66	80	2.8	3.6	−0.4	0.0	-	-	-	-
28	66	80	2.8	3.6	0.0	+0.4	-	-	-	-
29	66	80	2.8	3.6	+0.4	+0.7	1.83×10^{-2}	2.8	7.6	8.1
30	66	80	2.8	3.6	+0.7	+1.0	7.15×10^{-3}	3.8	18.8	19.2
31	80	91	1.2	1.6	−1.0	−0.7	5.17×10^{-1}	0.9	2.8	2.9
32	80	91	1.2	1.6	−0.7	−0.4	3.08×10^{-2}	3.6	4.1	5.4
33	80	91	1.2	1.6	−0.4	0.0	-	-	-	-
34	80	91	1.2	1.6	0.0	+0.4	-	-	-	-
35	80	91	1.2	1.6	+0.4	+0.7	3.05×10^{-2}	3.6	4.2	5.5
36	80	91	1.2	1.6	+0.7	+1.0	5.28×10^{-1}	0.9	2.8	3.0
37	80	91	1.6	2.0	−1.0	−0.7	1.26	0.7	3.0	3.0
38	80	91	1.6	2.0	−0.7	−0.4	1.04	0.7	2.2	2.3
39	80	91	1.6	2.0	−0.4	0.0	5.55×10^{-3}	7.9	5.4	9.5
40	80	91	1.6	2.0	0.0	+0.4	5.04×10^{-3}	7.5	5.9	9.5
41	80	91	1.6	2.0	+0.4	+0.7	1.04	0.7	2.2	2.3
42	80	91	1.6	2.0	+0.7	+1.0	1.28	0.6	3.0	3.0
43	80	91	2.0	2.4	−1.0	−0.7	1.27	0.9	2.4	2.6
44	80	91	2.0	2.4	−0.7	−0.4	2.72	0.5	1.8	1.9
45	80	91	2.0	2.4	−0.4	0.0	7.36×10^{-1}	0.6	2.3	2.4
46	80	91	2.0	2.4	0.0	+0.4	7.27×10^{-1}	0.6	2.5	2.5
47	80	91	2.0	2.4	+0.4	+0.7	2.68	0.5	2.1	2.2
48	80	91	2.0	2.4	+0.7	+1.0	1.24	0.9	2.3	2.5
49	80	91	2.4	2.8	−1.0	−0.7	1.13	0.7	2.4	2.5
50	80	91	2.4	2.8	−0.7	−0.4	2.55	0.6	2.4	2.5
51	80	91	2.4	2.8	−0.4	0.0	1.11	0.6	2.1	2.2
52	80	91	2.4	2.8	0.0	+0.4	1.10	0.6	2.2	2.3
53	80	91	2.4	2.8	+0.4	+0.7	2.52	0.6	2.6	2.6
54	80	91	2.4	2.8	+0.7	+1.0	1.13	0.6	2.6	2.7

Bin	M_{ee} [GeV]		$\lvert y_{ee}\rvert$		$\cos\theta^*$		σ [pb/GeV]	δ^{stat} [%]	δ^{syst} [%]	δ^{tot} [%]
55	80	91	2.8	3.6	−1.0	−0.7	5.99×10^{-1}	0.6	3.3	3.3
56	80	91	2.8	3.6	−0.7	−0.4	5.93×10^{-1}	0.5	2.1	2.2
57	80	91	2.8	3.6	−0.4	0.0	-	-	-	-
58	80	91	2.8	3.6	0.0	+0.4	-	-	-	-
59	80	91	2.8	3.6	+0.4	+0.7	5.83×10^{-1}	0.5	2.4	2.4
60	80	91	2.8	3.6	+0.7	+1.0	5.90×10^{-1}	0.6	3.5	3.6
61	91	102	1.2	1.6	−1.0	−0.7	6.45×10^{-1}	0.8	2.4	2.5
62	91	102	1.2	1.6	−0.7	−0.4	3.65×10^{-2}	3.5	3.5	4.9
63	91	102	1.2	1.6	−0.4	0.0	-	-	-	-
64	91	102	1.2	1.6	0.0	+0.4	-	-	-	-
65	91	102	1.2	1.6	+0.4	+0.7	3.90×10^{-2}	3.5	3.9	5.2
66	91	102	1.2	1.6	+0.7	+1.0	7.45×10^{-1}	0.8	2.2	2.4
67	91	102	1.6	2.0	−1.0	−0.7	1.51	0.6	2.5	2.6
68	91	102	1.6	2.0	−0.7	−0.4	1.13	0.7	1.9	2.0
69	91	102	1.6	2.0	−0.4	0.0	5.95×10^{-3}	7.7	10.3	12.9
70	91	102	1.6	2.0	0.0	+0.4	5.66×10^{-3}	8.0	10.9	13.6
71	91	102	1.6	2.0	+0.4	+0.7	1.29	0.7	1.7	1.8
72	91	102	1.6	2.0	+0.7	+1.0	1.77	0.6	2.3	2.4
73	91	102	2.0	2.4	−1.0	−0.7	1.46	0.9	2.8	2.9
74	91	102	2.0	2.4	−0.7	−0.4	2.92	0.5	2.1	2.1
75	91	102	2.0	2.4	−0.4	0.0	8.02×10^{-1}	0.7	2.1	2.2
76	91	102	2.0	2.4	0.0	+0.4	8.92×10^{-1}	0.6	1.9	2.0
77	91	102	2.0	2.4	+0.4	+0.7	3.46	0.5	1.9	2.0
78	91	102	2.0	2.4	+0.7	+1.0	1.79	0.9	2.5	2.6
79	91	102	2.4	2.8	−1.0	−0.7	1.23	0.7	2.7	2.8
80	91	102	2.4	2.8	−0.7	−0.4	2.63	0.6	2.4	2.4
81	91	102	2.4	2.8	−0.4	0.0	1.23	0.6	2.4	2.5
82	91	102	2.4	2.8	0.0	+0.4	1.41	0.6	2.2	2.3
83	91	102	2.4	2.8	+0.4	+0.7	3.32	0.5	2.1	2.2
84	91	102	2.4	2.8	+0.7	+1.0	1.63	0.6	2.4	2.5
85	91	102	2.8	3.6	−1.0	−0.7	6.50×10^{-1}	0.6	3.6	3.7
86	91	102	2.8	3.6	−0.7	−0.4	5.66×10^{-1}	0.6	2.6	2.7
87	91	102	2.8	3.6	−0.4	0.0	-	-	-	-
88	91	102	2.8	3.6	0.0	+0.4	-	-	-	-
89	91	102	2.8	3.6	+0.4	+0.7	7.56×10^{-1}	0.5	2.3	2.3
90	91	102	2.8	3.6	+0.7	+1.0	9.02×10^{-1}	0.5	3.1	3.2
91	102	116	1.2	1.6	−1.0	−0.7	3.02×10^{-2}	4.7	12.7	13.6
92	102	116	1.2	1.6	−0.7	−0.4	1.14×10^{-3}	22.9	37.2	43.7
93	102	116	1.2	1.6	−0.4	0.0	-	-	-	-
94	102	116	1.2	1.6	0.0	+0.4	-	-	-	-
95	102	116	1.2	1.6	+0.4	+0.7	1.66×10^{-3}	20.6	37.7	42.9
96	102	116	1.2	1.6	+0.7	+1.0	5.44×10^{-2}	3.4	7.5	8.2
97	102	116	1.6	2.0	−1.0	−0.7	5.17×10^{-2}	3.8	6.9	7.9
98	102	116	1.6	2.0	−0.7	−0.4	3.19×10^{-2}	4.4	6.6	8.0
99	102	116	1.6	2.0	−0.4	0.0	-	-	-	-
100	102	116	1.6	2.0	0.0	+0.4	-	-	-	-
101	102	116	1.6	2.0	+0.4	+0.7	5.39×10^{-2}	3.3	4.6	5.6
102	102	116	1.6	2.0	+0.7	+1.0	1.05×10^{-1}	2.6	4.1	4.9
103	102	116	2.0	2.4	−1.0	−0.7	4.34×10^{-2}	5.3	12.9	14.0
104	102	116	2.0	2.4	−0.7	−0.4	7.14×10^{-2}	3.2	6.2	7.0
105	102	116	2.0	2.4	−0.4	0.0	2.35×10^{-2}	4.1	6.6	7.7
106	102	116	2.0	2.4	0.0	+0.4	3.10×10^{-2}	3.5	5.3	6.3
107	102	116	2.0	2.4	+0.4	+0.7	1.41×10^{-1}	2.3	4.1	4.7
108	102	116	2.0	2.4	+0.7	+1.0	1.07×10^{-1}	3.1	6.3	7.1
109	102	116	2.4	2.8	−1.0	−0.7	3.15×10^{-2}	3.7	13.2	13.7
110	102	116	2.4	2.8	−0.7	−0.4	5.52×10^{-2}	4.2	9.3	10.2
111	102	116	2.4	2.8	−0.4	0.0	3.10×10^{-2}	3.9	7.5	8.5
112	102	116	2.4	2.8	0.0	+0.4	5.23×10^{-2}	3.1	5.4	6.3
113	102	116	2.4	2.8	+0.4	+0.7	1.38×10^{-1}	2.7	5.9	6.5
114	102	116	2.4	2.8	+0.7	+1.0	9.89×10^{-2}	2.2	6.7	7.0

Bin	M_{ee} [GeV]		$\lvert y_{ee}\rvert$		$\cos\theta^*$		σ [pb/GeV]	δ^{stat} [%]	δ^{syst} [%]	δ^{tot} [%]
115	102	116	2.8	3.6	−1.0	−0.7	1.51×10^{-2}	3.4	19.0	19.3
116	102	116	2.8	3.6	−0.7	−0.4	1.04×10^{-2}	4.1	13.6	14.2
117	102	116	2.8	3.6	−0.4	0.0	-	-	-	-
118	102	116	2.8	3.6	0.0	+0.4	-	-	-	-
119	102	116	2.8	3.6	+0.4	+0.7	3.33×10^{-2}	2.4	7.5	7.9
120	102	116	2.8	3.6	+0.7	+1.0	5.34×10^{-2}	2.0	11.4	11.6
121	116	150	1.2	1.6	−1.0	−0.7	6.35×10^{-3}	9.4	39.0	40.1
122	116	150	1.2	1.6	−0.7	−0.4	-	-	-	-
123	116	150	1.2	1.6	−0.4	0.0	-	-	-	-
124	116	150	1.2	1.6	0.0	+0.4	-	-	-	-
125	116	150	1.2	1.6	+0.4	+0.7	4.21×10^{-4}	32.8	69.5	76.8
126	116	150	1.2	1.6	+0.7	+1.0	1.64×10^{-2}	4.7	15.6	16.3
127	116	150	1.6	2.0	−1.0	−0.7	9.66×10^{-3}	8.4	31.4	32.5
128	116	150	1.6	2.0	−0.7	−0.4	4.66×10^{-3}	7.6	13.4	15.4
129	116	150	1.6	2.0	−0.4	0.0	-	-	-	-
130	116	150	1.6	2.0	0.0	+0.4	-	-	-	-
131	116	150	1.6	2.0	+0.4	+0.7	1.17×10^{-2}	4.4	6.0	7.4
132	116	150	1.6	2.0	+0.7	+1.0	2.90×10^{-2}	3.9	11.7	12.3
133	116	150	2.0	2.4	−1.0	−0.7	7.45×10^{-3}	11.5	48.6	50.0
134	116	150	2.0	2.4	−0.7	−0.4	1.19×10^{-2}	5.6	12.9	14.1
135	116	150	2.0	2.4	−0.4	0.0	3.44×10^{-3}	7.3	18.8	20.2
136	116	150	2.0	2.4	0.0	+0.4	7.26×10^{-3}	4.7	8.1	9.3
137	116	150	2.0	2.4	+0.4	+0.7	3.02×10^{-2}	3.6	6.0	7.0
138	116	150	2.0	2.4	+0.7	+1.0	3.00×10^{-2}	4.1	12.3	13.0
139	116	150	2.4	2.8	−1.0	−0.7	3.29×10^{-3}	16.3	35.5	39.1
140	116	150	2.4	2.8	−0.7	−0.4	8.19×10^{-3}	7.5	15.5	17.2
141	116	150	2.4	2.8	−0.4	0.0	5.55×10^{-3}	6.0	10.0	11.6
142	116	150	2.4	2.8	0.0	+0.4	1.06×10^{-2}	4.5	5.9	7.4
143	116	150	2.4	2.8	+0.4	+0.7	2.89×10^{-2}	3.8	5.2	6.5
144	116	150	2.4	2.8	+0.7	+1.0	2.84×10^{-2}	3.3	5.4	6.3
145	116	150	2.8	3.6	−1.0	−0.7	1.73×10^{-3}	11.0	31.7	33.5
146	116	150	2.8	3.6	−0.7	−0.4	1.42×10^{-3}	8.7	17.1	19.2
147	116	150	2.8	3.6	−0.4	0.0	-	-	-	-
148	116	150	2.8	3.6	0.0	+0.4	-	-	-	-
149	116	150	2.8	3.6	+0.4	+0.7	6.46×10^{-3}	3.7	5.0	6.2
150	116	150	2.8	3.6	+0.7	+1.0	1.21×10^{-2}	3.1	6.8	7.5

Table B.4: Summary table of the three-dimensional differential cross-section measurement at Born-level. The relative statistical, systematic, and total uncertainties are also given. A luminosity uncertainty of 1.9% has not been included.

$\lvert y_{ee}\rvert$		M_{ee} [GeV]		A_{FB}	δ^{stat}	δ^{syst}	δ^{tot}
1.2	1.6	66	80	−0.2435	0.044	0.062	0.076
1.2	1.6	80	91	0.0097	0.006	0.004	0.008
1.2	1.6	91	102	0.0700	0.006	0.004	0.007
1.2	1.6	102	116	0.2825	0.026	0.041	0.049
1.2	1.6	116	150	0.4517	0.042	0.122	0.129
1.6	2.0	66	80	−0.2316	0.017	0.020	0.026
1.6	2.0	80	91	0.0027	0.003	0.002	0.004
1.6	2.0	91	102	0.0733	0.003	0.002	0.004
1.6	2.0	102	116	0.3103	0.016	0.019	0.025
1.6	2.0	116	150	0.4795	0.026	0.073	0.078
2.0	2.4	66	80	−0.2858	0.012	0.016	0.020
2.0	2.4	80	91	−0.0081	0.003	0.002	0.004
2.0	2.4	91	102	0.0839	0.003	0.002	0.004
2.0	2.4	102	116	0.3381	0.013	0.019	0.024
2.0	2.4	116	150	0.4945	0.021	0.071	0.074
2.4	2.8	66	80	−0.3250	0.011	0.013	0.017
2.4	2.8	80	91	−0.0038	0.003	0.003	0.004
2.4	2.8	91	102	0.1108	0.003	0.003	0.004
2.4	2.8	102	116	0.4215	0.012	0.019	0.022
2.4	2.8	116	150	0.5987	0.018	0.040	0.044
2.8	3.6	66	80	−0.4671	0.011	0.020	0.023
2.8	3.6	80	91	−0.0080	0.003	0.004	0.005
2.8	3.6	91	102	0.1541	0.003	0.003	0.004
2.8	3.6	102	116	0.5457	0.011	0.026	0.028
2.8	3.6	116	150	0.7100	0.019	0.051	0.054

Table B.5: Summary table of the forward-backward asymmetry measurement at Born-level. The absolute statistical, systematic, and total uncertainties are also given.

Appendix C

Combination

The measurements presented in this dissertation are a part of an ATLAS analysis [36] that is in the process of being published in a physics journal[1]. Along with the central-central and central-forward analyses, a third measurement of Drell-Yan production in the muon channel,

$$q\bar{q} \to Z/\gamma^* \to \mu^-\mu^+,$$

was made [112]. The *muon-muon* measurement is completely analogous to the central-central one sharing the same fiducial volume and analysis binning. At Born-level the differential cross-section and forward-backward asymmetry results of the two should be identical.

In this appendix chapter, the central-central and muon-muon measurements are averaged or *combined* using a χ^2-minimization technique [113, 76] and the results are presented. Though having very different topologies, a comparison can also be made between the *central* measurements (central-central and muon-muon) and the central-forward results. The central-central, muon-muon, and central-forward differential cross-section measurements can be extrapolated to a common fiducial volume using an acceptance correction allowing them to be compared. This appendix concludes with a discussion on the compatibility of all three measurements.

Please note that the combination of the central-central and muon-muon cross-sections and the comparison between all three measurements were not performed by the author of this dissertation. The author's contributions to the content presented here will be clearly stated.

[1] As of August 14, 2017.

C.1 Muon Momentum Corrections

Problems were observed in the alignment of the muon spectrometer with respect to the inner detector [114]. As a solution, muon momentum in the muon-muon analysis is calculated solely using measurements from the inner detector as opposed to using both subdetectors as is typically done. To further complicate matters, momentum measurements from the inner detector were found to show a charge bias where, depending on the charge of the muon, the inner detector would respond differently. Corrections – later found to be crucial to the combination of the central-central and muon-muon analyses – were derived by the author to minimize these differences.

Muon momentum, p^{μ}, corrections Δ are calculated using $Z \to ee$ data and signal MC events from the central-central analysis. Under the assumption that the electromagnetic calorimeter response is the same for electrons and positrons, charge dependent biases in momentum measurements due to the inner detector reveal themselves as differences in the energy-momentum, E/p, ratios of electrons and positrons where E is measured from the calorimeter and p, the inner detector [115]. The corrections are defined as

$$\Delta = \frac{\langle E/p \rangle^{-} - \langle E/p \rangle^{+}}{2\langle E_T \rangle}, \tag{C.1}$$

where $\langle E/p \rangle^{-}$ and $\langle E/p \rangle^{+}$ are the means of the E/p distributions of electrons and positrons, respectively; and $\langle E_T \rangle$ is the mean transverse energy (measured from the calorimeter) of both. Derived in 4 bins in ϕ,

$$\phi = [-\pi, -\pi/2, 0, \pi/2, \pi], \tag{C.2}$$

and 40 bins in η,

$$\eta = [-2.5, -2.375, -2.25, ..., 0, ..., 2.25, 2.375, 2.5], \tag{C.3}$$

the corrections are applied in the following way in order to obtain a corrected muon momentum:

$$p^{\mu}_{\text{corr}} = \frac{p^{\mu}}{1 + q\, p^{\mu}_{T}\, \Delta}, \tag{C.4}$$

where q is the charge and p^{μ}_{T} is the transverse momentum of the muon.

In both Figures C.1 (data) and C.2 (signal MC) are two example E/p distributions,

one corresponding to the electron and the other, the positron. A crystal ball function, which consists of a Gaussian core with a power-law tail, is fitted to each of the distributions using software package RooFit [116]. The means $\langle E/p \rangle^-$ and $\langle E/p \rangle^+$ are extracted from the fits while $\langle E_T \rangle$ is calculated as a simple average. With these values, Equation (C.1) is used to determine Δ. This process is repeated for all $4 \times 40 = 160$ bins, for data and MC. The difference between the corrections obtained from data and those from MC is taken as the uncertainty on the data corrections which are illustrated in Figure C.3.

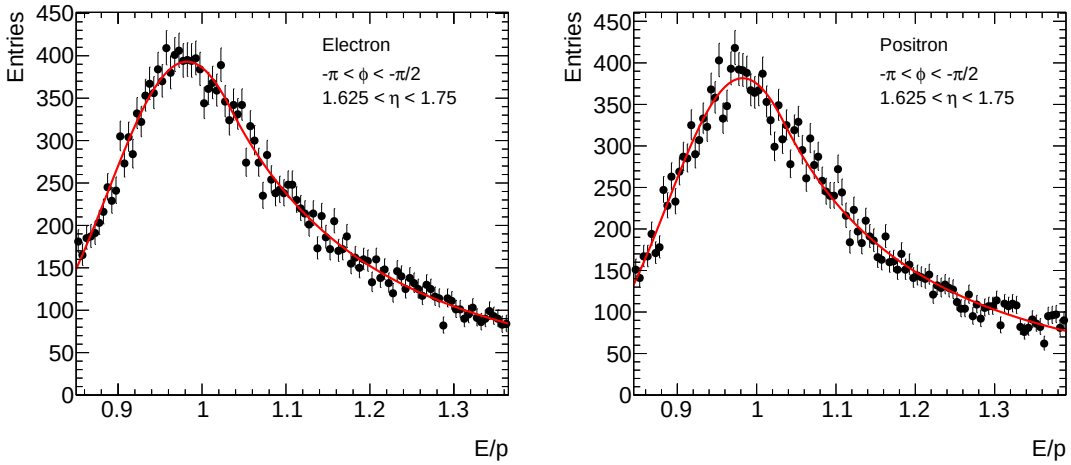

Figure C.1: Crystal ball fits of electron (left) and positron (right) E/p distributions from data.

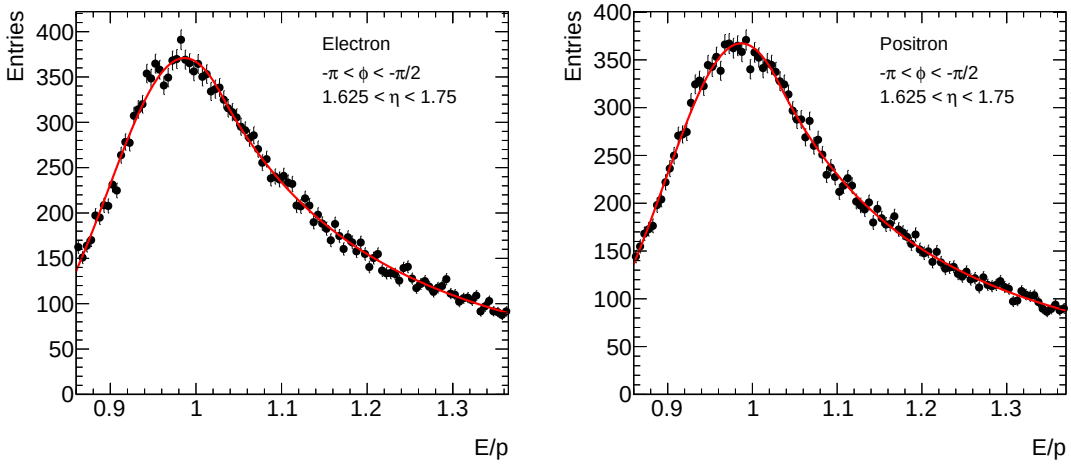

Figure C.2: Crystal ball fits of electron (left) and positron (right) E/p distributions from signal MC.

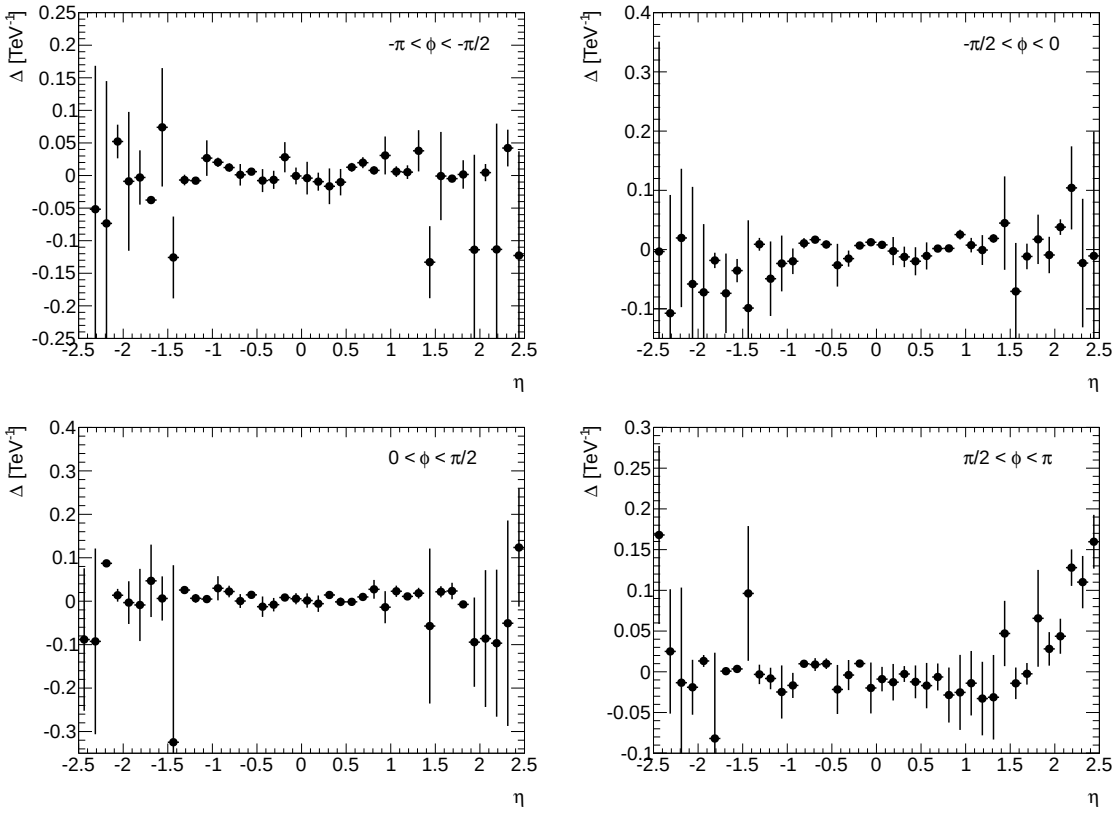

Figure C.3: Corrections applied to data muons used to correct for charge biases due to misalignment of the inner detector.

Applied in the muon-muon analysis, the resulting Δ-corrections were found to correct for much of the charge bias that was observed in data. Moreover, the uncertainty on these corrections were propagated to the three-dimensional cross-section measurement which brought the data and POWHEG prediction into better agreement [36]. The corrections were found to be especially important when measuring A_{FB} as charge biases can have a significant impact on the measurement of $\cos\theta^*$. It was also discovered that they were required for a successful combination of the central-central and muon-muon measurements.

C.2 χ^2-Minimization

The combination of the central-central and muon-muon channels is performed using software developed for deep inelastic scattering cross-section data. The method assumes that the measurement of observable $\sigma \pm \delta$ in bin i is distributed according to

a Gaussian probability distribution function

$$P(t) = \frac{1}{\sqrt{2\pi}\delta} e^{-\frac{(t-\sigma)^2}{2\delta^2}}, \tag{C.5}$$

where t is the *true* value of what is being measured. By taking the natural log of Equation (C.5), a χ^2 function is obtained:

$$\chi^2(t) = \frac{(t-\sigma)^2}{\delta^2}. \tag{C.6}$$

For N analysis bins, the χ^2 function takes the form

$$\chi^2(t) = \sum_{i=1}^{N} \frac{(t_i - \sigma_i)^2}{\delta_i^2}. \tag{C.7}$$

To find the set of t values that best describes the data, Equation (C.7) must be minimized,

$$\frac{d\chi^2}{dt} = 0, \tag{C.8}$$

and solved for t in each bin.

The method used to combine the central-central and muon-muon measurements builds off the general principles presented above. It uses nuisance parameters to represent correlations between the analysis bins of the individual measurements and correlations across multiple measurements. To account for these, Equation (C.7) is modified to include several new terms. For a single measurement m, e.g. considering only the central-central measurement, the χ^2 function takes the form

$$\chi^2_m(t,\rho) = \sum_{i=1}^{N} \left(\frac{t_i - \sigma_i^m - \sum_{c=1}^{C} \Gamma_{ic}^m \rho_c}{\delta_i^m} \right)^2 - \sum_{c=1}^{C} \rho_c^2, \tag{C.9}$$

where $c = 1, 2, ..., C$ are the correlated sources of uncertainty and ρ_c is a nuisance parameter corresponding to source c. Quantity Γ_{ic}^m is the shift in the measured cross-section due to source c; mathematically, it is defined as

$$\Gamma_{ic}^m = \frac{t_i}{\sigma_i^m} \frac{\partial \sigma_i^m}{\partial \alpha_c^m}, \tag{C.10}$$

where α_c^m is the central value of the correlated uncertainty due to c.

For multiple, M, measurements, e.g. now considering both the central-central and

muon-muon measurements, the χ^2-statistic corresponding to their combination is

$$\chi^2_{\text{com}}(t,\rho) = \sum_{m=1}^{M} \chi^2_m(t,\rho). \tag{C.11}$$

By minimizing Equation (C.11) with respect to t, the combined values $t = \bar{\sigma}$, averaged nuisance parameters $\rho = \bar{\rho}$, and uncorrelated uncertainties $\delta = \bar{\delta}$ of the observable of interest are obtained. To quantify the consistency between the measurements used in the combination, the minimum χ^2_{com} is divided by the number of degrees of freedom,

$$N_{\text{df}} = N_{\text{in}} - N_{\text{out}} \tag{C.12}$$

where N_{in} is the number of input σ values from all measurements and N_{out} is the number of output combined values. A $\chi^2_{\text{com}}/N_{\text{df}}$ close to unity signifies agreement between the measurement.

C.3 Central-Central and Muon-Muon

Electrons and muons are measured in very different ways using the ATLAS detector. Although both use the inner detector, electron energy is determined using information from the EM calorimeter while muon momentum is typically measured using both the inner detector and muon spectrometer and therefore are affected by different sources of systematic uncertainties. Comparing the two at generator-level (after unfolding) is a test of how well they were measured at reconstruction-level.

In Figures C.4 to C.10, the combined three-dimensional differential cross-sections are plotted with the individual central-central and muon-muon results and a theoretical prediction generated using POWHEG. Both the statistical and total uncertainties on the combined results are also given. By using two measurements, there is a significant reduction in the statistical and total uncertainties. Rather than using the individual central-central and muon-muon results, it is the combined measurement that will be used to extract parton distribution function information and a measurement of the weak mixing angle θ_{W}. The central-central and muon-muon measurements achieve a consistency score of $\chi^2_{\text{com}}/N_{\text{df}} = 489.4/451$ which corresponds to an acceptable p-value of 0.10.

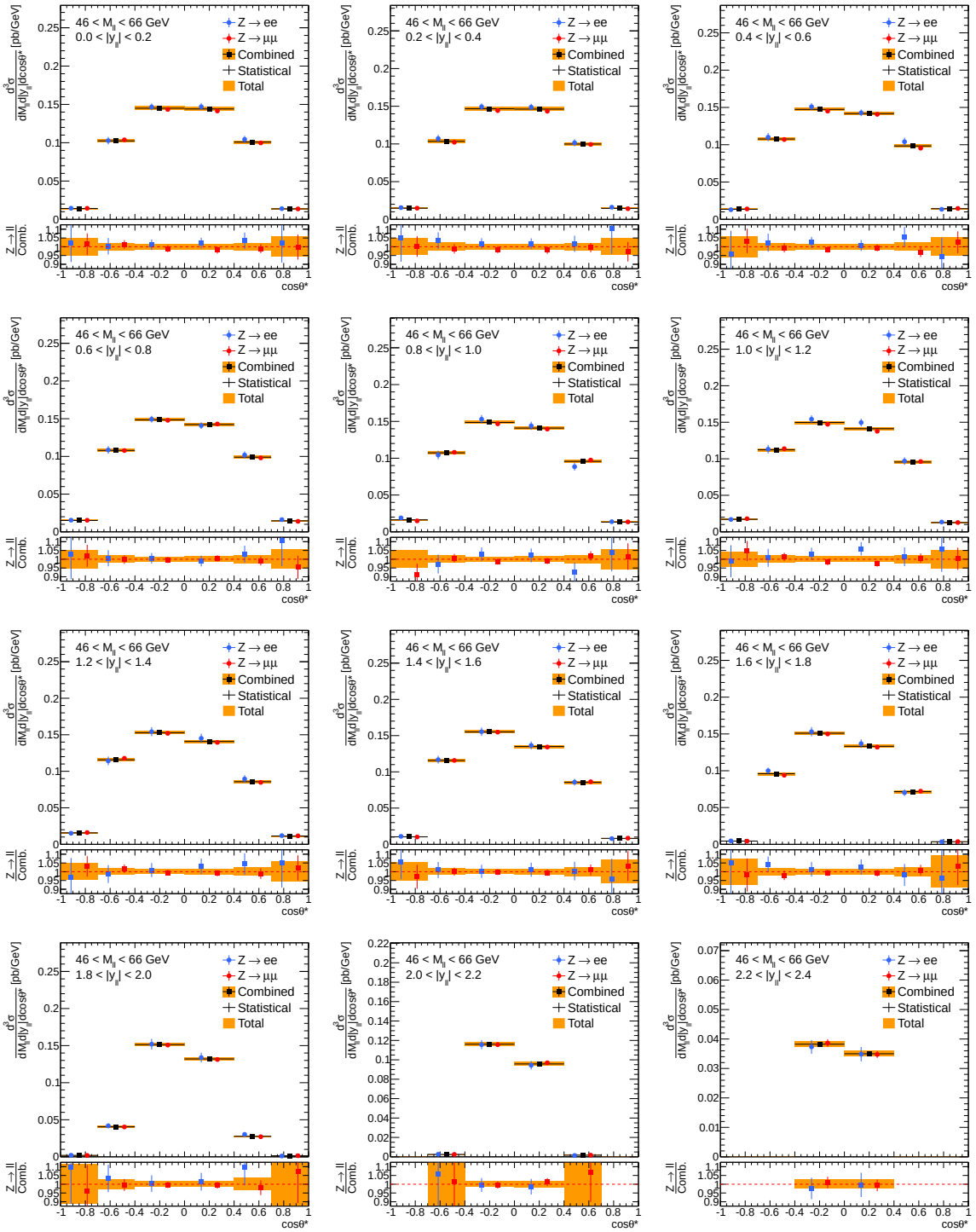

Figure C.4: Combined three-dimensional differential cross-section $\frac{d^3\sigma}{dM_{\ell\ell}d|y_{\ell\ell}|d\cos\theta^*}$ results for invariant mass bin $M_{\ell\ell} \in [46, 66]$ GeV and for the entire rapidity range of interest, $0.0 < |y_{ee}| < 2.4$.

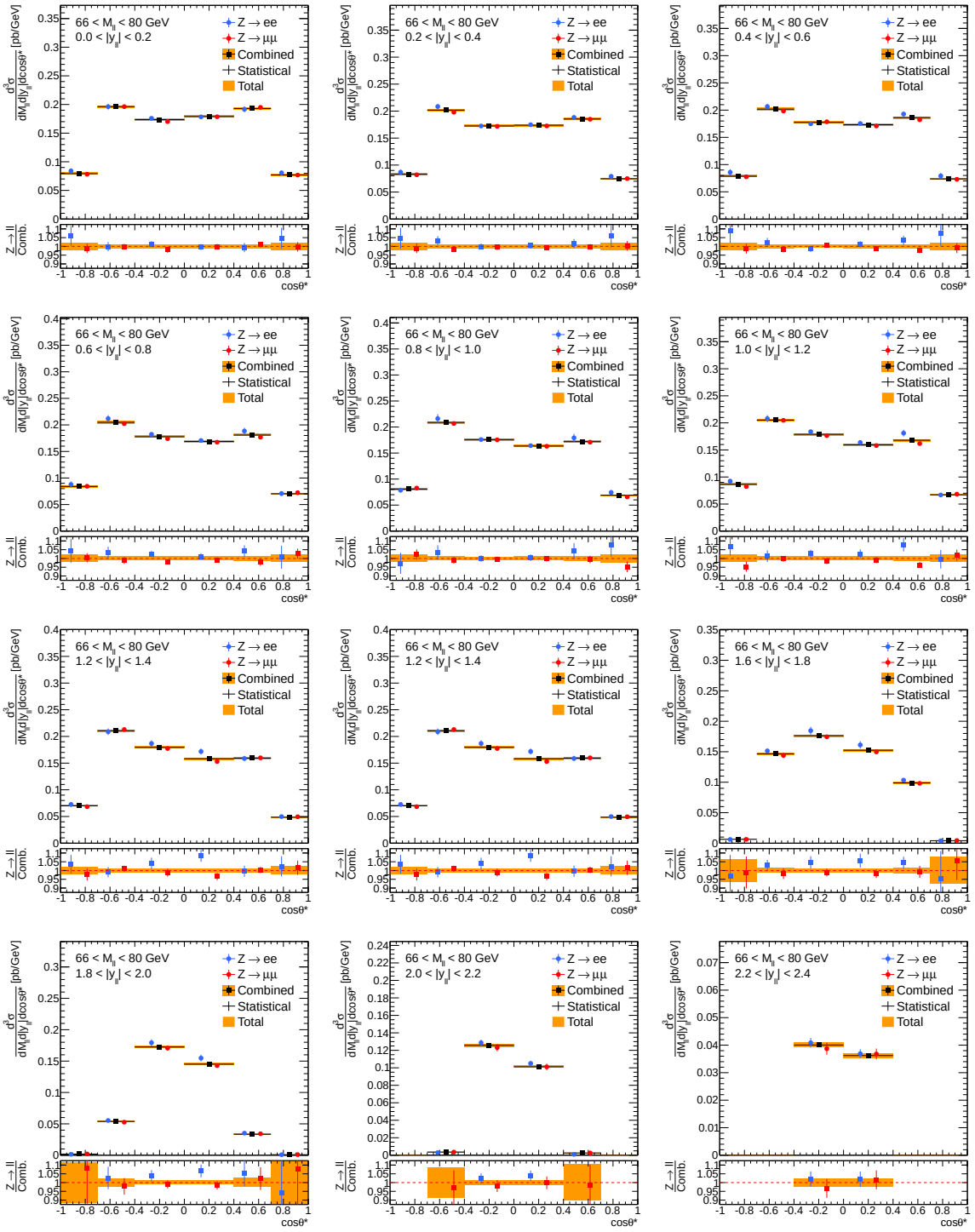

Figure C.5: Combined three-dimensional differential cross-section $\frac{d^3\sigma}{dM_{\ell\ell}d|y_{\ell\ell}|d\cos\theta^*}$ results for invariant mass bin $M_{\ell\ell} \in [66, 80]$ GeV and for the entire rapidity range of interest, $0.0 < |y_{ee}| < 2.4$.

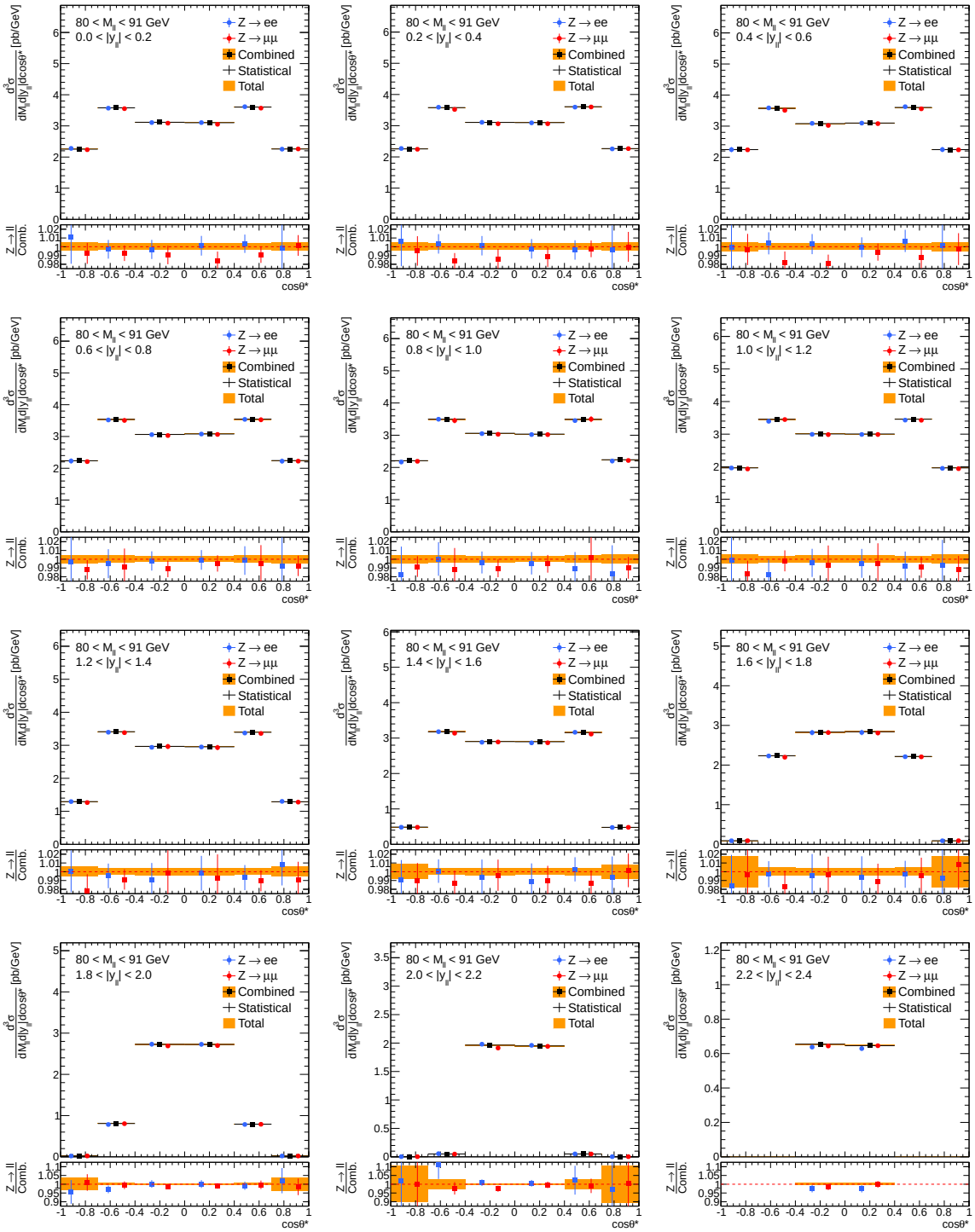

Figure C.6: Combined three-dimensional differential cross-section $\frac{d^3\sigma}{dM_{\ell\ell}d|y_{\ell\ell}|d\cos\theta^*}$ results for invariant mass bin $M_{\ell\ell} \in [80, 91]$ GeV and for the entire rapidity range of interest, $0.0 < |y_{ee}| < 2.4$.

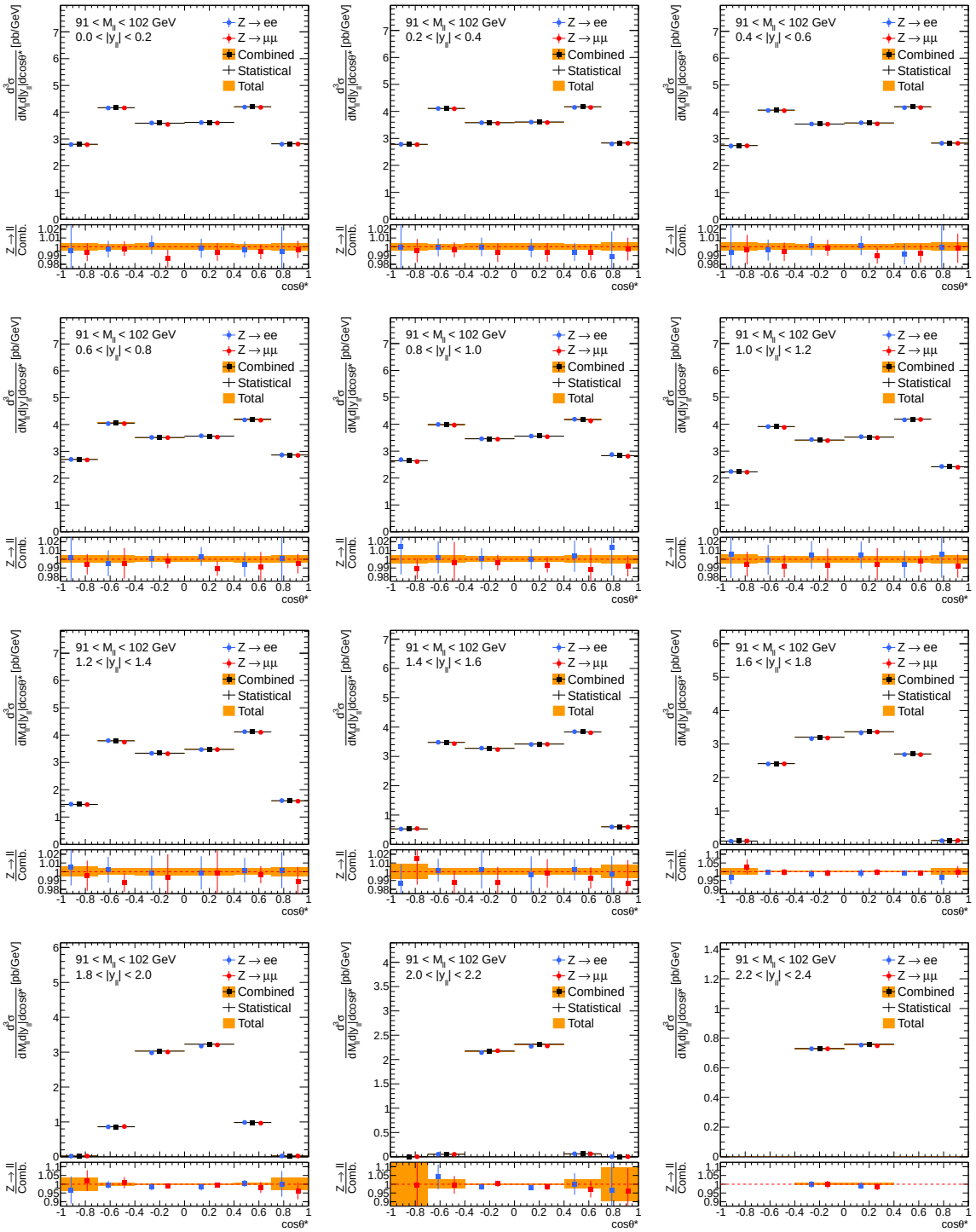

Figure C.7: Combined three-dimensional differential cross-section $\frac{d^3\sigma}{dM_{\ell\ell}d|y_{\ell\ell}|d\cos\theta^*}$ results for invariant mass bin $M_{\ell\ell} \in [91, 102]$ GeV and for the entire rapidity range of interest, $0.0 < |y_{ee}| < 2.4$.

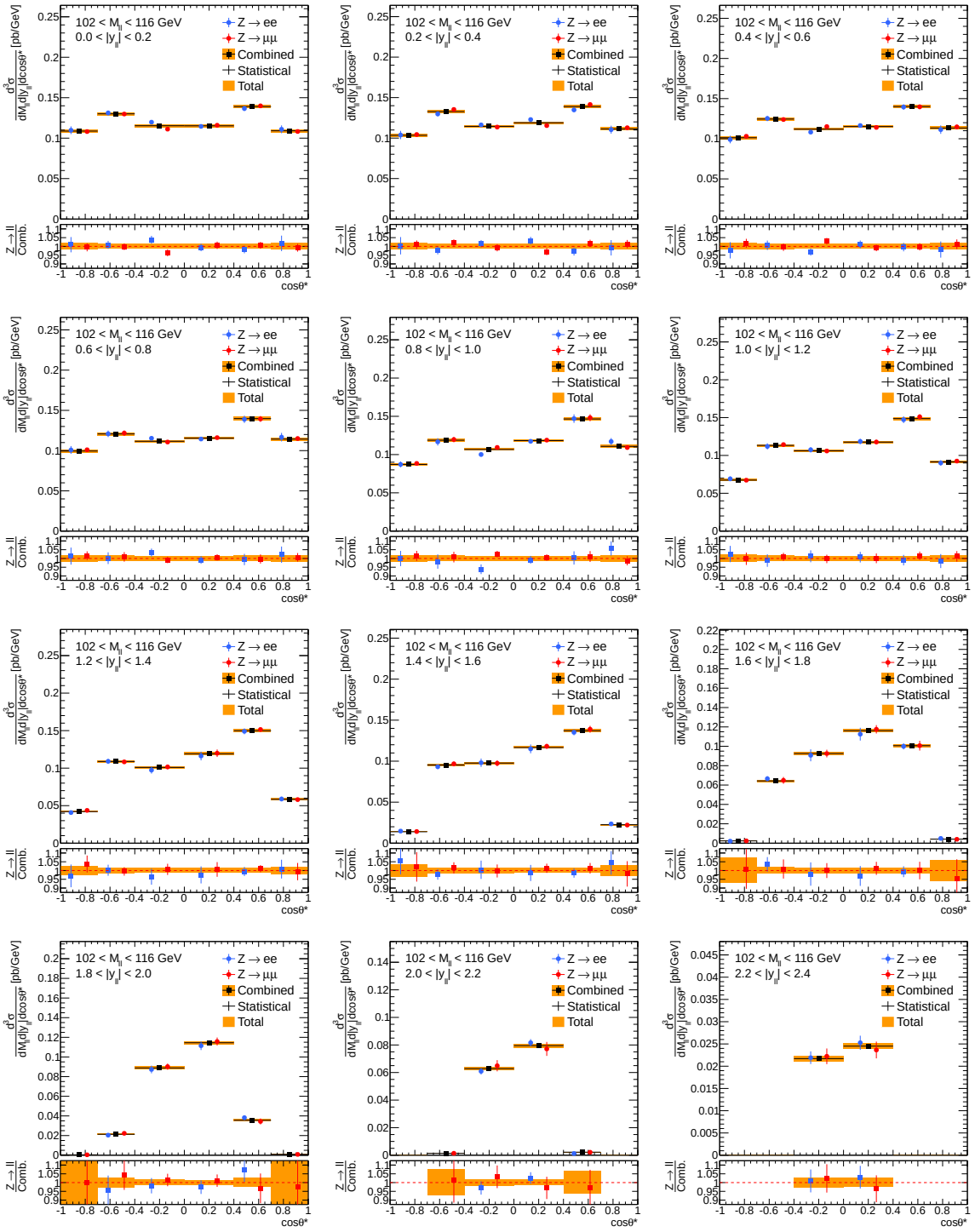

Figure C.8: Combined three-dimensional differential cross-section $\frac{d^3\sigma}{dM_{\ell\ell}d|y_{\ell\ell}|d\cos\theta^*}$ results for invariant mass bin $M_{\ell\ell} \in [102, 116]$ GeV and for the entire rapidity range of interest, $0.0 < |y_{ee}| < 2.4$.

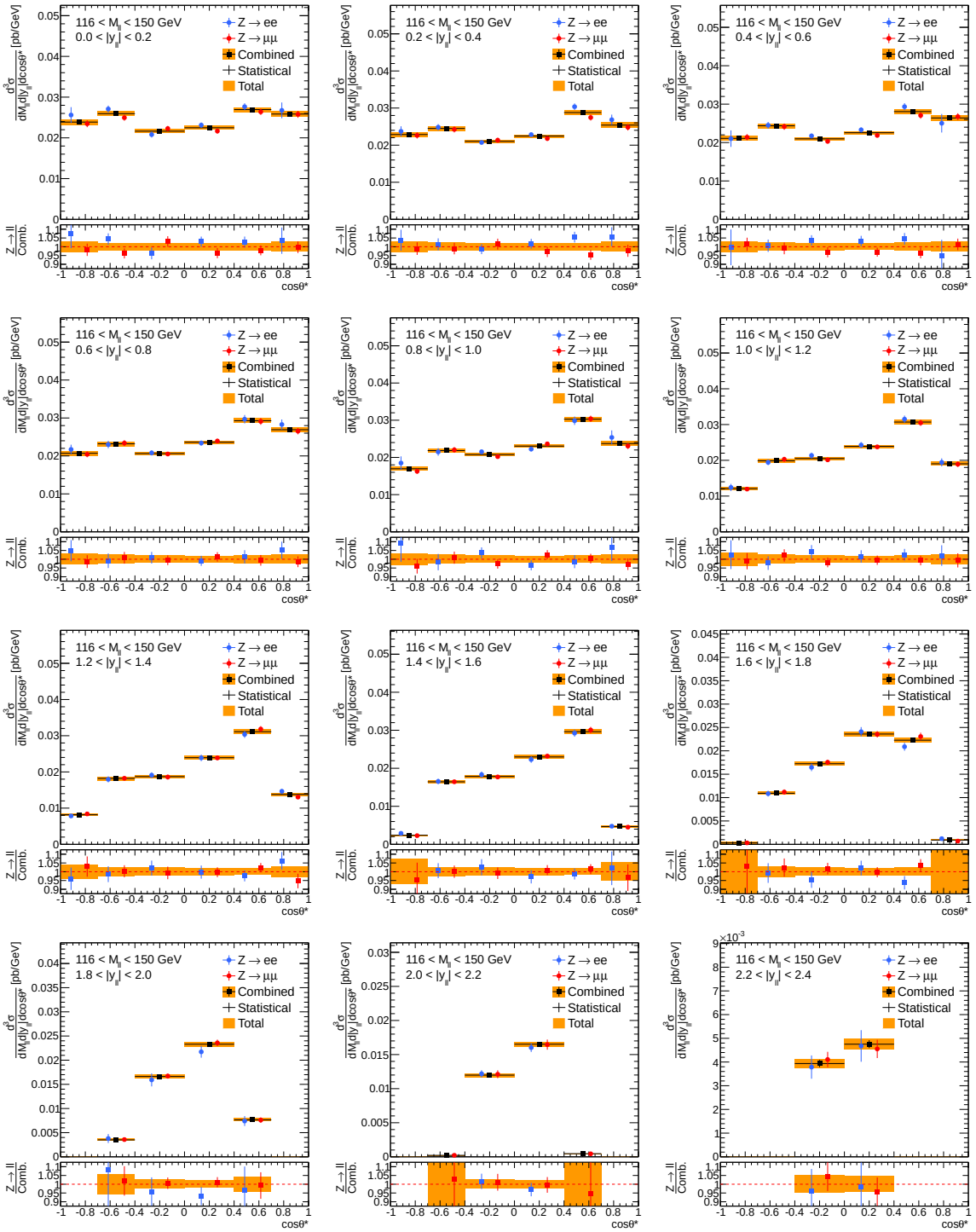

Figure C.9: Combined three-dimensional differential cross-section $\frac{d^3\sigma}{dM_{\ell\ell}d|y_{\ell\ell}|d\cos\theta^*}$ results for invariant mass bin $M_{\ell\ell} \in [116, 150]$ GeV and for the entire rapidity range of interest, $0.0 < |y_{ee}| < 2.4$.

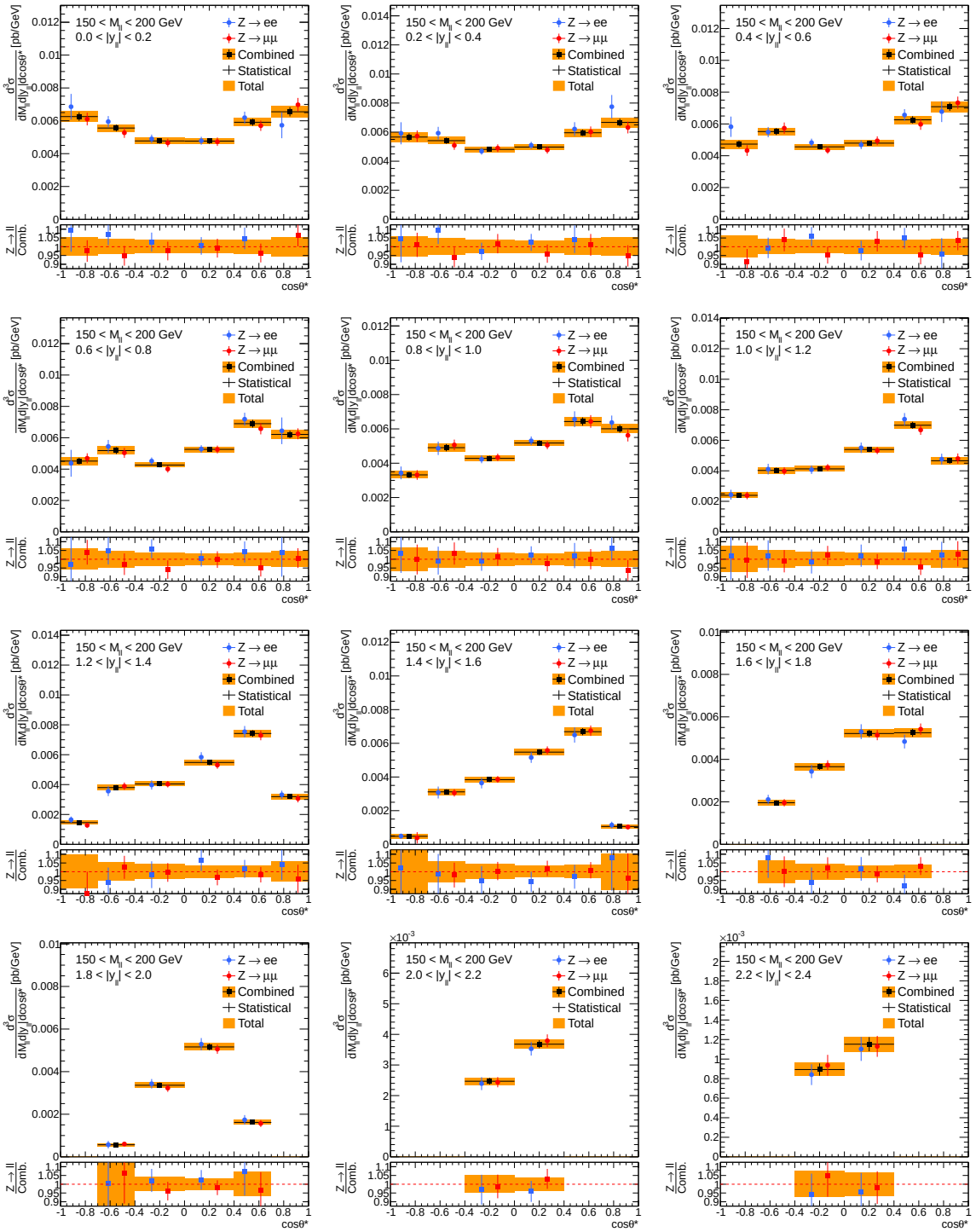

Figure C.10: Combined three-dimensional differential cross-section $\frac{d^3\sigma}{dM_{\ell\ell}d|y_{\ell\ell}|d\cos\theta^*}$ results for invariant mass bin $M_{\ell\ell} \in [150, 200]$ GeV and for the entire rapidity range of interest, $0.0 < |y_{ee}| < 2.4$.

C.4 Central-Forward Comparisons

And finally, a comparison is made between the cross-section results of the central analyses and the central-forward analysis. In order to be able to make this comparison, all three measurements must be extrapolated to a common fiducial volume using bin-by-bin acceptance corrections. The *common* volume is defined as

$$66 < M_{\ell\ell} < 150 \text{ GeV}, \qquad p_T^{\ell} > 20 \text{ GeV}.$$

Invariant mass bins $M_{\ell\ell} \in [46, 66]$ and $[150, 200]$ GeV of the central analyses are removed and no requirement on lepton η^{ℓ} is made. Being a large extrapolation in phase space, the correction is expected to be marked by large theoretical uncertainties such as those from parton distribution functions. The acceptance corrections, calculated by the author using signal MC, are

$$A_i = \frac{N_i^{\text{com}}}{N_i^{\text{fid}}}, \quad i = 1, 2, ..., 504, \qquad B_j = \frac{N^{\text{com}}}{M_j^{\text{fid}}}, \quad j = 1, 2, ..., 150, \tag{C.13}$$

where index i runs over the analysis bins of the central analyses and j over the bins of the central-forward analysis; N^{com} is the number of generated events in the common volume; and N^{fid} and M^{fid} are the numbers in the fiducial volume of the central analyses and central-forward analysis, respectively. Acceptance A is applied to the central measurements while B is applied to the central-forward one.

The extrapolated differential cross-sections for all three measurements are binned in $|y_{\ell\ell}|$, the results of which can be seen in Figures C.11 to C.15. Visually, the agreement between the central-forward and the central measurements is good, except in the regions near the Z-peak (Figures C.12 and C.13). The discrepancy is most likely due to residual problems with the energy calibration and resolution of forward electrons.

Quantitative comparisons between the central-forward and central results are performed using the same χ^2-minimization procedure described above. The green bands shown in Figures C.11 to C.15 indicate which data points are included in the compatibility check. Assigning a conservative 1% anticorrelated uncertainty to the acceptance correction [36], a compatibility of $\chi^2_{\text{com}}/N_{\text{df}} = 32/30$ between the two electron channel measurements is attained which corresponds to a p-value of 0.63 indicating a strong compatibility. A compatibility of $\chi^2_{\text{com}}/N_{\text{df}} = 39/30$ for an acceptable p-value of 0.12 is found for the muon-muon and central-forward measurements.

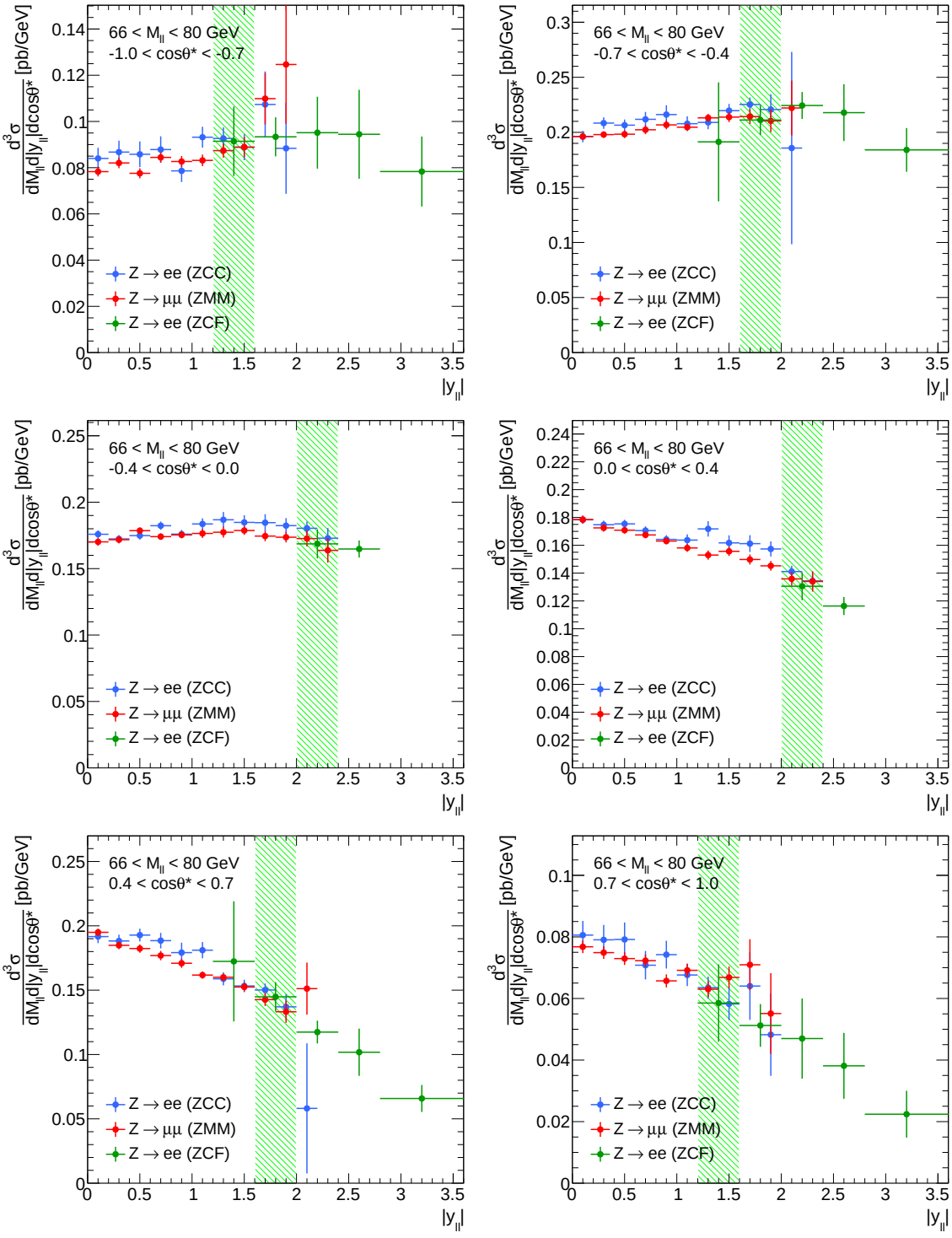

Figure C.11: Central-central, muon-muon, and central-forward three-dimensional differential cross-section $\frac{d^3\sigma}{dM_{\ell\ell}d|y_{\ell\ell}|d\cos\theta^*}$ results for invariant mass bin $M_{\ell\ell} \in [66, 80]$ GeV and for the entire polar angle range of interest, $-1.0 < \cos\theta^* < 1.0$.

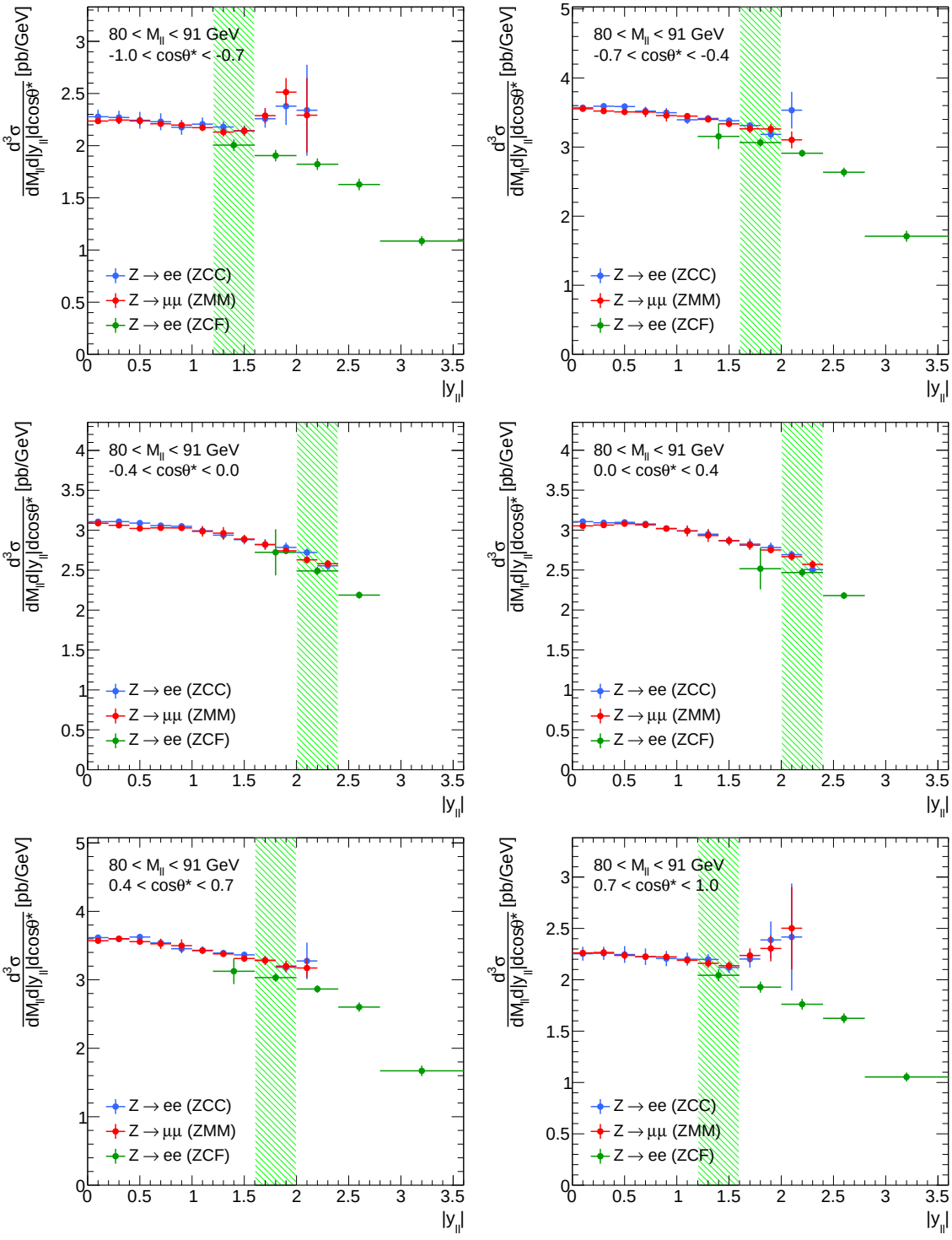

Figure C.12: Central-central, muon-muon, and central-forward three-dimensional differential cross-section $\frac{d^3\sigma}{dM_{\ell\ell}d|y_{\ell\ell}|d\cos\theta^*}$ results for invariant mass bin $M_{\ell\ell} \in [80, 91]$ GeV and for the entire polar angle range of interest, $-1.0 < \cos\theta^* < 1.0$.

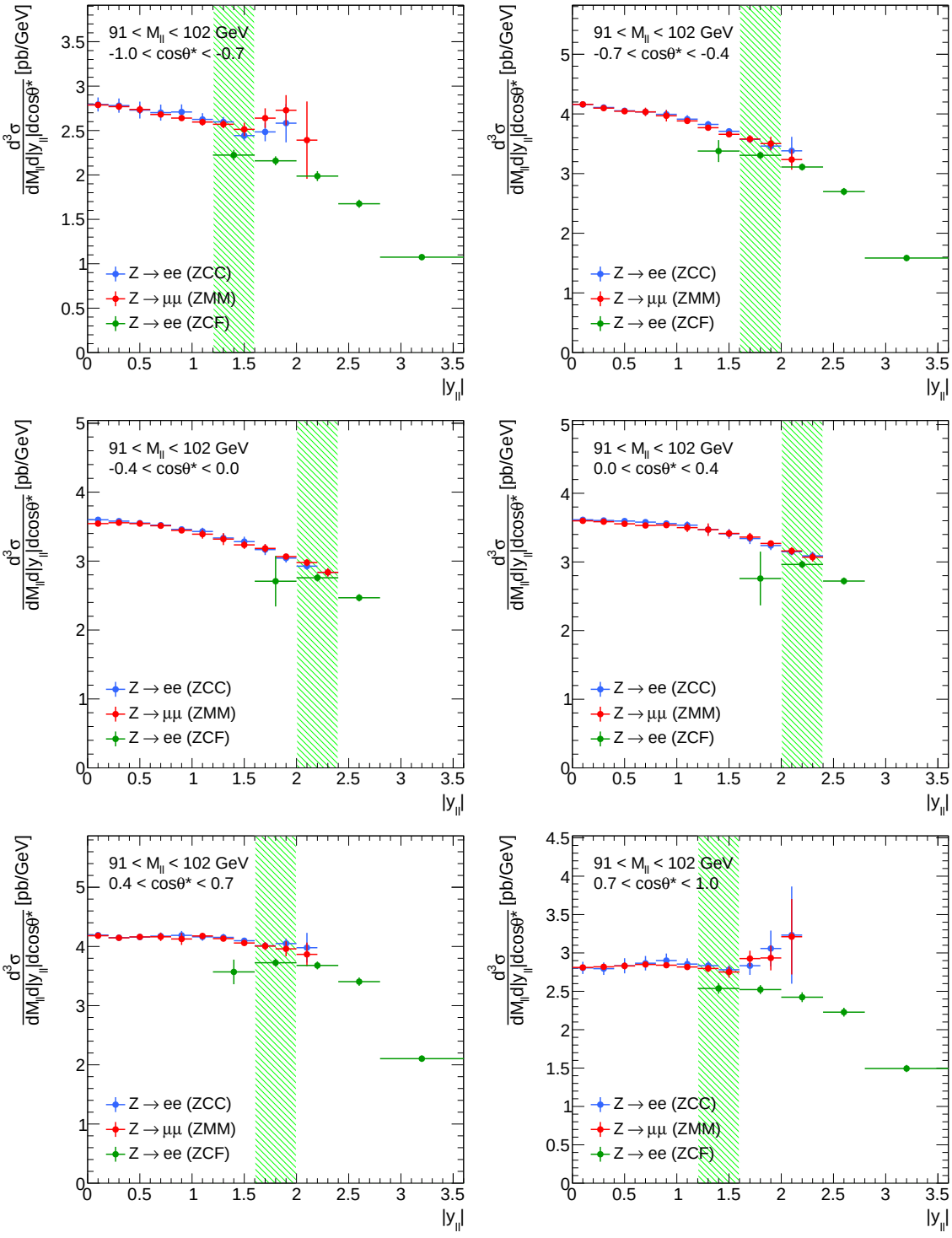

Figure C.13: Central-central, muon-muon, and central-forward three-dimensional differential cross-section $\frac{d^3\sigma}{dM_{\ell\ell}d|y_{\ell\ell}|d\cos\theta^*}$ results for invariant mass bin $M_{\ell\ell} \in [91, 102]$ GeV and for the entire polar angle range of interest, $-1.0 < \cos\theta^* < 1.0$.

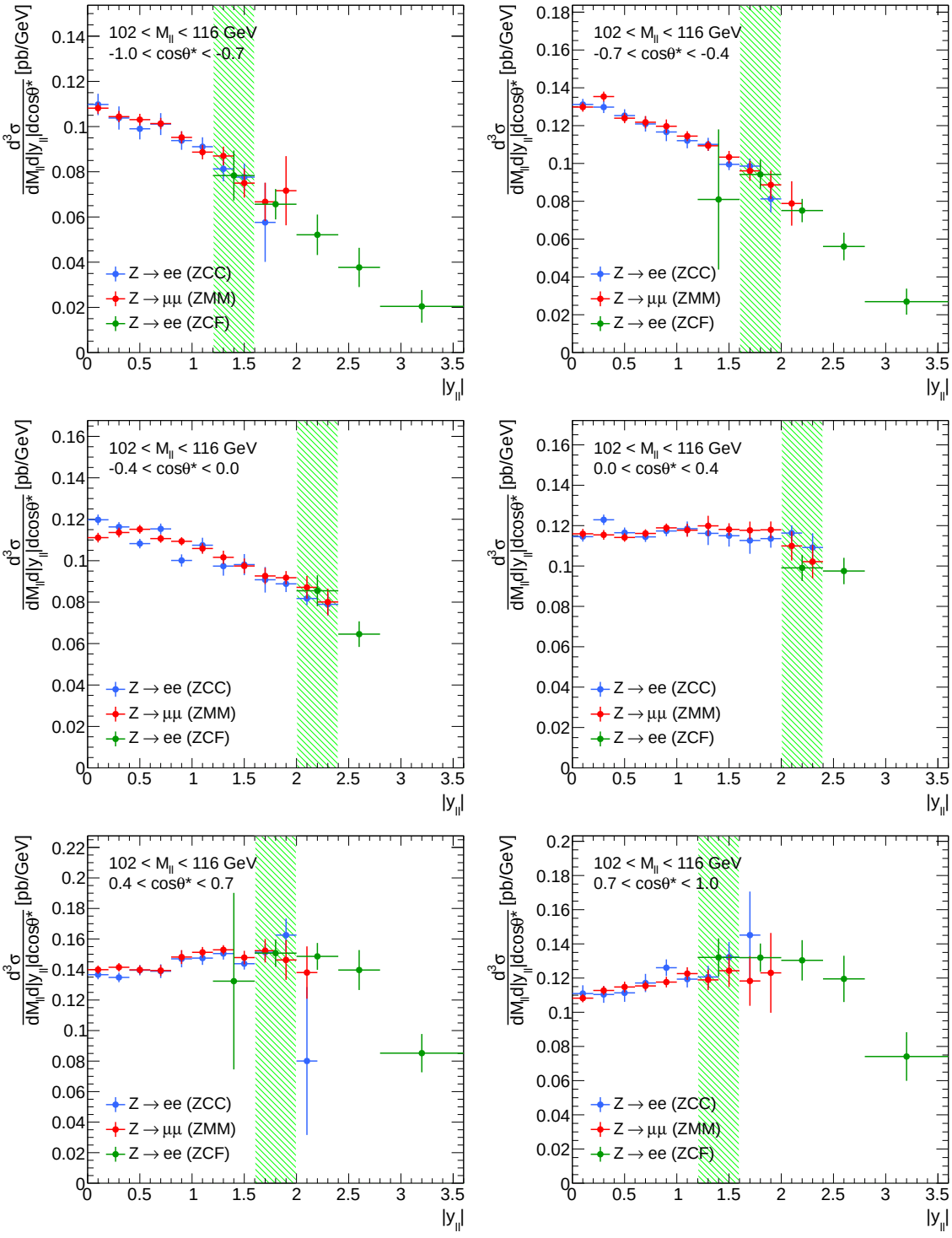

Figure C.14: Central-central, muon-muon, and central-forward three-dimensional differential cross-section $\frac{d^3\sigma}{dM_{\ell\ell}d|y_{\ell\ell}|d\cos\theta^*}$ results for invariant mass bin $M_{\ell\ell} \in [102, 116]$ GeV and for the entire polar angle range of interest, $-1.0 < \cos\theta^* < 1.0$.

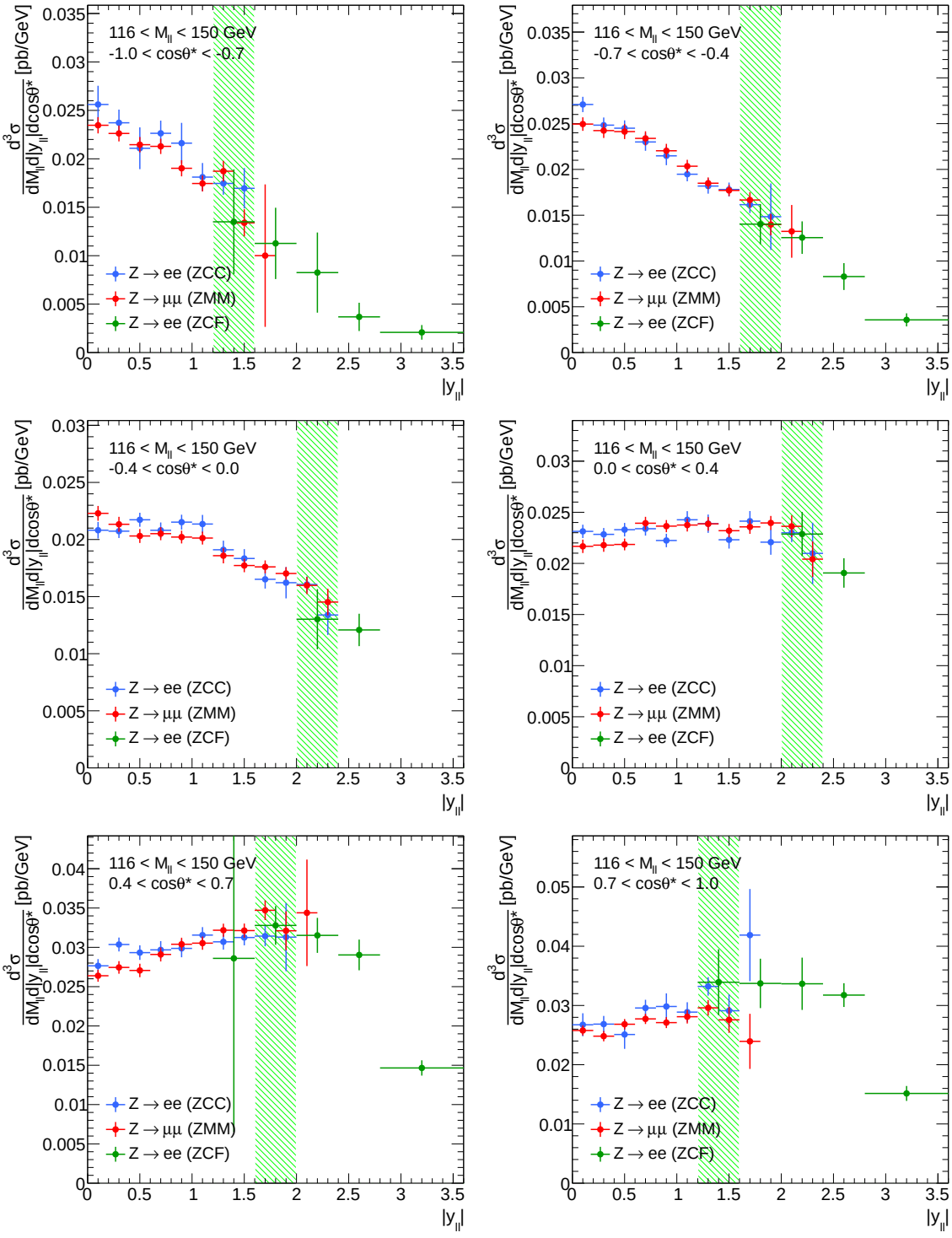

Figure C.15: Central-central, muon-muon, and central-forward three-dimensional differential cross-section $\frac{d^3\sigma}{dM_{\ell\ell}d|y_{\ell\ell}|d\cos\theta^*}$ results for invariant mass bin $M_{\ell\ell} \in [116, 150]$ GeV and for the entire polar angle range of interest, $-1.0 < \cos\theta^* < 1.0$.

References

[1] T. D. Lee, C. N. Yang. Question of Parity Conservation in Weak Interactions. *Phys. Rev.*, 104:254–258, 1956. (Cited on page 1.)

[2] C. S. Wu et al. Experimental Test of Parity Conservation in Beta Decay. *Phys. Rev.*, 105(4):1413–1415, 1957. (Cited on page 1.)

[3] S. D. Drell, T.-M. Yan. Massive Lepton-Pair Production in Hadron-Hadron Collisions at High Energies. *Phys. Rev. Lett.*, 25:316–320, 1970. (Cited on pages 1 and 16.)

[4] The LHC Study Group. *Design study of the Large Hadron Collider.* CERN, 1991. (Cited on page 2.)

[5] ATLAS Collaboration. The ATLAS Experiment at the CERN Large Hadron Collider. *JINST*, 3:S08003, 2008. (Cited on page 2.)

[6] P. W. Higgs. Broken symmetries, Massless Particles and Gauge Fields. *Phys. Lett.*, 12:132–133, 1964. (Cited on pages 2 and 11.)

[7] F. Englert, R. Brout. Broken Symmetry and the Mass of Gauge Vector Mesons. *Phys. Rev. Lett.*, 13:321–323, 1964. (Cited on pages 2 and 11.)

[8] P. W. Higgs. Broken Symmetries and the Masses of Gauge Bosons. *Phys. Rev. Lett.*, 13:508–509, 1964. (Cited on pages 2 and 11.)

[9] G. S. Guralnik, C. R. Hagen, T. W. B. Kibble. Global Conservation Laws and Massless Particles. *Phys. Rev. Lett.*, 13:585–587, 1964. (Cited on pages 2 and 11.)

[10] P. W. Higgs. Spontaneous Symmetry Breakdown without Massless Bosons. *Phys. Rev.*, 145:1156–1163, 1966. (Cited on pages 2 and 11.)

[11] S. P. Martin. A Supersymmetry primer. *Adv. Ser. Direct. High Energy Phys.18*, 1997. (Cited on page 2.)

[12] G. Bertone, D. Hooper, J. Silk, Joseph. Particle dark matter: Evidence, candidates and constraints. *Phys. Rept.*, 405:279–390, 2005. (Cited on page 2.)

[13] The CMS Collaboration. The CMS experiment at the CERN LHC. *JINST*, 3:S08004, 2008. (Cited on pages 2 and 26.)

[14] ATLAS Collaboration. Observation of a new particle in the search for the Standard Model Higgs boson with the ATLAS detector at the LHC. *Phys. Lett.*, B716:1–29, 2012. (Cited on page 2.)

[15] The CMS Collaboration. Observation of a new boson at a mass of 125 GeV with the CMS experiment at the LHC. *Phys. Lett.*, B716:30–61, 2012. (Cited on page 2.)

[16] The ATLAS and CMS Collaborations. Measurements of the Higgs boson production and decay rates and constraints on its couplings from a combined ATLAS and CMS analysis of the LHC pp collision data at $\sqrt{s} = 7$ and 8 TeV. *JHEP*, 08:045, 2016. (Cited on page 2.)

[17] The ATLAS and CMS Collaborations. SUSY searches: Recent results from ATLAS and CMS. *J. Phys. Conf. Ser.*, 631(1):012072, 2015. (Cited on page 3.)

[18] ATLAS Collaboration. Search for dark matter in events with a Z boson and missing transverse momentum in pp collisions at $\sqrt{s}$=8 TeV with the ATLAS detector. *Phys. Rev.*, D90(1):012004, 2014. (Cited on page 3.)

[19] ATLAS Collaboration. Search for dark matter in events with heavy quarks and missing transverse momentum in *pp* collisions with the ATLAS detector. *Eur. Phys. J.*, C75(2), 2015. (Cited on page 3.)

[20] K. G. Begeman, A. H. Broeils, R. H. Sanders. Extended rotation curves of spiral galaxies: Dark haloes and modified dynamics. *Mon. Not. Roy. Astron. Soc.*, 249:523, 1991. (Cited on page 3.)

[21] A. Refregier. Weak gravitational lensing by large scale structure. *Ann. Rev. Astron. Astrophys.*, 41:645–668, 2003. (Cited on page 3.)

[22] M. E. Peskin, D. V. Schroeder. *An Introduction to Quantum Field Theory*. Westview Press, 1995. (Cited on page 7.)

[23] I. J. R. Aitchison, Ian J R, A. J. G Hey. *Gauge Theories in Particle Physics: A Practical Introduction*. CRC Press, 2013. (Cited on page 7.)

[24] R. K. Ellis, W. J. Stirling, B. R. Webber. *QCD and Collider Physics*. Cambridge University Press, 2003. (Cited on page 8.)

[25] S. L. Glashow. Partial Symmetries of Weak Interactions. *Nucl. Phys.*, 22:579–588, 1961. (Cited on page 9.)

[26] A. Salam. Renormalizability of Gauge Theories. *Phys. Rev.*, 127:331–334, 1962. (Cited on page 9.)

[27] S. Weinberg. A Model of Leptons. *Phys. Rev. Lett.*, 19:1264–1266, 1967. (Cited on page 9.)

[28] R. P. Feynman. Very High-Energy Collisions of Hadrons. *Phys. Rev. Lett.*, 23:1415–1417, 1969. (Cited on page 13.)

[29] F. Close. *An Introduction to Quarks and Partons*. Academic Press, 1979. (Cited on page 13.)

[30] L. A. Harland-Lang, A. D. Martin, P. Motylinski, R. S. Thorne. Parton distributions in the LHC era: MMHT 2014 PDFs. *Eur. Phys. J.*, C75(5):204, 2015. (Cited on page 14.)

[31] G. Altarelli, G. Parisi. Asymptotic Freedom in Parton Language. *Nucl. Phys.*, B126:298–318, 1977. (Cited on page 14.)

[32] J. C. Collins, D. E. Soper, G. F. Sterman. Factorization of Hard Processes in QCD. *Adv. Ser. Direct. High Energy Phys.*, 5:1–91, 1989. (Cited on page 14.)

[33] E. D. Bloom et al. High-Energy Inelastic *e-p* Scattering at 6° and 10°. *Phys. Rev. Lett.*, 23:930–934, 1969. (Cited on page 14.)

[34] HERA. HERA - A Proposal for a Large Electron Proton Colliding Beam Facility at DESY. *DESY-HERA*, 81–10, 1981. (Cited on page 15.)

[35] The H1 and ZEUS Collaborations. Combined Measurement and QCD Analysis of the Inclusive $e^{\pm}p$ Scattering Cross Sections at HERA. *JHEP*, 01:109, 2010. (Cited on pages 15 and 134.)

[36] L. Armitage, S. Glazov, R. Keeler, T. Kwan, D. MacDonell, E. Rizvi, A. Sapronov, N. Vranjes, E. Yatsenko. Measurement of the Drell-Yan triple-differential cross-section in pp collisions at $\sqrt{s}$= 8 TeV. *ATL-COM-PHYS-2015-1575*, 2016. (Cited on pages 15, 170, 195, 198, and 208.)

[37] J. C. Collins, D. E. Soper. Angular distribution of dileptons in high-energy hadron collisions. *Phys. Rev. D*, 16:2219–2225, 1977. (Cited on page 17.)

[38] ATLAS Collaboration. Measurement of the forward-backward asymmetry of electron and muon pair-production in pp collisions at $\sqrt{s}$ = 7 TeV with the ATLAS detector. *JHEP*, 09:049, 2015. (Cited on page 19.)

[39] SLD Electroweak Group, DELPHI, ALEPH, SLD, SLD Heavy Flavour Group, OPAL, LEP Electroweak Working Group, L3. Precision electroweak measurements on the Z resonance. *Phys. Rept.*, 427:257–454, 2006. (Cited on page 20.)

[40] The CDF Collaboration. Measurement of $\sin^2\theta^{\rm lept}_{\rm eff}$ using e^+e^- pairs from γ^*/Z bosons produced in $p\bar{p}$ collisions at a center-of-momentum energy of 1.96 TeV. *Phys. Rev.*, D93(11):112016, 2016. (Cited on page 20.)

[41] L. Evans, P. Bryant. LHC Machine. *JINST*, 3:S08001, 2008. (Cited on page 25.)

[42] The ALICE Collaboration. The ALICE experiment at the CERN LHC. *JINST*, 3:S08002, 2008. (Cited on page 26.)

[43] The MoEDAL Collaboration. Technical Design Report of the MoEDAL Experiment. *CERN-LHCC-2009-006, MoEDAL-TDR-001*, 2009. (Cited on page 26.)

[44] The TOTEM Collaboration. The TOTEM experiment at the CERN Large Hadron Collider. *JINST*, 3:S08007, 2008. (Cited on page 26.)

[45] The LHCf Collaboration. The LHCf detector at the CERN Large Hadron Collider. *JINST*, 3:S08006, 2008. (Cited on page 26.)

[46] The LHCb Collaboration. The LHCb Detector at the LHC. *JINST*, 3:S08005, 2008. (Cited on page 26.)

[47] S. Holmes, R. S. Moore, V. Shiltsev. Overview of the Tevatron Collider Complex: Goals, Operations and Performance. *JINST*, 6:T08001, 2011. (Cited on page 26.)

[48] The CDF and D0 Collaborations. Tevatron Higgs results. *EPJ Web Conf.*, 60:02003, 2013. (Cited on page 26.)

[49] ATLAS Collaboration. Measurement of the total cross section from elastic scattering in pp collisions at $\sqrt{s} = 8$ TeV with the ATLAS detector. *Phys. Lett.*, B761:158–178, 2016. (Cited on page 28.)

[50] ATLAS Collaboration. ATLAS: Detector and physics performance technical design report, Volumes I and II. *CERN-LHCC-99-15/16*, 1999. (Cited on page 28.)

[51] ATLAS Collaboration. ATLAS inner detector: Technical design report, Volumes I and II. *CERN-LHCC-97-16/17*, 1997. (Cited on page 30.)

[52] C. Patrignani et al. Review of Particle Physics. *Chin. Phys.*, C40(10), 2016. (Cited on pages 30 and 33.)

[53] ATLAS Collaboration. ATLAS pixel detector: Technical design report. 1998. (Cited on page 31.)

[54] ATLAS Collaboration. The barrel modules of the ATLAS semiconductor tracker. *Nucl. Instrum. Meth.*, A568:642–671, 2006. (Cited on page 31.)

[55] ATLAS Collaboration. The ATLAS semiconductor tracker end-cap module. *Nucl. Instrum. Meth.*, A575:353–389, 2007. (Cited on page 31.)

[56] ATLAS Collaboration. The ATLAS Transition Radiation Tracker (TRT) proportional drift tube: Design and performance. *JINST*, 3:P02013, 2008. (Cited on page 32.)

[57] ATLAS Collaboration. ATLAS liquid argon calorimeter: Technical design report. *CERN-LHCC-96-41*, 1996. (Cited on page 34.)

[58] ATLAS Collaboration. ATLAS tile calorimeter: Technical design report. *CERN-LHCC-96-42*, 1996. (Cited on page 36.)

[59] ATLAS Collaboration. ATLAS muon spectrometer: Technical design report. *CERN-LHCC-97-22*, 1997. (Cited on page 37.)

[60] ATLAS Collaboration. ATLAS first level trigger: Technical design report. *CERN-LHCC-98-14*, 1998. (Cited on page 40.)

[61] ATLAS Collaboration. ATLAS high-level trigger, data acquisition and controls: Technical design report. *CERN-LHCC-2003-022*, 2003. (Cited on page 40.)

[62] ATLAS Collaboration. Luminosity determination in pp collisions at $\sqrt{s} = 8$ TeV using the ATLAS detector at the LHC. *CERN-EP-2016-117*, 2016. (Cited on pages 42, 44, and 109.)

[63] ATLAS Collaboration. Proposal for truth particle observable definitions in physics measurements. 2015. (Cited on page 46.)

[64] S. Agostinelli et al. GEANT4: A simulation toolkit. *Nucl. Instrum. Meth.*, A506:250–303, 2003. (Cited on page 47.)

[65] ATLAS Collaboration. Improved luminosity determination in pp collisions at *sqrts* = 7 TeV using the ATLAS detector at the LHC. *Eur. Phys. J.*, C73(8):2518, 2013. (Cited on pages 48 and 51.)

[66] S. Alioli, P. Nason, C. Oleari, E. Re. A general framework for implementing NLO calculations in shower Monte Carlo programs: the POWHEG BOX. *JHEP*, 06:043, 2010. (Cited on page 48.)

[67] T. Sjostrand, S. Mrenna, P. Z. Skands. A Brief Introduction to PYTHIA 8.1. *Comput. Phys. Commun.*, 178:852–867, 2008. (Cited on page 48.)

[68] P. Golonka, Z. Was. PHOTOS Monte Carlo: A Precision tool for QED corrections in Z and W decays. *Eur. Phys. J.*, C45:97–107, 2006. (Cited on page 48.)

[69] G. Corcella et al. HERWIG 6: An Event generator for hadron emission reactions with interfering gluons (including supersymmetric processes). *JHEP*, 01:010, 2001. (Cited on page 49.)

[70] J. M. Butterworth, J. R. Forshaw. Photoproduction of multi-jet events at HERA: A Monte Carlo simulation. *J. Phys.*, G19:1657–1663, 1993. (Cited on page 49.)

[71] S. P. Baranov, O. Duenger, H. Shooshtari, J. A. M. Vermaseren. LPAIR: A generator for lepton pair production. In *Workshop on Physics at HERA Hamburg, Germany, October 29-30, 1991*, pages 1478–1482, 1991. (Cited on page 49.)

[72] P. Nason. A new method for combining NLO QCD with shower Monte Carlo algorithms. *JHEP*, 11:040, 2004. (Cited on page 49.)

[73] S. Frixione, P. Nason, C. Oleari. Matching NLO QCD computations with parton shower simulations: The POWHEG method. *JHEP*, 11:070, 2007. (Cited on page 49.)

[74] M. Guzzi et al. CT10 parton distributions and other developments in the global QCD analysis. *arXiv*, 1101.0561, 2011. (Cited on pages 50 and 112.)

[75] ATLAS Collaboration. Summary of ATLAS Pythia 8 tunes. *ATL-PHYS-PUB-2012-003, ATL-COM-PHYS-2012-738*, 2012. (Cited on page 50.)

[76] ATLAS Collaboration. Measurement and QCD Analysis of Differential Inclusive $W^{\pm} \to \ell\nu$ and $Z \to \ell\ell$ Production and Leptonic Decay Cross Sections with ATLAS. *ATL-COM-PHYS-2013-217*, 2013. (Cited on pages 51, 137, and 195.)

[77] J. M. Campbell, R. K. Ellis. An Update on vector boson pair production at hadron colliders. *Phys. Rev.*, D60:113006, 1999. (Cited on page 51.)

[78] J. M. Campbell, R. K. Ellis, C. Williams. Vector boson pair production at the LHC. *JHEP*, 07:018, 2011. (Cited on page 51.)

[79] M. Cacciari, M. Czakon, M. Mangano, A. Mitov, P. Nason. Top-pair production at hadron colliders with next-to-next-to-leading logarithmic soft-gluon resummation. *Phys. Lett.*, B710:612–622, 2012. (Cited on page 51.)

[80] P. Baernreuther, M. Czakon, A. Mitov. Percent Level Precision Physics at the Tevatron: First Genuine NNLO QCD Corrections to $q\bar{q} \to t\bar{t} + X$. *Phys. Rev. Lett.*, 109:132001, 2012. (Cited on page 51.)

[81] N. Kidonakis. Two-loop soft anomalous dimensions for single top quark associated production with a W^- or H^-. *Phys. Rev.*, D82:054018, 2010. (Cited on page 51.)

[82] D. Bardin, S. Bondarenko, P. Christova, L. Kalinovskaya, L. Rumyantsev, A. Sapronov, W. von Schlippe. SANC integrator in the progress: QCD and EW contributions. *JETP Lett.*, 96:285–289, 2012. (Cited on page 52.)

[83] S. G. Bondarenko, A. A. Sapronov. NLO EW and QCD proton-proton cross section calculations with mcsanc-v1.01. *Comput. Phys. Commun.*, 184:2343–2350, 2013. (Cited on page 52.)

[84] ATLAS Collaboration. Measurement of exclusive $\gamma\gamma \to \ell^+\ell^-$ production in proton-proton collisions at $\sqrt{s} = 7$ TeV with the ATLAS detector. *Phys. Lett.*, B749:242–261, 2015. (Cited on page 52.)

[85] ATLAS Collaboration. ATLAS inner detector results from the 2004 combined test beam data. 2006. (Cited on page 51.)

[86] ATLAS Collaboration. Energy linearity and resolution of the ATLAS electromagnetic barrel calorimeter in an electron test-beam. *Nucl. Instrum. Meth.*, A568:601–623, 2006. (Cited on page 51.)

[87] ATLAS Collaboration. Measurement of the double-differential high-mass Drell-Yan cross section in pp collisions at $\sqrt{s} = 8$ TeV with the ATLAS detector. *JHEP*, 08:009, 2016. (Cited on page 53.)

[88] Y. Li, F. Petriello. Combining QCD and electroweak corrections to dilepton production in the framework of the FEWZ simulation code. *Phys. Rev. D*, 86:094034, 2012. (Cited on page 53.)

[89] ATLAS Collaboration. Improved electron reconstruction in ATLAS using the Gaussian Sum Filter-based model for bremsstrahlung. Technical report, 2012. (Cited on page 55.)

[90] W. Lampl et al. Calorimeter clustering algorithms: Description and performance. *ATL-LARG-PUB-2008-002, ATL-COM-LARG-2008-003*, 2008. (Cited on pages 56 and 57.)

[91] ATLAS Collaboration. Electron performance measurements with the ATLAS detector using the 2010 LHC proton-proton collision data. *Eur. Phys. J.*, C72:1909, 2012. (Cited on pages 58 and 111.)

[92] ATLAS Collaboration. Combined performance studies for electrons at the 2004 ATLAS combined test-beam. *JINST*, 5(11):P11006, 2010. (Cited on page 60.)

[93] ATLAS Collaboration. Electron and photon energy calibration with the ATLAS detector using LHC Run 1 data. *Eur. Phys. J.*, C74(10):3071, 2014. (Cited on pages 61, 62, and 110.)

[94] ATLAS Collaboration. Electron efficiency measurements with the ATLAS detector using the 2012 LHC proton-proton collision data. *ATLAS-CONF-2014-032*, 2014. (Cited on pages 63 and 165.)

[95] ATLAS Collaboration. Electron reconstruction and identification efficiency measurements with the ATLAS detector using the 2011 LHC proton-proton collision data. *Eur. Phys. J.*, C74(7):2941, 2014. (Cited on page 64.)

[96] G. D'Agostini. A Multidimensional unfolding method based on Bayes' theorem. *Nucl. Instrum. Meth.*, A362:487–498, 1995. (Cited on page 75.)

[97] G. D'Agostini. Improved iterative Bayesian unfolding. *arXiv*, 1010.0632, 2010. (Cited on page 75.)

[98] ATLAS Collaboration. Measurement of the transverse momentum and ϕ^*_η distributions of DrellYan lepton pairs in protonproton collisions at $\sqrt{s} = 8$ TeV with the ATLAS detector. *Eur. Phys. J.*, C76(5):291, 2016. (Cited on page 77.)

[99] B. Efron, R. J. Tibshirani. *An Introduction to the Bootstrap*. Chapman and Hall, 1993. (Cited on pages 79 and 107.)

[100] ATLAS Collaboration. Evolution and Performance of Electron and Photon Triggers in ATLAS in the year 2011. *ATL-DAQ-PROC-2012-016*. (Cited on page 80.)

[101] ATLAS Collaboration. Monitoring and data quality assessment of the ATLAS liquid argon calorimeter. *JINST*, 9:P07024, 2014. (Cited on page 81.)

[102] T. Adye. Unfolding algorithms and tests using RooUnfold. In *Proceedings, PHYSTAT 2011 Workshop on Statistical Issues Related to Discovery Claims in Search Experiments and Unfolding, CERN,Geneva, Switzerland 17-20 January 2011*, pages 313–318, Geneva, 2011. CERN, CERN. (Cited on page 101.)

[103] N. Andari, M. Boonekamp, L. Carminati, N. M. Lorenzo, M. Rimoldi, R. Turra, G. Unal. Calibration systematic uncertainties: Overview and correlations. *ATL-COM-PHYS-2013-1654*, 2013. (Cited on page 110.)

[104] J. Pumplin, D. R. Stump, J. Huston, H. L. Lai, P. M. Nadolsky, W. K. Tung. New generation of parton distributions with uncertainties from global QCD analysis. *JHEP*, 07:012, 2002. (Cited on page 112.)

[105] J. M. Campbell, R. K. Ellis. MCFM for the Tevatron and the LHC. *Nucl. Phys. Proc. Suppl.*, 205-206:10–15, 2010. (Cited on page 134.)

[106] A. D. Martin, W. J. Stirling, R. S. Thorne, G. Watt. Parton distributions for the LHC. *Eur. Phys. J.*, C63:189–285, 2009. (Cited on page 134.)

[107] R. D. Ball et al. Parton distributions with LHC data. *Nucl. Phys.*, B867:244–289, 2013. (Cited on page 134.)

[108] ATLAS Collaboration. Determination of the strange quark density of the proton from ATLAS measurements of the $W \to \ell\nu$ and $Z \to \ell\ell$ cross sections. *Phys. Rev. Lett.*, 109:012001, 2012. (Cited on page 134.)

[109] ATLAS Collaboration. Measurement of the low-mass Drell-Yan differential cross section at $\sqrt{s} = 7$ TeV using the ATLAS detector. *JHEP*, 06:112, 2014. (Cited on page 137.)

[110] E. Yatsenko. *Measurement of Neutral Current Drell-Yan production using ATLAS data collected at $\sqrt{s}$ = 8 TeV*. PhD thesis, University of Hamburg, 2015. (Cited on page 154.)

[111] N.D. Gagunashvili. Comparison of weighted and unweighted histograms. *arXiv*, 0605123, 2006. (Cited on page 158.)

[112] L. J. Armitage. *Measurement of the DrellYan triple-differential cross-section in pp collisions at $\sqrt{s}$ = 8 TeV with the ATLAS detector*. PhD thesis, Queen Mary, University of London, 2016. (Cited on page 195.)

[113] A. Glazov. Averaging of DIS Cross Section Data. *AIP Conf. Proc.*, 792:237–240, 2005. (Cited on page 195.)

[114] ATLAS Collaboration. Study of alignment-related systematic effects on the ATLAS Inner Detector tracking. *ATLAS-CONF-2012-141*, 2012. (Cited on page 196.)

[115] ATLAS Collaboration. Measurement of the W-boson mass in pp collisions at $\sqrt{s} = 7$ TeV with the ATLAS detector. *arXiv*, 1701.07240, 2017. (Cited on page 196.)

[116] W. Verkerke, D. P. Kirkby. The RooFit toolkit for data modeling. *eConf*, C0303241:MOLT007, 2003. (Cited on page 197.)